Characterisation of DNA Delivery through Fluctuation Correlation Spectroscopy

Stephen Paul Mieruszynski

Doctor of Philosophy (PhD)

A thesis submitted in the fulfilment of the Doctor of Philosophy degree

School of Science and Health

University of Western Sydney

In collaboration with the Laboratory for Fluorescence Dynamics, University of California, Irvine, USA

DEDICATION

This thesis is dedicated to my recently wedded wife Jasmyne Cossette (Middleton) Mieruszynski.

PROJECT OVERVIEW

The delivery process of non-viral gene vectors through the cell face a number of barriers, many of which have not been fully characterised. A key limitation has been the inability to quantify the dynamic behaviour of delivered DNA as it traffics through the live cell. However, recent developments in the field of Fluorescence Correlation Spectroscopy (FCS) now provide a means to study the fluctuations of individual particles from image series. Such approaches have the ability of extract information on the dynamics and aggregation of fluorescently labelled particles.

Throughout this thesis a series of image-based FCS approaches have been applied to gain a deeper understanding of DNA processing when delivered through lipofection. Across these studies DNA sequences of various lengths labelled with a small molecular probe were delivered into myoblast cells.

Before this work, no previous studies have applied such techniques to the uptake of macromolecules, therefore, this thesis focuses on four major factors that are critical in gene delivery and cell biology; (i) how the DNA moves through the cell (RICS and iMSD), (ii) quantifying the aggregation of delivered DNA (N&B), (iii) determining the extent of degradation that occurs (ccRICS and ccN&B), and (iv) how the cellular physiology can affect the delivered DNA behaviour.

The novel application of these techniques demonstrated that DNA processing exhibited a clear predefined pathway. Studies on the dynamics of the delivered DNA revealed that the rate of motion were similar across different DNA sizes, which also exhibited a spatial dependence on the transport mechanisms. The aggregation of delivered DNA was quantified for the first time, showing that extensive aggregation occurs throughout the cell and is influenced by the DNA size and sequence, and serum concentrations. The rate of degradation was explored, which has exhibited a slow rate of degradation in the lipoplex delivered DNA with a longer half-life compared to previous studies. Degradation was also shown to be dependent on a number of factors, including the amount of DNA present, aggregation, and the transport mechanism and location of the cell. Finally, the effects of membrane states was explored, demonstrating that the membrane plays a pivotal role in how the DNA is taken up, and behaves within the cell.

The techniques applied to study the molecular mechanisms of delivered DNA, provide the opportunity to better understand the gene delivery process through the study of the dynamics of the cell. In addition, this work also presents a model to study the update and processing of other macromolecules.

STATEMENT OF AUTHENTICITY

The work presented in this thesis is, to the best of my knowledge and belief, original except as acknowledged in the text. I hereby declare that I have not submitted this material, either in full or in part, for a degree at this or any other institution.

.....

ACKNOWLEDGEMENT

I would like to thank my supervisors Mark Jones, Enrico Gratton and Michelle Digman for providing me with the opportunity to do this work. Their guidance, patience, and generosity have been greatly appreciated. Thanks to your support I have not only managed to grow as a scientist, but you have all had an impact on my life in so many more aspects.

I would also like to thank all of the technical staff that provide the necessary support to allow the facilities I have worked in possible, in particular Karen Stephenson (UWS) and Milka Stakic (LFD).

Finally, I would like to thank my family for their support throughout my education.

THESIS CONTENTS

RESULTING PUBLICATIONS

From this thesis four publications have results:

- Stephen Mieruszynski, Candida Briggs, Michelle A. Digman, Enrico Gratton, Mark R Jones "Live Cell Characterization of DNA Aggregation Delivered through Lipofection", Scientific Reports, Status: accepted and in press
- Stephen Mieruszynski, Michelle A. Digman, Enrico Gratton, Mark R Jones "Characterisation of the molecular mechanisms behind DNA lipoplex mobility", Scientific Reports, Status: first review received 16/03/2015, now awaiting revised manuscript to be submitted.
- Stephen Mieruszynski, Michelle A. Digman, Enrico Gratton, Mark R Jones "Quantifying the Real-time Degradation of Intracellular DNA Lipoplexes", Manuscript in final stages of drafting.
- Stephen Mieruszynski, Ottavia Golfetto, Michelle A. Digman, Enrico Gratton, Mark R Jones "The Effects of Membrane State on Intracellular Lipoplex Dynamics", in draft.

FIGURES

TABLES

EQUATIONS

ACRONYMS

2D	Two Dimension	N	Apparent Number
3D	Three Dimension	*n*	True particle number
ACF	Auto-Correlation Function	N&B	Number and Brightness
APD	Avalanche Photodiode	NE	Nuclear Envelope
AS	Anomalous Subdiffusion	NLS	Nuclear Localising Signal
AT	Active Transport	NPC	Nuclear Pore Complex
B	Apparent Brightness	PCH	Photon Counting Histogram
B-UB	Bunding-Unbinding	PCR	Polymerase Chain Reaction
ccRICS	cross-correlated Raster Image Correlation Spectroscopy	PEI	Polyethylenimine
CD	Confined Diffusion	PLL	Poly-L-Lysine
cpsm	counts per second per molecule	PML	Promyelocytic Leukemia bodies
CT/s	Chromosome Territory/ies	PNA	Protein-Nucleic Acid
DMEM	Dulbecco's Modified Eagle's medium	PSF	Point Spread Function
DNA	Deoxyribonucleic Acid	RD	Random Diffusion
ECM	Extra-cellular Matrix	RICS	Raster Image Correlation Spectroscopy
FBS	Fetal Bovine Serum	RNA	Ribonucleic Acid
FCCS	Fluorescence Cross-Correlated Spectroscopy	ROI	Region-Of-Interest
FCS	Fluorescence Correlation Spectroscopy	SAF-A	Nuclear Scaffolding protein
FFT	Fast Fourier Transform	SCAF	Spatial Auto-Correlation Function
FISH	Fluorescence in situ Hybridization	SPT	Single Particle Tracking
flDNA	Fluorescently-labelled DNA	SV40	Simian Virus 40
FLIM	Fluorescence Lifetime Imaging Microscopy	TC	Transient Confinement
FRAP	Fluorescence Recovery After Photobleaching	TCS-SP5	True Confocal Scanner – Spectro-Photometer 5
GFP	Green Fluorescent Protein	TUNEL	Terminal deoxynucleotidyl transferase dUTP nick end labelling
iMSD	image-Means Square Displacement	WGA	Wheat Germ Agglutinin
MA	Moving Average	ε	True molecular brightness
MSD	Means Square Displacement		

CHAPTER 1

Introduction

Gene delivery or gene therapy involves the coupling of a nucleic acid sequences with a delivery vehicle, such as viruses or lipids, to facilitate uptake into the target cell. During the delivery of the exogenous nucleic acid sequences a number of obstacles are faced. As a result there has been a significant emphasis on developing an understanding of the processes involved. To date most studies have focused on limited time intervals or small regions of the cell, or fixed samples. Developing a real-time, multi-level information approach to characterise the live cell responses to exogenous nucleic acid sequences is expected to underpin optimising Gene Therapy methodology. In addition, it is likely this approach could be applied to drug delivery and enhance our understanding of cellular processing.

Fluorescence Correlation Spectroscopy (FCS) is one approach to analyse single molecules of extremely low concentration with high spatial and temporal resolution (for example, 600 particles are expected to be within the illumination volume at a given time in a 1 μM solution of a small molecule). Compared to other fluorescence-based approaches FCS measures the spontaneous intensity fluctuations caused by minute changes in particle behaviour, rather than relying on the emission intensity of fluorescence. Fundamentally, FCS has the potential to measure and fully quantify all physical processes occurring in a cell that give rise to fluctuations in the fluorescence signal including mobility and aggregation.

Although a powerful technique, a significant limitation in the FCS approach is that only a single, small volume can be observed at one given time. Therefore, several approaches have been devised that involve scanning the FCS volume across a sample essentially obtaining a large number of FCS

measurements in the form of an image. Such approaches have demonstrated their potential to extract information on mobility, aggregation and molecular interactions [1-4]. In addition, the approach requires a process where the particle of interest must be fluorescently labelled.

FCS based approaches now offer a means of further characterising the delivery of therapeutic molecules, including but not limited to synthetic drugs, gene delivery vectors and other nanoparticles, or potentially detrimental amalgams such as toxins or viruses, all of which have the potential to be labelled with small fluorescence tags. Therefore, this study aims to fill this void by studying macromolecule delivery through the application of FCS-based techniques including:

- Raster Image Correlation Spectroscopy (RICS),
- Number and Molecular Brightness (N&B),
- Image-based Means Square Displacement (iMSD), and
- Spectral phasor

For this study the non-viral gene delivery approach, lipofection, has been used as a model, as lipoplexes (the composition of DNA and lipids) have the potential to be a relevant model for other delivery systems. This thesis has been structured to first provide an insight into the principle concepts of FCS, followed by an in depth review of processes for lipoplex delivery through the cell. The relevant background for each bioimaging tool is introduced at the beginning of the respective chapter, which address critical factors that can influence gene delivery outcomes: Including mobility and dynamics, aggregation, degradation, and how the cell physiology can affect them.

1.1 Fluorescence Correlation Spectroscopy

Fluorescence Correlation Spectroscopy (FCS), or point-FCS, is a sensitive technique that was initially developed to study the dynamic processes of fluorescently labelled molecules within equilibrium environments [5]. The technique provides information of many molecules at a single

molecule level and, by averaging the behaviour of the molecules enable comprehensive statistical data and analysis [6].

The principles and concepts of FCS were first developed in the 1970's by Magde *et al.* (1972) who studied the binding of ethidium bromide to double stranded DNA [7]. Although the principles of the technique were established they could not be applied due to limited technology. The necessary technology for FCS, developed in the 1990's, included the confocal microscope and efficient photon detectors [5,6,8].

The FCS field was originally derived from the dynamic light scattering technique [6], which depends on the scattering of light from particles within the volume of a sample [9]. Instead, FCS takes advantage of fluorescence fluctuations emitted from fluorophores passing through a small illumination volume [6]. A small open-volume is created by focusing a laser beam into a sample (termed, Point Spread Function (PSF), beam waist, or ω) [5]. Within the confocal volume, fluorophores will be excited resulting in a burst of fluorescence photons (or signals) (Figure 1.1). Time courses of fluctuations contain information on the dynamic processes and chemical kinetics of the molecules within the defined illumination volume (Figure 1.2). Molecules will enter and/or exit the excitation volume, leading to changes in the fluorescence signals that are detected [5]. The FCS technique is sufficiently sensitive to detect single molecules within the excitation volume [6].

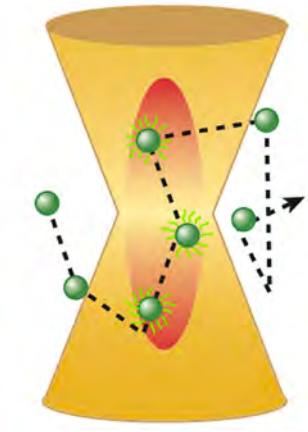

Figure 1.1 – A Single Molecule in FCS Illumination Volume
As a molecule (green) moves in a solution via Brownian motion it passes though the volume of excitation (red) and fluoresces to emit photons, which are detected as statistical signals. (Sourced from Digman and Gratton, 2011 [6])

The FCS analysis is commonly achieved by applying correlation functions, however a number of other methods and approaches have also been proposed [6,10,11]. This project focused on using the correlation function approach, in which two aspects are calculated in a fluctuation record [6]. The first

aspect is the determination of the temporal spectrum of fluctuations through the application of the Autocorrelation Function (ACF) approach [6]. The second aspect applies the Photon Counting Histogram (PCH) (or fluctuation intensity distribution analysis) in order to analyse the amplitude spectrum of the fluctuation range [6] (Figure 1.2).

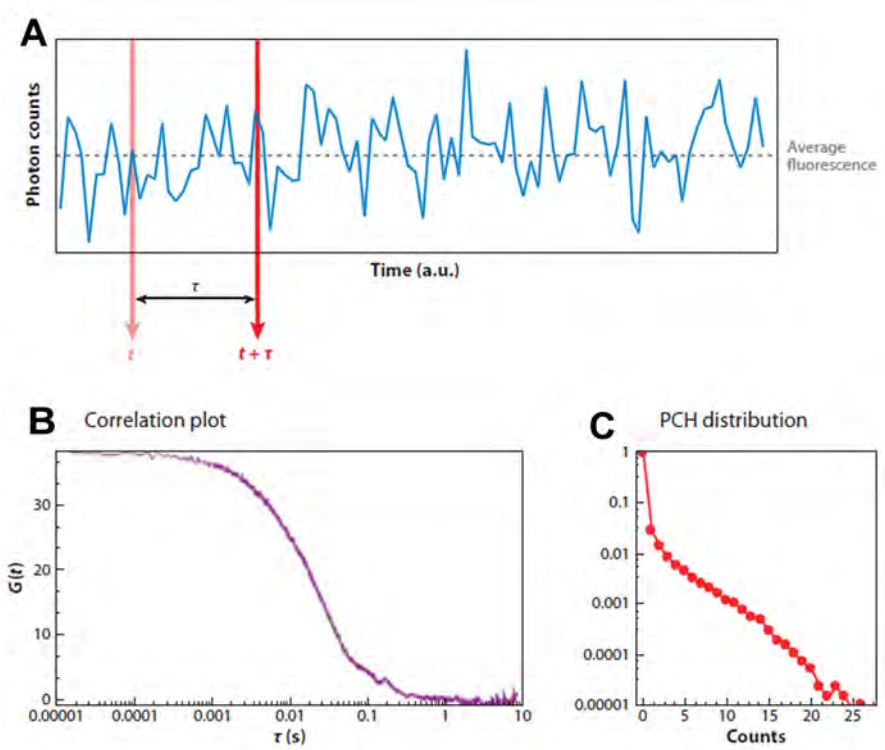

Figure 1.2 – Fluorescence Correlation Spectroscopy Data and Analysis

Fluctuations in photons are counted over time (A), the analysis of these fluctuations of the sampling period enables the rate of motion to be calculated through the autocorrelation function $G(\tau)$ (B) and provides the photon counting histogram (PCH) analysis (C). (Sourced from Digman and Gratton, 2011 [6])

The diffusion constant for translational movement is calculated from the ACF ($G(\tau)$), which relates to the fluorescence intensity (F) at a given time (t) to the given τ seconds later:

$$G(\tau) = \frac{\langle \delta I(t) \cdot \delta I\ (t+\tau) \rangle}{\langle I(t) \rangle^2}$$

Equation 1 - Normalised Autocorrelation Function

where δI denotes the fluctuation of the fluorescence intensity around the mean value $\langle I(t) \rangle$ [5,6].

The PCH approach focuses on the probability distribution to detect photons per sample time. The distribution of the detected photons enables the characterisation of the average number of molecules (N) and the molecular brightness (ε) of a fluorescence fluctuation experiment [12].

1.1.1 Scanning Correlation Spectroscopy

A significant limitation of FCS is the inability to acquire spatial information on the fluctuations occurring outside of the relatively small measured volume. Many processes involved in chemistry, physics and biology require spatial details. However, by moving the excitation volume in a defined pattern (i.e. a circular orbit, raster scan or straight line), at a rate that is relative to the movement of the molecules during the defined period, will provide a record of the intensity fluctuations and will contain spatial information about where these fluctuations have occurred within a sample. Since scanning introduces a spatial and temporal structure to the observation, both the spatial and temporal information can be extracted and related to the physical processes that have occurred in biological systems, such as mammalian cells [6].

Scanning FCS entails the acquisition along a specific pattern, by the laser, over a sample in a laser scanning microscope [6]. The principle of scanning FCS is to calculate the Spatial Auto-Correlation Function (SACF) of a data series or an image. Within the cell, the technique provides information on the mobility, degree of aggregation and number of fluorescently labelled molecules [6].

The concept of extending FCS to study images has resulted in the development of a number of bioimaging tools, which include (but are not limited to) the Raster Image Correlation Spectroscopy (RICS), image-based Means Square Displacement (iMSD) and Number and molecular Brightness (N&B) approaches, all of which are applied throughout this project; enabling the determination of mobility rates, mechanisms of motion and degree of aggregation, respectively.

1.2 Intracellular Trafficking of Nucleic Acid Sequences

Gene delivery involves the trafficking of the introduced nucleic acid sequences, coupled with a vector, through the cellular milieu within the cytoplasm, the nucleus or another organelle, depending on its fate, which may include nucleic acid degradation, recycling, toxic build up, and expulsion. During gene trafficking, the nucleic acids are expected to encounter a number of obstacles, which are the cause of many limitations in current gene therapy approaches, many of which have yet to be fully characterized in real time.

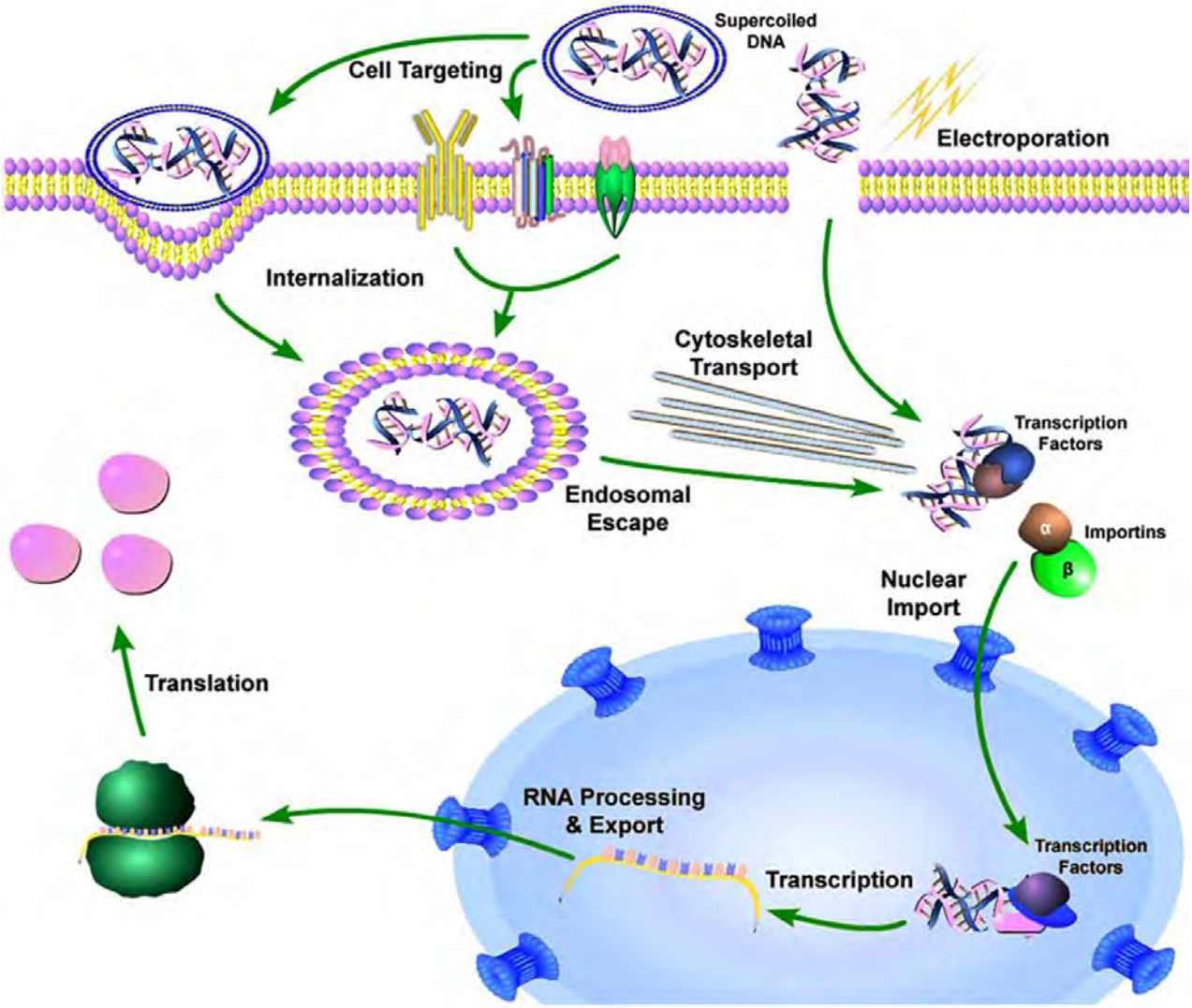

Figure 1.3 – Trafficking Overview of Non-viral Gene Delivery

Firstly, the vector encounters the extra-cellular matrix where it may be immobilized by certain compounds within the matrix (such as albumin). During entry into the cell, the vector interacts with membrane receptors or membrane compounds leading to the internalization of the vector complex, a similar process occurs for some viruses. However, the vector can be internalised through mechanical means, such as electroporation. The vector is transported within a vesicle to fuse with early endosomes, where it is either released back out of the cell or further processed into late endosomes. The vector must escape from the endosome, be transported along the microtubule network and then enters the nucleus either during mitosis or through a nuclear pore complex after interacting with cytoplasmic components. (Sourced from Vaughan et al. 2006 [13])

Initially, the nucleic acid will encounter the extracellular matrix (ECM) (unless it is directly inserted into the cell through microinjection). It then must enter the cell through the plasma membrane, most likely via endocytosis, and if internalized through endocytosis, the nucleic acid sequences appear to become entrapped within membrane bound vesicles, known as endosomes, and risk being degraded by lysosomes.

It is not certain if the nucleic acid sequences are transported towards the peri-nuclear region within endosomes or free within the cytoplasm, regardless, it has been established that transportation is achieved through the exploitation of the microtubule network and motor proteins [14]. If targeted for the nucleus, the nucleic acid sequences must transverse the nuclear envelope, which has been identified as the most significant physical barrier to non-viral gene delivery [15]. Once within the nucleus, which is maintained as a complex and organized structure, the nucleic acid sequences may induce the desired effect on the cell's expression profile. Due to the approaches employed by this project, the main focus is on trafficking of synthetic non-viral vectors. A pictorial overview of the gene trafficking process is shown above (Figure 1.3).

1.3 Gene Therapy Vectors

The primary role of a gene therapy vector is to provide the delivered nucleic acid sequence passage in the cell, in particular a route through the plasma membrane into the cytoplasm. Initially, gene transfer started with basic mechanisms of nucleic acid sequence delivery but rapidly evolved applying specialized viruses, polymers and lipids. Due to the interest in gene therapy, an abundance of vectors have been developed, optimized and applied [16]. These vectors can be placed in two main categories: viral vectors, and non-viral vectors (further subdivided into physical mechanisms and synthetic vectors).

1.3.1 Viral Vectors

Viral vectors are a class of viruses exploited to deliver foreign nucleic acid sequences into targeted cells. To-date, viral vectors have been the most commonly applied vectors in clinical trials. Viruses have had millennia to develop efficient nucleic acid sequence transfer into mammalian cells. Viruses can now be commercially engineered to contain foreign nucleic acid sequences within their genomes'. Then through the viruses' natural mechanisms, the foreign nucleic acid sequences can be delivered to the targeted cell with relative efficiency [17].

Viral vectors can be: integrating vectors (which insert their genome into the host's genome), and non-integrating vectors (whose genomes persist within the cell's nucleus usually (but not always) as

an extrachromosomal episome) [17,18]. Common viral vectors include (but are not limited to) retroviruses, lentiviruses, adenoviruses, adeno-associated viruses and herpes simplex viruses.

1.3.2 Non-Viral Vectors

Non-viral gene therapy vectors are those not utilizing live viruses and can be: (i) physical forces or methods, and (ii) chemical-based vectors. Non-viral gene therapy offers a number of advantages over viral vectors including being less immunogenic [19] and having no size limit of the nucleic acid that must be delivered [16]. Non-viral vectors are also generally time and cost efficient to produce, with the potential for repeated administration when non-immunogenic [19]. Non-viral vectors have not been generally regarded as efficient as their viral counterparts. Non-viral vectors offer the potential to deliver to many different cell types and culture systems, making them a feasible approach for *ex vivo* applications. However, there has been little success achieving efficient and safe gene transfer *in vivo* [16].

Physical & Mechanical Mechanisms

A large number and array of physical or mechanical methods of transferring nucleic acid sequences have emerged in gene therapy over the past few decades and include (but are not limited to) direct injection of the naked nucleic acid, transfer by Gene Gun, Electroporation, Optoporation, Sonoporation and Hydrodynamic gene transfer. The main aim of many physical methods of gene delivery is to by-pass cellular membranes and generally utilize 'naked' nucleic acid sequences, such as direct injection, which involves the injection of the nucleic acid into the tissue or cells of interest [20,21].

Chemical-based or Synthetic vectors

Chemical-based or synthetic vectors are by far the most popular non-viral gene therapy strategy and applications to date. The approach of synthetic non-viral gene therapy involves the packaging of naked nucleic acid sequences (most commonly plasmid DNA) with either cationic lipids (lipoplex), or polymers (either synthetic or organic) (polyplex), or a combination of both (lipopolyplex) [16]. The cationic chemical vector forms condensed complexes with the negatively charged nucleic acids through electrostatic interactions, which then facilitate the nucleic acid in trafficking into and through the cell [16,19].

Cationic Lipids (Lipoplex)

Cationic lipid-based gene transfer was first pioneered by Felgner and colleagues in 1987 [22]. Forming lipoplexes with nucleic acids, liposome-mediated gene delivery (also termed lipofection) is the most extensively researched and commonly used non-viral gene therapy approach in use. Since 1987, hundreds of different lipids have been developed, however, they all share the common structure of a positively charged hydrophilic head and hydrophobic tail that are connected by a linker structure. The positively charged head group, usually composed of primary, secondary, tertiary amines or quaternary ammonium salts, is necessary for binding to the negatively charged phosphate backbone in nucleic acids. The hydrophobic tails are usually composed of two types of hydrophobic moieties, aliphatic chains, cholesterol or other types of steroid rings. The linker between the heads and tails are commonly ester, carbamate, or amide bonds, which reflect the rate of biodegradability of the lipid and therefore, the toxicity of the vector [22].

Transfection efficiencies of lipofection varies dramatically depending on the structure of the cationic lipid, including the overall geometric shape, the number of charged groups per molecule, the nature of the lipid anchor, and the linker bondage; the charge ratio used to form lipoplexes, and the properties of any colipid (helper lipid) used [23]. Upon mixing the nucleic acid with the cationic lipids, lipoplexes spontaneously form. The process involves two steps, first an initial and rapid association of the cationic liposomes and anionic DNA through electrostatic interactions, then followed by a slower lipid rearrangement process [24]. Forming the compacted structure called a lipoplex, the nucleic acid molecules are surrounded by the positively charged lipids. Lipoplexes come in various forms, influenced by the packing parameter (*P*), which is defined as the ratio of the hydrophilic head volume and the length of the hydrophobic tail [25]. When the value of *P* is at or very close to 1, the nucleic acid molecules lends to be sandwiched between cationic lipid bilayers (L_{α}^{c}) (Figure 1.4A). When above a *P* value of 1, the lipids will form inverted micelle or inverted hexagonal structures, in which the nucleic acid will be internal and separated from the external environment (Figure 1.4B). For a *P* value less than 0.3 a micelle structure is expected to form and when between 0.3 to 1, a hexagonal structure should form, in which the nucleic acid will be bound to the external surface of the lipoplex (Figure 1.4C) [26,27].

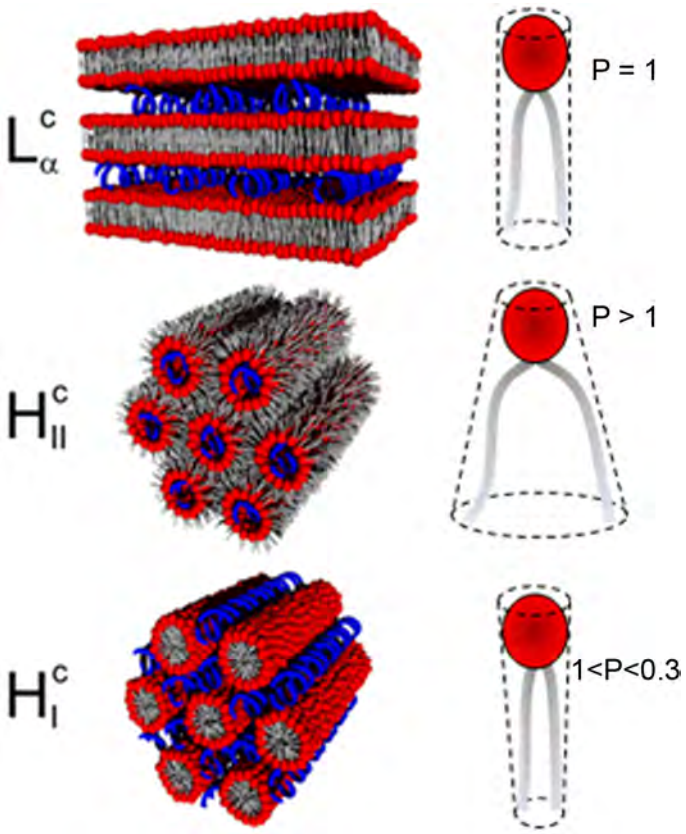

Figure 1.4 – Phase Structure of Lipoplexes based on their Packing Parameter

Lipoplexes contain three regions: hydrophilic head (in red), hydrophobic tail (in grey) and linker. The structure of the lipid is based on the packing parameter P, which is defined as the ratio of the hydrophilic head volume and the length of the hydrophobic tail. When the P value at or very close to 1, the nucleic acid molecules (in blue) lend to be sandwiched between cationic lipid bilayers (L_α^c). As the values becomes greater than 1 the lipids will form a inverted hexagonal structure (H_{II}^c), in which the nucleic acid will be internal. For a P value between 0.3-1, a hexagonal structure should form, in which the nucleic acid will be bound to the external surface of the lipoplex. (Sourced from Tresset, 2009 [28])

Cationic Polymers (Polyplex)

Cationic polymers are another class of chemical-based non-viral gene therapy vector which have been used extensively for gene transfer [19]. Cationic polymer-based gene delivery utilizes cationic polymers, either synthetic or naturally occurring, that form nanosized complexes with nucleic acids (termed polyplexes) [19]. Typically polyplexes are more stable than lipoplexes [19].

Poly-L-lysine (PLL) was one of the first cationic polymers to be used for *in vivo* gene transfer [29]. However, like cationic lipid transfer, over the years a large number of carriers have been applied for both *in vitro* and *in vivo* gene delivery. This class of vectors includes PLL [29], polyethylenimine (PEI) [30-32], polyamidoamine [33], cationic dextran [34], chitosan [35], cationic proteins [36], and cationic peptides [37,38]. Although most cationic polymers share the function of condensing DNA particles and facilitating their transfer into and through the cell, their transfection efficiency and cell toxicity differ dramatically [19]. Transfection efficiency and toxicity of cationic polymers depends on the molecular weight, configuration, the charge ratio of the polymer to the DNA, and the biodegradability of the polymer [19].

Nanoparticles

An emerging class of non-viral vectors utilize inorganic nanoparticles. Usually prepared with metals, including iron, gold and silver; inorganic salts or ceramics, such as phosphate or carbonate salts of calcium, magnesium or silicon, complexes are typically between 10 – 100 nm in diameter [39]. The surface of the nanoparticles are coated with the nucleic acid, which facilitates the uptake of the nucleic acid sequence transported into the cell through specific membrane receptors or nucleolin, thus delivering the nucleic acid sequence to the nucleus and by-passing endosomal/lysosomal degradation [40]. Additionally due to the small size of these complexes, most physiological and cellular barriers are avoided, gene expression is generally higher (compared to other non-viral approaches), they tend to show little or no toxicity and typically do not activate an immune system response [41,42].

1.4 Extracellular Matrix

Within the ECM, the nucleic acid sequence/vector complex is expected to face a number of obstacles. Depending on the vector applied it may induce an immune response once within the body, which has demonstrated to have the potential to kill [43]. If injected intravenously, the nucleic acid complex is expected to travel from the site of injection and through the vascular system to the heart and lungs. Then enter back through the circulatory system to reach the targeted tissue or organ [44-46].

Once within the ECM, nucleic acid sequences complexed with cationic particles have a propensity to interact with endogenous proteins and other constituents, such as glycosaminoglcans [47], serum albumin [48], lipoproteins and immunoglobulins [49], when the vector complex is produced with an excess positive charge. Additionally, positively charged nucleic acid/vector complexes often manifest in reduced colloidal stability, as the increased ionic strength encountered once introduced into the cellular environment may also have an effect on the complexes' physical properties [50]. Physical studies demonstrated that the interaction of positively charged nucleic acid complexes and serum may results in a number of undesirable effects, including aggregation, ζ-potential neutralization, destabilization of the lipoplex structure leading to early nucleic acid release, and degradation [50,51]. When complexes near charge neutrality, aggregation between the vector complexes is frequently observed [50]. When *in vitro*,

nucleic acid and cationic vector complexes may also bind non-specifically to cells, including erythrocytes, lymphocytes and endothelial cells, and to ECM proteins and components [49].

The presence of nucleases within the extracellular milieu also pose a significant obstacle to *in vivo* gene transfer [50]. Degradation of nucleic acids may be rapid when administrated both intravenously [52] and intramuscularly [53].

1.5 Cellular Uptake

The internalisation of the nucleic acid vector by the targeted cell represents the first step in the gene delivery process. It was first believed that cationic lipoplexes were internalized through a fusion process [22], however more recently it has been determined that only a few posses this ability [54,55] (Table 1). It has now been accepted that internalisation occurs through endocytosis, where the binding to or association of the cationic vector with surface receptors activates intracellular signalling pathways promoting endocytosis [56]. Confocal and electron microscopy studies have confirmed endocytosis. For example, cationic lipoplexes were visualized within endosomal compartments within one hour of administration using electron microscopy [57], and the localization of gold-labeled DNA complexes represented cytoplasmic vesicles, most likely endosomes [58]. Further the process of internalisation has been reported as one of the most witnessed processes of gene trafficking [15] (Table 1).

Mammalian cells demonstrate several forms of importation of extracellular components, including clathrin- and caveolae-mediated endocytosis and macropinocytosis. Each of these processes has been implicated in the internalisation of various vectors, both viral and non-viral, across a wide range of cell lines (Table 1).

1.5.1 Clathrin-mediated Endocytosis

Clathrin-mediated endocytosis is involved in the majority of receptor-ligand complexes entering the cell [59]. The process is generally triggered by receptor binding, leading to the accumulation of clathrin structures on the cytoplasmic surface of the plasma membrane as it begins to form clathrin-coated pits [56]. The coat is composed of heavy and light clathrin chains, which assemble into triskelions

Table 1 - Summary of Internalisation Processes Employed by Delivery Vectors

Internalisation Mechanism	Vector Class	Vector Type	Cell Line	Reference
Fusion	Liposome	Fusogenic liposome	HeLa	54
	Lipopolyplex	Targeted lipopolyplex	HUVEC	60
Clathrin-Dependent	Polyplex	Chitosan	A549, Caco-2	61,62
		Histidylated PLL	HepG2	63
		Polystyrene (<200nm)	B16	64
		PEI	A549, HeLa	65
	Lipoplex	Targeted Lipofectamine	Fetal tracheal epithelial cells	66
		pH-sensitive liposomes	COS7	67
		DOTAP	A549, HeLa	65
		SAINT-2/DOPE	COS7	68
	Lipopolyplex	Targeted PEGylated liposome	HUVEC	60
	Viral-based	AAV	HeLa	69
		HIV-I	HeLa	70
		HIV-TAT	T–Cell (Jurkat)	71
		Coxsackievirus	HeLa	72
		Hepatitis C	293T, Huh7	73
		Hepatitis B	HepG2, COS7	74
Caveolae-Dependent	Polyplex	Targeted PLGA	A549	75
		Polystyrene (200-500nm)	B16	64
		PEI	A549, HeLa	65
	Lipoplex	pH-sensitive liposomes	COS7	67
	Viral-based	HIV-1 TAT	HeLa, COS1, Jurkat	76
Macropinocytosis	Vector-free	Naked DNA	Human keratinocytes	77
	Polyplex	Histidylated PLL	HepG2	63
		Chitosan	A549	61
		PLGA	RCEC	78
	Lipoplex	Targeted DC-cholesterol: DOPE	293-T7	79
	Viral-based	TAT fusion peptide	HeLa	80

and associate with adaptor proteins. As the pit continues to invaginate, vesicles are pinched off through a process involving dynamin, a GTPase [81,82], facilitated by a number of different effector proteins [83]. The vesicles are then uncoated by an ATP-dependent protein [84] and transported rapidly to early endosomes (to be discussed next) (Figure 1.5).

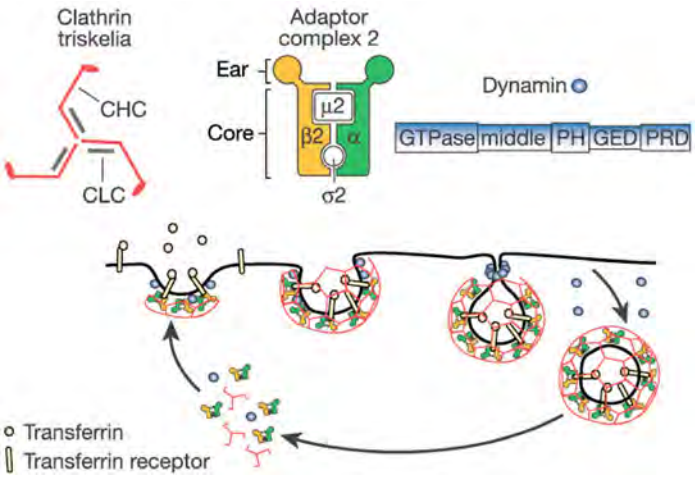

Figure 1.5 – Clathrin-mediated Endocytosis

The core components of clathrin-mediated endocytosis include clathrin triskelions (composed of three clathrin heavy chains and three tightly associated light chains, Adaptor Complex 2 and Dynamin. Mediated by the adaptor complex 2, clathrin triskelions form a lattice to help form the membrane into a coated pit. Then the cargo interacts with receptors within the pit and accumulates. Dynamin is recruited to the neck of the pit, where is assembles into a 'collar' and releases the clathrin-coated vesicle. The vesicle is subsequently uncoated, so the constituents can be recycled. (Image sourced from Conner and Schmid, 2003 [85])

1.5.2 Caveolae-mediated Endocytosis

Caveolae-mediated endocytosis poses as the second form of receptor-mediated endocytic process employed for cellular entry. Caveolae are flask-shaped invaginations in the plasma membrane, composed of the integral membrane protein cavelin-1 and 2 [86,87]. The process of caveolae-mediated endocytosis is similar to that of clathrin-dependent endocytic processing, and is first driven by the clustering of receptors on the membrane surface with the ligand [88], thereby, inducing the polymerization of caveolin-1 and 2, which is a ATP-, GTP- and Mg^{2+}-dependent process [87]. The caveolae flask-shaped pit is then budded off by dynamin [89]. The caveolae vesicles are then transported into the cell, but are not uncoated [88]. The still coated vesicles are processed through two pathways, either fusing with endosomes, or form with structured called caveosomes, which appear to have distinct properties from endosomes, including a neutral pH [88] (Figure 1.6).

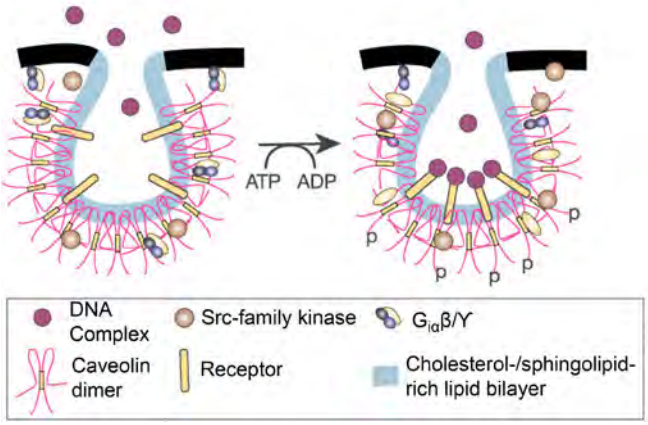

Figure 1.6 – Caveolae-mediated Endocytosis

Complex binds to and is assumed to cluster membrane-bound receptors in the caveolae-coated pit, resulting in the activation of Giα and Src kinases, thereby triggering endocytosis. (Sourced from Connor and Schmid, 2003 [85])

1.5.3 Macropinocytosis

Macropinocytosis is a clathrin- and receptor-independent endocytic pathway, which was first described morphologically in 1931 [90]. Actin-mediated membrane ruffling of the plasma membrane drives macropinocytosis. Most of the lamellipodia formed by the ruffling retract back into the cell. However, some of the lamellipodia may fold back onto themselves and fuse with the membrane creating large and irregular-shaped vesicles termed macropinosomes (Figure 1.7) [91]. Macropinosomes are distinct from any other endocytic vesicle; they have no apparent coat structures, and are heterogeneous in size, however are considered to be larger than 200nm in diameter [92,93], considerably larger than clathrin- or caveolae-derived vesicles. Once formed, macropinosomes undergo a

maturation process; however, it is unlikely that the maturation follows a common pathway in all cell types [91].

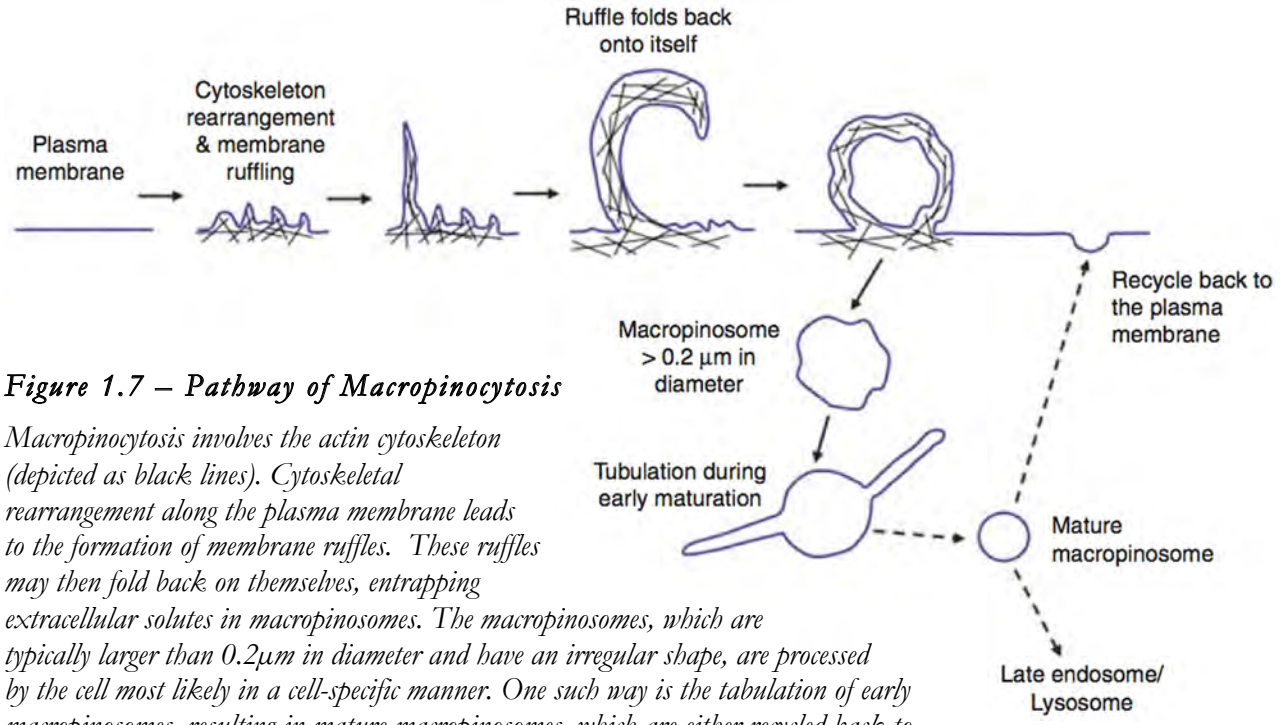

Figure 1.7 – Pathway of Macropinocytosis

Macropinocytosis involves the actin cytoskeleton (depicted as black lines). Cytoskeletal rearrangement along the plasma membrane leads to the formation of membrane ruffles. These ruffles may then fold back on themselves, entrapping extracellular solutes in macropinosomes. The macropinosomes, which are typically larger than 0.2µm in diameter and have an irregular shape, are processed by the cell most likely in a cell-specific manner. One such way is the tabulation of early macropinosomes, resulting in mature macropinosomes, which are either recycled back to the plasma membrane, or digested by early endosome or lysosomes. (Sourced from Lim and Gleeson, 2011 [91])

Evidently, there is no single internalisation pathway for a delivery vector (Table 1), it would appear a number of factors are involved in the process, such as the properties of the vector complex, including the size, charge, composition, and stability of the complex, and the cell type targeted [15]. Complex size has been known to have an impact on the ability to cross plasma membranes, with smaller complexes repeatedly demonstrating to better penetrate cells [94-96]. Larger complexes (up to 500 nm) generally enter the cell through receptor- and clathrin-independent endocytosis, whereas, smaller complexes (<200 nm) are internalised through receptor dependent endocytosis, such as clathrin- and caveolae-mediated endocytosis [97]. Other studies however, have concluded that the charge or ζ-potential has a greater influence over internalization efficiencies than size [61,98]. Farrell et al. (2007) had demonstrated a 30- to 50-fold greater uptake of PEI polyplexes compared to PPL polyplexes with similar size distributions, indicating that composition is a critical aspect of internalization [99].

However, a contradicting study demonstrated the uptake of particles was not governed by particle size, charge, or composition of polyplexes in a BHK-21 cell line [100]. Therefore, the cell type

must also play a pivotal role in which internalization pathway is undertaken by nucleic acid sequence delivery vectors. Douglas *et al.* (2006) demonstrated that chitosan polyplexes (~150 nm) were internalized via clathrin- and caveolae-dependent pathways in kidney embryonic (293T) and fibroblast (COS-7) cells, however were internalized strictly via caveolae-mediated pathways in ovarian (CHO) cells [101].

Like synthetic non-viral vectors, viral vectors are believed to enter the cell through either fusion or endocytic processes. Direct entry, or fusion, is thought to be reserved to non-enveloped viruses, however, accumulating evidence is showing that even non-enveloped viruses are capable of entering the cell through the same endocytic processes as enveloped viruses [69,72]. The process of endocytosis employed by viral vectors differs between clathrin- [71-73] or caveolae-mediated [76], and also macropinocytosis [80] (Table 1).

The cellular penetration of physical vectors on the other hand is entirely dependent on the approach undertaken. For example, microinjection involves the direct injection of the nucleic acid into the site of interest within the cell, thereby, completely bypassing the plasma membrane [102]. Whereas, electroporation disrupts the integrity of the plasma membrane, and through the electric current created, the nucleic acids travel into the cell, without the assistance of the cell in any way [103].

1.6 Endosome

Efficient gene delivery by vectors internalized through clathrin-, caveolae-mediated and macropinocytosis endocytosis requires the escape of the vector from membrane-bound compartments into the cytosol [15]. These vesicles may eventually form endosomes (in most cases), containing ATPase proton pumps, which lower the pH from 7.4 to ~5.0. In the later stages of endosome processing, they fuse with lysosomes (the main degradative compartments of the cell), which also maintain the lumen at low pH, and contains high concentrations of nucleases [104]. As a consequence, the failure to escape from endosomal compartments results in the nucleic acid sequences becoming transfection-incompetent through vesicle entrapment, or lysosomal degradation [15].

The transfer to and degradation in lysosomes has been proposed as one of the most significant barriers in non-viral gene delivery [65]. Confocal microscopy studies demonstrated the gradual change of punctate fluorescence patterns, indicative of entrapped fluorescently-labelled complexes, to diffuse homogenous fluorescence throughout the cytoplasm, providing evidence of escape from endosomal compartments [101,105]. Other studies observed the fluorescence colocalisation decrease over time between labelled complexes, and an early endosomal marker, suggested that the complexes had escaped from the vesicles [106,107].

Although the exact mechanisms of endosomal release have eluded research efforts to-date, a number of theories have been developed, which support these and studies [15]. The release processes appear to be dependent on the vector type utilized; lipoplexes escape through a flip-flop or membrane destabilization process, whereas, polyplexes may utilize a mechanism termed the "proton-sponge escape" theory [15,108]. Of note, the mechanisms involved in complex escape from caveosomes, or macropinosomes has yet to be determined, however, if these compartments acidify the mechanism should follow the same principles.

1.6.1 The Flip-Flop Theory

Zelphati and Szoka (1996) proposed a theory of lipoplex release from endosomal compartments, wherein: Electrostatic interactions between the cationic lipids of the lipoplex and anionic phospholipids of the endosomal membrane results in the spontaneous release of the naked DNA into the cytoplasm after the disruption of the endosomal membrane [109]. With the stability of lipoplexes based on the electrostatic interactions between cationic lipids and anionic nucleic acids, the disruption of this interaction may release the nucleic acids from these complexes [110]. The release of the nucleic acids into the cytoplasm is then further enhanced through lipid: lipid interactions causing a flip-flop effect of the lipids, ultimately leading to a cascade effect [111], eventually disrupting the endosomal membrane integrity and releasing the naked nucleic acid sequences (Figure 1.8).

Fluorescence studies to date support this theory by demonstrating that the combination of ion-pairing and hydrophobic interactions between cationic and anionic lipids is stronger than the

electrostatic forces maintaining lipoplexes intact [112]. *In vitro* studies also demonstrate that the cationic and anionic lipids together form inverted hexagonal phases when combined [113-115] (Refer back to Figure 1.4C). Inverted hexagonal phases are known to disrupt the barrier properties of membranes [116], and may also be instructional for the release of naked DNA from the lipoplex and into the cytoplasm [117-119].

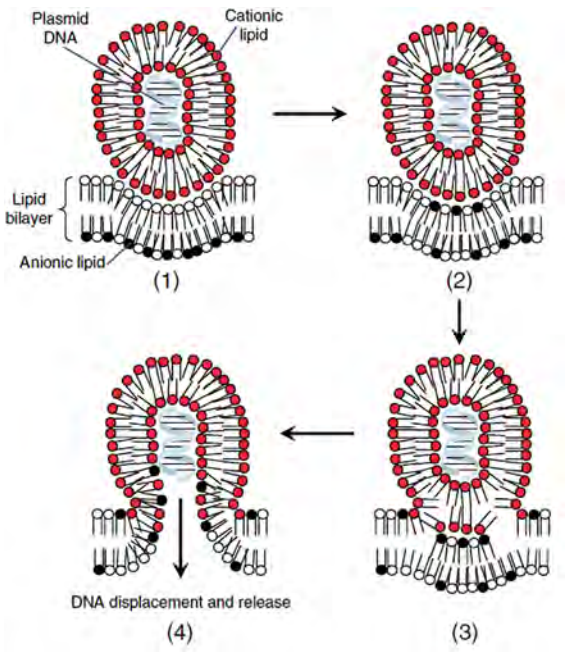

Figure 1.8 – The Flip-flop Theory

The flip-flop mechanism first requires the endocytosis of the lipoplex. The interaction lipoplex and endosomal membrane is lead by the electrostatic charge of cationic lipids (red) and anionic lipids (black) (1). Destabilisation of the endosomal membrane is caused by the flipping of anionic lipids from the cytoplasmic face to the endosomal lumen (2). The anionic lipids then form charge neutral ion pairs with the cationic lipids of the lipoplex (3), thus displacing the DNA and releasing it free into the cytoplasm (4). (Sourced from Medina-Kauwe at al., 2005 [56])

The membrane disruption and nucleic acid release from lipoplexes appears to occur within endosomal compartments rather than the cell surface. It has been suggested that the flip-flop theory is pH independent [120]. The selective interaction with endosomal membranes rather than the plasma membrane may be due to differences in composition. It has been reported that endosomal membranes contain twice as much phosphatidylserine than the plasma membrane [121]. Phosphatidylserine lipids have a negative charge, the interaction of the cationic lipoplex with another membrane may be critically dependent on the fraction of anionic lipids within the other membrane [122].

1.6.2 The "Proton-Sponge" Theory

The Proton Sponge hypothesis was first proposed by Pollard et al. (1998) to explain the endosomal escape of PEI-based polyplexes [123]. According to this theory, 1-6 nitrogen atoms of the polymer are protonated at physiological pH. Upon the acidification of the endosomal compartment, an increase in the proportion of protonated nitrogens occurs, buffering the pH of endosomal compartments. The generation of a charge gradient induces the influx of protons and chloride ion (Cl^-).

The induced charge also results in a water influx into the compartment, ultimately causing the swelling and eventual rupture of the endosome [108,124] (Figure 1.9).

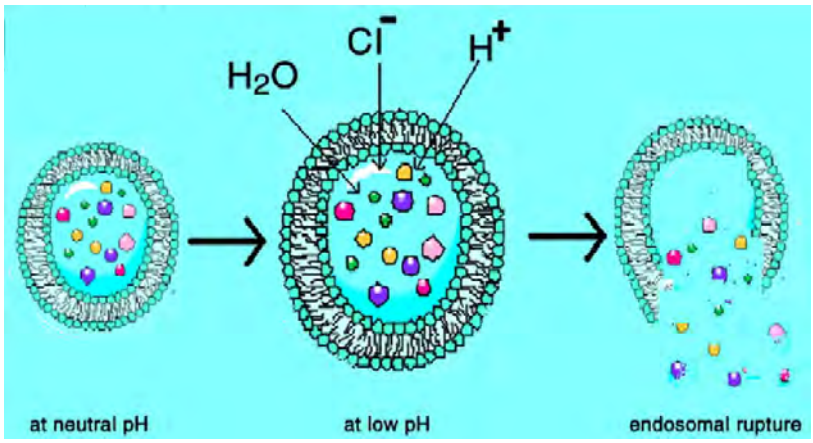

Figure 1.9 – The Proton-sponge Theory

The proton sponge theory involves the acidification of the endosomal space containing polyplexes. This acidification causes a buffering effect, during which a charge is generated, leading to a scavenging of Cl^- and H^+ ions. The influx of charged ions into the endosomal compartment drives a water influx also, ultimately causing the swelling and rupture of the endosome. (Sourced from Varkouhi et al., 2011 [125])

Evidence and support of this theory derives from several studies, including the observation of decelerated acidification, elevated chloride concentration and a 140% increase in the relative volume of endosomes containing PEI complexes [126]. In addition, the transfection efficiency of PEI-polyplexes was reduced 20-fold with the removal of protonatable amine groups [127].

This theory cannot fully explain the endosomal escape of many polyplexes. Therefore, more work must be conducted on the molecular mechanisms of polyplex behaviour within the endosomal milieu [124].

1.6.3 Viral Release from Endosomes

Viral vectors on the other hand, are believed to escape from endosomal compartments through the use of fusogenic peptides, which constitute part of the viral capsid. Many enveloped viruses fuse their membrane envelope with the endosomal membrane after the exposure of a fusogenic peptide, induced by acidification [128]. On the other hand, the Hepatitis B virus is trafficked through the cell to lysosomes, where membranes are destabilized by the proteolytic cleavage of surface proteins, releasing the virus into the cytoplasm [74]. Non-enveloped viral vectors however, expose hydrophobic domains to the endosomal membrane upon acidification due to conformation changes, thereby, destabilizing the membrane and releasing the virus [73,129]

1.7 Cytoplasm

Once released from endosomal compartments the nucleic acid sequences, either naked or still associated to its vector, face the cytoplasmic milieu. During this stage of gene delivery two major obstacles are faced by the nucleic acid sequence: (i) the exposure to cytoplasmic nucleases, and (ii) limited mobility.

1.7.1 Cytoplasmic Degradation

The presence of calcium-sensitive cytosolic nucleases pose the next barrier to non-viral gene delivery [130,131]. Pollard *et al.* (2001) demonstrated that the half-life of free DNA within the cytoplasm is 50-90 min due to the rate of degradation. Several studies reported results supporting the rate and nature of degradation that occurs. However, still much is not known, including the mechanisms (i.e. the nuclease) involved and exactly where the degradation occurs within the cytoplasm.

Through the application of Fluorescent *in situ* Hybridization (FISH), Lechardeur *et al.* (1999) have shown that the disappearance of microinjected DNA occurs in a time dependent manner. The analysis of decay kinetics demonstrated that 50% of the FISH signal was eliminated within 1-2h in HeLa (cervical) and COS-1 (kidney) cells [131], and 4h in C2C12 (myoblast) and myotube cells [132]. This rapid metabolism of free DNA was independent of a number of factors, including the copy number (1,000 – 10,000 plasmids/cell), and the conformation of the DNA (whether linearized or supercoiled, and single- or double-stranded) [108]. The disappearance of the plasmid DNA could not be attributed to cell division, since the degradation was observed in cell cycle arrested cells [131].

Although the metabolic instability of DNA within the cytoplasm has been studied, the actual mechanisms are yet to be uncovered and the extent of degradations that occurs during synthetic vector delivery is unknown. A number of cellular endonucleases and exonucleases have been recognized as potentially involved; however, their functions and subcellular localization are still poorly understood [133-136]. A recent study applied FCS to identify the mechanisms behind degradation, suggested that exonucleases pose the degradative barrier to gene delivery as opposed to other nucleases (DNase I and BAL31) within the cytoplasm of cells [137]. The role of DNases has been suggested to be unlikely, due to

their cellular function and location [137]. This nuclease has been identified to play a role in chromosomal DNA degradation during apoptosis, localizing to the nucleus [138,139]. Therefore, DNases are unlikely to translocate between the cytoplasm and nucleus to target cytosolic DNA [131]. The digestion of plasmid DNA with purified cytoplasm had also demonstrated to be divalent-cation dependent, and thermosensitive. The activation and inactivation patterns were distinctly different from those of apoptotic nucleases, and DNases I and II [130].

1.7.2 Diffusion Properties of Nucleic Acids

Once within the cytoplasm, nucleic acids also face mobility challenges. Fragments of DNA of 250bp and 2000bp diffuse 17- and >100-times slower, respectively, than in water [140]. Lukacs *et al.* (2000) had set the foundations of DNA diffusion within the cytoplasm and nucleus. In this study, a number of DNA fragments were assessed, including 21-, 50-, 100-, 250-, 1000-, 1200-, 2000-, 3000- and 6000-bp, through a technique termed Fluorescence Recovery After Photobleaching (FRAP). These DNA fragments were fluorescently labeled and microinjected. Then using FRAP, a region where the DNA was contained was photobleached through a pulse of high laser power and the recovery of fluorescence observed, resulting in semi-quantitative information on the diffusion rate [140]. This study concluded that DNA fragments <250bp were able to freely diffuse though the cell and into the nucleus, whereas particles >2000bp are virtually immobile. The decreased mobility of the DNA fragments were partially attributed to molecular crowding of the plasmid, but also due to the increased viscosity of the cytoplasm compared to water [140]. However, provided that transfections do occur, the delivered DNA must be mobile to an extent. The FRAP approach applied does not enable the study of single particles, rather only the regional fluorescence. Additionally, the microinjection technique applied deposits all of the DNA load into a single location of the cell, therefore immobility could be a result of molecular crowding of the DNA or because the cell does not process the DNA. As a consequence, the 2000 Lukacs' study does not represent the cellular processing or mobility of DNA when delivered through lipofection; a more relevant approach of nucleic acid delivery than microinjection.

1.8 Microtubules

Larger DNA fragments (>2000bp) appear to have low mobility within the cytoplasm, which suggests an active mechanism must be employed to transport DNA into the peri-nuclear region for transfections to be successful. It has since been established that this is achieved through the exploitation of the microtubule network [14]. Through a study undertaken by Vaughan and Dean (2006), who applied spin-down assays and confocal microscopy, the relationship between DNA plasmids with the microtubule network, dynein and adaptor proteins was shown. This study had concluded that DNA plasmids transport through the cytoplasm along the microtubule network; a cytoskeletal meshwork, via active transport. Dynein, the ATP driven motor protein, linked to the dynein proteins through adaptor proteins appears to the involved in trafficking DNA [14].

The study undertaken by Vaughan and Dean (2006) has since been supported by a number of later publications. For example, Drake and Pack (2008) observed decreases in PEI-DNA delivery efficiency ranging from 50-98% as a result of inhibition of either actin or microtubule polymerization, or dynein or kinesin activity [141]. Further, the notion that DNA is trafficking along the cytoskeleton, via active transportation, has been supported by studies applying Two-Dimensional (2D) Single Particle Tracking (SPT). In which case the trajectory of particles within the cytoplasm were indicative of active transportation through Mean Square Displacement (MSD) calculations [142] which displayed reduced mobility when cytoskeletal polymerization is inhibited [143].

Viral vectors are also well known to utilize the cellular cytoskeleton to traffic throughout the cell. For example, reports have documented HIV-1 virus first engages in early trafficking along the actin network when the virus first enters the cell [144-146]. Followed by processing of the virus within the cytoplasm, the HIV-1 virus then traffics through the cell via the microtubule network utilizing the dynein motor protein [147]. Viruses including the HSV [148], Human Cytomegalovirus [149], Adenoviruses [150], Parvoviruses [151] and Simian Virus 40 (SV40) [152], traffic along the microtubule network powered by either dynein or kinesin motor proteins [153].

1.9 Nuclear Translocation

Following the transportation of the nucleic acid into the cell, through the plasma membrane, escape from endosomal compartments, and trafficking through the cytoplasm, the nucleic acid enters the peri-nuclear region in order to enter the nucleus, defined as the ultimate obstacle for gene delivery. Studies on the comparison of transfection efficiency demonstrated that no more than 0.1-0.001% of cytosolically injected plasmid DNA entered the nucleus [154]. Additionally, studies applying confocal and electron microscopy demonstrated only 20% of cells contained PEI polyplexes within the cytoplasm had expressed the reporter gene of interest [155]. Similarly, a study utilizing bone marrow stromal cells revealed that approximately 75% of cells contained the PEI or PLL vector, but less than 10% of these cells actually contained DNA within the nucleus [99].

Although the processes of nuclear translocation have been extensively studied, the exact processes involved are still not clearly understood. However, it is apparent that the nuclear translocation of DNA complexes is dependent on a number of biological aspects, including the phase of the cell cycle, cell type, nucleic acid sequence and the vector applied. For example, it has been demonstrated that the translocation efficiency of single-stranded DNA is about 10-fold greater than that of double-stranded DNA [156]. In regards to the vector applied, one study reported that chitosan polyplexes enter the nucleus as early as 4h post-treatment, while PPL complexes had not reached the nucleus at all [157]. In a similar study, de Semir *et al.* (2002) had compared a number of commercialized lipoplexes, with finding demonstrating that only one achieved nuclear localization of the DNA [158]. Also the size of the DNA fragment plays a critical role in the nuclear translocation of the complex. Fragments <250bp have the ability to diffuse freely through the cytoplasm and into the nucleus [140]. Leonetti *et al.* (1991) showed that the translocation of small DNA fragments (<100bp) is independent of the temperature, cytosolic ATP and concentration of DNA [159].

Although the exact processes involved in nuclear translocation still remain unclear, there are two likely means of this occurrence: either (i) the nucleic acid complex enters the nuclear region during cell division, or (ii) enters through Nuclear Pore Complexes (NPC) of the Nuclear Envelope (NE).

1.9.1 Entry during Cell Division

One potential process in which introduced nucleic acids can enter the nucleus is while the cell is dividing, and the NE no longer poses a physical barrier [160,161]. Several studies indicate that by blocking the cell cycle in the G1 phase, a dramatic decrease in reporter gene expression occurs in lipofection and increases as cells pass through mitosis [56,161-164]. A key study on the increased efficiency of gene transfer in cells transfected in S or G2 phases versus the G1 phase compared the efficiency of lipoplexes (Lipofectamine), polyplexes (PEI and PLL) and adenoviruses. While cell populations were dividing a minor four-fold increase was observed in adenoviral gene delivery. However, a 500-fold increase was noted in lipoplex and polyplex transfection, suggesting that these vectors may have a dependence on mitosis [160].

On the contrary, while cell division does appear to have an influence in delivery efficiency of non-viral vectors, some studies suggested that the dependence on cell division is cell specific. For example, Dowty *et al.* (1995) had shown that microinjected DNA readily migrated into the nucleus from the cytoplasm in rat myotubes. Through the co-injection of Wheat Germ Agglutinin (WGA) (a lectin which binds to N-acetylglucosamine residues on NPC proteins, thereby effectively blocking NPC translocation [165]) a 20-fold decrease in gene transfer was observed, indicating that the plasmids were entering the nuclei via the NPC [166].

1.9.2 Entry through NPCs

The passage of nucleic acids must occur through means other than just entering the nuclear space during cell division. Dowty *et al.* (1995) indicated that gene expression of a reporter gene was detected when the plasmid DNA was injected into the cytoplasm of primary myoblasts, implying that the plasmid DNA is able to enter post-mitotic nuclei [166]. In the same study, Dowty *et al.* (1995) visualized gold-labelled plasmids in close proximity with NPC, and inside the nucleus through electron microscopy. This early work was then supported in 1999, when the translocation of plasmid DNA into the nucleus was identified to be temperature-sensitive, energy-dependent and inhibited by WGA [167].

The NPCs are cylindrical supramolecular structures, each composed of a central cylinder anchored to the NE surrounded by spoke-ring complexes [168,169], termed the luminal domain (Figure 1.10). They are composed of ~50 proteins, forming aqueous channels through the NE, are about 130nm in diameter and 70nm thick, and are collectively known as nucleoporins [168]. Cytoplasmic and intranuclear filaments (fibrils) extend out 50-100nm into their associated compartments, and is expected to interact with incoming and outgoing receptor complexes [170,171].

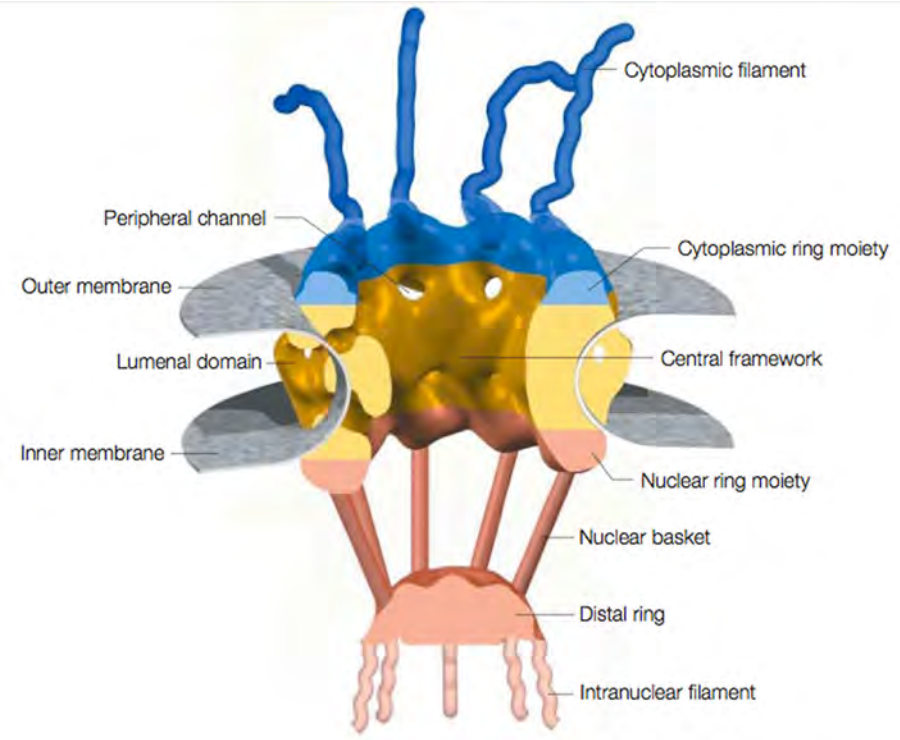

Figure 1.10 – The Nuclear Pore Complex

The NPC is composed of two regions: the luminal domain containing the central framework (yellow) and forms the channel through the nucleoporin, the cytoplasmic ring moiety (blue) containing the cytoplasmic fibrils, which extend into the cytoplasm, and the nuclear ring moiety (red) composed of the nuclear basket and intranuclear fibrils, extending out into the nuclear space. (Sourced from Fahrenkrog and Aebi, 2003 [172])

Molecules smaller than ~40kDa can passively diffuse through the channel. However, macromolecules larger than 60kDa must either contain a Nuclear Localizing Signal (NLS) or associate with other polypeptide(s) incorporating NLS to traverse the NPC in an energy dependent manner [173]. The diameter of the NPC channel reaches a maximum of 25nm during active transportation, but has a cross section of 9nm when engaged in passive transport. The conformation change may explain the ability of NPCs to permit passage of molecules as large as 25-50MDa [174,175]. During active transportation, the NLS of the cargo is recognized by the importin-α adapter, which then complexes with importin-β via the importin-β binding domain, forming a pore targeting complex [176,177]. The pore targeting complex docks to the NPC by associating with the protruding fibrils, it is then believed the conformation change occurs as a response to calcium changes [178]. The complex and cargo then passes

through the NPC channel. Following the translocation, the association with Ran-GTP initiates the release of the imported cargo from the importins [177].

Without association with a NLS, or if NPC-dependent active transportation is blocked, DNA can be excluded from the nucleus [179]. Due to the potential size of DNA constructs, the introduced DNA appears to be undergoing active transport into the nucleus. A number of approaches have been employed to enhance this process. One such example is the attachment of NLS either covalently, or non-covalently [110]. Peptides including SV40 T-antigen [180], TAT [181], Vp22 [182] and μ [183] have been successfully tested to enhance nuclear translocation. Another emerging approach is the incorporation of DNA targeting sequences into the sequence of the DNA plasmid, such as the 72bp enhancer sequence from the SV40 virus [184]. The addition of such a sequence renders the plasmid nucleophilic, since the enhancer sequence offers the ability to bind to various transcription factors. The nuclear import of the plasmid is then facilitated since the transcriptional factors have their own NLS [110].

1.9.3 Viral Entry of the Nucleus

Like non-viral vectors, viral-based gene delivery also appear to be hampered by the NE. Viral vectors generally show greater nuclear translocation compared to non-viral vectors, due to their incorporated NLS domains. However, their ability to penetrate the nucleus is not significantly greater than non-viral nuclear translocation [15]. For example, Hama *et al.* (2006) reported that the nuclear entry of adenoviruses was only 2.5 times greater than that of lipoplex delivery [185].

The NE is also a rate limiting step in viral transduction for other viruses, including AAV [186]. However, in the case of the MLV retrovirus, early experiments indicate that this virus is only able to enter the nucleus during cell division [187,188], thus explaining why the MLV vectors cannot infect non-dividing cells as the NE is a complete barrier. In contrast, Lentiviruses, including HIV-1, have the mechanisms to infect both dividing and non-dividing cells. This implies these viruses can pass through NPCs in non-dividing cells [189]. This ability has been attributed to the abundant presence of viral NLSs [190]. Recent studies suggest other factors are involved in lentiviral nuclear import, including the central DNA flap structure [191], the CA protein [192], the cellular importin 7 [193] and nucleoporin proteins [194].

1.10 Nuclear Architecture

In many studies on nucleic acid sequence delivery, the cytoplasm has been the major research focus, resulting in the nucleus becoming a 'black box' to gene delivery. The nucleus is a complex organelle composed of several sub-compartments, which are likely to play a role in the fate of introduced nucleic acid sequences. Although it is still not fully understood, it is clear that eukaryotic nuclei are dynamics structures, well organized and consist of several distinct non-membrane bound compartments [195-197] (Figure 1.11).

The arrangement of compartments inside the nuclear space is termed the nuclear architecture [197]. These nuclear compartments can be readily visualized using light and electron microscopy [195] and consist of specific resident proteins [195,197]. A prominent compartment of the nucleus is the nucleolus (Figure 11B), which is the site of ribosomal RNA transcription and RNA processing. Other compartments include nuclear speckles (Figure 1.11A), the splicing factor compartment, Cajal bodies (Figure 1.11C), sites for small nuclear ribonucleoprotein assembly, and Promyelocytic Leukemia bodies (PML) (Figure 1.11D), believed to play a role in cellular processes including transcription and cell cycle progression, as well as apoptosis and DNA repair [198].

The genomic DNA, which is packed in the form of chromatin composed of DNA, histones and additional architectural proteins [199]. The histones condensing the DNA are subject to a large variety of post-translational modifications that regulate the chromatin accessibility and ultimately gene expression [197]. Within the compartments chromatin is well organized; it appears that gene-rich regions tend to be found in the nuclear interior, and transcriptionally active regions are usually kept as decondensed euchromatin. Whereas, regions of transient gene expression and silenced genes tend to be found towards the periphery and if generally inactive, kept as more condensed heterochromatin [196,197]. Chromosomes themselves are also organized into distinct sub-volumes of the nuclear space, termed Chromosome Territories (CTs) [200] (Figure 1.11E, F). The positions of each gene locus is also subject to strict regulation, and CTs, are non- random, tissue, cell-type and developmental-stage specific [201]. In a study undertaken by Cremer *et al.* (2003), multiple normal cells were compared to their

malignant equivalents, showing a change in nuclear architecture with alterations in CT and gene loci positions.

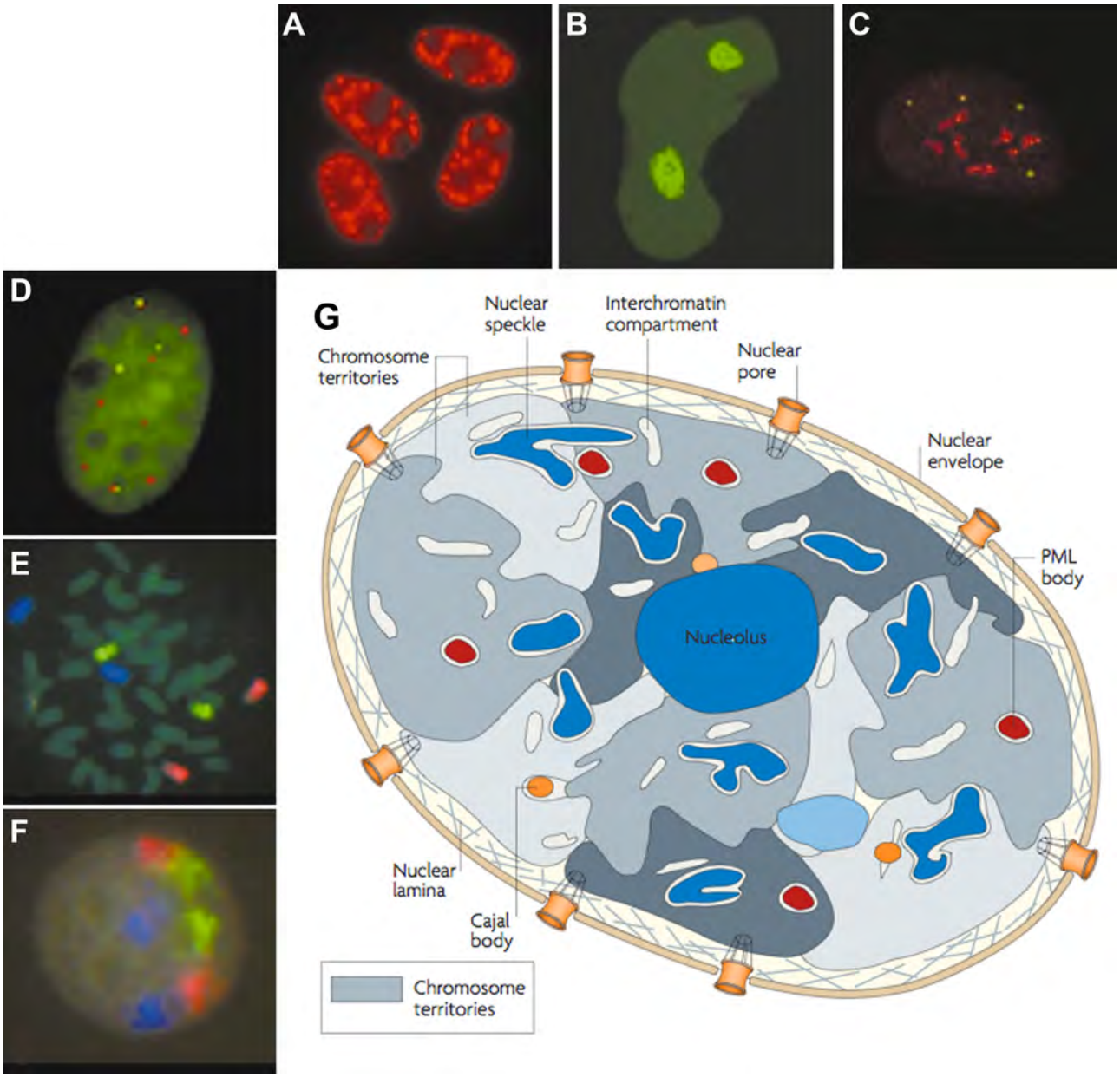

Figure 1.11 - Nuclear Architecture and Chromosomal Territories
The centre schematic diagram indicates where the compartments are relative to each other, with fluorescent images surrounding the schematic diagram to show how they appear in a eukaryotic cell during interphase. The surrounding images include nuclear speckles (A), nucleolus (B), Cajal bodies (C), PML bodies (D) and mouse chromosomes 13 (blue), 14 (red) and 15 (green) during metaphase (E) and during interphase in clear chromosome territories (F). (Schematic diagram obtained from Lanctôt et al. 2007 [196], Images modified from Dundr & Misteli, 2001 [195]).

1.11 Nuclear Environment

Due to the complexity of the nucleus, it is not expected that the delivery nucleic acid sequences will simply enter the nucleus and be expressed by the cellular machinery. Several factors must be

addressed and elucidated, including: (i) whether the nucleic acid sequence dissociates from the vector complex in order to be transcribed, (ii) where the nucleic acid sequence localizes, (iii) how long the nucleic acid sequence is retained within the nucleus, and (iv) how the cell homeostasis is affected by the transfection process.

1.11.1 Vector Dissociation

It still remains unclear whether the nucleic acid sequence dissociates from the vector to function within the nucleus. However, evidence suggests that free DNA is required [15,108]. Studies show that the transfection efficiency of linear PEI polyplexes is higher than branched PEI polyplexes [106]. It has also been suggested that lower molecular weight polyplexes result in a high transfection efficiency [128,202]. The higher transfection efficiency can be contributed to the easier dissociation of the nucleic acid from the vector, making it readily available to be transcribed. Similarly, lipoplexes with a higher charge ratio have been reported to reduce transfection efficiency, although internalisation and destabilization of endosomes is increased. The higher charge ratio is thought to reduce DNA release, thereby reducing transcription [203,204]. Although the mechanisms of vector dissociation remains unclear, it has been suggested that anionic proteins or the large amount of DNA and RNA within the nucleus may cause the displacement of the vector from the introduced nucleic acid [106,205,206]. Such propositions involving endogenous RNA have been supported by observations where PEI accumulates near the nucleoli, but does not interact with chromosomal DNA [155,208].

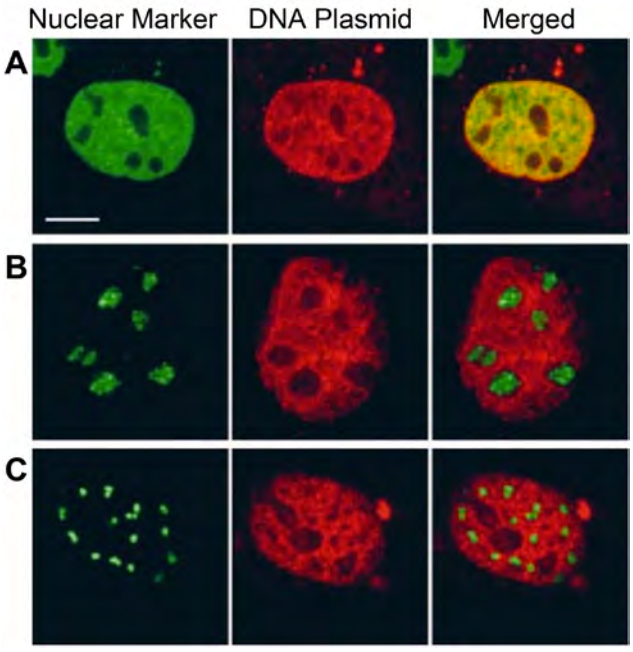

Figure 1.12 – Localisation of Plasmid DNA in Mammalian Nuclei

Plasmid DNA localises into specific sub- compartments of the nucleus. COS7 (fibroblast-like) cells were transfected with SAF-A (A), hFibrillarin (B), highlighting the nucleolus, and PML (C). After overnight incubation, plasmid DNA signals had demonstrated a exclusion from the nucleolus (B) and PML (C) compartments, whereas, distribution was very similar to the SAF-A (A) scaffolding protein. (Sourced from Mearini et al. 2004 [207])

1.11.2 *Nuclear Localisation*

Within the nucleus, plasmid DNA has been reported to localize in specific nuclear regions. Mearini *et al.* (2004) identified plasmid DNA displays a heterogeneous distribution within the nucleus, including nucleoli exclusion (Figure 1.12B) and PML bodies (Figure 1.12C). Mearini's study also demonstrated the distribution of plasmid DNA was similar to the nuclear scaffolding protein (SAF-A) (Figure 1.12A). However, following further experimentation, no association was identified. The study concluded that plasmid DNA has a rapid association with nuclear substructures, which dramatically reduce mobility and render the DNA resistant to treatment with detergents and elevated salt concentrations [207]. A prior study had similar results, where SV40 viral DNA was observed within the nucleus in a similar pattern, being excluded from the nucleoli and other nuclear sub-compartments [209].

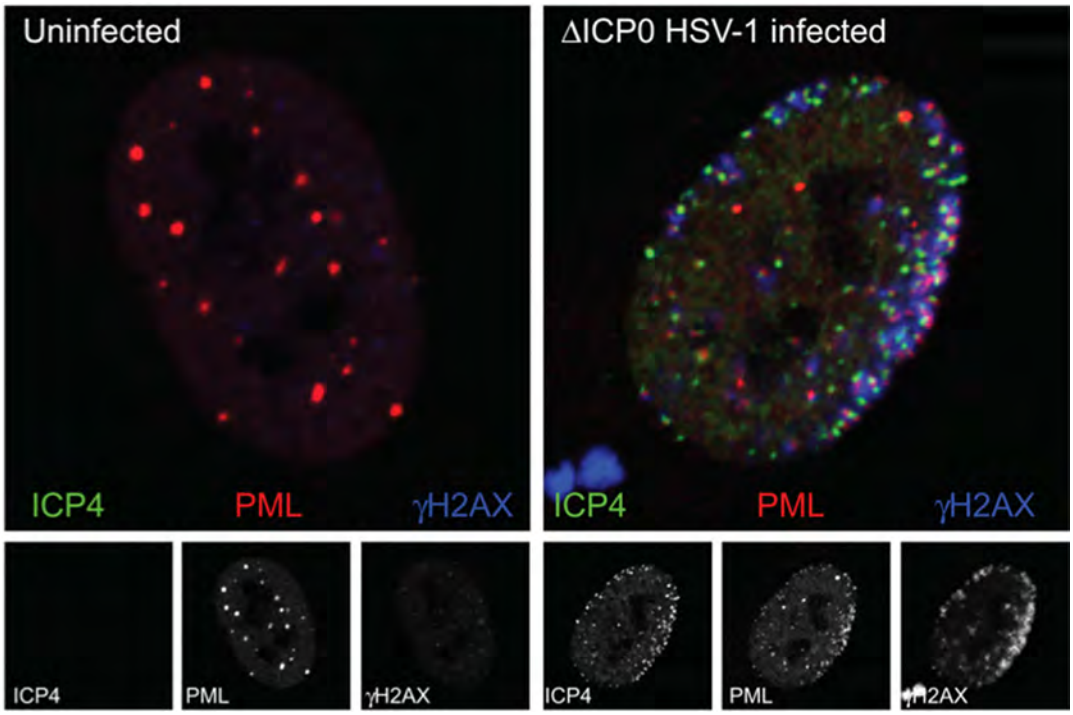

Figure 1.13 - Nuclear Localisation of HSV-1 Vector
The uninfected nucleus of human fibroblast cell shows the typical distribution of PML bodies (red) and little activity of γH2AX (blue), a DNA damage response protein. One the contrary, the HSV-1 infected nucleus (right) shows a redistribution of the PML bodies that closely associate to the viral genome, indicated by the viral transcriptional activator ICP4 (green). A DNA repair response resulted from the presence of the viral vector, indicated by the increased in γH2AX in regions close to the viral genome. (Sourced from Everett, 2013 [210])

Nuclear localization of some viral vectors demonstrate a different trend, for example, the large genomes of the HSV vector, which have a limited mobility within the nucleus, have been observed to

localize along the periphery of the nucleus where they would have entered through NPCs [211,212]. Following nuclear entry, the HSV vector displayed strong association to PML bodies and the activation of DNA repair pathways [210] (Figure 1.13).

1.11.3 Nuclear Retention

One aspect of non-viral gene delivery is the maintenance and retention of the introduced nucleic acid, especially when it remains episomal. Gasiorowski and Dean (2005) investigated this issue through the introduction of plasmid DNA with different modifications. When the DNA was imaged using a FISH approach or the use of Protein-Nucleic Acid (PNA)-fluorescence labelling, the DNA was observed within daughter cells (Figure 1.14A). However, when the DNA was imaged using covalent labelling kits, the DNA was excluded from the nucleus following cell division (Figure 1.14B, C) [213]. Gasiorowski *et al.* (2005) demonstrated that the modification of nucleic acids could have an effect on the overall lifetime of transgene expression.

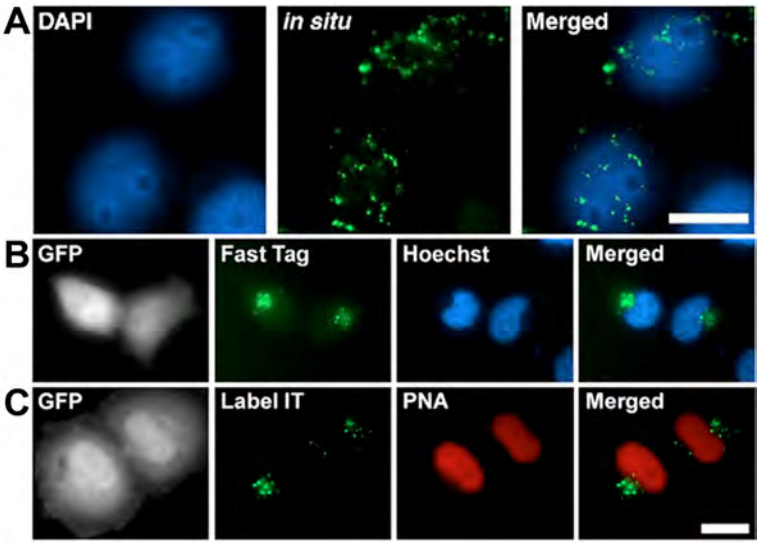

Figure 1.14 – Nuclear Retention of Fluorescently Labelled Plasmid DNA

Unmodified naked DNA was injected in the nucleus of HeLa cells and observed 12-18 hours later once the cells had divided, demonstrating that the introduced DNA remained within the nucleus (A). Comparatively, when the plasmid DNA was labelled with Texas Red Fast Tag (green) (B) or a mixture of Cy5 Label IT (green) and Cy3-PNA (red) (C), the DNA labelled with Texas Red Fast Tag and Cy5 Label IT (C) were not retained in the nucleus following cell division. (Sourced from Gasiorowski and Dean, 2005 [213])

1.11.4 Cellular Responses

Until recently few studies have addressed cellular responses at the molecular level in response of non-viral gene delivery. Recently, Plautz *et al.* (2011) had applied microarray analysis to identify alternations in gene expression, in response to trafficking lipoplexes in two different cell types: human embryonic epithelial kidney cell and mouse fibroblast cells. In Plautz's study, cells containing lipoplexes were separated into two populations, based on whether (GFP+) or not (GFP-) the Green Fluorescent Protein (GFP) reporter gene was expressed, and compared these and a non-treated control

[214]. The expression patterns of GFP+ and GFP- populations revealed three genes that were statistically different: *RAP1A, HSP70B'* and *PVT1* (a non-protein coding oncogene), all up regulated in GFP+ populations. Additionally, the GFP+ population exhibited statistically significant expression levels in 19 genes compared to the control. Up regulated genes of interest in the GFP+ population included the activating transcription factor 3 (*ATF3)*, damage-specific DNA binding protein 2 (*DDB2*) (which facilitates responses to DNA damage) and a death effector domain-containing gene (*PEA15*) [214].

The *RAP1A* gene was up regulated in GFP+ and GFP- populations (compared to controls), therefore, it may play a role in the internalisation of DNA complexes [214]. The gene encodes a GTPase involved in a range of cell proceses, including integrin-mediated adhesion [215]. The up regulation of this gene was explained as the link between the ECM and non-viral gene delivery, since ECM molecules have been demonstrated to enhance non-viral gene delivery strategies [216,217], where the plasmid is immobilized to the surface supporting the cell, and internalized while promoting cell adhesion [214,218].

The *HSP70B'* gene, encodes for a heat shock protein, a chaperone involved in protein folding and stabilization, which is strictly induced by various cellular stress [219]. *HSP70B'* is usually silenced in many cell types [220], and is important in maintaining cell viability [219] and cytoprotection [221]. Therefore, the expression of this gene may be important for maintaining cell viability during transfection [214]. It has also been identified that *HSP70B'* has a role in and enhances nuclear localization of viral particles [222], and therefore, may promote nuclear entry of non-viral vectors [214].

Finally, the *ATF3* gene was up regulated in transfected cells. This inducible gene alters gene expression to adjust for various intra- and extra-cellular stresses and stimuli, including the induction of apoptosis [223]. Whether the expression of this gene is protective or detrimental is dependent on the stimuli and cell type [223]. The up-regulation of this gene indicates that a survival response was triggered, which correlates with the up-regulation of other genes involved in apoptosis [214].

CHAPTER 2

Characterisation of the Molecular Mechanisms of Exogenous DNA Mobility

2.1 Introduction

Within a biological system a fundamental question that is frequently raised is at what rate a particle or compound moves, and how it does so. Over time a number of bioimaging tools and approaches have been developed to achieve such an insight into the real-time dynamics occurring in live cells.

One such example that is commonly applied is the FRAP approach. This technique involves the photobleaching of a fluorescent population through a pulse of high-powered laser, followed by the observation and calculation of how fast the unbleached population moves into the bleached region [224]. Although this approach is commonly utilised, it is highly invasive due to the energy that must be exerted onto the cell in order to achieve photobleaching, therefore the approach can influence the mobility of particles through local heating and cellular damage. Additionally, FRAP is not sensitive enough to observe small fluctuations and will only capture events within the small region selected.

FCS on the other hand (as discussed earlier), offers a means to observe the fluctuations at a single-particle level. The FCS approach is not invasive and enables the absolute quantification of particle mobility and dynamics. However like FRAP, FCS is limited to the observation of a single small area, and events occurring outside of this Region-of-Interest (ROI) will be missed. Therefore, the FCS approach has been extended to several techniques, including Raster Image Correlation Spectroscopy (RICS) and image-based Means Square Displacement (iMSD); enabling entire frames and images to be

correlated, thus extracting quantitative information of particle dynamics, including mobility, binding-events and mechanisms of motion [225,226].

2.1.1 Raster Image Correlation Spectroscopy

The RICS approach applies a raster scan to obtain dynamic information of fluorescently labelled particles, including diffusion and mobility, binding and concentration over time and space. In the raster scan the laser starts at one point (Point A, Figure 2.1) and scans across the sample acquiring pixels and collecting intensity information to form a line (to Point B, Figure 2.1). The laser then retraces to the beginning of the next line, then scans, and so on to acquire an entire image, after which it retraces back to the beginning (Point A, Figure 2.1) to obtain consecutive images as required. During the scanning, the pixel time, line time and retracing times must be taken into account [227].

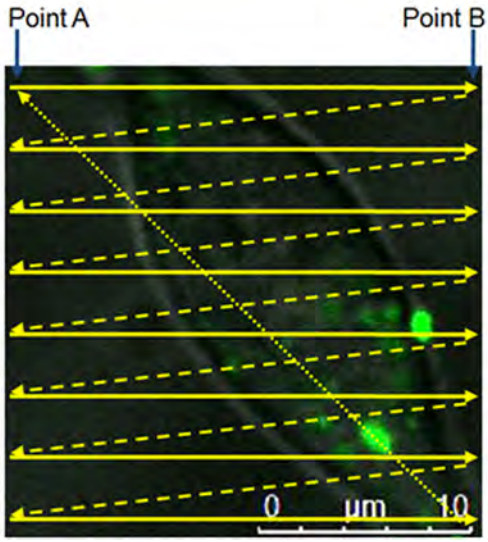

Figure 2.1 – The Raster Scan

In a raster scan the laser starts from point A and scans across the sample acquiring pixels to Point B (scanning indicated by the solid yellow lines). The laser retraces down to the next line (indicated by the dashed lines) and continues until an entire image has been acquired. The laser then retraces back to the beginning of the sample, point A (indicated by the dotted line) to acquire consecutive images as required. (Image obtained from previous unpublished data)

During the raster scan, every pixel acquired contains fluctuation information that can be used to extract the dynamics of particles within the sample. Spatial correlation of diffusing/moving particles is dependent on the overlap of adjacent pixels, and therefore, the sample must be sampled in such a way that the PSF of each pixel slightly overlaps [225]. As the raster scan acquires an image, the intensity of a single pixel is measured for a very brief time, then immediately after the neighbouring pixel's intensity will be measured. If a particle moves from the first pixel to the second, the intensity fluctuations will be correlated with a certain time delay. The scale of this correlation will be dependent on the rate of mobility of the given particle/s and may involve several neighbouring pixels [228]. On the other hand, in

the case that the particle is moving very slowly and remains within a location for a long period of time, there would be little or no transfer of fluctuations amongst adjacent pixels. Therefore, the spatial correlation will have a different distribution compared to the case of faster mobility [228].

In the case of slower moving particles, the fluctuations particles have a higher probability of being detected in nearby pixels, but in a smaller number of pixels (for example, in pixels 1-3 in Figure 2.2A). When these pixels are correlated a strong correlation amongst adjacent pixels is obtained but the correlation will decay as the particles are no longer seen (Figure 2.2C). On the contrary, faster moving particles have a lower probability of being detected in adjacent pixels, but will be observed much further in time (Figure 2.2B). Due to this characteristic of faster moving particles the ACF will broaden (Figure 2.2C) [225].

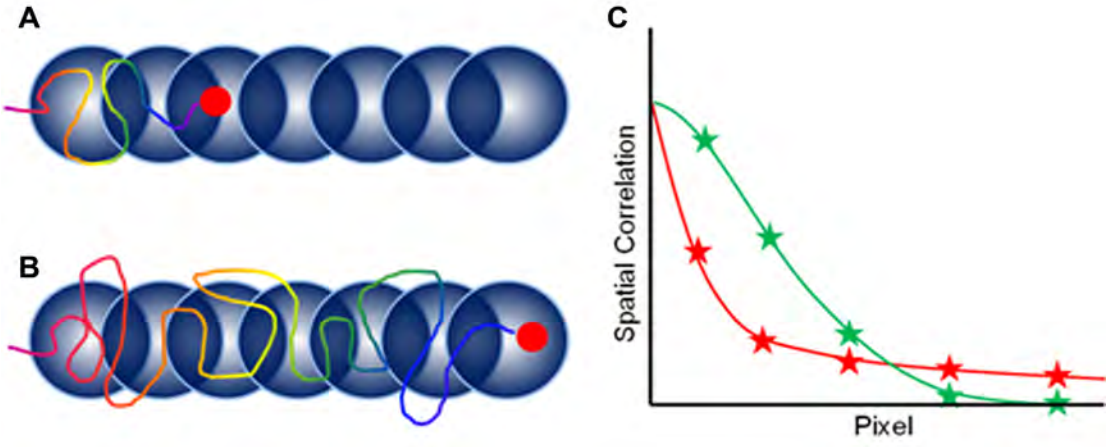

Figure 2.2 – Temporal Information within the Raster Scan

During the raster scan the pixels must be overlapped for the RICS approach. In the case of a slow moving particle, fluctuations have a higher probability of being detected in nearby pixels but over a lesser number of pixels (A). Whereas, a faster moving particle has a lesser probability of being detected in neighbouring pixels, but will be detected in further pixels (B). The colour code represents time evolution of the trajectory. In these cases, the ACF will take on a characteristic broadening for faster moving particles since fluctuations are observed much further. However, the ACF will decay much faster in the case of slower moving particles as the fluctuations of particles will be detected in less pixels. (Image sourced from Digman, 2010 [229])

The SCAF and mobility co-efficient are calculated through a few mathematical algorithms. Firstly, the image must be divided into four quadrants (for example, an image of 256x256 pixels is divided into four equal fractions of 128x128 pixels). Each quadrant is shifted by a single pixel in the x direction and then multiplied by its unshifted equivalent, with each pixel providing a point for the SACF. The calculation is performed on each pixel of an image and then performed again with a shift in

the *y* direction to obtain the full SACF (Figure 2.3). This operation is repeated for each frame over a stake and the SACF of each frame is finally averaged [6].

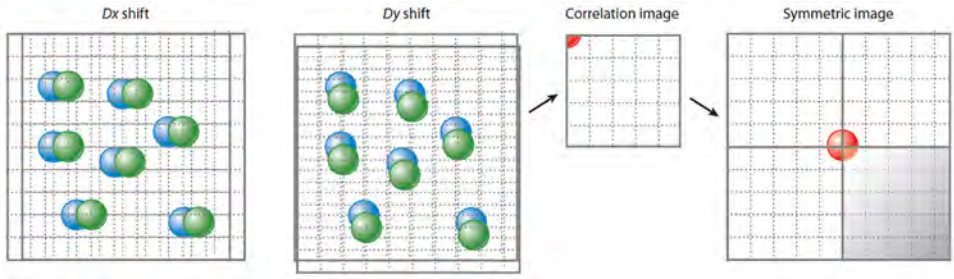

Figure 2.3 – Calculation of the Spatial Auto-Correlation Function

In order to calculate the SACF an image is divided into four equal quadrants. Each quadrant is shifted in the x direction by a single pixel and then multiplied by its original quadrant. Each pixel contributes to a point of the SACF. This operation is repeated with a shift in the y direction. The calculation is performed on all pixels of each quadrant in order to obtain a full SACF. (Image sourced from Digman and Gratton, 2011 [6]

Mathematically, the 2D SACF is calculated where temporal information is taken into account:

$$G_{RICS} = \frac{\langle I(x,y)\, I(x+\xi, y+\psi)\rangle}{\langle I(x,y)\rangle^2}$$

Equation 2 - RICS 2D SACF

where the variables ξ and ψ represent the spatial increments in the *x* and *y* directions, respectively [225]. The equation states that for each pixel, the intensity (*I*) is multiplied by its shifted equivalent and divided by its squared self. The Fast Fourier Transform (FFT) method is applied in order for these calculations to be computed efficiently [228].

The diffusion coefficient can be determined through the RICS approach:

$$G_{RICS}(\xi,\psi) = S(\xi,\psi) \times G(\xi,\psi)$$

Equation 3 - RICS Diffusion Coefficient

A molecule moves independently of whether or not the sample is being scanned. Therefore, the SACF is the product of two terms: (i) the scanning parameters (*S*), and (ii) the diffusion/movement of the particle (*G*) [1]. Considering the process of diffusion, the diffusion kernel is described by:

$$P(r,t) = \frac{1}{(4\pi Dt)^{3/2}}\, exp\left(-\frac{r^2}{4Dt}\right)$$

Equation 4 - RICS Diffusion Kernel

where *P* is the probability of finding the molecule in the distance *r* in the given time *t*. This expression is composed of two parts: (i) the temporal term, which describes the amplitude of the SACF, and (ii) the spatial Gaussian term, which is dependent on time. In the case of a fast time scale, the diffusion kernel broadens as the width of the Gaussian increases and the amplitude decreases as a function of time [225].

A 3D fit can be obtained to determine space and time relationships. This is calculated with a 3D Gaussian equation (similar to one used for single point FCS):

$$G(\xi,\psi) = \frac{\gamma}{N}\left(1+\frac{4D\left(\tau_p\xi+\tau_l\psi\right)}{\omega_0^2}\right)^{-1}\left(1+\frac{4D\left(\tau_p\xi+\tau_l\psi\right)}{\omega_z^2}\right)^{-1/2}$$

Equation 5 - RICS 3D SACF Fit

which takes the pixel time (τ_p) and the line time (τ_l) into account. The geometrical factors or the waist of the beam path are represented by the acronym ω [228].

A common problem with many FCS techniques is cellular artefacts and especially for RICS, immobile fractions. Nonetheless, the RICS approach applies a basic concept in order to remove artefacts in order to only correlate fluctuations due to mobile particles. An average of the image series can be applied by calculating the average intensity of each pixel of an overall image series, $\overline{I(x,y)}$. This average is then subtracted from the frames over the data series isolating the fluctuations of only the mobile particles. However, this yields some negative values, therefore, a scalar must be added, $a = \bar{I}$ [229]. This operation is expressed as below:

$$F_i(x,y) = I_i(x,y) - \overline{I(x,y)} + a$$

Equation 6 - Average Subtraction in RICS

However, the operation detailed above does not remove artefacts including bright or very slow moving structures, such as organelles of the cell. Therefore, a moving average can be applied to isolate and extract the fluctuations of the particles of interest in the presence to slow moving artefacts. As the frames are correlated, the set of frames that are averaged move accordingly [229]. For example, in a moving average of 10, the average intensity of frames 1-10 is calculated. The correlation calculation

starts from frame 5 and removes the average intensity of frames 1-10. As the calculation processes correlate pixels of frame 6 the intensity average of frames 2-11 is removed and so on. As a result, slowly moving components are filtered out and the fluctuations of much faster components are obtained [229].

2.1.2 Image Means Square Displacement

The Means Square Displacement (MSD) is a common approach to determine particle trajectory over time. The analysis provides information on the directionality and motion of a particle [230]. Consequently, the MSD can determine the possible mechanism of motion based on the nearest-neighbour algorithm [230-232]. MSD analysis is typically performed from Single Particle Tracking (SPT), however SPT typically requires specialized equipment, such as circular scanning capabilities [143]. However, an image-based MSD (iMSD) approach has recently been developed [226]. Similar to single particle approaches, the iMSD approach provides a value of MSD providing an insight into the directed motion, flows, directionality of particles, within a 2D image series using correlation functions [226]. A range of mechanisms or means of motion can be determined through this technique, including Random Diffusion (RD), Active Transport (AT), Transient Confinement (TC), Anomalous Subdiffusion (AS), Confined or Corralled Diffusion (CD) and Binding-Unbinding events; Figure 2.4 presents the expected iMSD curves for the mechanisms of motion outlined.

The iMSD function is calculated as follows:

$$G(\xi,\chi,\tau) = g(\tau)\cdot\exp\left(-\frac{\xi^2+\chi^2}{\sigma_r^2(\tau)}\right) + g_\infty(\tau)$$

Equation 7 - iMSD Function

which takes into account three components, the temporal correlation function, iMSD component (where the variance is of the spatial G term) and constant offset. The spatial and temporal correlation function is the same of that for the STICS approach:

$$G(\xi,\chi,\tau) = \frac{\langle I(x,y,t)\cdot I(x+\xi,y+\chi,\tau+t)\rangle}{\langle I(x,y,t)\rangle^2} - 1$$

Equation 8 - iMSD Spatial and Temporal Correlation Function

The 3D Fast Fourier Transform (FFT) algorithm is used to calculate the correlation function:

$$G(\xi,\chi,\tau) = g_0 \cdot p(\xi,\chi,\tau) \otimes W(\xi,\chi)$$

Equation 9 - iMSD Correlation Function

where g_0 is the usual G(0) of FCS and it depends on the number of particle, P depends on the physics of the motion and W is the point spread function.

The iMSD component takes into the account the Fick's Law:

$$p(\xi,\chi,\tau) = \frac{1}{\pi 4D\tau} exp\left(-\frac{\xi^2+\chi^2}{4D\tau}\right)$$

Equation 10 - iMSD Fick's Law

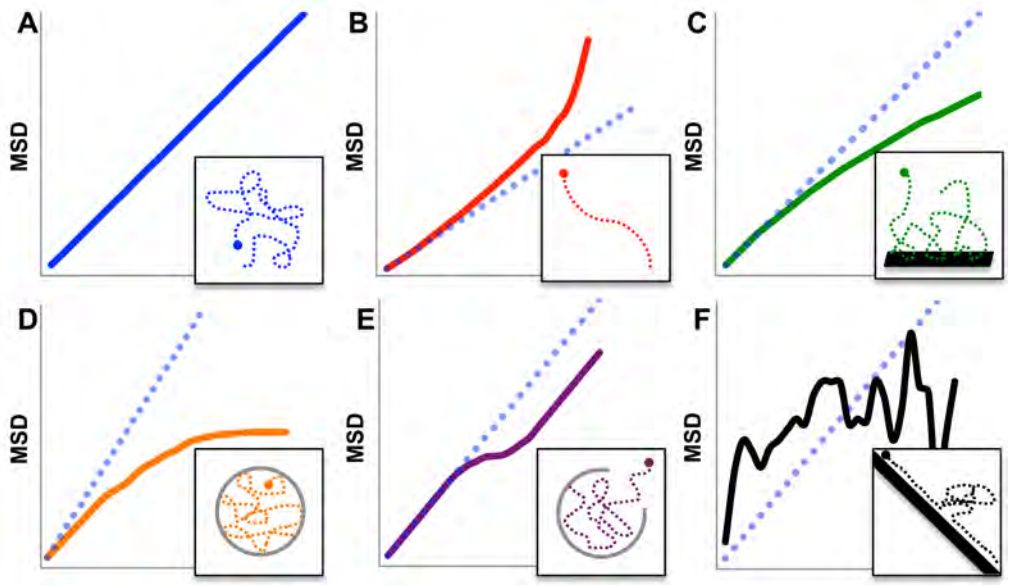

Figure 2.4 – Examples of MSD Curves

Expected iMSD curves for the variety of different mechanisms of motion with pictorial representations of the motion in smaller boxes at the right of each curve. Means of motion include random diffusion (A), active transport (B), anomalous subdiffusion (C), confined diffusion (D), transient confinement (E) and binding unbinding (F). (Image created based on Levi & Gratton, 2008 [233])

2.1.3 Lipoplex Dynamics

The mobility and dynamics of delivered DNA has long been in the spotlight since these properties play a critical role in the success of this therapeutic approach. As a result, a number of approaches to study the delivery process have been applied. During the processing of lipoplexes (the complex formed between DNA and transfection lipids), a number of barriers and obstacles are faced, potentially impeding mobility of the DNA complexes (as discussed in Chapter 1).

The free diffusion of DNA of varying lengths has been established in previously published work. Lukacs *et al.* (2000), for instance demonstrated the rate of motion of DNA fragments ranging from 21bp-6kbp through microinjection. The study identified that DNA >1000bp were immobile within the cytoplasm, and all sizes were immobile when delivered directly to the nucleus when analysed through the application of FRAP. However, the reduced mobility in the cytoplasm could possibly be due to molecular crowding as a result of the microinjection delivery approach, as accounted for by Lukacs *et al.* [140].

Since the DNA was microinjected in the study by Lukacs et al. (2000), it is also likely that the DNA was immobile since it would not interact or be processed by the cell compared to the lipofection process. Following entry into the cell, lipoplexes are expected to be trapped in endocytic vesicles and therefore, must escape these cellular organelles [185]. Within the cytoplasm, the nucleic acid is required to be trafficked towards the nucleus, and does so along the microtubule network facilitated by motor proteins [14]. Commonly described as the ultimate obstacle of gene delivery [184,234], the delivered DNA most likely enter the nucleus through nuclear pore complexes [235], or by associating with chromatin during cell division [161,236].

Coppola *et al.* (2013) on the other hand applied a SPT approach to lock onto and track individual lipoplexes over time [143]. Coppola's study enabled the analysis of the rate of motion and mechanisms behind the motion (i.e. random diffusion or active transport) at a single compound level, however it is limited to a single particle. The behaviour of the delivered lipoplexes in Coppola *et al.*'s study was similar to a study undertaken by Ruthardt and Brauchle (2010) who applied SPT to track polyplexes [237]. In both studies, the delivered DNA compound demonstrated a similar behaviour as viral vectors, where confined and anomalous diffusion was observed along the periphery of the cell followed by active transportation throughout the cytoplasm.

Although the processing of lipoplexes has been well documented, no study has yet to characterize the mobility of lipoplexes formed from a range of different fluorescently labelled DNA (flDNA) sizes within the cellular milieu, specifically addressing the rates and means of motion

throughout locations of the cell simultaneously. Therefore, the research effort presented in this thesis applied the two techniques, RICS and iMSD; enabling the quantification and identification of the rates and means of motion of single flDNA particles from a range of sizes (21bp-5.5kbp) when delivered through lipofection.

2.2 Materials and Methods

2.2.1 Production of DNA Fragments

The 5485bp fragment was obtained by labelling PCI-Neo mammalian vectors (Promega, Madison WI) with Alexa Fluor 488 through a UYLSIS nucleic acid labelling kit (Molecular Probes, Eugene OR). The labelled plasmid was either kept circular or linearized by digesting with BgI II.

The Alexa Fluor488 labelled 21bp oligonucleotide (5'-AF488-TCAATATTGGCCATTAGCCAT-3') was synthesised by Integrated DNA Technologies (Coralville, IA) and used as a forward primer to produce 120, 240, 495, 1000 and 1985bp fragments (reverse primers: 5'-GGACATGAGCCAATATAAATGTACA-3', 5'-GGGCCATTTACCGTAAGTTATG-3', 5'-ACGTAGATGTACTGCCAAGTAGGA-3', 5'-GATGTCAGTAAGACCAATAGGTGC-3', 5'-GTGTGAAATACCGCACAGATG-3', respectively) using PCI-Neo plasmids as template (refer to SI-3 for sequences). DNA fragment lengths were confirmed through agarose electrophoresis, using TAE buffer and 1.5% agarose gels.

Mobility of flDNA and flDNA lipoplexes was characterized at a 50ng/100uL concentration. Lipoplexes were formed and data acquired and analysed as detailed below.

2.2.2 Cell Culture and Transfection

Rat L6 myoblast cells were cultured and maintained in Dulbecco's Modified Eagle Medium (DMEM) (Gibco, UK) supplemented with Fetal Bovine Serum (FBS) (10% v/v), Penicillin/Streptomycin, Amphostat-B and β-Mercaptoethanol at 37°C in a humidified atmosphere of 5% CO_2. Trypsinized cells ($1x10^4$) were seeded onto glass chamber slides (Thermo Fisher Scientific, Australia) in antibiotic- and phenol red-free DMEM (10% v/v FBS) 24h prior to transfections.

The cells were transfected by the DNA fragments using X-Treme Gene 9 (Roche, Germany), according to the manufactures' guidelines. For each well, 100ng of the flDNA was mixed with 0.3 µL of transfection reagent (1:3 DNA:lipid ratio) in antibiotic- and FBS-free DMEM. The lipoplex solution was added directly to the cell cultures within chamber slides. For cytoplasmic measurements, the cells were imaged between 4-8hr after introduction of the lipoplexes, whereas, nuclear measurements were imaged after 36hr. Cell nucleic were counterstained with Hoechst 33342 (1µg/mL) when required.

2.2.3 Image Acquisition and Data Analysis

Confocal, RICS, iMSD and N&B data was acquired using a Leica True Confocal Scanner – Spectro-Photometer 5 (TCS-SP5) inverted confocal microscope (Leica Microsystems, Germany). RICS, iMSD and N&B data was acquired using Avalanche Photodiodes (APDs) (Leica Microsystems, Germany) through an ISS Vista Becker and Hickl FCS card and software (Becker & Hickl, Germany).

Images and data were collected using a 63X (1.4 NA) water immersion objective. The Argon laser with the 488 laser line activated was set to 4%, 1%, 2% or 0.2% maximum power for either 21-1985bp fragments and lipoplexes in solution, plasmid in solution, 21-1985bp fragments in cells or plasmids in cells, respectively. APDs were fitted with a 500-550nm filter. 256x256 format and pixel dwell speed of 32 µs. 633nm laser was used for transmission images, and a 405nm laser for Hoechst 33342. A heated stage was set at 37°C during imaging.

RICS, N&B and iMSD data was analysed using the Globals software package, SimFCS 2.0, developed at the Laboratory for Fluorescence Dynamics (University of California, Irvine) (www.lfd.uci.edu/globals). The PSF waist was determined with eGFP as previously described [227]. All statistical analyses were performed with Microsoft excel using an unpaired, two-tailed student's t-test.

2.3 Results

2.3.1 Characterisation of DNA fragments and Lipoplexes

DNA fragments (120-1985bp) were amplified through PCR. To ensure sample purify and product lengths, samples where run through agarose gel electrophoresis (Figure 2.5). All samples

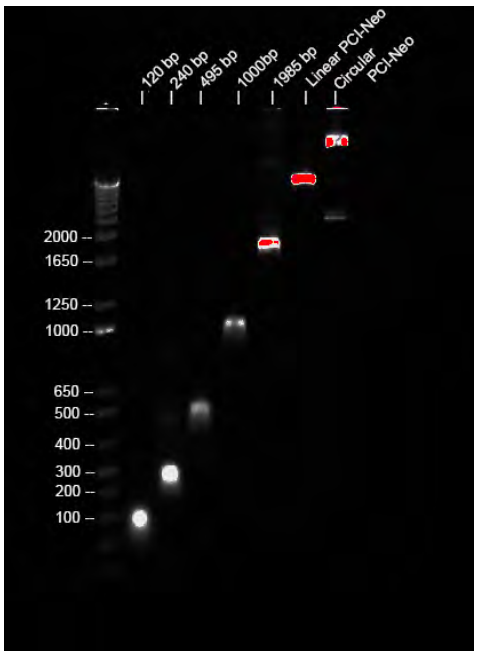

Figure 2.5 – Electrophoresis of DNA Fragments

PCR products ranging from 120bp to 1985 and the PCI-Neo plasmid in its linear and circular form were run through a 1.5% agarose gel to ensure sample purify and product lengths.

showed a single band at the appropriate length compared to the molecular weight marker. The PCI-Neo expression vector was also loaded to the gel in its linear and circular form, the circular form had shown two bands demonstrating this plasmids tendency of supercoiling.

The diffusion of flDNA either complexed or uncomplexed with lipids was determined through the RICS. The range of flDNA sizes assessed (21-5485bp) had demonstrated a size dependent mobility regardless of whether the flDNA was alone or complexed as lipoplexes (Figure 2.6, Table 2). The DNA lipoplexes had demonstrated to be between 60-80% slower than that of the DNA alone. However, the circular form of PCI-Neo was faster as a lipoplex, most likely due to the packaging of the flDNA into the lipoplex that could have caused further compaction of the supercoiled construct. The circular DNA

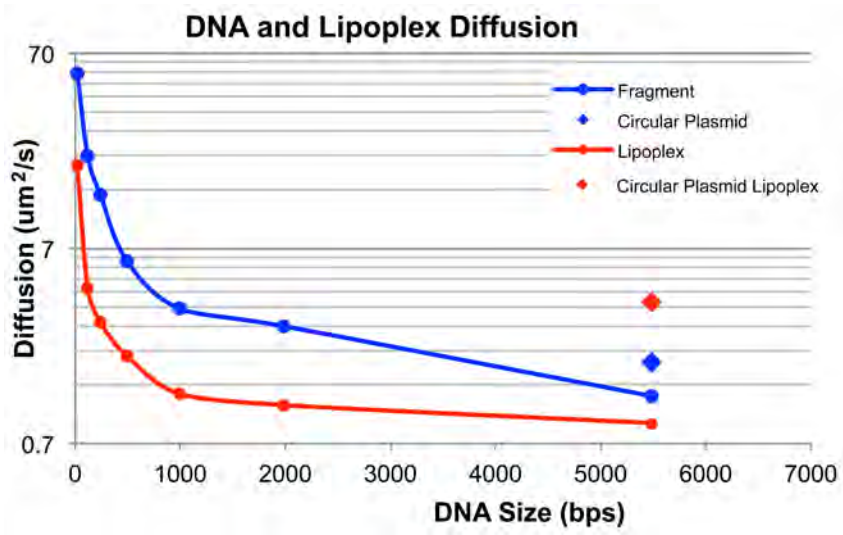

Figure 2.6 – DNA Fragment and Lipoplex Diffusion

The free diffusion of the DNA fragments, 21bp, 120bp, 240bp, 495bp, 1kbp, 2kbp and 5.5kbp (linear and circular) and lipoplexes composed of these fragments demonstrate a size dependent mobility. A summary of the values obtained has been presented in Table 2.

plasmid had also demonstrated a faster diffusion compared to the linearized form, although the base pair sequences were the same, PCI-Neo is known to supercoil, which can be avoided by linearising the plasmid (Figure 2.5).

Table 2 – Summary for the Diffusion of DNA Fragments and Lipoplexes

DNA Size (bp)	Fragment Diffusion ($\mu m^2/s$)	Lipoplex Diffusion ($\mu m^2/s$)
21	55.11±0.94	18.65±3.30
120	20.86±0.48	4.37±0.55
240	13.16±0.50	2.94±0.27
495	6.01±0.32	1.96±0.16
1,000	3.43±0.10	1.26±0.05
1,985	2.80±0.10	1.10±0.10
5485 (Linear)	1.23±0.02	0.89±0.05
5485 (Circular)	1.83±0.03	3.71±0.10

#refer to SI-4 for complete data series

2.3.2 Cytoplasmic Mobility and Dynamics

In order to elucidate DNA lipoplex mobility properties a global cytoplasmic analysis was performed, in which the entire cytoplasm of transfected cells were analysed through RICS. This global analysis provided spatial correlations that fit a two species model, a faster species demonstrating a size dependent decay in mobility as the flDNA size increased, and a slower species, which was size independent (Figure 2.7A and SI 5A).

Statistical analysis demonstrated that the differences in the fast species were statistically significant using the T test, however most of the slow species were statistically insignificant (Figure SI 5C). The population of cells transfected with different sized flDNA constructs exhibited a large range of mobility especially in the slower species, this resulted in a large variance and standard deviation, therefore skewing statistical analysis (Figure SI 5A).

As a result a more detailed analysis approach was employed termed ROI analysis, where small discrete areas were analysed (Figure 2.7B and Table 3). Through this approach, only the slower species was isolated, as the fast species moved through the ROI too rapidly to be correlated, in which case the spatial correlation fit a single species. The ROI analysis provided an average range of motion between 0.66 $\mu m^2/s$ (21bp) to 0.31 $\mu m^2/s$ (linear plasmid) and did demonstrate a size dependency in motion

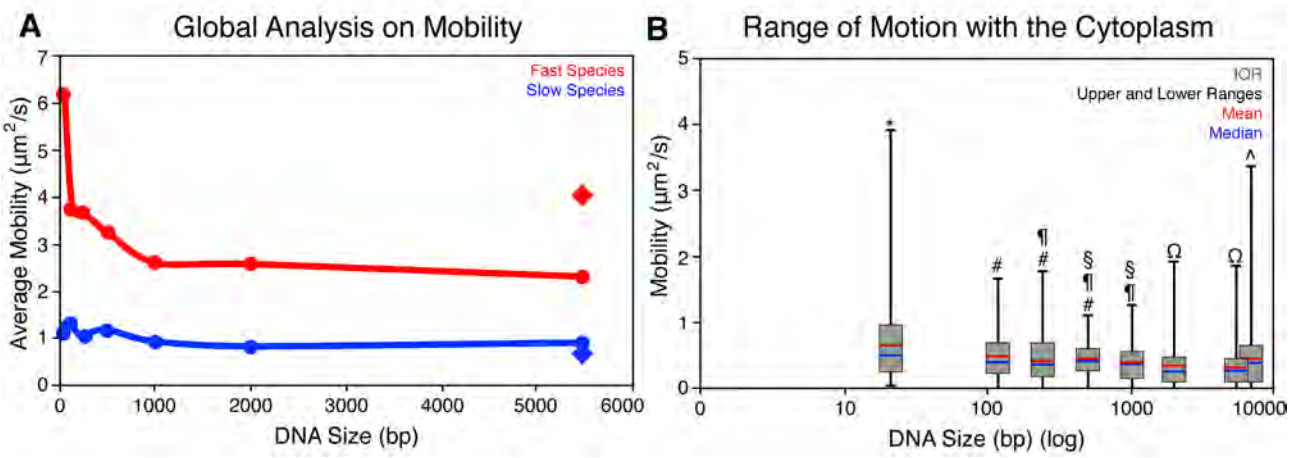

Figure 2.7 – Cytoplasmic Mobility of DNA

*(A) The entire cytoplasm of transfected cells was first analysed through the RICS approach providing a global view on the mobility of the delivered DNA. Two species were isolated, a slow species exhibiting statistically insignificant differences, and a fast species with a size dependent decay in mobility that was between 3.5-8-fold faster than the slow species (n = 27-51 cells). (B) Small areas of the cells (about 2x2μm in size) in the ROI analysis. The DNA within the cytoplasm demonstrated a large range of mobility across all DNA fragments. DNA sizes exhibited a mobility rate that was size dependent however a large variance was observed. Additionally, besides the 21bp and circular plasmid, all demonstrated a similar maximum rate of motion. All DNA size exhibited complete immobility except for the 21bp indicated by *. (minimum cell number = 15, minimum number of values = 83) (^Column was shifted to the right for the circular plasmid as it overlapped and covered the graph for the linear plasmid). #, ¶, §, Ω indicate statistically insignificant pairs. (diamond in graphs represents circular plasmid) (All values and statistical analysis have been presented in SI 5)*

(Figure SI 5A,B). The ROI analysis resulted in a large range of mobility, the largest being the 21bp fragment, 0.02-3.92 $\mu m^2/s$. In addition, the 21bp lipoplex was the only flDNA sequence that did not demonstrate complete immobility (Figure 2.7B). Due to the large range of motion a relatively large variance factor was calculated, ranging from 0.37 to 0.06 (21bp and 495bp, respectively) (Figure S1 5A).

Comparing the two plasmids, the circular conformation had demonstrated a faster rate of motion compared to its linearized counterpart even though the base pair size was the same. The circular plasmid was on average 40% faster (0.44 $\mu m^2/s$ and 0.31 $\mu m^2/s$, circular to linear respectively). In addition, the circular conformation had shown a maximum rate of motion 2-fold faster than the linear (3.39 $\mu m^2/s$ compared to 1.88 $\mu m^2/s$) (Figure 2.7B).

Since the ROI analysis involves small areas of the cell the signals obtained and analysed in the ROIs can be categorised to address how certain factors that influence the mobility of the flDNA, such as the location within the cell (Figure 2.8A SI 5D) and the size of flDNA clusters (Figure 2.8B and SI

5D,E). Firstly, the flDNA signal obtained in the cytoplasm was sorted to provide information on how the cellular milieu affects mobility along the cell extremity, in the cytoplasm, and the peri-nuclear area.

Table 3 - Summary of Cytoplasmic Localised DNA Particles

Fragment	Location	Average	Min	Max	Std Dev	Cytoplasmic Avg
21mer	Extracellular	29.787	13.214	55.045	14.857	
	Diffuse	0.674	0.089	1.397	0.462	
	Small	0.827	0.130	3.917	0.755	0.662
	Large	0.549	0.025	1.888	0.478	
120bp	Extracellular	4.064	4.064	4.064		
	Diffuse	0.781	0.119	1.113	0.288	
	Small	0.559	0.058	1.667	0.347	0.484
	Large	0.272	0.000	0.752	0.210	
240bp	Extracellular	3.170	2.586	3.753	0.825	
	Diffuse	0.489	0.033	1.421	0.364	
	Small	0.462	0.000	1.788	0.340	0.433
	Large	0.349	0.000	1.094	0.281	
495bp	Extracellular	2.070	1.132	2.654	0.657	
	Diffuse	0.602	0.165	1.119	0.341	
	Small	0.470	0.128	1.052	0.197	0.482
	Large	0.373	0.000	1.062	0.247	
1,000bp	Extracellular	1.330	1.234	1.422	0.133	
	Diffuse	0.480	0.000	0.862	0.261	
	Small	0.406	0.010	0.973	0.240	0.424
	Large	0.387	0.000	1.297	0.318	
1,985bp	Extracellular	1.185	0.846	1.630	0.317	
	Diffuse	0.511	0.000	1.940	0.461	
	Small	0.352	0.000	1.667	0.301	0.361
	Large	0.218	0.000	0.640	0.189	
Linear Plasmid	Extracellular	1.119	0.793	1.626	0.284	
	Diffuse	0.317	0.077	0.962	0.286	
	Small	0.380	0.000	1.889	0.324	0.302
	Large	0.243	0.000	0.880	0.222	
Circular Plasmid	Extracellular	2.759	1.608	3.950	0.782	
	Diffuse	0.658	0.000	3.392	0.708	
	Small	0.480	0.000	1.827	0.428	0.447
	Large	0.337	0.000	1.537	0.317	

*mobility units = $\mu m^2/s$

Within the cell, the cytoplasm exhibited faster mobility and the extremity of the cell the slowest. These three locations all demonstrated a size dependent reduction in mobility; however, the cell extremity had a greater decay where the plasmid demonstrated a 55% decrease in mobility, comparing the linear plasmid to the 21bp. Whereas, the cytoplasm and peri-nuclear area displayed decreases of

30% and 37%, respectively. In all three areas, the circular plasmid demonstrated a faster mobility compared to the linear.

The ROI analysis also enabled the discrimination between flDNA based on the cluster size (Figure 2.8B). Here the flDNA signal was sorted based on whether it was not clustered (diffuse), or as small (<500nm diameter) or large (>500nm diameter) clusters. Besides the linear plasmid, all diffuse linear DNA had demonstrated to be faster than when it clusters and, large clusters were the slowest. As previously observed, the circular DNA had demonstrated to be faster than its linear equivalent.

The ROI analysis demonstrated that the mobility of flDNA was influenced by the location in the cell and the cluster size. Across the flDNA sizes assessed, a similar rate and range of motion was found between 120-5472bp, most of which were found to be statistically significant. Due to the large variance in mobility it was clear that there is no standard rate of motion in the flDNA. Therefore, the mechanisms behind the motion were investigated through the utilisation of the iMSD approach.

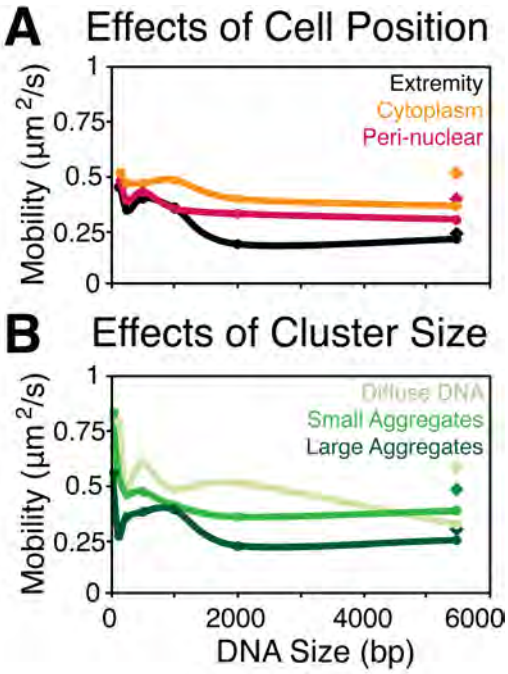

Figure 2.8 – Influence of Cell Location and Cluster size on Mobility

(A) The ROI analysis performed also highlighted that the position of the DNA influenced the rate of the motion, as DNA within the cytoplasm exhibited the faster rate of motion, followed by the peri-nuclear then cell extremity regions. (B) ROI analysis enabled the separation of the delivered DNA based on the size of the cluster it was contained in. Either non-clustered (diffuse), small aggregates (<500nm) or large aggregates (>500nm) were selected and all exhibited a size dependent mobility. Additionally, the size of the clusters influenced the rate of motion as the non-clustered DNA was the fastest, followed by the small and then large aggregates. (diamond in graphs represents circular plasmid)

(B)

2.3.3 Determining the Mechanical Processes behind DNA Mobility

The iMSD approach was applied to further characterize the mobility of lipoplex delivered flDNA, of various sizes, by distinguishing between the different mechanisms that could have occurred within the cell. The iMSD analysis was able to discriminate between a variety of different mechanisms

including random diffusion, active transport, subdiffusion, confined diffusion, transient confinement and binding-unbinding events (Figure 2.9 and SI 6). Random diffusion was observed to be the slowest mechanism and with a reduction in mobility as the flDNA increased in size (Figure 2.9A and SI 6A). By contrast, active transport had been the fastest mechanism observed, and did not appear to have a size dependent trend.

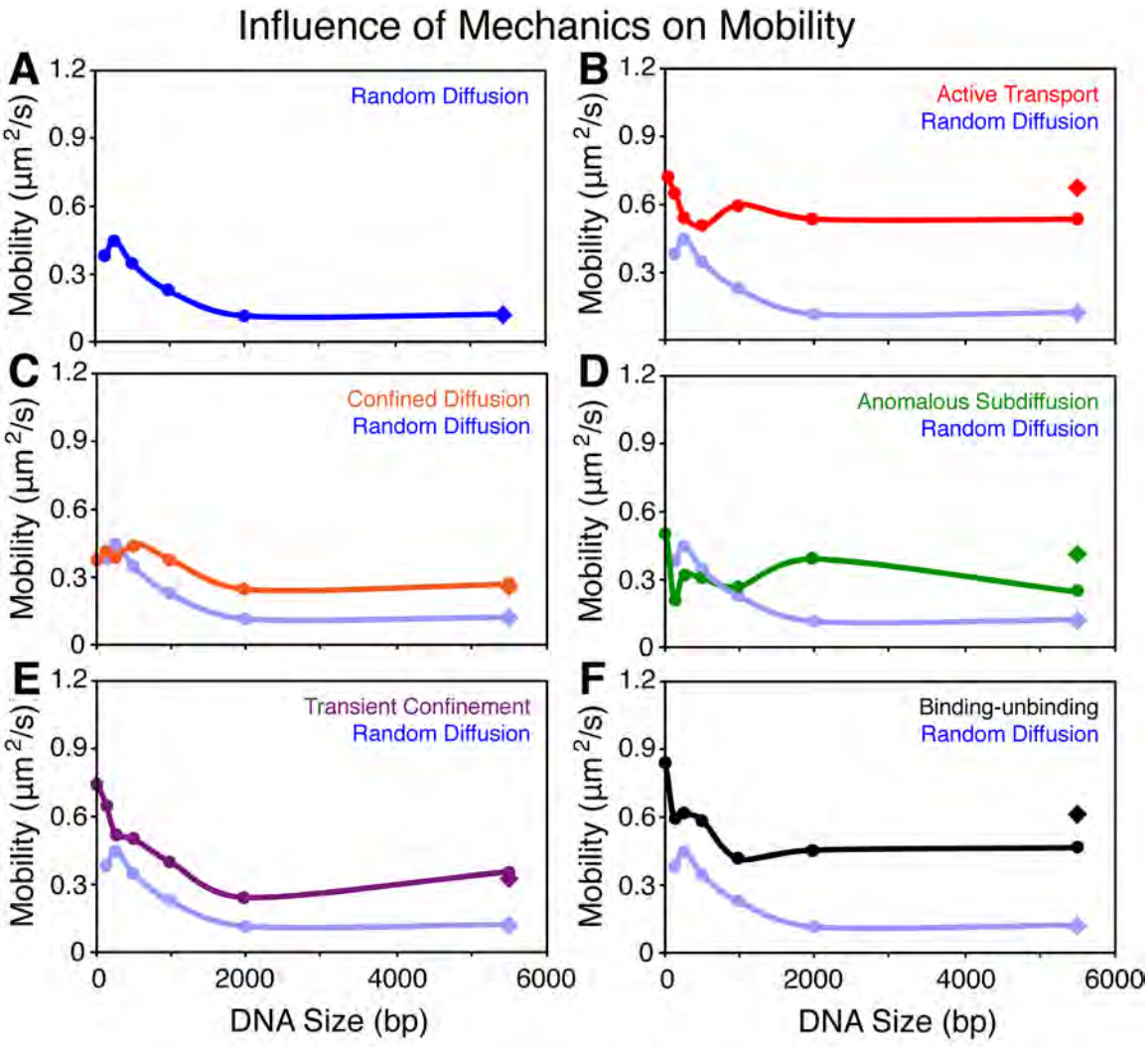

Figure 2.9 – iMSD Analysis of Lipoplex DNA

iMSD analysis demonstrated that DNA size did not influence all means of motion. Motion through AT, CD and AS did not demonstrate size dependency additionally these other means of motion had a higher mobility rate than that of RD (A-C). Whereas, motion through RD and TC had demonstrated a size dependency across the DNA sizes assessed (D). A summary of the values obtained has been presented in Table 4.

The mechanism of confined diffusion had demonstrated no significant differences between the 21-1000bp range, until the 1985bp and plasmids, which had shown a 30% reduction in mobility (Figure 2.9A and S6D). Anomalous subdiffusion has shown an inconsistent range of motion across the flDNA

sizes, which has shown an almost horizontal linear trend. Transient confinement is defined as a temporary entrapment of the particle being observed, which is released during the observation. This mechanism of motion displayed a similar size dependent trend as random diffusion, however, was on average 2-fold faster. The binding-unbinding events on the other hand had a similar trend to active transport, however had a reduced rate of motion of around 25% across the flDNA sizes.

By including the mechanism of motion in the study of flDNA mobility, the variance in the populations was greatly reduced. In the ROI analysis (Figure SI 5A) the average variance in the populations was 0.14 ranging from 0.06-0.37 (495bp and 21bp, respectively), whereas the average variance determined from the iMSD analysis was 0.05 and ranged from 3.3^{-6}-0.16 (240bp random diffusion and 495bp transient confinement, respectively) (Figure SI 6A-F).

Table 4 – DNA Transport Mechanism vs. Mobility Rate

	DNA Fragment (bp)							
Means of Motion	**21**	**120**	**240**	**495**	**1000**	**1985**	**5485 (Linear)**	**5485 (Circular)**
Random Diffusion	NA	0.398	0.450	0.340	0.222	0.118	0.125	0.126
Active Transport	0.711	0.648	0.543	0.503	0.598	0.533	0.533	0.676
Anomalous Subdiffusion	0.509	0.213	0.619	0.317	0.283	0.402	0.260	0.422
Confined Diffusion	0.384	0.429	0.399	0.449	0.457	0.437	0.306	0.259
Transient Confinement	0.727	0.635	0.519	0.492	0.387	0.237	0.350	0.327
Binding-Unbinding	0.741	0.459	0.468	0.450	0.319	0.368	0.356	0.493

*mobility units = $\mu m^2/s$

#refer to SI-6 for complete data series

In addition, the iMSD approach also demonstrated a spatially distributed trend in the mechanisms of motion observed (Figure 2.10). Along the cell extremity, more non-active mechanisms were detected including; confined diffusion and subdiffusion, as well as transient confinement, which may have been the release of the DNA lipoplexes from endosomes. Binding-unbinding events typically attributed to 25-30% of events regardless of the location. Motion within the cytoplasm on the other hand was mostly attributed to active transportation. Once within the peri-nuclear region, the flDNA motion was mostly due to non-active mechanisms again (i.e. confined diffusion and subdiffusion). Finally in the nucleus, only confined diffusion and subdiffusion was exclusively observed. Across the

flDNA sizes this trend was observed regardless of the size delivered. The only major difference between fragments was an increase in immobility as the flDNA increased in size (charts for all DNA sizes are shown in Figure SI 6G).

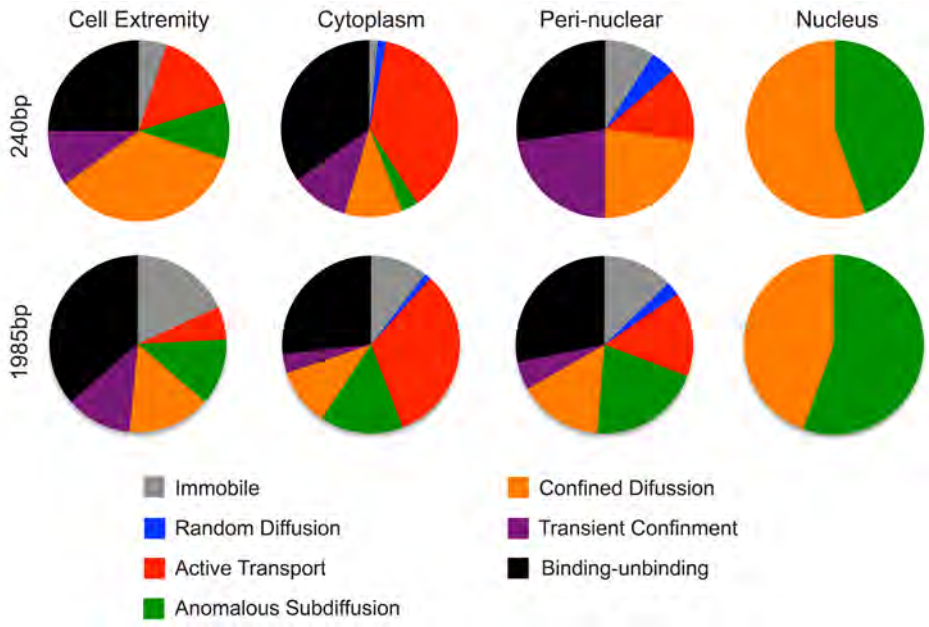

Figure 2.10 – Location-specific Distribution of Transport Mechanisms

The mechanisms of motion were sorted based on the location within the cell as being either along the extremities of the cell, within the cytoplasm, in the peri-nuclear area or within the nucleus. In this figure the cell populations transfected with the 240bp and 1985bp fragments have been presented. The 1985bp population had demonstrated a greater distribution of immobility compared to the 240bp. Along the cell extremities and in the peri-nuclear region, a greater amount of AS, CD and TC was present compared to the mobility within the cytoplasm which had a greater distribution of AT. Within the nucleus, only AS and CD was observed. Pie charts for all DNA sizes have been presented in SI 6G.

Within a cellular system there is expected to be variability, which was observed and presented in Figure 26, showing cells transfected with the 120bp, 1000bp, 1985bp or linearized 5485bp plasmid fragments (A-D, respectively). In Figure 2.11, each cell is presented with ROI's each relevant to a specific iMSD curve example. The expected iMSD curve of each mechanism of motion has been previously presented (Figure 2.4). Additionally, for each cell the number of each mechanism of motion and range of motion has been shown. Within the single cell a range of mobility was observed, in some cases ranging 10-fold (Figure 2.11D). The range of mobility has been attributed to the variety of mechanisms of motion that are involved in the mobility of the flDNA. Each cell analysed and those presented here contain a range of different means of transport mechanisms, including RD, AT, AS,

CD, TC and binding-unbinding events. Across the cell populations acquired and analysed this was observed for all DNA constructs. Additional examples have been provided in SI 7.

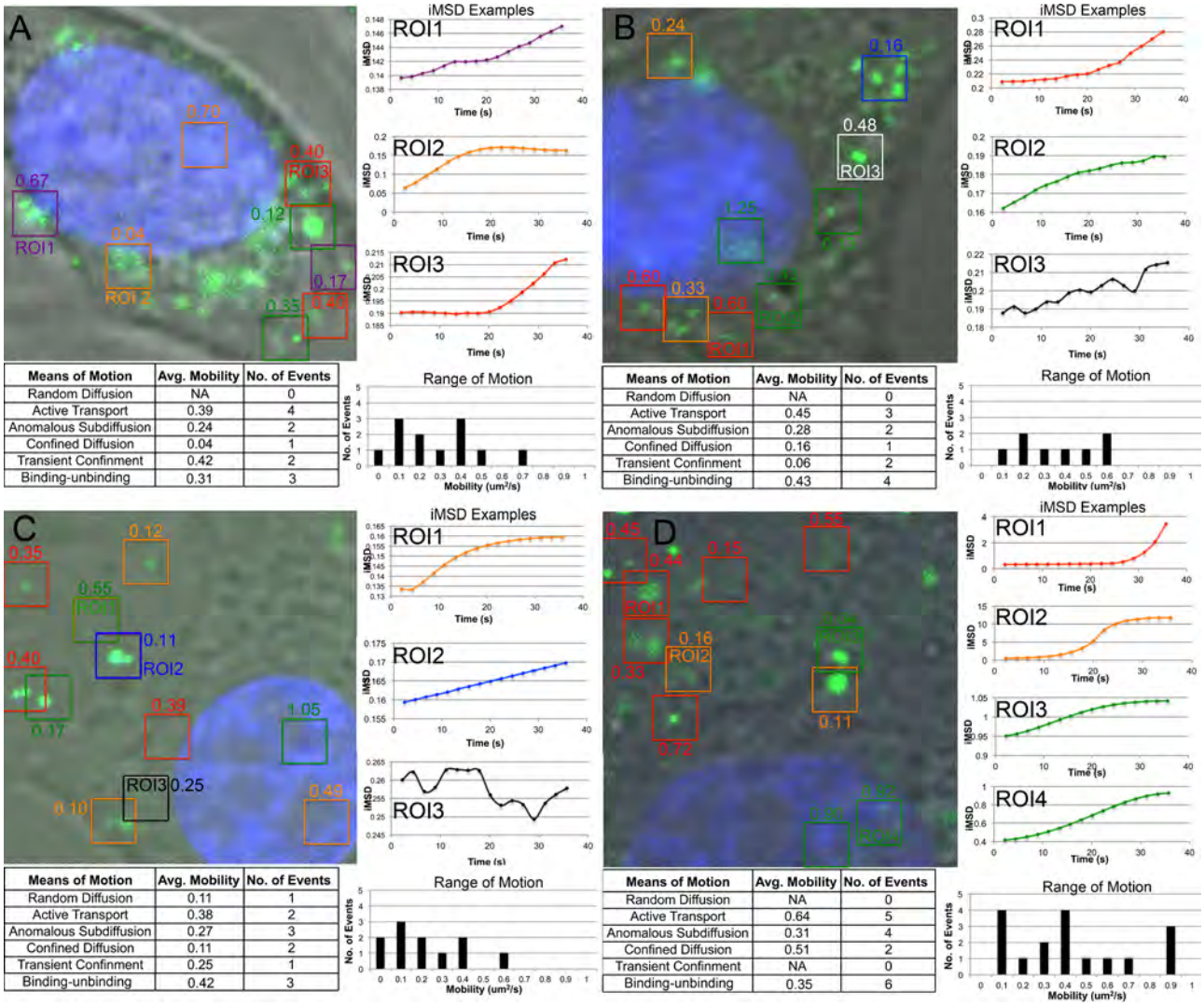

Figure 2.11 – Examples of DNA dynamics of varying sizes

Example of RICS and iMSD analysis on cells transfected by 120, 1000, 1985 and linear 5.5kbp fragments (A-D) demonstrate that within a single cell a range of different means of motion and rates of mobility can be identified examples of. For the individual cells the occurrence of each means of motions has been tabulated, as well as the range of mobility observed. The mechanism of motion have been selected for each cell showing RD (Blue), AT (Red), AS (Green), CD (orange) and Binding-unbinding (Black). Size of is 16.5x16.5um.

2.3.4 Nuclear Dynamics

Finally the dynamics of the flDNA within the nucleus was explored (Figure 2.12 and SI 8). These events were less frequently observed (approximately 25% of cells containing cytoplasmic flDNA), however RICS analysis had demonstrated a rapid mobility in the nucleus compared to the cytoplasm that had fit a single species model. Within the nucleus, the flDNA had shown a 3.4- to 6.5-

fold (120 and 1000, respectively) increase compared to the cytoplasm. The overall trend in mobility had shown a size dependence, however the 120-495bp fragments had anomalous values from this trend.

In addition to the mobility being explored, the extent of nuclear localisation was explored by quantifying the flDNA through Number and Molecular Brightness (N&B) analysis. Through the number (N) component of the approach, it was found that the 240bp fragment had accumulated in the nucleus the most (Figure 2.12B and C). The amount of nuclear localisation of flDNA decreased as the fragment size increased. The two plasmids appeared to have the lowest amount of flDNA (120bp fragment N = 2.2 compared to N=0.44 and 0.18 in the linear and circular plasmids, respectively). The flDNA ≤1985bp had shown a diffuse distribution in the nucleus, whereas the linear and circular plasmid were maintained in clusters, mostly along the edge of the nucleus.

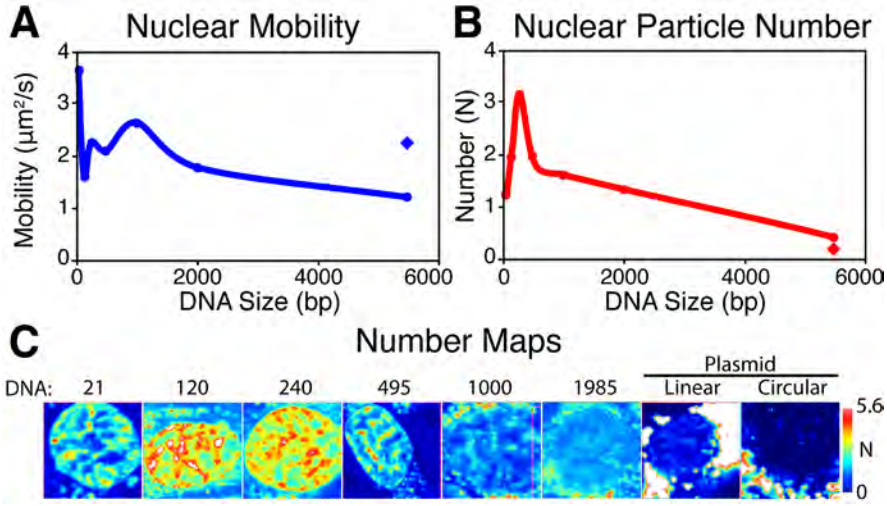

Figure 2.12 – Nuclear Localised DNA/Lipoplex

Nuclear Dynamics and Particle Number of Delivered DNA. (A) Size dependent mobility and (B) DNA particle number (N) in cells transfected with a range of DNA sizes. (C) N&B analysis provides the number calculation with an N map showing the DNA particle number within the nucleus after 36h. All images are to the small scale. (n = 10 (21-1985bp) and 8 (plasmids)) (images 16.5x16.5µm) (diamond in graphs represents circular plasmid)

2.4 Discussion and Conclusion

Characterisation of the different DNA fragments ranging between 21bp-5.5kbp demonstrated a mobility rate and size dependent diffusion consistent to previously published studies [140]. Except for the 495bp fragment and 5.5kbp linear fragment, in which case the mobility rates were 2-fold and 1.5-fold faster than Lukacs et al. (2000), respectively. However, the study undertaken by Roberston et al. 2006, who quantified DNA diffusion by tracking Brownian motion identified a similar mobility rate for a

5.9kbp fragment, and additionally demonstrated that circular DNA has a faster mobility rate than linear, consistent with to the work presented here using RICS [238].

The rate of motion throughout the cytoplasm had a significant range of mobility, in some cases having a range of 10- to 100-fold in a single cell, which has been demonstrated in a previous study [239]. However, the rate of mobility identified through RICS was considerably different to other studies also, such as the one carried out by Lukacs et al. (2000) monitoring DNA diffusion through FRAP. The study reported by Suh, et al. 2004 [240], had shown a similar range of mobility in a DNA fragment of 2kbp but with an average rate 2-fold less than the results reported in study. This inconsistency in mobility rates supports the notion that the mobility of DNA lipoplexes is the combination of cell type, DNA specific and delivery-mode dependent nature of lipoplex gene delivery but could also be influenced by the approach of analysis applied.

Nonetheless, the rates of mobility reported in this thesis are similar to those expected within the cell. Given that the DNA lipoplexes are anticipated to be entrapped within endosomes after cellular entry [185], the mobility of the DNA lipoplexes should reflect the transport properties of endosomes. The rate of motion of retrograde acidified compartments at 37°C has been identified to be at 0.45 um^2/s [241] and dynein-mediated transport estimated to reach up to 0.7 um^2/s [242], these rates match the approximate range of active transport observed within the cytoplasm of this study.

The biophysical mechanisms behind the flDNA mobility demonstrated a similar course of a virus (influenza) [243] and PEI-DNA complex [142], which follows a 3 phase process; (i) slow directed into the cell, (ii) confined motion along the edge of the cell, followed by (iii) fast directed motion along microtubules. RICS and iMSD analysis of lipoplex delivered flDNA demonstrate further phases of mobility including: non-active motion within the peri-nuclear area, and then confined- and sub-diffusion in the nucleus.

Suh et al. (2004) identified that approximately 80% of DNA/PEI complexes displayed AS and immobile transport characteristics, which would include CD, in half of their observations. This however, has not been the case in this study, which demonstrates one third of the observations

accounting for AT and a combination of CD, TC, RD and AS responsible for another third of the observations. The final third of iMSD observations demonstrated a binding-unbinding signature and had a similar mobility rate as the AT events. This phenomenon is most likely due to binding and unbinding events of the DNA with microtubules and other cellular structures and/or components [240], possibly due to the on-off kinetics of endosomes along microtubules [244,245].

It was noted that an increase in immobility was observed as the DNA size increased, which was expected, as the larger particles would be restricted in how fast they can diffuse within the cytoplasm. However, since the occurrence of immobility was the only means of motion influenced by the DNA size it can be concluded that DNA, up to 5.5kbp does not influence the mechanisms of motion involved in the cell. A series of further studies could have been utilised to support this statement for this project such as reducing temperatures, ATP reduction experiments or microtubule depolymerisation through drugs such as nocodazole, however these experiments have already been performed by others [50,143,217,239]. These studies demonstrate that by inhibiting or reduction active transportation the rate of motion is reduced in gene delivery or the expression of the transgene is either reduced or completely inhibited.

Entry into the nucleus creates a bottleneck in the cytoplasm, resulting in the accumulation of the flDNA in the peri-nuclear region, consistent with the study by Suh et al. (2004), who also found that the main means of motion in this area is AS and CD.

Once within the nucleus, the flDNA in this study demonstrated a very different mobility to previous reports. Lukacs et al. (2000) identified a rapid accumulation from the cytoplasm into the nucleus of only a 21bp fragment, while larger DNA fragments were also assessed in their study. When microinjected directly to the nucleus all DNA fragments were found to be immobile [140]. In contrast, Shimizu et al. (2005) demonstrated that microinjected DNA <400bp rapidly diffused throughout the nucleus, however the mobility rate was not recorded in the study [102]. Nevertheless, studies addressing the nuclear dynamics of other macromolecules have shown a similar range to that observed here for flDNA. Politz *et al.* (1998) found the mobility of oligonucleotides to be 9 um^2/s [246]. Further,

endogenous intranuclear mRNA, appeared to move at an average rate of 0.6 um^2/s [247], transcription factors ranging from 0.34 – 1.99 um^2/s [248] and nuclear proteins, HMG17, SF2/ASF and Fibrillarin diffuse at 0.45, 0.24 and 0.53 um^2/s [199], respectively. The mobility values of flDNA analysed via RICS and iMSD are consistent with the nuclear dynamics of other macromolecules reported above.

Within the nucleus, the flDNA analysed here, demonstrated only two forms of motion, either CD or AS. This occurrence fits the model of nuclear dynamics of macromolecules around chromatin structures presented by Hinde *et al.* (2011). Hinde *et al.* (2011) demonstrated that chromatin poses as either a complete barrier or a penetrable barrier where eGFP was able to pass through the structure [249]. It is likely AS would be due to the chromatin and intra-nuclear DNA and other structures acting as a barrier and crowding the space, whereas the confined diffusion could be a result of either crowding within the area or as a result of the delivered DNA passing through less dense chromatin.

The distribution of nuclear localized flDNA in our study had shown a similar pattern to a previous study. Mearini et al. (2004) had shown that 3000bp DNA plasmid delivered in the nucleus is excluded from specific nuclear compartments including the nucleolus and PML bodies but had a similar distribution, to but no association with the SAF-A nuclear scaffolding protein [207]. In the results presented here, the flDNA between 21bp-2kbp had shown a similar pattern within the nucleus as Mearini et al. (2004), but the largest flDNA fragment (5.5kpb) did not. However, it has been identified that some DNA viral vectors move very little within the nucleus from their site of entry, resulting in accumulation of the viral vector genome along the periphery of the nucleus [210].

In summary, the application of RICS and iMSD to characterise the mobility of different flDNA particle sizes, delivered to live cells, has enabled the quantification and the mechanics of the motion of these lipoplexes. The goal of the study was to assess how the DNA size influences the dynamics and mechanics of motion throughout the cell in real time. Further, this model can be applied to track any form of nucleotide, such as RNA and lncRNA, or other macromolecules that can be fluorescently labelled. In addition, the study has demonstrated the potential of the RICS and iMSD approaches for future investigations into the dynamics of delivered macromolecules.

CHAPTER 3

Live Cell Characterisation of DNA Aggregation Delivered through Lipofection

3.1 Introduction

Molecular aggregation within the live cell can have a significant biological, pathological and clinical impact, however it has received limited attention to date. Several examples of aggregation significance includes the necessary aggregation of proteins in adhesion complexes [4], aggregation of proteins in disease states such as Huntington's Disease [250] and Alzheimer's Disease [251], which can influence disease progression, and aggregation nanoparticles in therapeutic delivery that can hamper drug delivery [252].

A likely reason for this lack of research efforts has been a limitation in quantifying aggregation within the live cell. It is possible to observe cluster formation and determine cluster size, however quantifying aggregation states appears to be a difficult task at this juncture. Nevertheless, the FCS-based Number and Brightness (N&B), more recently developed, enables the real-time quantification of aggregation in live cell samples by acquiring the number and brightness (aggregation) of mobile particles within a sample [2,253].

3.1.1 Number and Molecular Brightness Approach

Before the development of N&B, a common and challenging problem was determining the average number and brightness of molecules within fluorescence microscopy images [2]. A common practice that was widely applied to estimate the number of molecules within a pixel was to calibrate the fluorescence intensity with a fluorescent solution of a known concentration. However, even though

this practice provides the total number of fluorophores, it does not provide any information on the state of aggregation of the fluorophores as a few bright aggregates can show the same fluorescence intensity as many dim molecules [2].

It is possible to obtain the brightness of a particle separately from the number of particles using FCS in a given sample. FCS has been used to determine the degree of aggregation of fluorescent proteins within a solution as the occupation number of particles in an open volume follows a Poisson distribution [2].

Moment analysis was then proposed by Qian and Elson (1990), which involved the application of FCS to determine the number of particles by calculating the ratio of the variance to the square of the average intensity, which is proportional to 1/N (where N is the number of particles in an open volume) [254]. The brightness of fluorescent particles is then obtained by calculating the ratio of the average intensity to the number of particles. However, the approach can only be applied to homogenous systems, as multiple species of different brightness cannot be resolved [2].

A recently proposed approach, known as Photon Counting Histogram (PCH) analysis, is capable of resolving multiple species of brightness in a homogenous solution. The PCH analysis considers the entire distribution of photon counts rather than only the first and second moments (moment analysis) in a given solution [2,12]. However, the PCH method is computationally slow for live cell analysis as it requires a relatively large number of observations at each pixel [2].

Moment analysis, PCH and correlation methods are all capable of determining the number and state of aggregation to an extent. The N&B approach, is a combination and extension of these methods, and is capable of determining the number and degree of aggregation of multiple species of molecules within a live cell in real time [2,253].

In order to obtain the number and brightness of particles at each pixel of an image, the first and second moments of intensity must be calculated to determine the variance factors of the fluctuations [2]. This is performed by the following equations:

$$\langle k \rangle = \frac{\sum_i k_i}{K}$$

Equation 11 - N&B First Moment – Average

$$\sigma^2 = \frac{\sum_i (k_i - \langle k \rangle)^2}{K}$$

Equation 12 - N&B Second Moment - Variance

where K equals the number of frames, which should be 2 when using consecutive images and k_i is the intensity at a given pixel.

Following Figure 3.1, there are two examples, pixel k that contains very large aggregates and pixel j, which contains a pool of many monomeric particles. Following the first moment calculation the same average of the fluctuations over time is obtained, demonstrating that confocal microscopy cannot distinguish between aggregative states. However, following the second moment calculation, the variance of the frequency can be used to distinguish between the states of aggregation. The variance of intensity measurements can be led by a combination of two terms, variance due to occupation number (σ_n^2) and variance due to the count statistics (or shot noise) of detectors (σ_d^2); other intensity changes to pixels, such as bleaching and cell movement are also corrected.

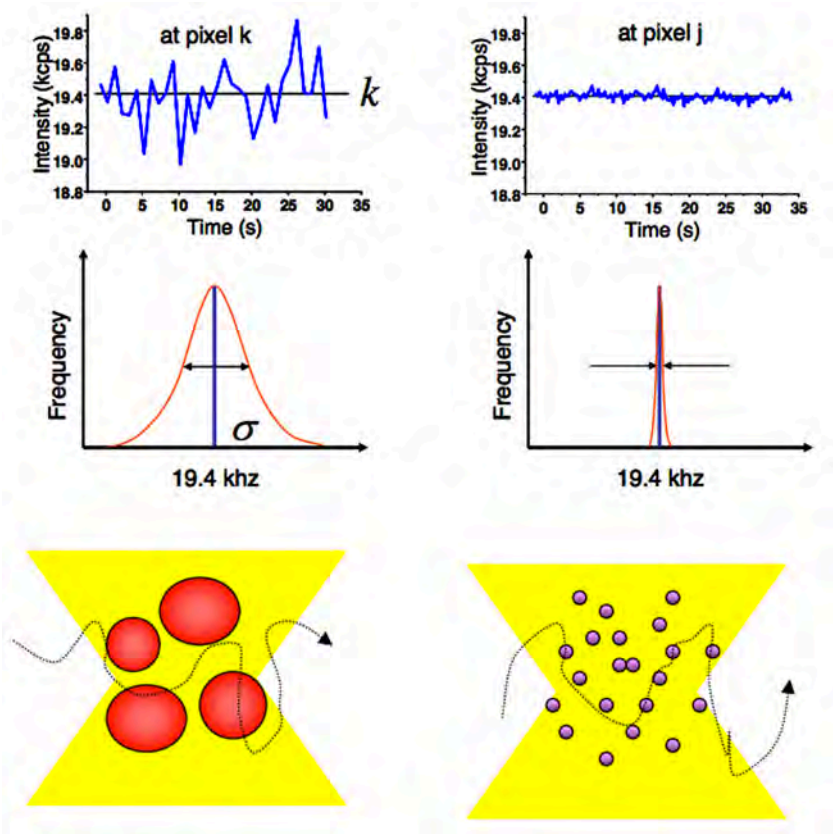

Figure 3.1 – N&B First and Second Moments

In this schematic two examples have been presented, pixel k containing few large aggregates and pixel j containing many monomeric particles. In both examples the average intensity is the same (black line in top graph), however over time pixel k has larger fluctuations. This critical difference results in pixel k having a greater and broader variance σ than pixel j (lower graphs). Thereby enabling the aggregative state to be determined. (Image courtesy of Dr Michelle A. Digman)

The values obtained in the first and second moment calculations are then used to determine the aggregative state and particle number using additional algorithms. The molecular brightness (ε) is defined as "the number of photons emitted per second per molecule when the molecule is in the centre of the illumination volume" and is represented as the units counts/second/molecule (cpsm), reflecting the cluster or aggregation of fluorophores, and n indicates "the average number of molecules in the illuminated volume" [2].

The apparent brightness (B) for each pixel is defined as "the ratio of the variance to the average intensity" and the apparent number of particles (N) is defined as "the ratio of the total intensity of B". These values are calculated by the following equations:

$$B = \frac{\sigma^2}{\langle k \rangle} = \frac{\sigma_n^2}{\langle k \rangle} + \frac{\sigma_d^2}{\langle k \rangle} = \frac{\varepsilon^2 n}{\varepsilon n} + \frac{\sigma_d^2}{\langle k \rangle} = \varepsilon + 1$$

Equation 13 - N&B Apparent Brightness B

$$\boldsymbol{N = \frac{\langle k \rangle^2}{\sigma^2} = \frac{\varepsilon n}{\varepsilon + 1}}$$

Equation 14 - N&B Apparent Number N

An important note to take in these calculations is that the value of B is related to the brightness of particles (ε) but independent to the number of particles, and the value N is directly proportional to the number of particles (n). The equations for Apparent N and B are rewritten to give a value for the true number of molecules (n) and the true molecule brightness (ε), as expressed below:

$$\varepsilon = \frac{\sigma^2 - \langle k \rangle}{\langle k \rangle}$$

Equation 15 - N&B True Molecular Brightness

$$n = \frac{\langle k \rangle^2}{\sigma^2 - \langle k \rangle}$$

Equation 16 - N&B True Particle Number

The variation due to the occupation number is proportional to the square of the molecular brightness and variance due to the detector being equal to the average intensity. The variations seen can be defined by the following equations:

$$\sigma_n^2 = \varepsilon^2 n$$

Equation 17 - N&B Variance due to Particle Number Fluctuations

stating that the variance is due to the number fluctuations depending on the particle brightness squared.

$$\sigma_d^2 = \varepsilon n$$

Equation 18 - N&B Variance due to Detector Shot Noise

stating that the detector variance is equal to the intensity.

$$\langle k \rangle = \varepsilon n$$

Equation 19 - N&B Average Intensity

stating that the average intensity is due to the molecular brightness times the average particle number.

At present the N&B approach has been applied to quantify aggregation of proteins, which are fluorescently labelled, in which sequences encoding for the protein of interest is tagged to a fluorescent protein by way of a fusion gene. Through this process a number of significant studies have resulted including the quantification of the huntington protein in Huntington's Disease [250], oligomerization of the LRRK2 protein, which is relevant in Parkinson's Disease [255], and aggregation of the VP40 protein in Ebola virus infections, a protein that has biological significance in the virus' lifecycle including viral transcriptional morphogenesis, packaging and budding of mature virions [256]. These noted studies address processes involved with endogenous proteins, rather than the delivery of components of therapeutic interest including lipoplexes, carbon nanoparticles and drugs, which are likely to interact with the cell differently than endogenous or gene-encoded introduced proteins.

3.1.2 DNA Lipoplexes as an Aggregation Model

The aggregation of DNA complexed with cationic lipids forming lipoplexes for gene delivery has not been fully characterised or quantified within live cells. The aggregation of lipid-based gene delivery is of interest given that it has previously been noted as being a major barrier to gene delivery [50],

but the phenomena has yet to be addressed in live cells. Once aggregated, the delivery of DNA may be hampered for a number of reasons, such as an increase in size causing reduced mobility (as seen in the Chapter 2). However, aggregation of lipoplexes has yet to be assessed in the live cell and real time.

The aggregation of DNA complexed with (non-viral) delivery vectors has been addressed in several studies, including the potential mechanisms of aggregation [257] however, these were not cell-based studies [258,259]. To our knowledge no study has identified the location, state, nature or amount of aggregation that occurs within the cytoplasm or nucleus of live cells.

Some studies have addressed the aggregation of polyplex aggregation in solutions; for example, Sharma *et al.* (2005) determined that the aggregation of PEI complexes is reduced in decreased pH and higher viscosity (amongst other factors) [257]. A study undertaken by Escriou *et al.* (1998), assessed the effects of serum of gene delivery using DNA/lipopolyamine complexes and noted in the presence of serum the DNA complexes accumulate in many small masses, whereas in the absence of serum, the DNA was found in few but large bodies throughout the cytoplasm [260]. However, Escriou's research effort was unable to quantify the aggregation that may have occurred.

Through the application of the N&B approach a model for flDNA delivery in live cells has been presented to quantify intracellular aggregation. Aggregation in the delivery of such compounds poses as a significant barrier, in which case large aggregates may not be able to traffic through the cell. Additionally, the extent of delivered molecules that do not aggregate would be of interest as these could be therapeutically significant. Therefore, in this model the application of the N&B approach to characterise flDNA aggregation in live cells is presented.

3.2 Materials and Methods

3.2.1 DNA Fragments and Lipoplex formation

The PCI-Neo plasmid (5472bps) (Promega, Madison, WI) was labelled with Alexa Fluor®488 using the ULYSIS Nucleic Acid Labelling Kit (Molecular Probes, Eugene, OR) according to the manufacturers' guidelines: 1μg of the plasmid was denatured at 95°C for 5 minutes. The Alexa

Fluor®488 ULYSIS labelling reagent stock solution was added and the reaction was incubated at 80°C for 15 minutes, then stopped on ice. The labelled plasmid was either kept circular or linearized by digesting with BgI II.

Varying sizes of DNA were produced through PCR using an Alexa Fluor488 labeled 21bp oligonucleotide (5'-AF488-TCAATATTGGCCATTAGCCAT-3') (synthesised by Integrated DNA Technologies (Coralville, IA)) as a forward primer to produce 120, 240, 495, 1000 and 1985bp fragments (reverse primers: 5'-GGACATGAGCCAATATAAATGTACA-3', 5'-GGGCCATTTACCGTAAGTTATG-3', 5'-ACGTAGATGTACTGCCAAGTAGGA-3', 5'-GATGTCAGTAAGACCAATAGGTGC-3', 5'-GTGTGAAATACCGCACAGATG-3', respectively) using PCI-Neo mammalian vectors (Promega, Madison WI) as template.

Lipoplexes were formed using X-Treme Gene 9 (Roche, Germany) according to the manufactures' guidelines with a DNA:Lipid ratio of 1:3. Lipoplexes were formed and either transfected or imaged in Dulbecco's Modified Eagle Medium (DMEM) (0% FBS). Briefly, for each well 150ng of the labelled DNA was mixed with 0.45 μL of transfection reagent in antibiotic- and FBS-free DMEM and incubated for 20min before being used immediately.

3.2.2 Cell Culture

Rat L6 myoblast cells were cultured in DMEM supplemented with FBS (10% v/v), Penicillin/Streptomycin, Amphostat- B and β-Mercaptoethanol at 37°C in a humidified atmosphere of 5% CO_2. Trypsinized cells ($1x10^5$) were seeded onto 35mm diameter dishes with optic glass (MatTek, Ashland, MA) coated with poly-L-lysine (Invitrogen, Carlsband, CA) in antibiotic-free DMEM (10% v/v FBS) 24h prior to transfections.

3.2.3 Microscope Configuration for N&B and RICS Analysis

Data was collected on either a FluoView 1000 (FV1000) (Olympus, Japan) or a True Confocal Scanner – Spectro-Photometer 5 (TCS-SP5) (Leica Microsystems, Germany):

The FV1000 system was fitted with a 60X (1.2 NA) water immersion objective lens. Images were collected using a 505-525nm-bandwidth filter and a 488/543/633 dichroic mirror. The 488nm

laser pathway was activated and set to 0.5% power. Data acquisition was initiated through the SimFCS software. The TCS-SP5 was coupled with ISS Vista Becker and Hickl software (Becker & Hickl GmbH, Germany). Avalanche photodiodes (APDs) (Leica Microsystems, Germany) were utilised with a 500-550nm filter. The microscope was fitted with a 63X (1.4 NA) water immersion objective. The Argon laser with the 488-laser line activated. Data acquisition was initiated through the ISS Vista Becker and Hickl software. Both systems were set to acquire a pixel resolution of 256x256 or 512x512, with a pixel size of 50nm and pixel dwell time 32 μs, respectively. Sampling time was set to capture 100 frames.

Aggregation of DNA plasmids and lipoplexes were characterized at a 50ng/μL concentration (total volume: 300 μL, 150ng DNA) in DMEM without FBS.

To observe cellular entry and cytoplasmic localized lipoplexes the cells were imaged immediately after the introduction of the DNA and then continuously for 8 hours. In order to observe the lipoplex/DNA within the nucleus, cells were incubated between 24-48h in the presence of the lipoplex solution prior to imaging. In order to identify the positioning of the nucleus, cells were counterstained with Hoechst 33342 (1μg/mL) and imaged with a 405nm diode laser. The N&B and RICS data were analysed using the Globals software package, SimFCS, developed at the Laboratory for Fluorescence Dynamics at the University of California, Irvine (www.lfd.uci.edu/globals). For the N&B analysis data sets were detrended and a moving average of 10 frames was used for RICS analysis. The waist of the PSF was determined with (30nM) fluorescein for the RICS analysis.

3.3 Results

3.3.1 Solution Characterisation

In order to quantify aggregation the N&B approach presents a histogram known as a B vs. Intensity plot. In this plot every pixel of the image series has been processed through the algorithms presented earlier, as a result each pixel has it's own B value, which is used to calculate the aggregative state. Since B (the apparent brightness) is equal to the true brightness (ε) + 1, and ε is represented as

counts/second/molecule (cpsm), values can be substituted to obtain the true brightness of particles, which is used to determine the aggregative state of particles as a dimer (aggregate of 2) will be 2-fold brighter than a monomer (non-aggregated particle). The true brightness will increase magnitudes greater than that of the monomer depending on the aggregative state.

The N&B approach demonstrated flDNA alone in solution did not aggregate whereas flDNA and lipoplex do aggregate. However, once complexed with lipids forming lipoplexes the flDNA had demonstrated a substantial extent of aggregation with an 8-fold increase in the highest B values obtained (Figure 3.2A-C). The flDNA and lipoplexes in solution appeared to have average B values similar to the naked flDNA (a homogenous solution), whereas the lipoplexes had formed few but large aggregates. As a consequence, a majority of analysed area contained no signal, resulting in a lower average (Figure 3.2D).

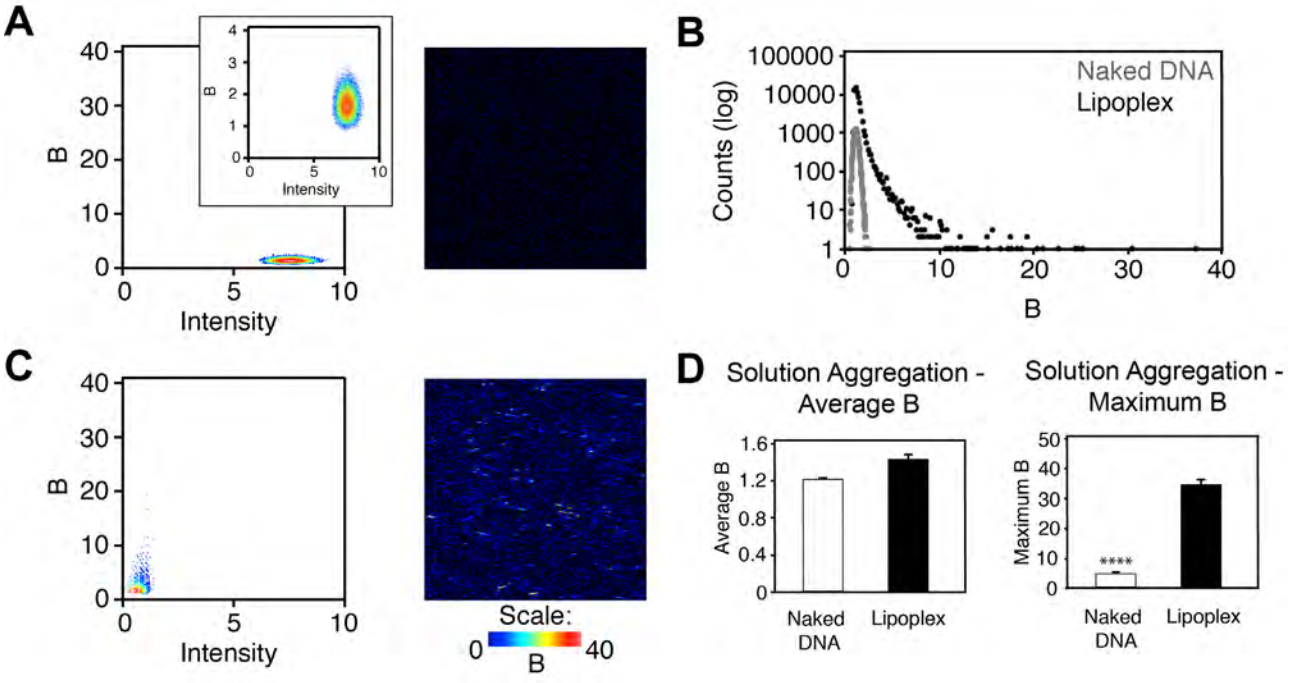

Figure 3.2 – Intrinsic Aggregation of DNA Plasmid and Lipoplexes

*The aggregation of either naked (A) or lipid-complexed (C) DNA was explored through the application of the N&B approach. The N&B approach provides information through a B vs Intensity plot, where each pixel is allocated a location based on these values, a series of maps including a B map (providing a pictorial presentation of aggregation) (A, C) and histograms (B). The N&B approach had demonstrated that the DNA alone did not aggregate, whereas once complexed with lipids forming lipoplexes, large aggregates were observed in solution. The maximum extend of aggregation was 8-fold greater in the lipoplexes, whereas the average B was similar (D). The similar average B was attributed to the naked DNA being a homogenous solution, whereas the lipoplex solution only contained few but large aggregates. (**** p <0.0001)) (graphs depict mean ± se)*

3.3.2 Characterising Live Cell Aggregation of Lipoplexes

During the characterisation of flDNA lipoplex aggregation in the model myoblast cell line, lipoplexes were formed with the flDNA plasmid. Once administered, the cells were imaged at various time points in order to elucidate aggregation at different times and processes. Initially, data acquisition and analysis was conducted, upon addition of the lipoplexes until 4h, internalisation of the lipoplexes.

An internalisation event was identified when the fluorescence signal (the flDNA coupled with lipids) had accumulated along the extracellular side of the membrane. When the event was identified images were collected over 1 hr or until the lipoplex was completely internalised (additional observations displayed in SI 8). The complete internalisation process of a single event is presented in Figure 3.3 (and more examples provided in SI 9).

During the internalisation of lipoplexes, the lipoplexes first accumulated along the plasma membrane where a membrane invagination was located (Column A). At the 5 min time point, the membrane invagination is clearly observed in the intensity image as the flDNA enters the forming pit (Ai). The N map (Aii) shows a small number of particles within the pit (N = 2.9), and both the B map (Aiii) and N&B analysis (Aiv, v) demonstrate average aggregation of B=1.4, within the invagination but along the membrane. After 5 min (Column B), the accumulated flDNA in the pit increased in intensity (Bi), number (Bii) and aggregation (Biii-v). By 20 min (Column C), the invagination of the membrane was very clear (Ci, ii) and the aggregation (B = 1.6) and particle number (N = 5.5) had increased, however the aggregation that appeared along the membrane, adjacent to the invagination dissipated or entered the invagination (Ciii-v). At the 30 min time point (Column D), the internalised flDNA within the pit shows a clear single aggregation (Di), that is both greater in number (Dii) (N = 5.8) and aggregative state (Diii-v) (B = 1.8) compared to previous time points. Finally, after an hour of imaging (Column E), the flDNA appeared to have pulled away from the membrane (Ei) and the N&B analysis had demonstrated the largest amount to aggregation.

Signal for the flDNA was observed throughout the cell cytoplasm 6h after the administration of the flDNA lipoplexes (Figure 3.4A). The N&B analysis, which provides a series of maps enabled an

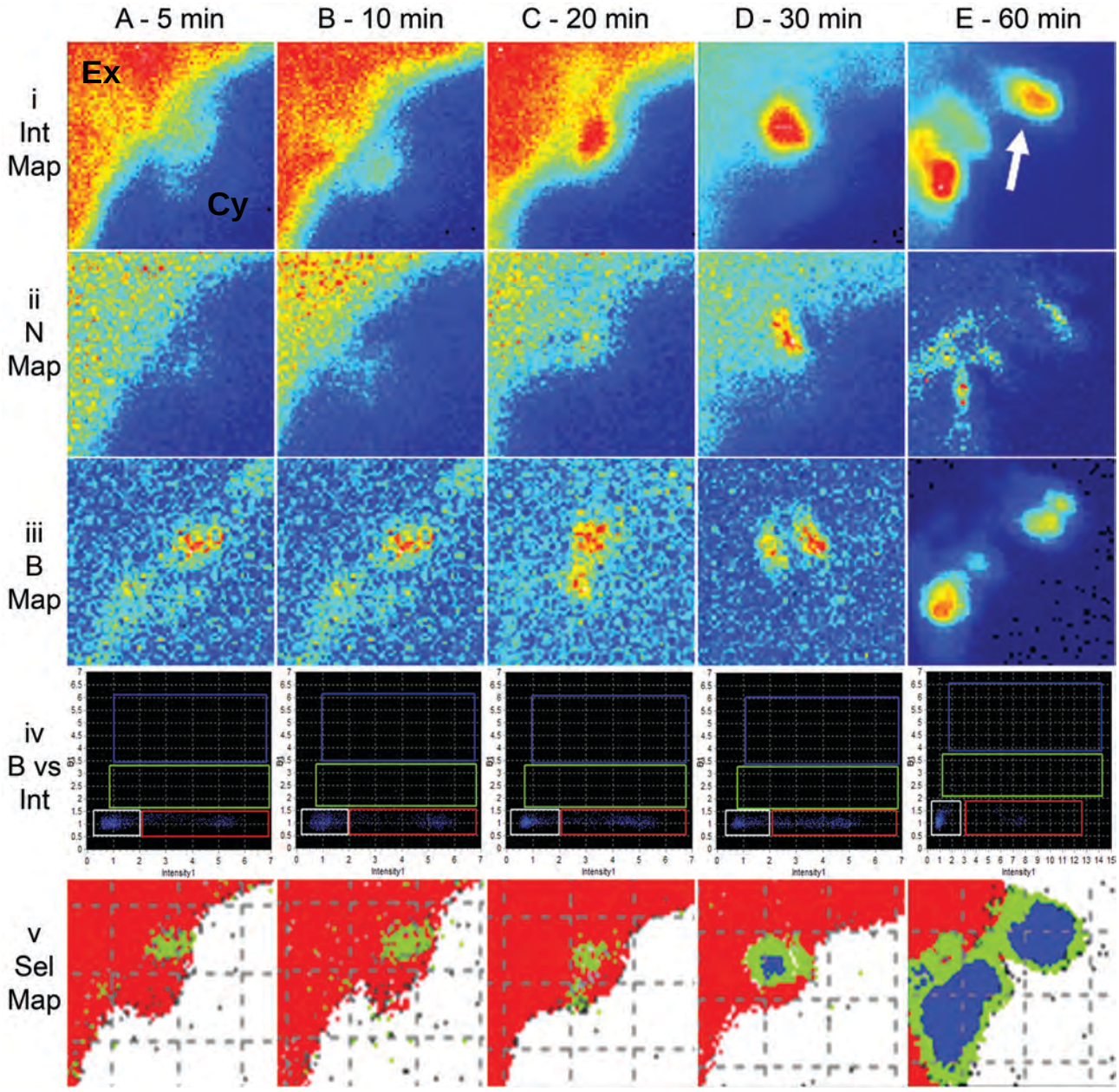

Figure 3.3 – Aggregation of DNA Lipoplexes during Internalisation

The internalisation process was observed over a one hour time period and presented at 5, 10, 20, 30 and 60min time points (Columns A-E). The intensity (Int) maps (Row i) show the fluorescence images (scale: Low  *High). Pictorial representation of the N and B values provides maps for both values (Rows ii and iii) (N scale: 0*  *100) (B scale: 0*  *10). The B vs. Intensity plots (Row iv) and Selection (Sel) maps (Row v) enabled the identification of the aggregative state. Through N&B analysis the pit had firstly contained mostly monomeric DNA particles (red, 330 cpsm) with the lesser aggregative state of 44 DNA particles forming within the pit (green, 14 670 cpsm). As the internalisation process continued, the aggregative amount and state present increased, which included aggregation of 110 DNA particles (blue, 37 670 cpsm). The combination of the B, N and selection maps demonstrate the aggregation of the DNA increasing as the lipoplexes accumulate within the pit during the internalisation process. The data sets were collected on the Olympus FV1000 system. 100 frames were used for these measurements. Ex and Cy represent the extracellular and cytoplasmic locations, respectively. Images are 5.4µm x 5.4µm.*

insight into the particle number within the cell, which appeared as an accumulation of the flDNA along the extremity of the cell, and the presence of flDNA throughout the rest of the cytoplasm (Figure 3.4B). In the cell presented, an extent of aggregation was found throughout the cell wherever the flDNA was present. Aggregate 'hotspots' were found primarily along the extremity of the cell, and in the peri-nuclear area. The highest aggregative state found in the cell was aggregates containing up to 124 flDNA particles (124mer) found in the peri-nuclear area (Figure 3.4 C, D).

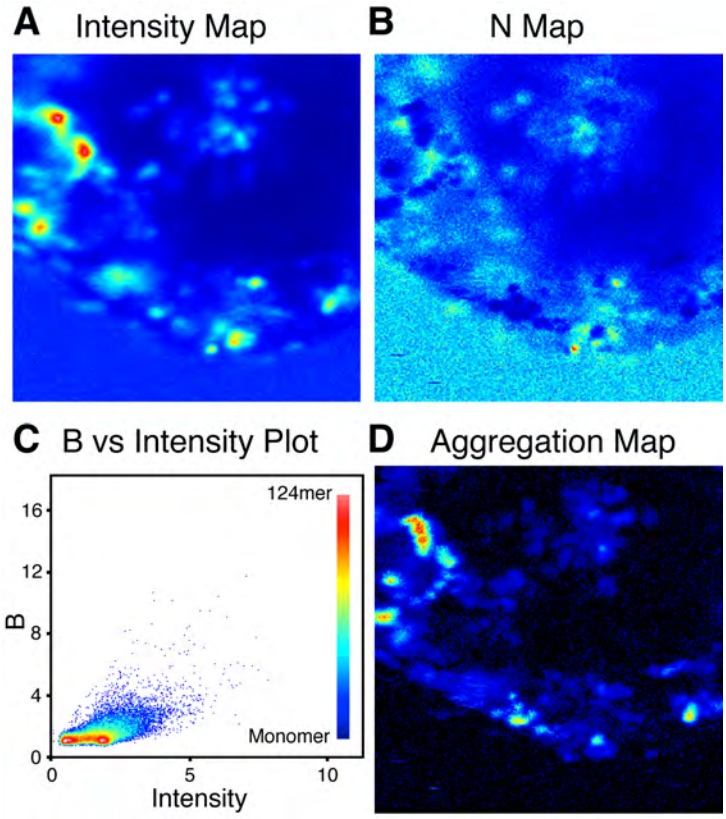

Figure 3.4 – Determining Aggregation in the Live Cell

Myoblast cells were transfected with an Alexa Fluor488 labelled DNA plasmid facilitated by lipofection. After 6h, the N&B analysis had demonstrated DNA distributed through the cell cytoplasm that had demonstrated extensive aggregation through the cell in an intensity map (A) and N map (B). The aggregative analysis demonstrated aggregation through the cytoplasm with a maximum aggregative state of 124 DNA particles, which were located in clusters and hotpots mostly in the peri-nucelar region and extremity of the cell (C, D).

Region-of-Interest (ROI) analysis was performed on the population of cells transfected with the plasmid DNA between 4-8h providing details on small areas within the cell. The N&B analysis had demonstrated a trend in the aggregation and particle number based on the location in the cell (Figure 3.5). The greatest extent of aggregation was generally observed along the cell extremity, followed by the peri-nuclear region and between these locations listed, the least amount of aggregation was identified in the core of the cytoplasm (Figure 3.5B). In addition, the N&B analysis provided details on the particle number of flDNA in these areas, showing that the extremity of the cell also contained the largest amount of flDNA. The particle number had decreased the further the flDNA traversed into the cell, as the peri-nuclear region had exhibited the lowest amount of flDNA (Figure 3.5C).

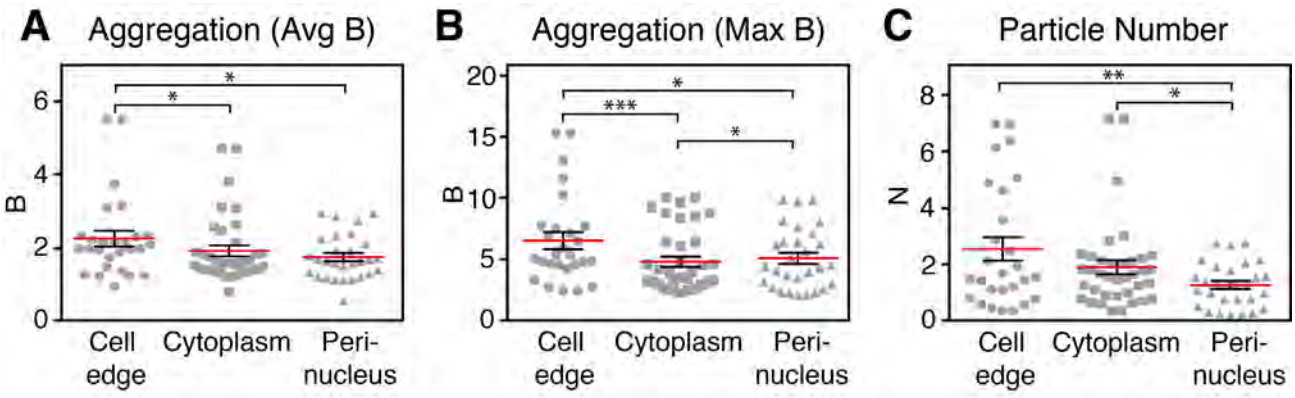

Figure 3.5 – Spatial Aggregation and Particle Number

A ROI analysis was performed highlighting the cell edge (circles), cytoplasm (squares) and peri-nuclear region (triangles) of the average B (A), maximum B (B) and particle number (C). The red line in the box represents the mean. (Data values presented in SI 10) ($p \leq 0.05$, ** $p \leq 0.01$, *** $p \leq 0.001$) (graphs depict mean ± se)*

Once with the cell a range of aggregation was observed resulting in a large variance between cells, and at different locations within a single cell (Figure 3.5). As seen in Figure 3.4, the flDNA within the cytoplasm is maintained in clusters containing different extents or degrees of aggregation. Therefore, the flDNA is not maintained at a single aggregative state, resulting in the wide variance observed.

During the ROI analysis, the Raster Image Correlation Spectroscopy (RICS) approach was also applied, providing a quantitative insight into the mobility of the areas addressed. Through this approach, it was demonstrated that the flDNA aggregation influenced the mobility of the flDNA. As the aggregation increased, the rate of motion had decreased in the three areas of the cell assessed (Figure 3.6). This trend was most apparent in the cytoplasm where all flDNA with a B value greater than 6, an aggregative state of approximately 50 flDNA particles, did not exceed a mobility rate of 0.25 um^2/s. On the contrary, the fastest rate of motion observed was 0.79 um^2/s in the region containing an

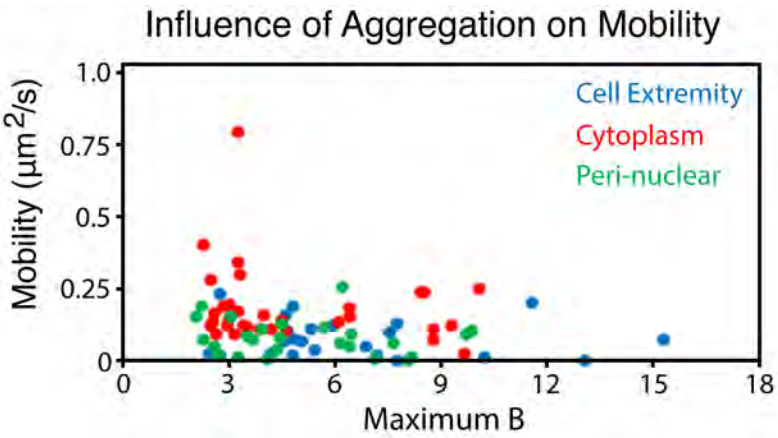

Figure 3.6 – Influence of Aggregative States on DNA Mobility

The addition of the RICS approach demonstrated that the ROIs selected had demonstrated a trend where the smaller aggregative states had a faster mobility rate (n = 12 cells, total of 81 ROIs). (Data values presented in SI 10)

aggregation of 20 flDNA particles (about 60% greater than the lowest aggregative state observed in the ROI analysis of 12 flDNA particles).

Following an incubation of 36h, the aggregation of the flDNA was observed within the nucleus (Figure 3.7). Cells were counterstained with Hoechst 33342 in order to identify the position of the nucleus demonstrating the localisation of flDNA within the nucleus (Figure 3.7A). Within the nucleus, flDNA aggregates up to 58 particles were maintained in small clusters around the periphery of the nucleus, and a larger cluster in the centre (Figure 3.7B, C). In addition to flDNA localised to the nucleus, an extensive extent of aggregation was also observed within the peri-nuclear area along the nuclear envelope. Comparing the aggregation and particle number between the nucleus and cytoplasm (Figure 3.7D), the N&B analysis demonstrated that the aggregative state was 3-fold lower in the nucleus. In addition, the particle number within the nucleus was shown to be 90% less than the cytoplasm.

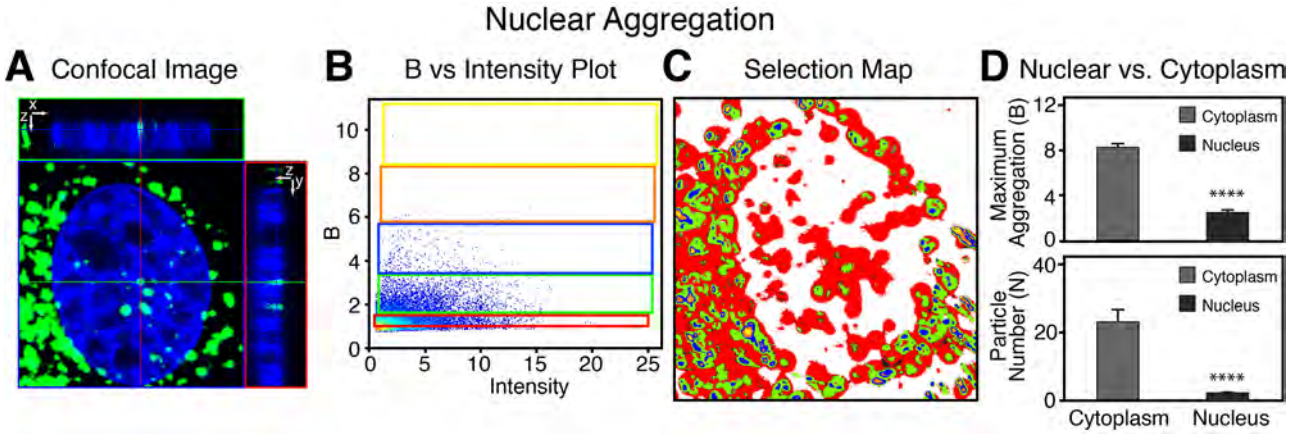

Figure 3.7 – Aggregation of Delivered DNA within the Nucleus

*Cells were incubated in the presence of the lipoplex for 36h to ensure nuclear localisation shown in a 3D image with orthogonal views (A). The N&B analysis had demonstrated aggregation within the nucleus and extensive aggregation in the peri-nuclear region (B, C). The aggregation and particle number were compared between the nucleus and cytoplasm (D). (n = 4 cells, in the graphs 43 ROIs were selected). (*** $p \leq 0.001$) (graphs depict mean ± se)*

3.3.3 Effects of Serum Concentration on DNA Lipoplex Aggregation

The effect of serum concentrations (2.5, 10 and 20%) on the intracellular aggregation of DNA and lipoplexes was also explored. A Region-of-Interest (ROI) analysis demonstrates a similar trend in the control cell population as before (Figure 3.5). The delivered DNA was distributed throughout the cell (Figure 3.8D), with the greatest extent of aggregation observed along the cell cytoplasmic edge and the lowest amount of aggregation in the cytoplasm (Figure 3.8B, circles). The DNA particle number

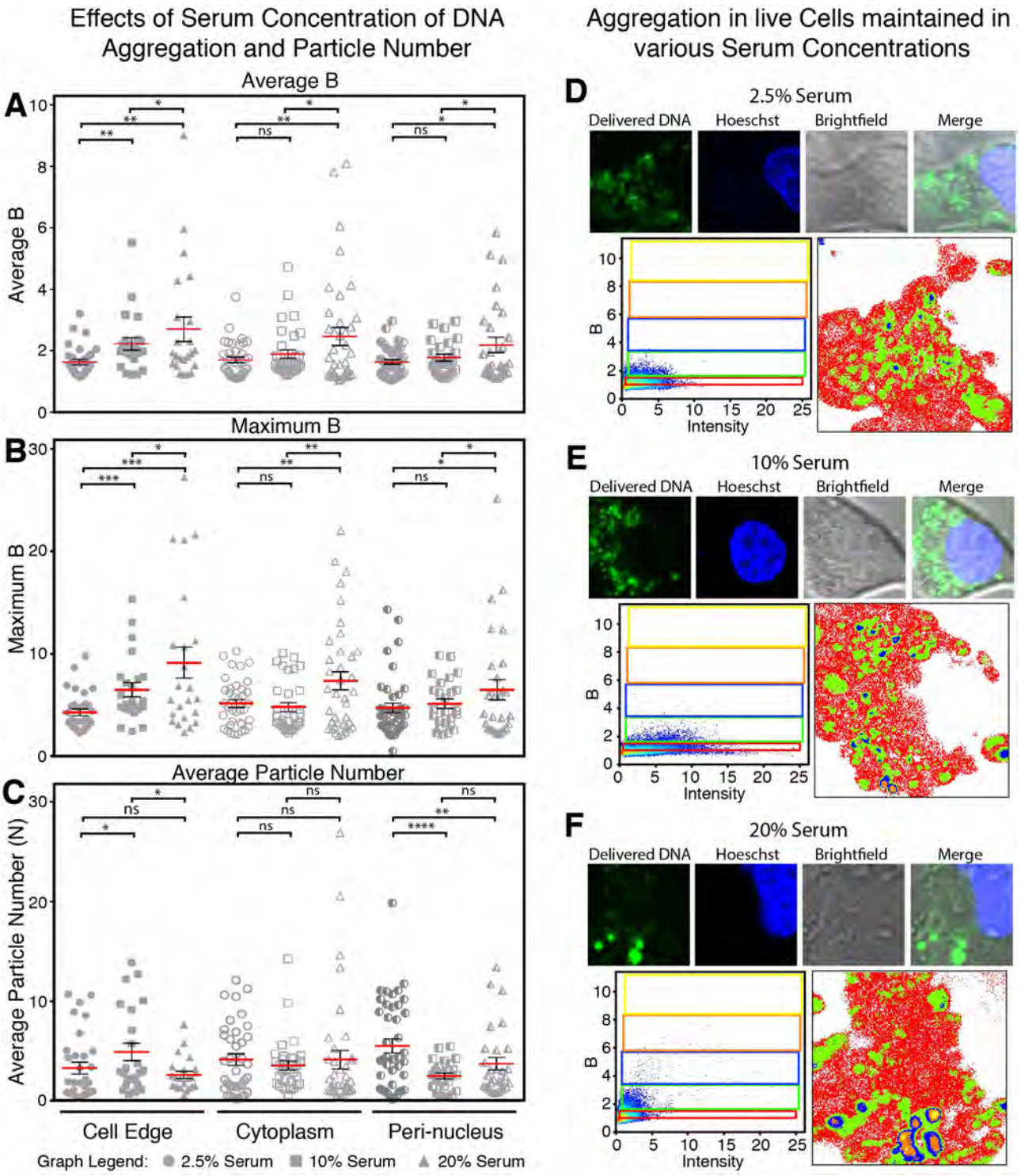

Figure 3.8 – Effects of Serum Concentration on DNA Lipoplex Aggregation

*The L6 myoblasts were maintained and transfected in different serum (FBS) (2.5, 10 or 20% v/v) concentrations to explore to effects on cytoplasmic aggregation. ROI analysis was performed highlighting the cell edge (circles), cytoplasm (squares) and peri-nuclear region (triangles) of the average B (A), maximum B (D) and particle number (C) (n = 22 cells, each condition). (C) Cells transfected and maintained in 2.5% (C), 10% (D) and 20% (F) serum showing DNA localization and aggregation. Aggregation is presented at 5 extents: monomers, 2- 12mers, 12-25mers, 25-40mers and 40-58mers (red, green, blue, orange and yellow, respectively). Each cell has been presented with a confocal image and associated N&B analysis. Each example has been presented with a confocal image and associated N&B analysis. (image size 12.8x12.8 μm) (ns = no significantly difference, * $p \leq 0.05$, ** $p \leq 0.01$, *** $p \leq 0.001$, **** $p < 0.0001$) (graphs depict mean ± se) (Data values presented in SI 11).*

was also the greatest along the cell extremity (N = 2.5), which had dropped by 28% in the cytoplasm (N = 1.8) and was half within the peri-nuclear area compared to the cell edge (N = 1.3) (Fig 3.8C, circles).

When starved and maintained in 2.5% serum, a decrease in aggregation was observed in all three locations compared to the control (Figure 3.8E). In the average brightness, the most significant change occurred along the edge of the cell with a decrease of 28% (Figure 3.8A, B, squares). Within the peri-nuclear region however, the highest extent of aggregation observed was 50% higher than the control (B = 14.3 compared to 9.8) (Figure 3.8B, squares). When starved, the DNA particle number demonstrated the least amount of DNA along the cell edge, and the greatest particle number in the peri-nuclear region. Within the cytoplasm a similar amount was observed compared to the control (Figure 3.8C, squares). The distribution of DNA particle number in the starved condition was opposite to the control.

The cells maintained in 20% serum demonstrated fewer but larger clusters within the cell (Figure 3.8F). Through N&B analysis, the cell edge showed a significant increase (80%) in the highest state of aggregation observed and a 63% increase in the average B compared to the control (Figure 3.8A, B, triangles). Significant increases in aggregation were also determined in the cytoplasm and peri-nuclear areas, which demonstrated 70% and 97% increases in the average aggregation, respectively (Figure 3.8B, triangles). Compared to the controls, these cells exhibited a decrease of about 50 % in the particle number along the cell edge. The cytoplasm and peri-nuclear region however, showed increased averages of 16% and 49% compared to the controls, respectively (Fig 3.8C, triangles).

3.3.4 Size-Dependent Aggregation

The effects of DNA size on aggregation was investigated through the use of flDNA fragments ranging from 120bp to 2kbp, as well as the PCI-Neo plasmid in a linear and circular conformation. The aggregation of the lipoplexes was first characterised in solution (Figure 3.9).

The flDNA sizes assessed ranged from 120-5485bp (120-1985bp displayed in Figure 3.9) demonstrated a size dependent aggregation. However, the size or length of the flDNA did not only

influence the extent of aggregation amongst these lipoplexes, it was also observed that the physical size of the lipoplex aggregates influences the number of lipoplexes that formed. For example, the 500 bp lipoplex had a relatively low extent of aggregation (20% lower than 1985 bp lipoplex) but with the highest B average (60% higher than 1985 bp lipoplex). The aggregation was not greater than the larger fragments, but due to the number of lipoplexes present in each frame, the B average was higher than the larger fragments (Figure 3.9B-E). Additionally, the linear plasmid appeared to aggregate slightly less (by 10%) than the circular plasmid. However, the results are not presented in Figure 3.9 since the labelling techniques applied differed (see data presented in SI 12).

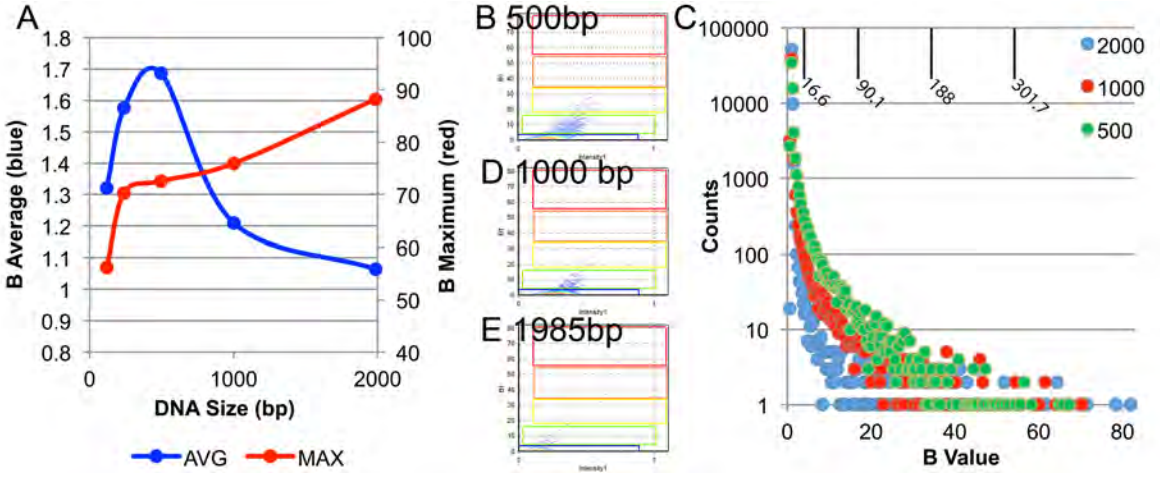

Figure 3.9 – Size Dependent Aggregation of DNA Lipoplexes

Aggregation of DNA was determined to be size dependent within solution. Through the application of N&B analysis, the average and highest extent of aggregation was extracted from 8 samples of each (A). As the DNA size increased so did the maximum extent of aggregation, the average B value however was found to decrease. Examples of the B vs Intensity histograms have been presented for DNA samples of 500, 1000 and 1985 bp (B-E). The B histograms obtained during the analysis were collated for these DNA sizes (C), demonstrating that although the maximum extent of aggregation increased as the DNA size did, the average B value decreased. In the collated B histogram, the orders of aggregation selected in the B vs Intensity histograms (B-E) have been identified along the top of the graph. (Data values presented in SI 12)

Once transfected into live cells, the lipoplexes formed from varying lengths of flDNA, and all exhibited cytoplasmic aggregation to some extent. Through the application of the N&B approach, the extent of aggregation and particle number were quantified within the cytoplasm of at least 8 cells transfected with the varying lengths of flDNA and imaged at 8h and 24h time points following the addition of the lipoplex (Figure 3.10).

The N&B results indicate that the aggregation of the flDNA occurred in a size dependent manner, where the cells transfected with the smaller DNA constructs exhibited a higher extent of

aggregation (Figure 3.10A-C). However through the Number component of the N&B analysis, the particle number was lower within the cytoplasm of those cells compared to the larger flDNA constructs (Figure 3.10D).

In addition, it was also found that the conformation of the flDNA influenced the aggregative state of the flDNA. Populations of cells were transfected with the PCI-Neo plasmid (the same plasmid used previously), but was either kept circular or linearised through a restriction enzyme digest. Through this approach, the N&B analysis demonstrated that the circular form of the flDNA aggregated significantly more (on average 4-fold more) than it's linear counterpart (Figure 3.10A-C). This analysis also demonstrates that over the first 8 hours, the particle number and therefore, gene delivery efficiency was lower for the circular form of the plasmid. By 24h, the linear and circular plasmid had demonstrated a similar particle number of the plasmid within the cytoplasm (Figure 3.10D).

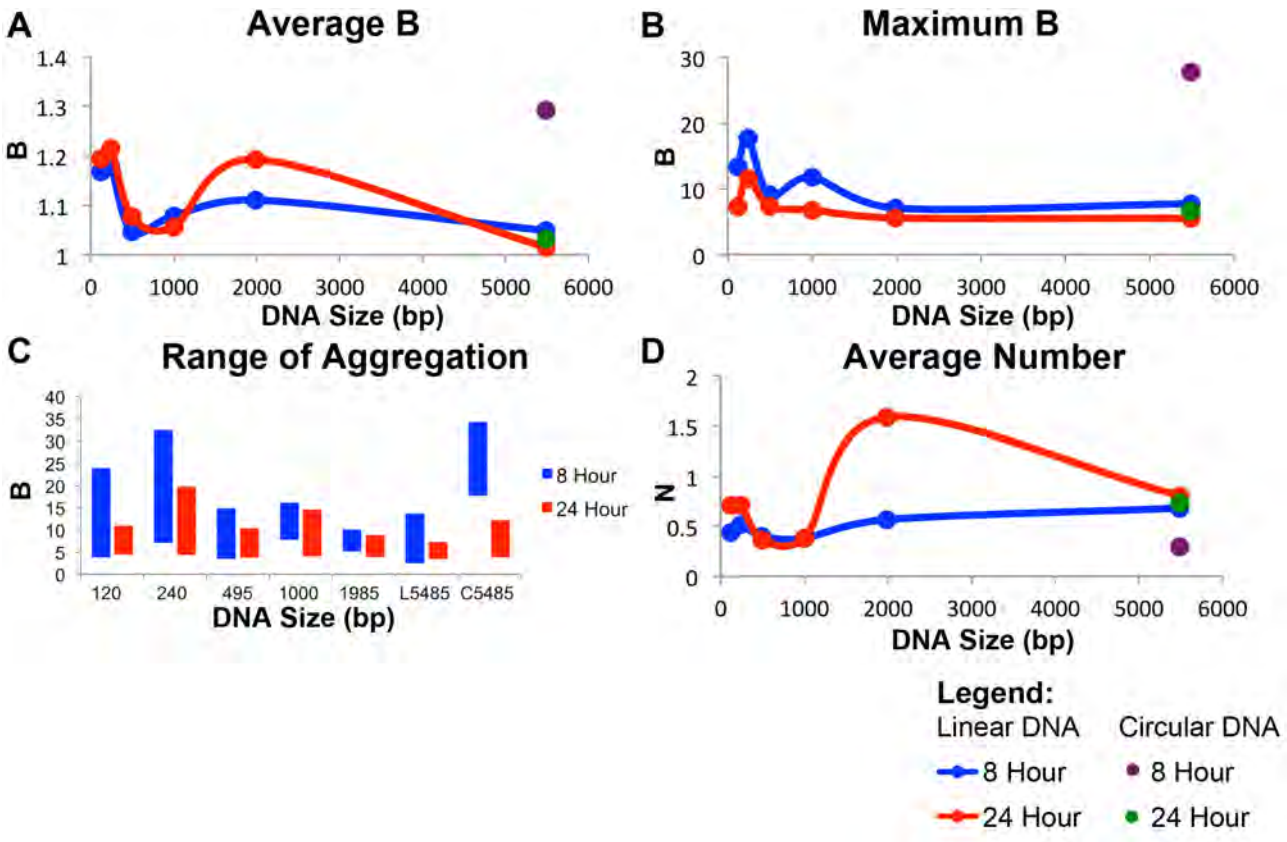

Figure 3.10 – Size Dependent Aggregation within the Cytoplasm

Myoblast cells were transfected with DNA of varying sizes (120bp to 5.5kbp), and plasmid DNA that was either circular or linear, and imaged at 8h and 24h time points. The application of N&B analysis provided an average B value (A), maximum extent of aggregation (B), range of the highest extent of aggregation (C), and the average particle number, N (D) for these samples. The values obtained for between 8-12 cells were averaged and graphed, refer to SI-15 for values. (Data values presented in SI 13)

Finally, this experiment demonstrates that the aggregation of flDNA was time dependent. Across the DNA sizes assessed, the flDNA had demonstrated a reduced extent of aggregation but increased particle number over time (Figure 3.10D). For example, Figure 3.11 presented two cells transfected with the 1985bp flDNA fragment that were imaged after 8h (Figure 3.11A-D), and 24h (Figure 3.11E-H). At the first time point, aggregation was observed and calculated throughout the cytoplasm ranging from a monomeric state (coloured blue) up to aggregates containing 246 flDNA particles (coloured in orange) (Figure 3.11A-C). However 16h later, the highest order to aggregation observed were 5 fold lower containing aggregates of up to 52 flDNA particles (coloured in green) (Figure 3.11E-G). As previously noted, the flDNA particle number within the cytoplasm increased over time (Figure 3.11D, H).

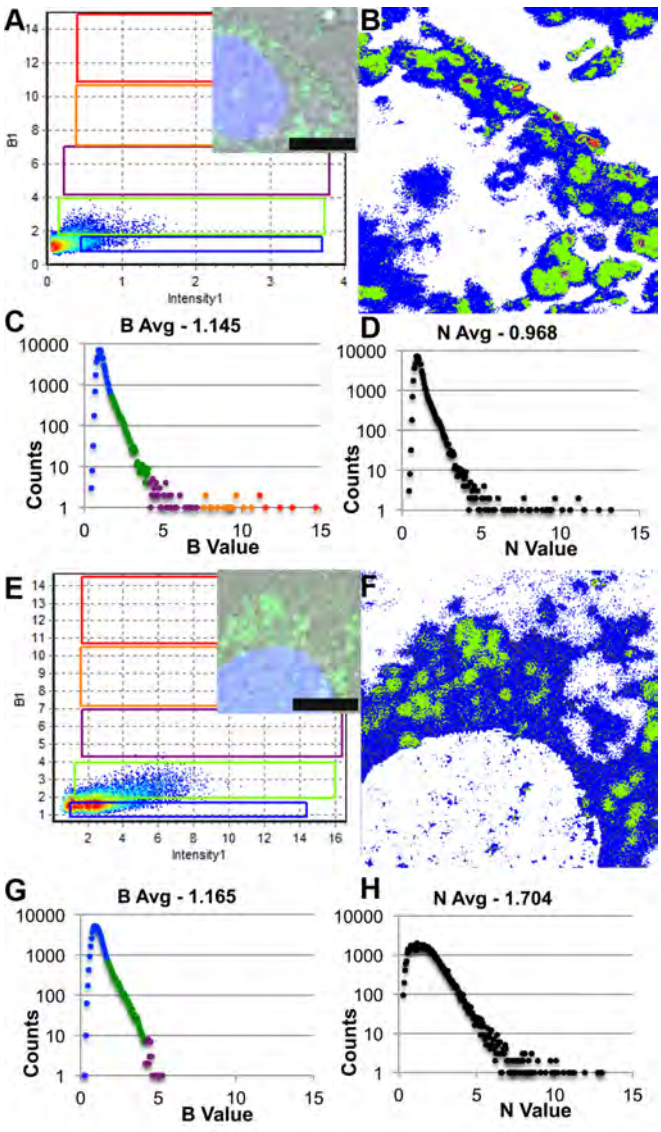

Figure 3.11 – Size Dependent Cytoplasmic Aggregation

Two cells transfected with the 1985bp DNA have been presented as examples for time related changes in DNA aggregation and particle number. The cells presented were imaged 8h (top A-D) and 24h (bottom E-H) after the addition of lipoplexes. In the B vs Intensity plots (A, E) pixels representing monomeric DNA (blue), 52mers (green), 141mer (purple), 246mer (orange) and 382mer (red) were selected. The fluorescence images provide orientation of the cell to be identified and the selection map is colored based on the pixels selected in the B vs Intensity plots (B, F). B histograms have been colored based on the B vs Intensity plots (C, G) and N histograms enable the delivered DNA particle number to be determined (D H). Scale bar equals 7.5µm.

3.4 Discussions and Conclusion

This study appears to be the first to address and quantify the extent of aggregation that occurs during the processing of lipoplexes in live cells. In this study, the N&B approach was applied to determine aggregation in real time at key points during the lipoplex gene delivery, including the internalisation along the cell plasma membrane, within the cytoplasm and nucleus. Additionally, a number of other factors were addressed including the influence of DNA size, conformation, and time has on the DNA aggregation.

The observed internalisation event appeared to be endocytosis (supported by several studies [64,65,68,83,261]), leading to the conclusion that the internalisation of lipoplexes is predominately through endocytosis and most likely clathrin-mediated [162,262]. Regardless, the aggregation of lipoplexes was observed numerous times (n = 10), at different time points over the first 4 hours of introducing the DNA. As a consequence, it would appear that the aggregation of lipoplexes along the plasma membrane is a phenomena involved in lipoplex uptake. The aggregation could be due to a number of possibilities. It may be possible the aggregation of lipoplexes along the plasma membrane induces endocytic processes [263]. Alternatively, the aggregation may be due to the accumulation onto membrane receptors, bringing them into closer proximity causing aggregation via hydrophobic interactions [56].

Interestingly, during a study using atomic force microscopy, Marty et al. (2009) noted that lipoplexes in solution aggregate in the presence of high lipid content. It could therefore, also be possible that the aggregation of lipoplexes during this event could be due to the interactions of the lipoplexes and plasma membrane. Thereby, causing the lipoplexes to aggregate [259].

Additionally, Fumoto *et al.* (2004) studied the aggregation of lipoplexes in different ionic conditions. Their findings show that lipoplexes going from non-ionic to high salt conditions result in aggregate formations [264]. Hence, the ionic change from the extracellular space to the cell is a probable cause to the aggregation of lipoplexes during internalisation observed in the work presented here.

Regardless of the mechanism involved, whether the aggregation is caused by one of the possibilities presented or a combination, the observed event is not a random event. Given that there is

a 30 min delay between the initiation of the event and the final internalisation of the DNA material the event is most likely dependent on cellular machinery.

Once within the cytoplasm of the cell, extensive aggregation of flDNA was observed. Through the combination of the N&B and RICS, it was found that as the aggregative state increased, while the rate of motion had decreased. This observation is also supported in the work presented in Chapter 2, where larger clusters of flDNA had a reduced mobility across varying sizes of DNA. Therefore, the aggregation of lipoplexes and delivered DNA presents a physical barrier to successful gene delivery.

At present, several publications have addressed the aggregation of the cationic polymer polyethylenimine (PEI) polyplexes in solution [257,258]. Although these two delivery vectors cannot be directly compared as the mechanisms of aggregation may be different, it was worth noting that research presented here of lipoplex aggregation within the cell, contradict those obtained of PEI complexes in solution. Sharma *et al.* (2005) identified that the aggregation of PEI complexes reduces in decreased pH and higher viscosity (amongst other factors) [257]. However, in this study, given that the lipoplexes were internalized through endocytic processes, it is expected that the lipoplexes would be enclosed within endosomes and possibly lysosomes, which may eventually acidify [56]. As a consequence, the pH would decrease, however an increase in aggregation when the lipoplexes/DNA were contained within distinct bodies within the cytoplasm was observed.

Currently, no other study has documented the aggregation of delivered DNA within the nucleus. In this study, the flDNA was distributed throughout the nucleus but does appear to be in distinct regions within the organelle, which has been recorded in viral transfections [210]. Given the lack of work published on this aspect, the aggregation of DNA within the nucleus cannot be attributed to any known process or characteristic. It is interesting, that an extensive amount of aggregation occurs within the peri-nuclear region, however flDNA still enters the nucleus. Therefore, further work must be undertaken to determine whether the aggregation of delivered DNA is detrimental to the gene delivery process, or if it facilitates certain events.

The size dependent aggregation has been attributed to the charge of the DNA, given that shorter DNA fragments has a lower net charge compared to their larger counterparts. The formation of lipoplexes is a random event, which relies on the electrostatic interactions between the negatively charge DNA backbone and positively charged (cationic) lipids. Therefore, it would appear that larger DNA fragments with a greater charge form larger lipoplexes.

The aggregation of delivered DNA and lipoplexes within the cytoplasm has been previously noted to occur and present as a barrier to non-viral gene delivery, however very little work has addressed these events within the cell. At present, most studies addressing lipoplex aggregation have focused on aggregation *in vitro* prior to delivery into cells. For example, Ross and Hui (1999) found a correlation between lipoplex size and transfection efficiency, larger lipoplexes result in greater efficiency [265]. A similar pattern was observed in our study in which the larger fragments resulted in greater aggregation *in vitro* and a larger particle number, following entry into live cells.

Recently, we had demonstrated that the N&B approach has the potential to quantify lipoplex aggregation in live cells and real time. In this study a circular form of DNA demonstrated to aggregation immediately upon cellular entry, which appeared to have occurred through endocytosis. After a period of time (>4h), extensive aggregation of the plasmid-lipoplex was observed throughout the cytoplasm of the cell.

The aggregation of lipoplexes may be a necessary phenomenon to an extent, in order to achieve successful gene delivery. Additional to noting that aggregation of lipoplexes leads to greater gene delivery efficiency, Ross and Hui (1999) found that serum has varying effects on lipoplex formation, including the reduction of lipoplex size resulting in reduced delivery efficiency. This suggests that aggregation to an extent facilitates lipoplex processing. It would be expected at a certain point, lipoplex aggregation would be unfavourable, and through the approach presented in this thesis such an understanding could be resolved.

This study demonstrates that the N&B approach is a valuable tool in the study of lipoplex delivery and is capable of quantifying the aggregation of delivered DNA. It appears that lipoplexes

aggregate the moment they start to interact with the cell, during internalisation, and from there the aggregative state of the DNA increases. Within the nucleus, the aggregation of the DNA decreases however it is still apparent. This study also demonstrates that larger DNA fragments aggregate less than their smaller counterparts and that DNA conformation and time play a role in the cytoplasmic aggregation. The aggregation of DNA and lipoplexes within cells may possibly be cell, lipid and DNA sequence dependent, however this study provides a powerful model that could be applied to further elucidate the mechanisms or factors causing aggregation.

CHAPTER 4

Quantifying the Real-time Degradation of intracellular DNA Lipoplexes

4.1 Introduction

4.1.1 DNA Degradation

Efficient delivery in gene therapy still remains a challenge. During the delivery process, the DNA and vector complex face a number of obstacles. One such barrier that has not been extensively studied is the stability of delivered DNA or vector complexes within the cytoplasm. It has been suggested that enzymatic activity and breakdown of delivered DNA in lysosomes within the cytoplasm, poses as a significant hurdle to successful nuclear translocation and nuclear uptake of therapeutic nucleic acids [131,137]. A key limitation in current literature is the lack of studies addressing the real time degradation of DNA delivered through viral or synthetic vector approaches, such as lipofection. It would appear that the focus has been on the microinjection of DNA [130,131]. Such an approach of DNA delivery results in many of the processes of delivery being by-passed, including cellular uptake and endosomal release that many other non-viral or viral vectors will be exposed to. Additionally, through the by-pass of such key steps of gene delivery, the injection into the cytoplasm could possibly result in the direct exposure of the DNA to cytoplasmic nucleases, which may have contributed to the short-half life of 50-90min for the DNA [131].

To date the studies that have investigated DNA degradation have had limited tools to do so. For example, Lechardeur *et al.* (1999) and Pollard *et al.* (2001) applied a combination of studying nuclease activity on DNA (from cell extracts using gel electrophoresis); observing the disappearance of

delivered DNA through Fluorescence in situ Hybridisation (FISH); visualisation of DNA fragmentation using Terminal Deoxynucleotidyl Transferase-mediated dUTP Nick End Labelling (TUNEL) assays; and radiolabeled ^{32}P-release from end-labelled fragmented DNA [130,131]. These approaches require cell fractions or fixed cells, which may not properly represent the events that occur in the live environment.

Pampinella *et al.* (2002) and Srinivasan *et al.* (2009) applied real time and live cell observations of DNA degradation through the application of confocal microscopy [132,266]. However, confocal microscopy lacks the sensitivity required to observe the degradation of single particles of DNA. For example in the study undertaken by Srinivasan *et al.* (2009), the authors developed a novel approach of dual labelling DNA plasmids with two different fluorophores. During degradation the DNA cleavage results in the separation of the two colours. In the case where both fluorophores were in close proximity the authors claimed that the DNA is still intact. However the DNA could have been degraded but remained within in the same area and confocal microscopy is not sensitive to detect this situation.

Sasaki and Kinjo (2010) presented a study, which applied the use of dual labelled DNA and two colour FCS. In the study the focus was to gain an insight into the type of nucleases that are likely the cause of cytoplasmic degradation [137]. This type of FCS analysis is limited to small volume of the cell at any one time.

Clearly, a complete understanding of the degradative behaviour of delivered DNA is paramount to achieve efficient gene delivery. Therefore, this study presents a model to quantify the degradation of DNA delivered through lipofection, both spatially and temporally in live cells through the application of two-colour RICS (also known as cross correlated RICS or ccRICS).

4.1.2 Cross Correlated RICS

The Raster Image Correlation Spectroscopy (RICS) approach applied in previous sections can be extended to study two different fluorophores [3]. Through the application of two-colour cross correlation the temporal and spatial distribution of focal adhesion kinase (FAK), paxillin and vinculin,

along adhesion complexes, has been reported [3,267]. Since positive cross correlation will only occur in the case that the two particles' fluctuations align [3], the ccRICS approach offers a non-invasive and highly sensitive approach to determine the molecular interactions of particles of a sample.

4.2 Materials and Methods

4.2.1 Production of Dual Labelled DNA

Fluorescent-labelled primers were bought from Integrated DNA Technologies (Coralville, IA):

Forward: 5'-AF488-TCAATATTGGCCATTAGCCAT-3'

Reverse: 5'-AF594-ACGTAGATGTACTGCCAAGTAGGA-3'

Two-coloured DNA fragments were generated by PCR. The PCR producing a fragment size of 495bp was performed using PCI-Neo (10ng) (Promega) was used as a template through the use of a Platinum Taq PCR kit (Invitrogen, Carlsbad USA).

For the study of degradation through the RICS G0 ratios, the 5485bp fragment was prepared by labelling PCI-Neo mammalian vectors with Alexa Fluor 488 through a UYLSIS nucleic acid labelling kit as detailed in previous sections.

4.2.2 Ase-I Degradation

The dual labelled DNA was digested using Ase-I (New England Biolabs) (cutting at base 160). The Ase I digestion was performed using a 1:1 ratio of DNA (ug) to Ase-I (U) and incubated at 37°C for 1h then heat inactivated at 65°C for 20min.

The samples were run on 1.5% w/v agarose gels with a 1kbp ladder and undigested DNA fragments were run. Two wells of the digested DNA product were run, one containing SYBR Green I (SG1) and one without.

4.2.3 Cell Culture and DNA Transfection

Rat L6 myoblast cells were cultured and maintained in DMEM supplemented with FBS (10% v/v), Penicillin/Streptomycin, Amphostat-B and β-Mercaptoethanol at 37°C in a humidified

atmosphere of 5% CO_2. Trypsinized cells ($1x10^4$) were seeded onto glass chamber slides (Thermo Fisher Scientific, Australia) in antibiotic- and phenol red-free DMEM (10% v/v FBS) 24h prior to transfections.

The cells were transfected by the DNA fragments using X-Treme Gene 9 (Roche, Germany), according to the manufactures' guidelines. A 1:3 ratio (dual labelled DNA:transfection lipid) was used.. The lipoplex solution was added directly to the cell cultures within chamber slides. Cells were imaged either immediately or incubated until required in the previously described conditions. To study the degradation of DNA in real time, and the mechanical and spatial influence on the degradation, a 150ng of DNA amount was introduced to each well of cells. In these studies, the cells were imaged immediately once the lipoplexes were introduced up until an 8 h time point, than at 24 and 48hr after the introduction of DNA. In the study of the effects of DNA dose, varying amounts of DNA were introduced into the cell cultures, including 50, 100, 200 and 400ng of DNA per well. Once transfected, these cells were imaged at both 8 and 24h after the introduction of the lipoplexes. In order to determine the DNA half life, cells were incubated in the presence of lipoplexes (150ng DNA per well) for 5h, then were washed three times in PBS and maintained in DMEM (FBS 10%). Cell nucleic were counterstained with Hoechst 33342 (1µg/mL) as required in all experiments. In order to determine the half-life of DNA plasmids through the application of RICS G0 ratios, the DNA plasmid was transfected into the cells with a 100ng DNA load, and then imaged immediately for 8h.

4.2.4 Data Acquisition and Analysis

Confocal series were obtained using a Leica TCS-SP5. The fluorescently labelled DNA was excited using an Argon Ion laser with the 488nm pathway activated to excite the Alexa Fluor488 and a Helium-Neon 594 nm laser to excite the Alexa Fluor594. Hoechst 33342 was excited by a 405nm Diode laser and transmission images were obtained using a Helium-Neon 633nm. ccRICS, and iMSD data was acquired using APDs through an ISS Vista Becker and Hickl FCS card and software. 256x256 format and pixel dwell speed of 32 µs were used. Emission bandwidths were detected between 500-

550nm (channel 1) and 603-687nm (channel 2). The microscope was fitted with a 63X (1.4 NA) water immersion objective. All samples were maintained on a stage heated at 37°C.

The ratio between the G0 of the cross channel and the two individual channels was performed to determine the rate of degradation over time:

$$\frac{G0\ of\ Cross-correlation}{Average\ (G0\ of\ channel\ 1\ and\ channel\ 2)}$$

Equation 20 - Degradation of dual labelled DNA

For half-life study utilising DNA plasmids, a RICS G0 ratio data was acquired with a Zeiss LSM710 META laser scanning microscope (Zeiss, Jena, Germany). The Alexa Fluor488 excited using an Argon Ion laser with the 488nm pathway activated and Hoechst 33342 was excited by a 405nm Diode laser. Signal for the DNA was collected with a 500-550nm bandwidth. Data was collected in a 256x256 format and pixel dwell speed of 25.61 µs were used. The microscope was fitted with a 63X (1.4 NA) water immersion objective. All samples were maintained on a stage heated at 37°C with 5% CO_2.

The RICS simulations and RICS, N&B and iMSD data were analysed using the Globals software package, SimFCS 2.0, developed at the Laboratory for Fluorescence Dynamics at the University of California, Irvine (www.lfd.uci.edu/globals). The waist of the PSF was determined with eGFP as previously described [227] (refer to SI-4 for further details).

4.2.5 Nuclear Extraction and PCR Detection

Cells were cultured within T75 culture flasks and transfected with unlabelled 495bp DNA fragment using X-treme Gene 9 transfection reagents. Following either an 8 or 24h incubation the cytoplasmic or nuclear factions of the cells were isolated through the use of a nuclear extraction kit (Millipore Merck, Sydney, Australia). The isolation was performed based on the manufacturers guidelines as detailed below.

Cells were first washed with warm 1X PBS, and then 0.5% Trypsin-EDTA was added to dislodge cells from the culture flasks. They were then transfers to a sterile centrifuge tube and

centrifuged at 250g for 5 min at 4°C. The cells were resuspended and washed in fresh 1X ice-cold PBS and centrifuged again as before. The supernatant was removed and the cells were suspended in 5 times the volume of the cell pellet with ice-cold cytoplasmic lysis buffer containing 0.5mM DTT and 1/1000 inhibitor Cocktail. Once incubated for 15 min, cell were centrifuged at 250g for 5 min at 4°C. The supernatant was discarded and the cells resuspended in two volumes of ice-cold Cytoplasmic Lysis Buffer. Cell clumped with broken up via pipetting at this point.

Cell were then centrifuged again at 8,000g for 20 min at 4°C. The supernatant obtained at this step was the cytoplasmic fraction, and the remaining pellet was the nuclear fraction, which was resuspended in 1X PBS. Samples were stored immediately at -80°C. This experiment was performed three times.

PCR was performed using a purified 495bp sample as a standard and using the KAPA SYBR PCR Master Mix (KAPA Biosciences, Sydney, Australia). The primers presented in section 6.2.1 were used to detect the presence of the plasmid in samples and standards but were not labelled. Each PCR reaction contained 15 µL 2X PCR master mix, a final concentration of 0.5µM of each primer, 5 µL of the cell fraction or the diluted plasmid for standards, and totalled to a volume of 30 µL with nuclease-free water. PCR reactions were performed on the Rotor Gene-Q real-time PCR machine (Qiagen, Sydney, Australia). Reactions were incubated at 95°C for 2 min, followed by 40 cycles of 95°C for 30s, 50°C for 45s and 72°C for 60s at which point green channel fluorescence was detected, followed by 72°C for 10 min. High resolution melt analysis was performed in order to check for sample purity and product amplification specificity (entire PCR experiment is available in SI-16 including the melt analysis)

4.3 Results

4.3.1 PCR Detection of DNA degradation

In order to determine DNA degradation the expected time period that intact DNA could be detected in live cells, a PCR detection method was applied. Since PCR can be highly sensitive, it was

expected that the DNA will only be detected and PCR amplification occur when the DNA is full intact with the cell. Through the application of real-time PCR, this approach was able to both qualitatively indicate with the DNA was intake or not, which has been presented in Figure 4.1, or quantify the amount of DNA present within the cell fractions at the two specified time points by comparing the cell fractions to standards.

The results of this experiment were consistent with those obtained through the microscopy-based approaches previously presented. At the 8 and 24h time points all cytoplasmic samples had demonstrated the presence of intact DNA. In all cases, the 24h samples had exhibited more DNA present as the real-time PCR curve starts to increase before the 8h sample (Figure 4.1, Table 5). The nuclear fractions demonstrated the presence of the intact DNA in some of the samples (1 or 3) in both the 8 and 24h time points. Consistent to the cytoplasmic samples, the 24h time point had more DNA than the 8h, but both had less compared to the cytoplasmic fractions. The PCR specificity was confirmed through high-resolution melt analysis by comparing the standards to the samples (these results can be found in SI 15).

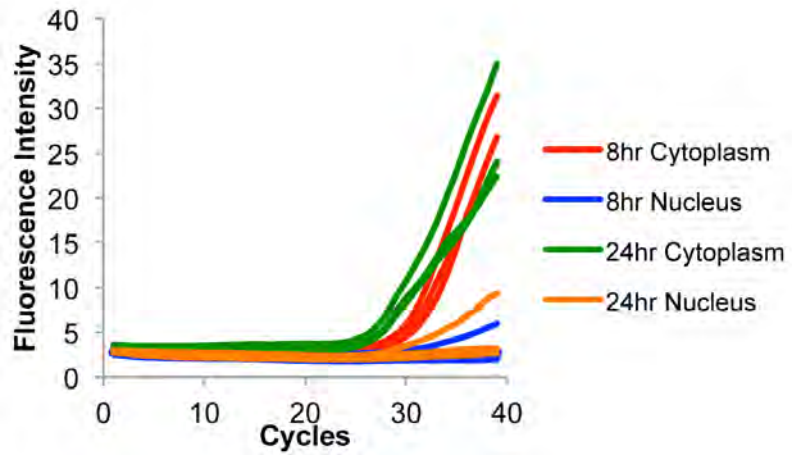

Figure 4.1 – PCR Detection of DNA in Cell Fractions
Cytoplasmic and nuclear cell fractions were obtained at 8h and 24h from cells transfected with a 495bp DNA fragment. Real-time PCR demonstrated the presence of intact DNA within the cytoplasm at both time points and in a single sample within the nuclear at both time points. Positive PCR amplification was identified with the PCR curve increases from the base line. Additional data including all of the samples and standards are available in SI-16.

Table 5 – Summary of PCR Results

Time Point	Location	Number of Samples	Positive Amplification	% Positive
8 Hour	Cytoplasm	3	3	100
	Nucleus	3	1	33
24 Hour	Cytoplasm	3	3	100
	Nucleus	0.3	1	33

4.3.2 In Vitro Degradation

In the design and application of the DNA constructs of this section, the concept is that the DNA was dual labelled by two different fluorophores. Through the application of ccRICS, the DNA will only be determined as being intact when the fluctuations of both fluorophores match perfectly. Initially, the dual labelled DNA was first exposed to DNA nucleases and analysed *in vitro* (Figure 4.2).

Dual labelled DNA was digested by the Ase-I nuclease, which resulted in the 495bp product being cleaved into two differently sized DNA fragments of 160 and 335bp (refer to supplementary material SI3 for cleave site). The digested DNA was run through an agarose gel to identify the resulting bands (Figure 4.2). In the agarose gel, the intact DNA displayed a clear band at the 500bp marker. In the gel, two digested samples were run, one containing SG1 and the other none. The sample containing SG1 (lane 3) enabled the observation of both bands (160 and 335bp), whereas the lane without SG1 (lane 4) only the 160bp fragment was only visible since it was labelled by Alexa Fluor 488.

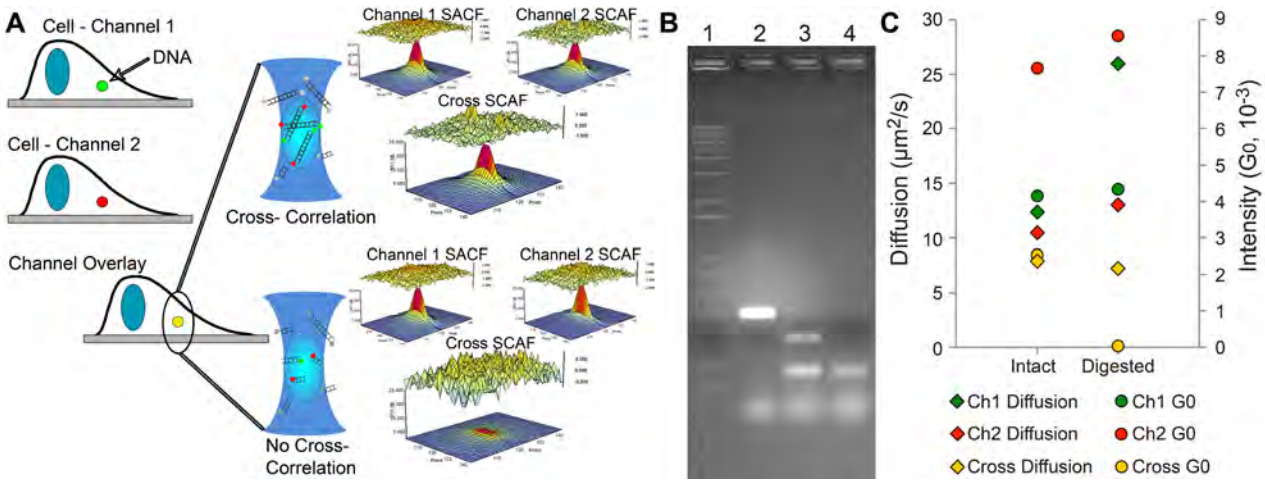

Figure 4.2 – Ase-I degradation of dual labelled DNA

(A) Within a single cell it is expected that introduced DNA will be degradation. In this study, the end of the DNA was labelled with different coloured probes. Once within the cell regions where DNA is presented are expected to be a combination of intact and degraded DNA, which could be present in the same pixel or area. The application of RICS will enable to differentiation between intact and degraded DNA as the probes will be required to have correlated fluctuations in order to be determined as intact. (B) The dual labelled DNA was digested by the Ase-I nuclease. DNA was run on an agarose gel with a 1kbp ladder (lane 1), intact DNA (lane 2), and the digested DNA, with SG1 (lane 3) and without SG1 (lane 4). (C) The DNA was than analysed using ccRICS where the intact DNA had demonstrated a large amount of cross-correlation. But once digested, the cross signal was 100-fold less than the intact, and the green and red channels had demonstrated an increase in mobility, consistent with the DNA fragment sizes.

Once it was established that the Ase-I nucleases cleaves the dual labelled DNA into two differently sized fragments, ccRICS was applied to confirm the imaging approach is capable of characterising DNA degradation in real time. Controls for the bleed through of Alexa Fluor488 into the red channel were performed (refer to supplementary material SI 14). When the green primer was imaged alone the bleed through into the red channel was 5% of the green signal. However, when the two (green and red) primers were imaged together, no cross correlation was detected.

Through ccRICS, the intact DNA demonstrated a mobility of 8.45 µm2/s (cross) and the two green and red channels had similar mobility rates (consistent to section 2 of this thesis). Once digested, the cross-correlation had identified a similar mobility rate, however the G0 (intensity) had dropped 100-fold, demonstrating a significant loss in the cross-correlation of the DNA. The green and red channels in the digested DNA however, had demonstrated an increase in the mobility rate consistent with the values obtained from section 2, but little change in the G0 (Figure 4.2C).

4.3.3 Real-Time Degradation

The dual labelled DNA was then transfected into the myoblast cell model and immediately imaged following the addition of the lipoplexes for the first 8h, than at 24 and 48h time points, totalling to 98 cells analysed. Through the application of ccRICS, it was determined that two species were present within the cells, a slow species ranging from 0 – 0.5 $\mu m^2/s$ and a fast species ranging from 0.68-5.75 $\mu m^2/s$. Across this population of cells a global analysis was preformed, typically including parts of the cytoplasm and nucleus (Figure 4.3), the analysis demonstrated a cross correlation in every cell. In Figure 4.3, three cells have been presented at 3.5, 8 and 24h time points. In these cells, the two mobility species have been identified and a positive cross for both species can be identified in all three cells.

Across the cells observed, the cross-G0 was always lower than the G0 of the green or red channels. Since a 100% cross correlation was never observed it is apparent that degradation has always occurred within the cells sampled. However, as presented in Figure 4.3, the rate of degradation appeared to be a lot slower compared to previously published work (as discussed in section 4.1.1). It is apparent in Figure 4.3, as cells even at 8h and 24h demonstrate positive cross correlation in both the

slow and fast species isolated, which do not have a significantly lower amplitude than the earlier time point.

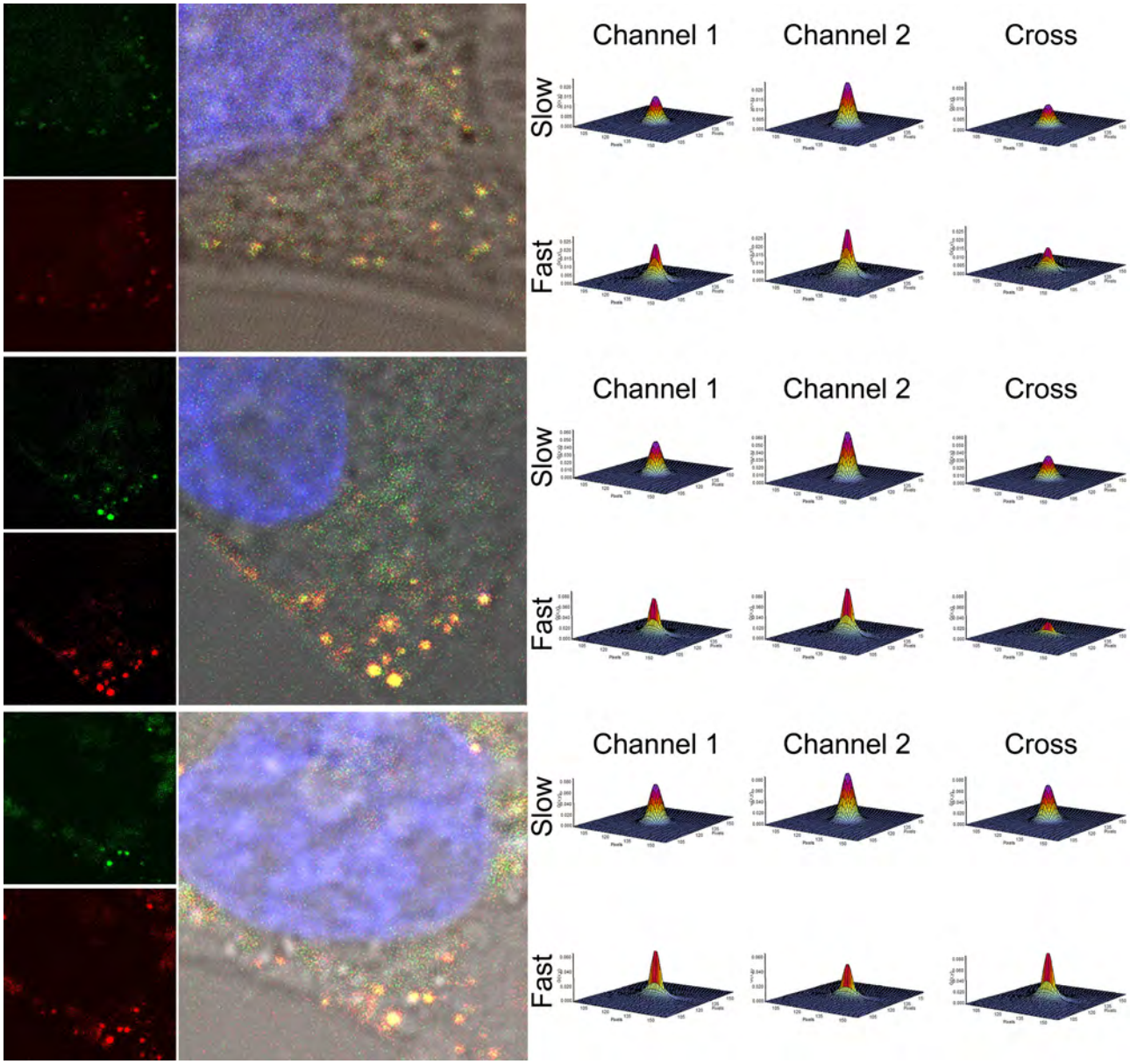

Figure 4.3 – Intracellular Real-Time Degradation

The dual labelled DNA was transfected into the myoblast cell model to imaged from the immediate addition of the lipoplexes up to 8h, then at 24 and 48h time points. Through the application of ccRICS the extent of degradation could be determined for the slow and fast species present within the cell in real time. Examples presented in this figure represent time points at 3.5, 8 and 24h (A, B and C, respectively). For each cell, channel 1 (i), channel 2 (ii) and the overlap of these channels (iii) with the transmission image and Hoechst (blue) enabling the nucleus to be identified; have been shown demonstrating that the two probes bound to the DNA are distributed throughout the cell. The ccRICS approach enables the study of DNA degradation by correlating the fluctuations of both channels. When the DNA is intact, it is expected to be cross-correlated, which adds to the G0 value (peak) of the SCAFs (iv). If the SCAF decreases in the cross-correlation it is indicative of degradation. Image sizes are 16.5 x 16.5 µm.

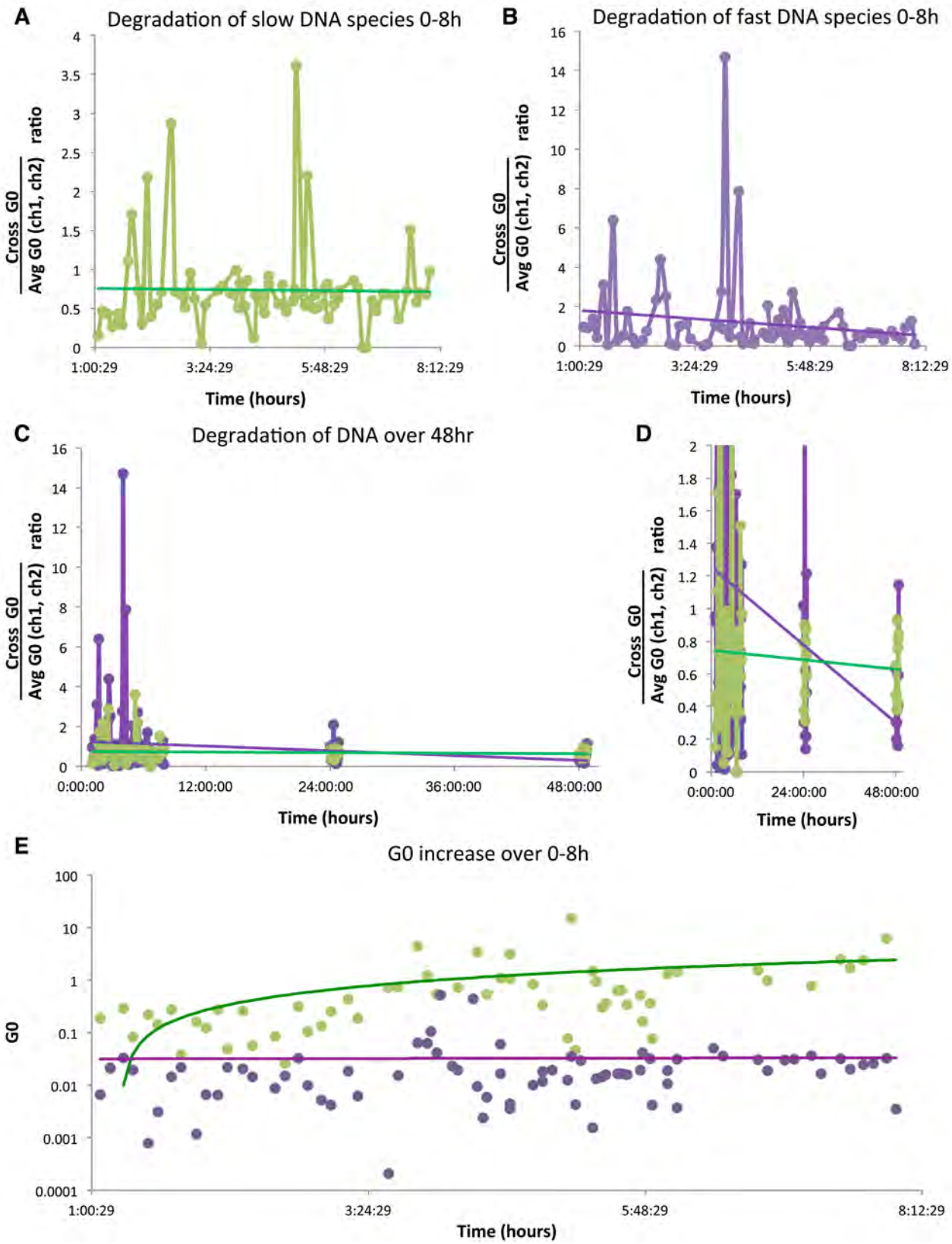

Figure 4.4 – Summary of Intracellular Degradation

In order to study the extent of DNA degradation occurring within the cell population the G0 value of the cross correlation was divided by the average of the two channels., thereby providing a ratio of the cross-correlated or intact DNA and the overall signal in the two channels. The ccRICS approach enables the differentiation between the two species present, either a slow species ranging from 0 – 0.5 μm2/s and a fast species ranging from 0.68-5.75 μm2/s. Over the first 8h of the transfection process, the trend of the slow species (green) demonstrated a minor decrease in the cross G0 ratio (A), compared to the faster species (purple), which had shown a steeper decrease in the trend line (B). Across the entire 48h analysed, the two species had demonstrated a similar trend (C, D), where the cross Go ratio declined more in the fast

species than the slow species. Chart D shown a zoomed in view of Chart C, enabling the difference in the slow and fast species to be seen more clearly. Over the first 8h of the transfection, the fast species appeared to have the same G0 value, whereas the slow species demonstrated a lag of about 4h before the G0 value started to increase (D). Number of cells analysed were 98, between 0-8h n = 78, at 24h and 48h n = 10 each.

The cell pollution transfected by the dual labelled DNA between 0-8h (Figure 4.4A, B) discriminates both the slow and fast species in order to identify the extent of degradation that occurred over the 8h time course. The ratio applied across the cross-correlation resulted in values independent of DNA concentration. In these calculations, since the cross channel value is the numerator degradation will be observed when the calculated integer decreases over time (i.e as the G0 value of the cross-correlation decreases, the denominator (green and red channel) is expected to remain the same, therefore the resulting value from these calculations will decrease as degradation occurs).

In the two mobility species across the 0-8h time course an overall trend indicated that DNA degradation occurred indicated by the downward slop of the trend line (Figure 4.4). However, the rate of degradation in the slow and fast species was different. In the slower species, a slow rate of degradation appeared to occur, whereas the faster species exhibited a steeper decrease in the cross-G0 ratio over time. When the later time points, 24 and 48h, were included in the calculations the trend in degradation demonstrated a similar occurrence to the earlier time points where the faster species demonstrated a more rapid degradation or reduced rate of cross correlation than the slower species (Figure 4.4B, C). The ratio of the cross-correlation and two individual channels had demonstrated a reduction in the 24 and 48h time points for both the slow and fast species compared to the earlier time points (0-8h). In all cells analysed (n = 98 cells), every cell demonstrated a positive cross-correlation for both the slow and fast species.

4.3.4 DNA Dose Dependency on Degradation

The effect of DNA dose on degradation was explored through the administration of different amounts of DNA (50, 100, 200 and 400ng; in the previous time series, section 4.3.2, 150ng of DNA was delivered). The rate of degradation was observed at 8 and 24h; and the same G0 ratio was calculated as previously. It was found that the higher amounts of DNA had resulted in a less amount of

degradation compared to the lower DNA doses. Additionally, the slow species (0-0.8$\mu m^2/s$) demonstrated a lesser extent of degradation compared to the fast species (0.9-5.5$\mu m^2/s$) (Figure 4.5A).

When comparing the 24h time point to the earlier one, the same trend had occurred; the slower species demonstrated a higher G0 ratio compared to the faster, and the larger DNA dose exhibited a lower rate of degradation. However, the G0 ratios were lower in the 24h measurements compared to the 8h indicating that degradation has occurred over time, which is consistent to the previous study of this project.

In order to provide an explanation into the effect of DNA dose, the N&B approach was applied to determine and quantify the extent of aggregation that had occurred in the ranging DNA doses and two time points (Figure 4.5B). The application of N&B had demonstrated that the larger DNA dose had resulted in a greater extent of aggregation; for example, the extent of aggregation was just over 3-fold higher in the 400ng dose compared to the 50ng dose at 8h.

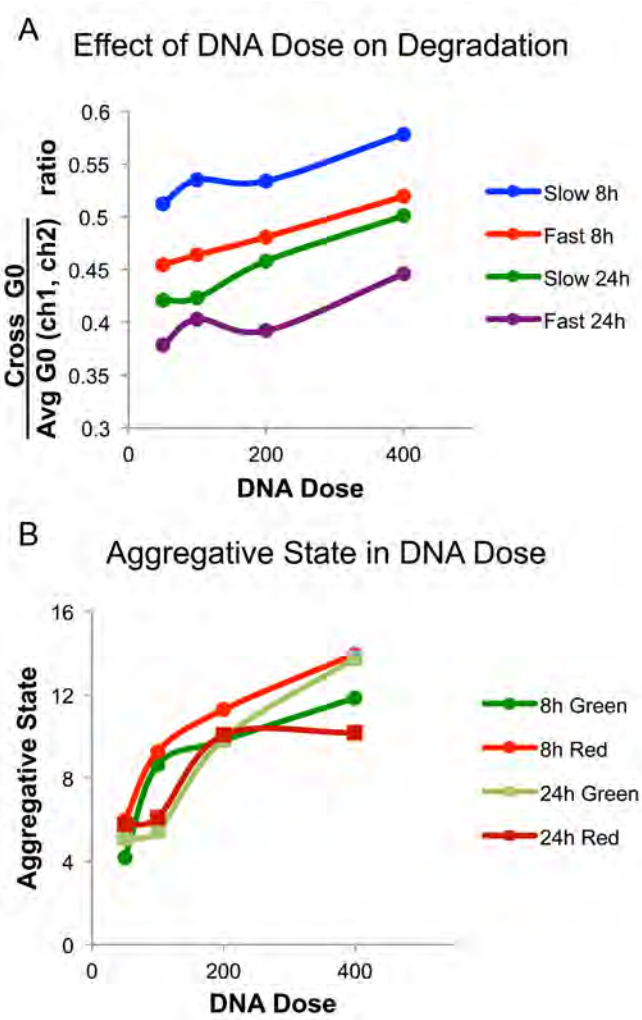

Figure 4.5 – Effects of DNA dose on intracellular degradation

The dual labelled DNA was transfected into cells at varying amounts: 50, 100, 200 and 400ng per well of cells, and imaged at 8 and 24h after the addition of the lipoplexes. The G0 ratio of cross-correlated over the average of channels 1 and 2 was performed for the slow and fast species (A). This approach demonstrated that the higher DNA doses resulted in less DNA degradation over all. Therefore, the N&B approach was applied to each channel (1 and 2) for the four DNA doses and two time points (B). Channel 1 is listed as Green and channel 2 as Red. The N&B approach demonstrated that the higher doses of DNA resulted in a larger extent of aggregation compared to the lower doses. 10 cells for each DNA dose and time point were used in these calculations.

4.3.5 Determining DNA Half Life

The application of ccRICS and dual labelled DNA demonstrated that degradation occurred across the cell population analysed here. However degradation had not occurred at the rapid rate previously reported in other studies, for example Lechardeur *et al.* (1999) reported a cytoplasmic half-life of 50-90min for microinjected DNA. When dual labelled DNA was delivered into the cells; following a 5h incubation in the presence of the lipoplexes (the optimal time indicated previously in Figure 4.4E) the cells were washed thoroughly to remove any superfluous lipoplexes. Given that no additional DNA or lipoplexes should be entering the cells the cellular lifetime of the DNA can be able to be determined.

Following the washing of extraneous lipoplexes, the cells were imaged immediately up to 4h (Figure 4.6A). Over the 4h time period, the fast and slow species were separated as before and the cross ratio calculation performed. The trend of both species, whether a linear average or moving average trend line was applied, a drop in the G0 ratio was minor, the slow species had demonstrated a 13% and fast species a 10% decrease in the G0 ratio.

The cells were then incubated overnight after the wash enabling measurements to be obtained 18h after washing the cells (Figure 4.6B). By including the earlier time points, it was found that the faster species resulted in a faster decay in the G0 cross ratio compared to the slower species. However, positive cross-correlation was still observed in the dual labelled DNA even after 18h. It is worth noting however that of the 33 cells measured between 0-4h following the removal of extracellular lipoplexes, one single cell did demonstrate a complete lack of cross-correlation between the two channels, and of the 5 cells measured at the 18h time point 2 cells presented with a lack of positive cross-correlation.

By following the tread lines of this study it would be expected that no correlation would occur in the slow species by 38h 20min and the fast species by 26h 30min, therefore, the calculated cytoplasmic half-life is in the order of 19h and 13h for the slow and fast species, respectively.

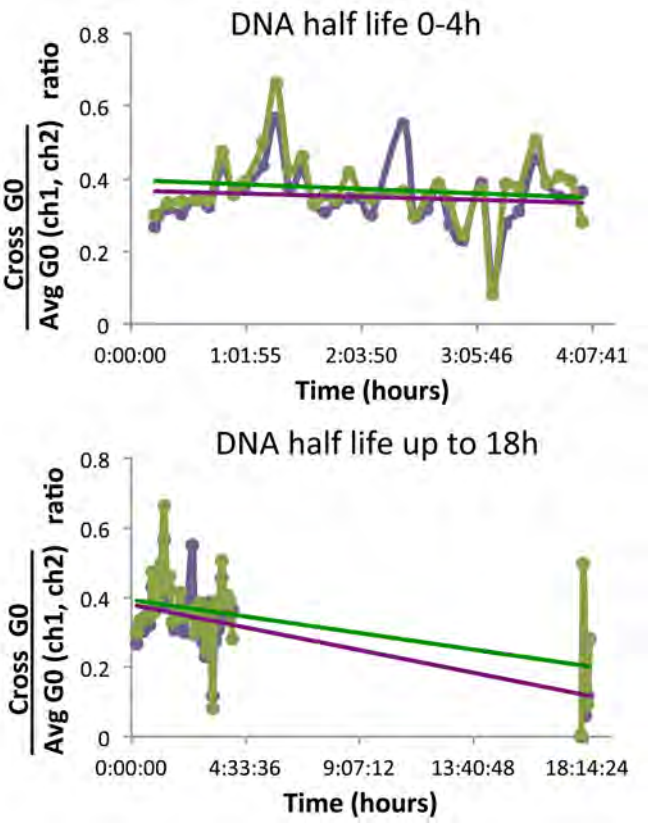

Figure 4.6 – Determining the DNA half-life through dual labelled DNA approach

The dual labelled DNA and ccRICS was applied to determine the DNA half-life for this model. The DNA was first delivered to the cells, incubated and then washed to remove excess lipoplex. Cells were then imaged immediately for 4h, which demonstrated very little degradation in both the slow (green) and fast (purple) species (A). Following a further incubation, cell were than imaged 18h after being washed showing that degradation had started to occur over this time period (B). Using the equation of the trend lines obtained in these charts it was calculated that the half-life of the slow species was 19h and 13h for the fast. In this study, 33 cells were imaged over the first 4h, and than 5 cells at 18h.

A second approach to determine the DNA half-life was applied through the application of a DNA plasmid. Through the application of a single channel RICS; the ratio between the slow and fast species was applied. This approach is based on the concept that as the DNA plasmid is degraded the mobility will increase as the plasmid is fragmented in the cell.

Across the time 6h series measured the calculated ratio decreased demonstrating an increase in the prominence of the faster species. In the earlier time points the slower species was more prominent over the faster as displayed in Figure 4.7A, B and E in cells, cells A and B represent time points 2hr and 3hr 15min respectively. The cells presented in Figure 45, have a G0 value (indicated by a height of peak in the SACF) of the slower species was 3-fold and 1.65-fold higher than that of the fast species. On the other hand, by 4.5h and 5h 10min (Figure 4.7C, D respectively) the prominent mobility species had shifted. In both cells C and D, the fast species had a G0 value 4-fold greater than the slower.

Additional to the shift in the mobility species distribution, this approach has also found changes in the mobility rate over time (Figure 4.7F). Over the time course the slow species had shown little

change in the rate of motion, whereas the faster species had demonstrated a consistently increasing rate of motion over time, from 4h onwards.

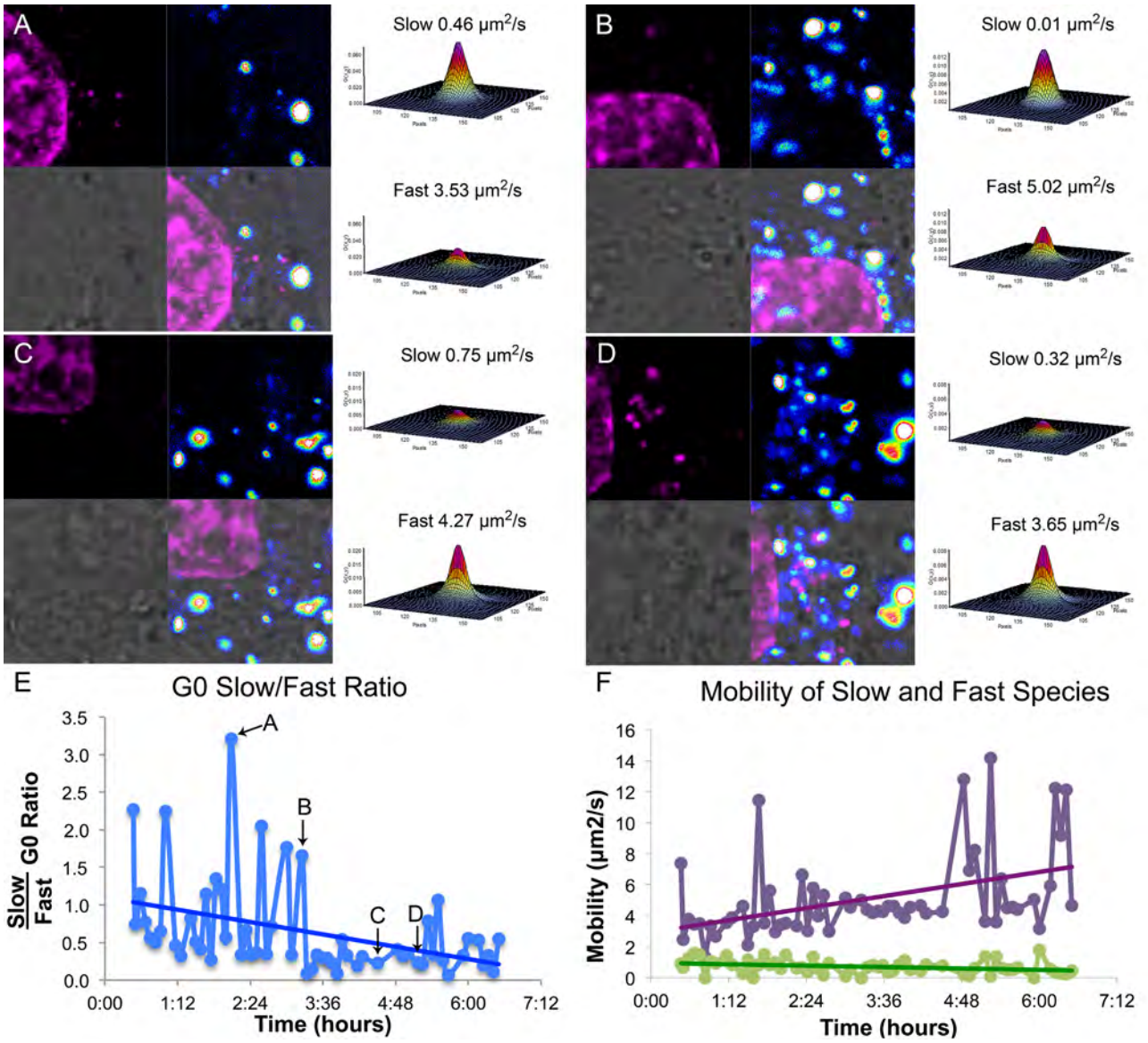

Figure 4.7 – Determining DNA half-life through G0 approach

The half-life of delivery cytoplasmic DNA was determined through a second approach, the used of a randomly labelled DNA plasmid and calculation of the ratio difference between the fast and slow species over time. Across all 4 cells present, there is a clear trend that the slow species started with a high G0 that steadily declined, whereas, the faster species had a G0 that increased. Cells A and B represent early time points at 2h 15min and 3h 15min, respectively. Both cells demonstrate a greater dominance of the slow species indicated by the height of the SACF, and the graph over time (E). Cells C and D show later time points at 4h 30min and 5h 10min, respectively. On the contrary to cells A and B, the fast species is more dominant than the slow in the later time points. In order to determine the DNA half-life, the G0 value of the slow species was divided by the fast. This ratio of the cell population of 68 cells has been plotted in a graph (E) with the positions of cells A-D indicated. Based on the average trend line applied it has been calculated that the approximate half-life of the DNA is 4h. The mobility rates of both species, slow green and fast purple; has also been plotted over time, demonstrating that the rate of motion in the slow species remained relatively the same whereas the fast species had demonstrated an increase in mobility over the 6.5h time course measured. Image sizes are 16.5 x 16.5 µm.

Finally, through the application of the slow and fast G0 ratio on a randomly labelled DNA plasmid, the DNA half-life could be determined. Although a complete absence of the slow species did not occur and is unlikely, following the trend presented in Figure 4.7E, the G0 ratio would meet zero at around 8h 10min. Therefore, the approximate half-life of the DNA plasmid in this myoblast cell model is approximately 4h.

4.3.6 Spatial and Mechanical Influence on Degradation

In Chapter 2 it was demonstrated that events are spatially oriented, therefore through the application of cursor analysis in ccRICS and iMSD approaches the impact of the location and mechanism of motion was explored. Through cursor analysis data files were analysed as 4 sections (100 frames were collected over 4 min, therefore, each quarter is equivalent to a minute), the iMSD analysis enabled the mechanism of motion to be determined and ccRICS allowed the rate of degradation to be determined over the 4 min time frame. In this analysis the cursor was moved as required between quadrants to ensure that the DNA/lipoplex of interest remained within the centre of the cursor. Through the application of the dual labelled cross over channels G0 ratio; three scenarios appeared during the time frame analysed; either the ratio decreased indicating degradation, the ratio remained the same suggesting that degradation did not occur or the ratio increased, which could be attributed to an event such as the accumulation of the DNA or rapid mobility.

Along the cellular extremities a range of mechanisms of motions were identified including confined diffusion (CD), anomalous subdiffusion (AS), transient confinement (TC) and binding-unbinding (B-UB) events (Figure 4.6, Figure 4.12). Within the example cell (Figure 4.8), CD and TC were identified along the extremities of the cell. The CD (ROI 1) in this example follows the pattern identified throughout the entire population analysed, which suggested that degradation does not occur during CD along the cellular extremities. Over the cells observed, CD identified along the cell edge exhibited a lack of degradation in all events isolated, as the cross-G0 ratio either remained unchanged or increased over time (Figure 4.12).

In the example below, the motion of TC displays an increase in the G0 ratio over the time observation (ROI 2). However, TC along the extremities show a variation in degradation across the entire population observed, including a combination of the ratio remaining the same, increasing and decreasing (Figure 4.12). The TC mechanism only specifies that the particles of interest are entrapped for a given period of time during the observation but could involve a variety of different events, as the iMSD approach cannot specify exactly what has occurred.

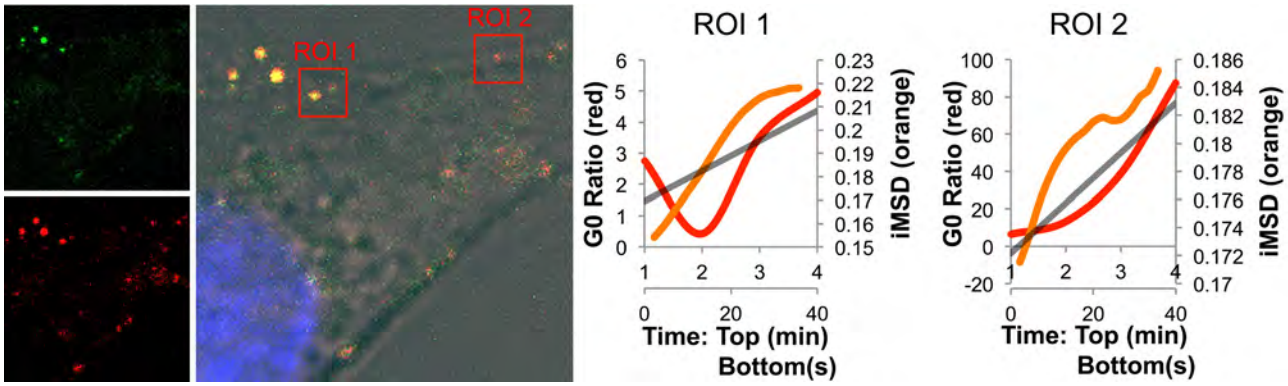

Figure 4.8 – The spatial and mechanical influence on DNA degradation – Cell Extremities
Dual labelled DNA along the cell extremity was selected and both ccRICS and iMSD analysis was applied. In both ROI displayed, the G0 ratio had increased in the presence of CD (ROI 1) and TC (ROI 2). In the graphs displayed the G0 ratio between the individual channels and cross-correlation have been displayed in red and are timed in minutes. When the ratio increases or remains the same the ratio of un-degraded DNA increases or remains the same, respectively, whereas in the occurrence of degradation, this ratio will decrease. In the same graphs, the iMSD has been presented in orange. The expected curves for the different mechanisms of motion have previously been detailed.

AS was identified along the extremities of the cell, which demonstrated a decrease in the G0 ratio and therefore occurrence of degradation in all observation of the event. Binding-unbinding events along the cell extremity appeared as a combination of degradation and no degradation (G0 ratio decreasing and increasing, respectively).

Similar to the study on DNA mobility (Chapter 2), only two forms of motion were prominent within the cytoplasm in the study of DNA degradation, active transport (AT), and binding-unbinding (Figure 4.9, Figure 4.12). Within the cytoplasm AT did not exhibit any evidence of degradation during these events, both within the example cell below (ROI 1, Figure 4.9) and across the entire population

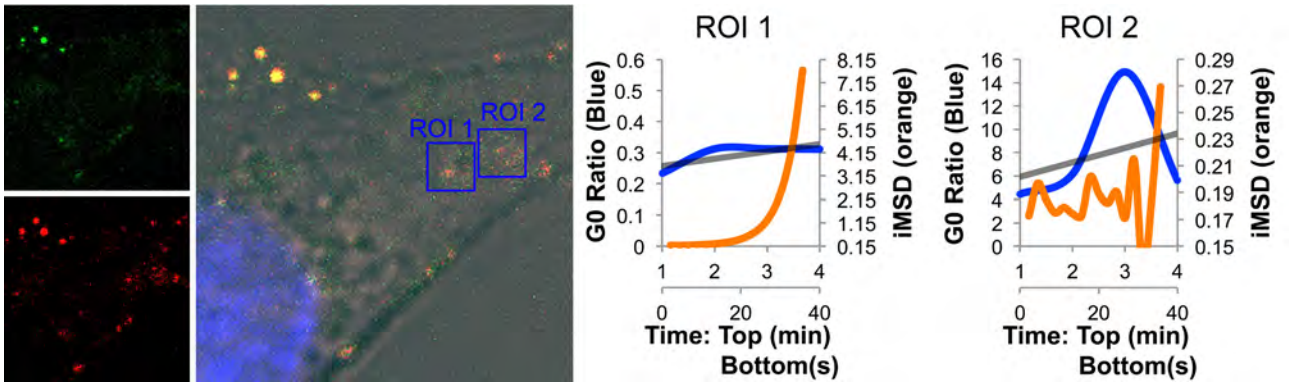

Figure 4.9 – The spatial and mechanical influence on DNA degradation – Cytoplasm
Dual labelled DNA within the cytoplasm of the cell was selected and both ccRICS and iMSD analysis was applied. Within the cytoplasm, the prominent mechanisms of motion were AT and binding-unbinding events so were displayed in this figure. ROI 1 exhibited AT, which had demonstrated very little change in the G0 ratio applied. ROI 2 on the other hand, had an overall G0 ratio that increased, but over time it increased and then decreased during the B-UB event observed. In the graphs displayed the G0 ratio between the individual channels and cross-correlation have been displayed in blue and are timed in minutes. When the ratio increases or remains the same the ratio of un-degraded DNA increases or remains the same, respectively, whereas in the occurrence of degradation, this ratio will decrease. In the same graphs, the iMSD has been presented in orange. The expected curves for the different mechanisms of motion have previously been detailed.

measured (Figure 4.12). The G0 ratio, during AT either remained the same or increased. The binding-unbinding events within the cytoplasm however displayed a similar trend as the same event along the cell extremity; the combination of the G0 ratio increasing and decreasing.

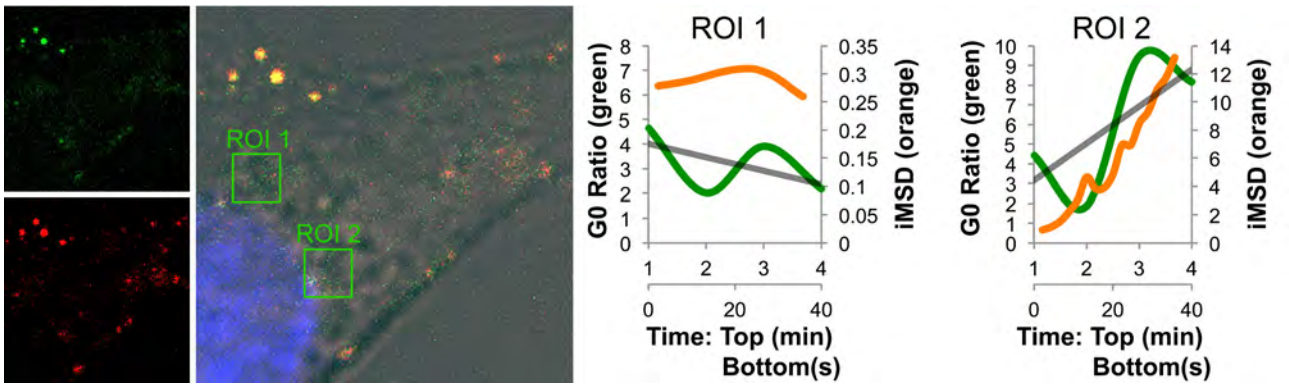

Figure 4.10 – The spatial and mechanical influence on DNA degradation - Peri-nuclear Area
Dual labelled DNA within the peri-nuclear region of the cell was selected and both ccRICS and iMSD analysis was applied. Within this region, two prominent mechanisms of motion were CD and TC events so were displayed in this figure. ROI 1 demonstrated a CD event, which had displayed a decrease in the G0 ratio applied, and therefore, degradation had occurred.. ROI 2 on the other hand, had an overall G0 ratio that increased, but over time it increased and then decreased during the TC event observed. In the graphs displayed the G0 ratio between the individual channels and cross-correlation have been displayed in orange and are timed in minutes. When the ratio increases or remains the same the ratio of un-degraded DNA increases or remains the same, respectively, whereas in the occurrence of degradation, this ratio will decrease. In the same graphs, the iMSD has been presented in orange. The expected curves for the different mechanisms of motion have previously been detailed.

At the nuclear membrane, in the peri-nuclear region, transport mechanisms were consistent as previously described in Chapter 2, including CD, TC and unbinding-unbinding events. Within this area of the cell CD had demonstrated a combination of CD that involved the G0 ratio remaining the same, increasing and decreasing (ROI 1 Figure 4.10, Figure 4.12). TC in the peri-nuclear region had shown a combination of the G0 ratio increasing (ROI 2 Figure 4.10) and decreasing, however, the decreasing ratio was more prominent suggesting degradation (Figure 4.12). The binding-unbinding events however had shown the opposite, containing events that had both increased and decreased G0 ratios, the increasing ratio was more apparent (Figure 4.12).

Events in the nucleus were less frequently observed, with two cells across the population of cells analysed displaying flDNA within the nucleus, once example being the cell presented in Figure 4.11. Events identified within the nucleus both display CD through iMSD analysis. It is worth noting, one of these cells presented a G0 ratio that trended upwards (Figure 4.11) and the other downwards. However, in both cases the average trends over the period observed were nearly horizontal. In Figure 4.11, the G0 increased over the 4 min observation by 20%, whereas the second observation had decreased by 8% over the same period.

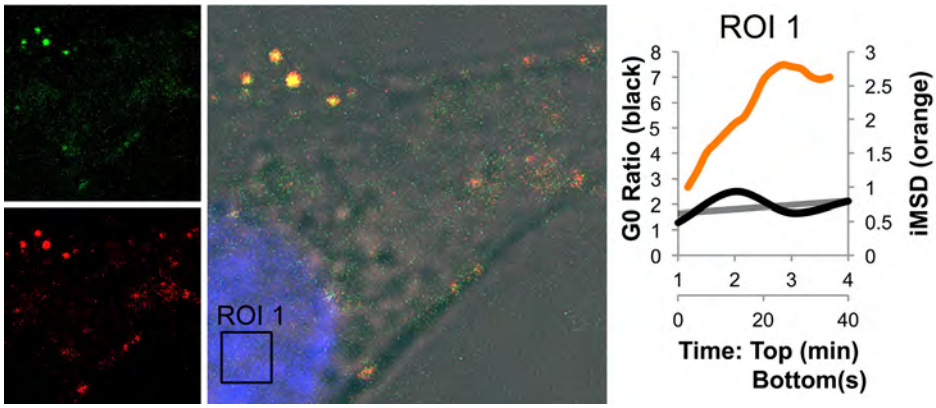

Figure 4.11 – The spatial and mechanical influence on DNA degradation – Nucleus
Observations of the dual labelled DNA within the nucleus were rare and therefore only one event was found in this cell example. Previously it was established that the mechanisms of motions found within the nucleus of delivered DNA were either CD or AS. In the event here where both ccRICS and iMSD analysis were applied, a CD event was isolated. This event had demonstrated a very little change in the G0 ratio, therefore, it would appear that degradation did not occur.

Following the ROI analysis of the dual labelled DNA, all cells analysed were collated together based on the mechanism of motion determined and whether the G0 ratio increased, decreased or

remained the same. The collection of results are presented in Figure 4.12. As previously observed, a range of mechanisms of motion were observed along the cell extremity, including CD, AS, TC and B-UB events. In Figure 4.12, the events have been colour coded based on the G0 ratios observed, where those that increased possibility accounting for events where DNA is recruited is in green, when the G0 ratio remained the same it was coloured yellow, and red presents the G0 ratios that decreased (indicated that degradation had occurred). No degradation appeared to have occurred in CD along the cell extremity, whereas TC and B-UB observations demonstrated approximately 50% degradation events, and AS had shown degradation in all events.

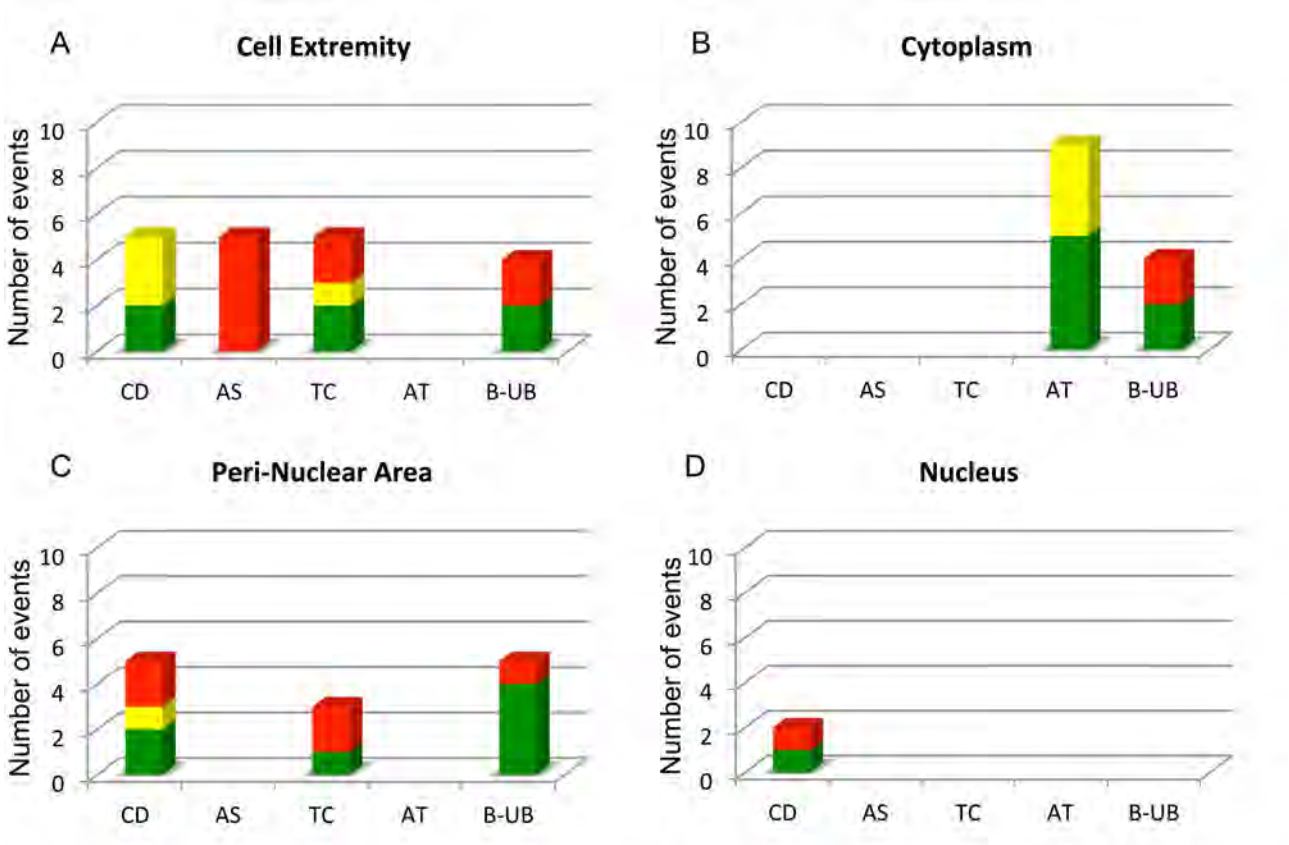

Figure 4.12 – Summary of Spatial and Mechanical Degradation
All of the ROI analysis through the combination of ccRICS and iMSD were combined providing an insight into the mechanical processes involved in DNA degradation. In the graphs presented in this figure, the four locations isolated; cell extremity (A), cytoplasm (B), peri-nuclear (C) and nuclear (D), has been presented showing the mechanisms motion analysed and whether degradation was determined or not. In the graphs when the G0 ratio increased it was coloured green, when the G0 ratio remained the same it was coloured yellow, and red presents the G0 ratios that decreased likely indicated that degradation had occurred.

Within the cytoplasm, only AT and U-UB events were observed, and no degradation was found when the DNA is moving via active motion. Once within the peri-nuclear area, the DNA had exhibited

CD, TC and B-UB events, all of which exhibited degradation, however TC had shown the most of the three mechanisms of motion while studying degradation.

4.4 Discussion and Conclusion

Most studies on DNA degradation used short DNA fragments known as oligonucleotides, which are not commonly applied in gene delivery, and have yielded a variety of results. DNA degradation has been claimed to occur significantly within 20h and 3h in a single study [159], and within 6h [235] and 60 min [268] in two others, all of which were performed using different fibroblast cell lines. A more relevant study utilised plasmid DNA that was microinjected in the cytoplasm of cells which uncovered a DNA half-life of 50-90 min [131]. These studies produced significantly different results for the most part. A critical disadvantage in the approach undertaken by these studies determined the occurrence of degradation on the decrease in fluorescence signals from labelled DNA. Such the decrease in fluorescence could be due to other factors including photobleaching, and the release of the DNA from cells [269].

Since the use of fluorescence imaging is not ideal to study DNA degradation other approaches are essential, which includes the application of more sensitive and specific tools such as FCS. For example, Kinjo *et al.* (1998) demonstrated that FCS could be applied to study DNA fragmentation, as smaller fragments are faster than larger ones. However, Kinjo and colleagues' study was limited to studying DNA degradation in solutions. Additionally, the cellular environment has demonstrated that DNA has capacity to move at a range of different speeds, therefore, faster mobility could likely be due to active transportation (as per previous sections of this thesis).

Sasaki and Kinjo (2010) applied a Fluorescence Cross-Correlation Spectroscopy (FCCS) approach to study the degradation of a dual labelled DNA fragment, which was delivered through a bead loading system. Their approach attempted to identify the likely nucleases responsible for the degradation of delivered DNA based in the changes in mobility. The study identified a reduced cross-correlation amplitude after 45 minutes indicative of degradation [137], however no half-life was presented or the point in time where cross correlation was no longer observed.

The DNA half-life obtained for the investigations presented here are in the order of 2 to 38 fold greater in the slower species and 1.3 to 26 greater in the faster species compared to previously published studies [159,268]. It is this study presents the most comprehensive analysis on DNA degradation to date, addressing the spatial and temporal degradation as well a DNA half-life, effects of DNA loads and also how the mechanical processes of the cell influences degradation, no study to date has achieved this.

Three major factors may have influenced the differences observed to date; the cell type, delivery processes and the DNA utilised. Across these studies a range of cell types have been used, including fibroblasts, ovarian cells and kidney cells. As each cell type has different physiology and function, they may result in different rates of degradation. Additionally, each study utilised different DNA constructs. Ratton *et al.* (2014) recently utilised a high-throughput sequencing approach to determine the most commonly cuts sites of a DNA plasmid during to cytoplasmic and nuclear degradation, demonstrating significance that the DNA sequence may have DNA degradation. In this case, Ratton and colleagues identified that the most commonly cut sequences were those of foreign regions, including viral promoters, antibiotic resistance genes, synthetic poly(A) and the bacterial origin of replication (*Ori*) [270]. Therefore, Ratton *et al.* demonstrate that the DNA sequence must be considered when studying DNA degradation.

The transport mechanisms appeared to have played a critical factor in the occurrence of degradation; previously this aspect has never been explored. It is expected that the DNA lipoplexes will be contained within endosomes following their uptake into the cell [15], during which the lipids of the lipoplex have been suggested to alter the biology of endosomes [109]. This phenomenon, and the mechanism of confined diffusion may protect the delivered DNA from cytosolic nucleases. Whereas, subdiffusion and transient confinement are likely to represent the DNA that has escaped endosomes, therefore exposed to nucleases [130] and explain why rapid degradation has been observed in studies employing microinjection [131].

Within the cytoplasm, the predominate transport mechanism was active transport, which exhibited the complete absence of any degradation. Such a process could not otherwise be demonstrated through many of the techniques applied to study DNA degradation [130,131]. Therefore, this observation highlights the requirement for live cell approaches to study such processes.

Along the peri-nuclear region, this study and others [240] have observed the accumulation of the exogenous DNA along the nuclear membrane. This region exhibited the greatest amount of degradation, and has previously been demonstrated to have poor mobility (Chapter 2), therefore, it was possible that the low mobility and accumulation provided the opportunity to recycle and degradation the exogenous DNA. Thereby, explaining the high rate of degradation that occurred within the peri-nuclear region.

The data presented in this chapter clearly demonstrates that DNA degradation plays a significant role in the efficacy of successful delivery of gene products. The application of ccRICS coupled with iMSD analysis has enabled the calculation of degradation and DNA half-life, in live myoblast cells. In addition, the approach employed identified that the process the mechanisms of motion are related to the rate or occurrence of degradation.

CHAPTER 5

The Effects of Membrane States on Intracellular Lipoplex Dynamics

5.1 Introduction

The physiology and state of a cell is a critical factor for successful gene delivery, for example, a number of studies have demonstrated that by simply treating cells with agents that destabilise cytoskeletal networks gene delivery can be hamper [14,143]. In addition, Ca^{2+} and ATP depletion have demonstrated that these small molecules are critical for gene vector uptake and endosome release [271]. The cell cycle can also play a pivotal role in successful delivery outcomes, for example some vectors such as retroviruses can only target dividing cell populations [15], or cell division can enhance nuclear translocation [50].

It is worth considering the membranes of the cell govern many interactions that a gene delivery vector will engage with. For example, the delivery vector such as a lipoplex must first interact with the plasma membrane in order to enter the cell, but then may be encapsulated within the endosome membrane. The nuclear envelope must also be traversed in order for the exogenous DNA to pass into the nucleus. Therefore, this section of the thesis aims to seek how the membrane physiology, i.e. the membrane state and composition, has an effect on the behaviour of delivered DNA lipoplexes.

5.1.1 Cellular Membranes

In mammalian cells, the plasma membrane defines the cell and separates the intra- and extra-cellular constituents, but membranes are also found throughout the cell, as membranes define

organelles including the nucleus and vesicles. All membranes are composed of three principal classes of lipids, (i) phospholipids, (ii) sphingolipids and (iii) cholesterol. The main building block of biomembranes are phospholipids which are composed of two segments, the head group which are hydrophilic and interact with the water interfaces, and the tail which are hydrophobic and are composed of the fatty acid side chain (Figure 5.1).

In aqueous environments, phospholipids will spontaneously form one of three structures, spherical micelles; liposomes or phospholipid bilayers (Figure 5.1). The bilayers, which form the plasma membrane and many others including those of organelles, such as the nuclear membrane and mitochondria, are highly specific depending on their location and function, containing different compositions of lipids but also proteins, such as transmembrane or lipid-anchored proteins of various functions including transport proteins and receptors (Figure 5.1).

Depending on a number of factors including the lipid composition, distribution of proteins and physiological conditions such as temperature and ion concentrations the membrane structure can differ. For example, the degree in membrane fluidity depends on the lipid composition, structure of phospholipid tails and temperature. Phospholipids containing long, saturated fatty acyl chains have a tendency to aggregate, thereby packing tightly together and forming a gel-like state. Whereas, short fatty acyl tails, which have less surface area cause fewer van der Waals interactions and form more fluid membranes.

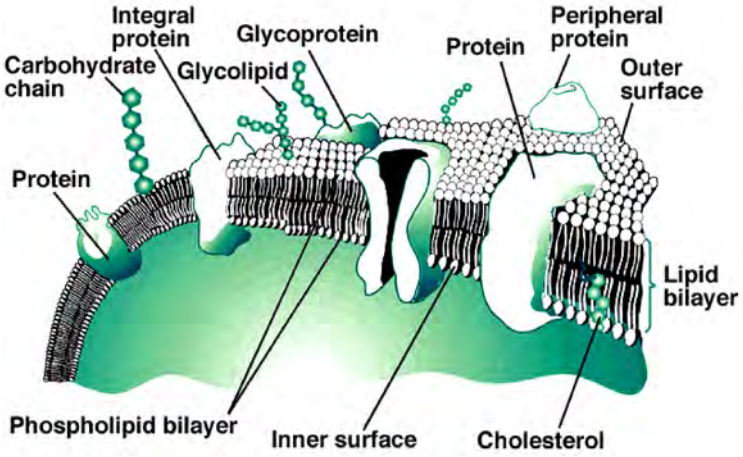

Figure 5.1 – Membrane Fluid Mosaic Model
A bi-lipid layer composed mostly of phosolipids forms the membrane of a cell, but depending on the function and location of the membrane other components can be found including cholesterols, membrane bound proteins, glycoproteins and carbohydrates.

A significant challenge in the study of biomembranes has been the difficulty to monitor and observe a number of characteristics of membranes in live cells, such as the state and composition. However, a number of bioimaging tools have recently emerged that provide a rapid and simple approach to characterise live cell membranes in real time.

5.1.2 Spectral Phasor Approach

The application of phasors to analyse typically difficult data has started to gain momentum in the field of bioimaging. One such example is the application of Fluorescence Lifetime Imaging Microscopy (FILM) that can be potentially difficult to interpret, however, once the data is converted in a phasor a relatively simple, graphical and fit-free analysis can be applied [272].

However, for the interest of this project the recent development of the spectral phasor approach will be the focused here. Cutrale *et al.* (2013) recently presented the theoretical background of translating multi-spectral data obtained from a commercial confocal microscope into a phasor, thus enabling the simple analysis of spectral data.

In the spectral phasor approach (and similar to the FLIM phasor analysis) the data is transformed into a phasor plot based on two equations that provide the *G* and *S* co-ordinates (*x* and *y*, respectively). The equations of the two co-ordinates have previously been outlined by Cutrale *et al.* (2013) as follows for each individual image (*i*):

$$G_i(\lambda) = \frac{\sum_{\lambda=\lambda_s}^{\lambda f} I(\lambda)\cos(n\omega\lambda)\,\Delta\lambda}{\sum_{\lambda=\lambda_s}^{\lambda f} I(\lambda)\,\Delta\lambda}$$

Equation 21 - G co-ordinate in Spectral Phasor

$$S_i(\lambda) = \frac{\sum_{\lambda=\lambda_s}^{\lambda f} I(\lambda)\sin(n\omega\lambda)\,\Delta\lambda}{\sum_{\lambda=\lambda_s}^{\lambda f} I(\lambda)\,\Delta\lambda}$$

Equation 22 - S co-ordinate in Spectral Phasor

where λ_s and λ_f are the starting and final wavelengths of the spectrum respectively, n is the harmonic number, and $\omega = 2\pi f$ where the frequency $f = (n \times spectral\ channels)^{-1}$. Once translated into the spectral phasor each pixel of an image is distributed within the phasor plot based

on its spectral properties within the spectral phasor presented in Figure 5.2. Then through cursor analysis, the area of phasor is selected and super-imposed over the imaged acquired.

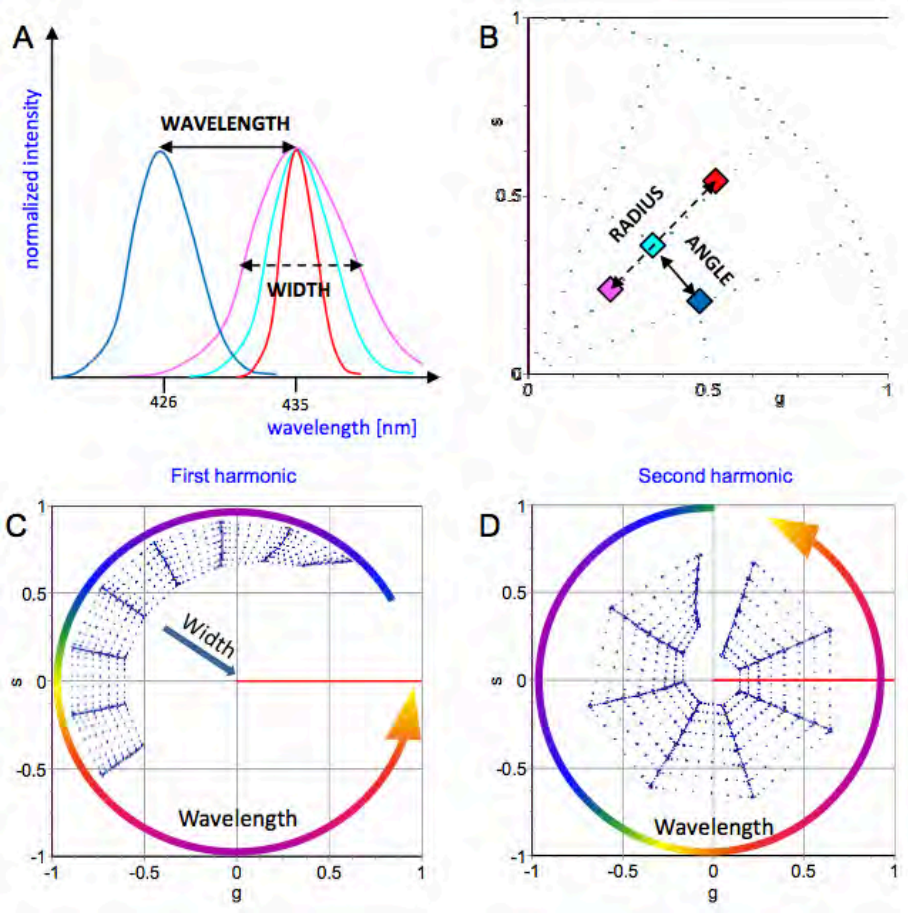

Figure 5.2 – Spectral Phasor
In the spectral phasor approach the first (A) and second (B) harmonics have been presented where λ represents the wavelength and σ the width or distance from the centre. The visual light spectrum is distributed across the phasor accordingly in an anti-clockwise manner (blue to red). The distribution of the spectrum has been presented based on a 32-channel simulation performed by Cutrale et al. (2013). In the simulation three examples have been calculated (C) and their perspective positions on the phasor plot identified (A, B). (Image obtained from Cutrale et al. 2013)

5.1.3 Laurdan and Nile Red

With respects to the spectral analysis of biomembranes there are several membrane specific, fluorescent dyes that enable the identification of membranes that are well characterised and readily available, two such examples are Laurdan and Nile red.

Laurdan is a useful membrane specific dye that fluoresces once within a lipid-rich environment. It has been characterised in several studies to specifically address membrane fluidity due to its property to sense the polarity of its environment. Laurdan has the ability to distinguish between two classes of bilayer membrane states, either solid-order or lipid-order (i.e. rigid or fluid).

As a result two recent studies have demonstrated that this dye has the capacity to characterise cellular membranes through the application of both FLIM and spectral phasors [273,274]. These two studies demonstrated that laurdan shows a shift in both the fluorescence lifetime and spectra depending on the fluidity of cellular membranes, which is directly related to the membrane lipid composition and water saturation [273].

Nile red on the other hand, which is also a lipid specific fluorescent dye, has the potential to discriminate between the type of lipid present, thereby determining the lipid composition of a biomembrane. In the instance of nile red, exhibits a spectral shift from yellow to red wavelengths, in the presence of non-polar lipids such as cholesterol and triglycerides, and polar lipids (including phospholipids), respectively [275].

Therefore, it is expected that the use of both laurdan and nile red are worthwhile stains to characterise cellular membranes through the application of the spectral phasor approach. In particular providing insight into physiology of cell membranes aimed to further the understanding into events that occur in therapeutic strategies such as gene delivery.

5.2 Materials and Methods

5.2.1 Cell Culture, Treatments and Transfection

L6 Rat Myoblast cells were cultured at 37°C in 5% CO2 in DMEM supplemented 0.5% Pen-Strep, and 2.5mM HEPES. Trypsinized cells were plated onto 8-well Labtek chamber slides. Cells were cultured in four conditions: (i) controls, media supplemented with 10% FBS, (ii) starved, media supplemented with 2.5% FBS, (iii) supplemented with 20% serum, or (iv) cholesterol treated, media supplemented with 10% FBS and a 2-fold increase in media cholesterol using a total cholesterol solubilized in ethanol (serum cholesterol was determined to be 0.85mmol/L using a cholesterol module of an Abbott Architect ci16200 (Abbott Diagnositics, Australia)). Laurdan (6-dodecanoyl-2-dimethylamino naphthalene; Invitrogen) was dissolved in dimethylsulfoxide (DMSO) and prepared at a 1.8 mM stock solution. Nile Red (9-diethylamino-5-5-benzo-α-phenoxazinone; Invitrogen) was

dissolved in acetone and prepared as a 7.8mM stock solution. Dyes were diluted 1:1000 into serum-free media to a working concentration, then added to the cells, incubated for 40 min at 37°C and then washed before imaging.

In order to determine the gene expression/delivery efficiency cells were transfected with a pAcGFP1-Actin (Clontech, USA), whereas DNA behaviour was studied with a 1,000bp DNA labeled with Alexa Fluor488 as detailed in Section 2.2.1. Lipoplexes were formed with a 3:1 ratio with the X-treme Gene 9 reagent as detailed in Section 2.2.2. Once the lipoplexes were administered to cells they were incubated in the above conditions and imaged a 8, 24 and 48h time points.

5.2.2 Spectra Phasor Imaging and Analysis

Spectral profile data for both solutions and cells were acquired with a Zeiss LSM710 META laser scanning microscope (Zeiss, Jena, Germany) coupled to a 2-photon Ti:Sapphire laser (Mai Tai, Spectra Physics, Newport Beach, CA) producing 80-fs pulses at a repetition of 80 MHz. Both Laurdan and Nile Red were excited at 780 nm.A 60X (1.4NA) water-immersion objective was used for all experiments. The data was acquired in the spectral mode of the Zeiss 710 using 32 channels covering the spectrum from 416.32 to 727.65 nm with 9.73 nm bandwidth per channel. All images were acquired using a pixel dwell time of 177.32µs and 256 × 256 pixel size frames. A 16-bit integer was used for all images.

RICS, N&B and iMSD data was collected within the Leica SP5 system as previously detailed (Section 2.2.3). The Globals software package, SimFCS 3.0 was used to reference and analyse spectral phasor data, and RICS, N&B and iMSD data was analysed using the same software.

5.3 Results

5.3.1 Changes in membrane physiology

The changes in cell membrane state and composition were first assessed through the application of the spectral phasor approach with cells maintained under different conditions with either laurdan or nile red.

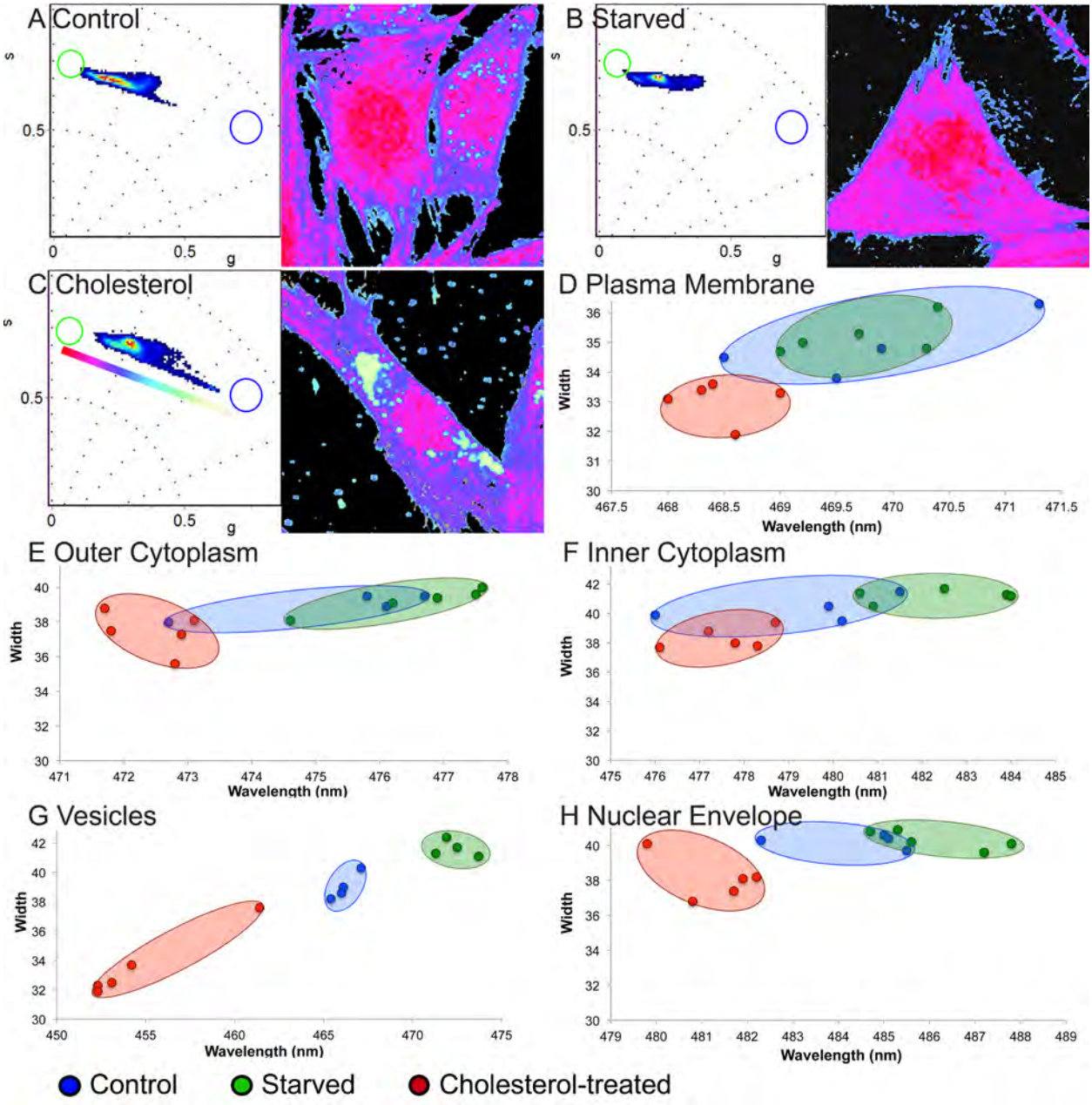

Figure 5.3 – Spectral distribution of Laurdan in cell treatments

Examples of spectral phasor images from cells used as controls (10%), were starved (2.5% FBS), or treated with a 2-fold increase in cholesterol and stained with Laurdan (A-C, respectively). Phasor plots are shown in the left, and cell images in the right. Two cursors were used and linked with a colour pellet, which has been superimposed in the phasor plot of the cholesterol treated sample (C). Cells are coloured based on their position between the cursors demonstrating their membrane fluidity, more rigid membrane are shown in a cream colour, and more fluid in the red colour. The phasor positions of specific membranes were isolated and presented in scatter plots identifying the membrane fluidity of each culture condition for the plasma membrane, outer and inner cytoplasm, vesicles and nuclear envelope (D-H, respectively). Number of cells for each population = 5.

Firstly, laurdan demonstrated the cells maintained in the three conditions, starved in low serum and controls in 10% serum and in a 2-fold increase in cholesterol, all exhibited different membrane states and fluidity (Figure 5.3). In summary, cells maintained in low serum exhibited more fluid membrane, demonstrated by the spectral shift towards to green wavelengths (Figure

5.3C) compared to the control cells (Figure 5.3A). The cholesterol-treated cells on the other hand showed a shift towards to blue wavelengths, indicative of more rigid membranes (Figure 5.3C).

The spectral phasor approach enables the analyses of small regions, providing details on specific membrane areas, including the plasma membrane, vesicles and nuclear membrane. The shifts in the spectral emission have been presented as scatter plots, enabling the discrimination of changes for the different conditions (Figure 5.3D-H).

Across the treatments, laurdan demonstrated changes in the plasma membranes of the cells; in particular, those treated with cholesterol exhibited more rigid states compared to the control and starved populations, which and shown a similar fluidity state (Figure 5.3D). Within the cytoplasm of these cells, the laurdan probe demonstrated that the starved cells were more fluid, whereas the cholesterol-treated were more rigid compared to the control cells, with an apparent spectral distribution in the centre of the starved and cholesterol-treated conditions (Figure 5.3E, F).

Vesicles in the cytoplasm and the nuclear envelope (NE) were isolated as they both play pivotal roles in gene delivery. Similar to the rest of the areas, the vesicles and NE revealed more fluid like behaviour when the cells are starved and more rigid when treated with cholesterol, the control cells remained with a distribution in the centre of the two treatments (Figure 5.3G, H).

When nile red was applied to cells, shifts in the emission spectra were observed, demonstrating characteristic changes in the alterations in membranes of the different conditions (Figure 5.4). The membranes, when starved, displayed a more polar state, whereas cholesterol treated cells appear to exhibit more non-polar membranes (compared to the 10% serum controls). The major differences were observed within the extremity of the cytoplasm and vesicles, which exhibited a significant shift towards the yellow wavelengths (587-589nm) in the cholesterol-treated vesicles, compared to the control (605-611nm) and starved (607-615nm) (Figure 5.4I). Interestingly, around the peri-nuclear region and the nucleus envelope the spectral emission of the cholesterol-treated cells showed a shift indicative of more polar membranes (towards red wavelengths), compared to the controls (Figure 5.4H, J).

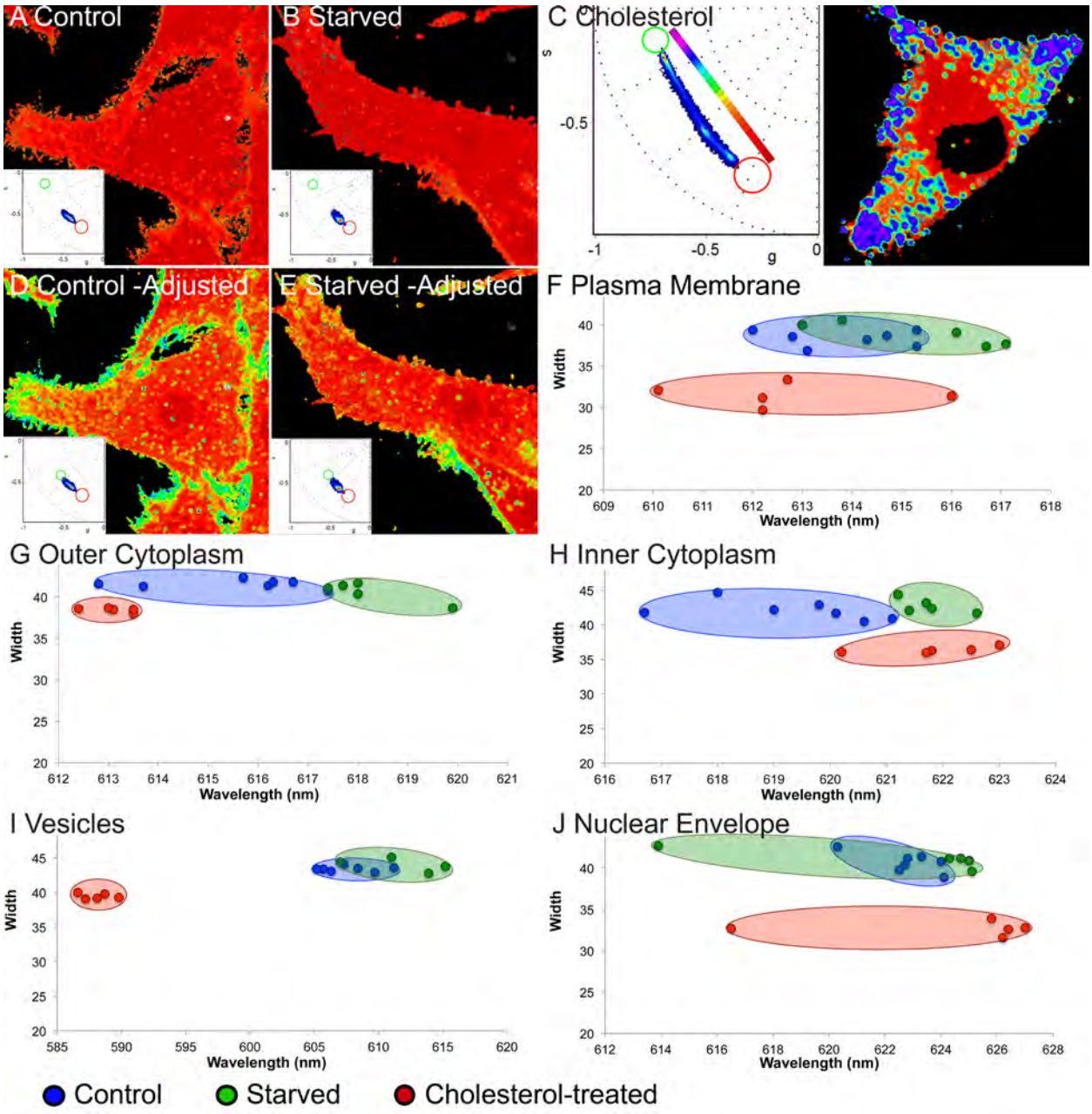

Figure 5.4 – Spectral distribution of Nile Red in cell treatments

Examples of spectral phasor images from cells used as controls (10%), were starved (2.5% FBS), or treated with a 2-fold increase in cholesterol and stained with Nile red (A-C, respectively). Phasor plots were superimposed in the control and starved examples, and due to the tight pixel distribution in the phasor plots, images where the cursor positions were adjusted have been also presented. Two cursors were used and linked with a colour pellet, which has been superimposed in the phasor plot of the cholesterol treated sample (C). Cells are coloured based on their position between the cursors demonstrating lipid polarity and charge; non-polar, neutrally charged lipids including cholesterol and triglycerides are shown in purple, and polar, negatively charged lipids such as phospholipids in the red colour. The phasor positions of specific membranes were isolated and presented in scatter plots identifying the membrane fluidity of each culture condition for the plasma membrane, outer and inner cytoplasm, vesicles and nuclear envelope (D-H, respectively). Number of cells for each population = 5.

Cells maintained with 20% serum exhibited similar spectral distributions for both laurdan and nile red as the control (10% serum) populations (SI 16).

5.3.2 Effects on DNA behaviour and expression

The effects of different membrane states and compositions were assessed through two approaches; the changes in transgene expression, and the behaviour of the flDNA, at a molecular level, in an effort to link gene delivery efficiency with the molecular mechanisms and behaviour of the flDNA.

Firstly, cell populations were cultured under different conditions and transfected with an expression vector encoding for an Actin-GFP transprotein. At 8, 24 and 48h time points, the percentage of cells expressing the fluorescent protein were counted (Figure 5.5). Across all conditions, the percentage of cells expressing the protein increased over the 3 time points observed. However all treatments; starved (2.5% FBS), stimulated (20% FBS) and cholesterol-treated (2-fold increase), exhibited a reduction of transgene expression to different extents.

By 48h almost 17% (89 of 534) of control cells had expressed the fluorescent reporter. In comparison, the other conditions demonstrated reduced transfection efficiencies; the starved population had a transfection rate of 13.5% (31 of 228), which was 80% of the control, the high serum at 9% (54 of 575 cells), almost half of the control, and the cholesterol treated having the lowest transfection efficiency of 3.8% (7 of 184 cells), being less than a quarter of the control.

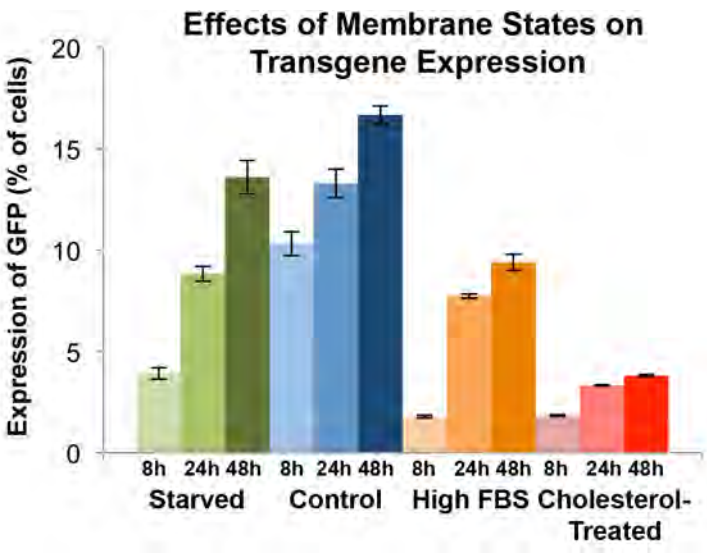

Figure 5.5 – Effects of Membrane States on Transgene Expression
Transfections with a GFP-actin expression vector were performed with cells under different conditions. The cells were counted at 8, 24 and 48h time points. Graph depicts the percentage of cells expression the GFP control. Across the cell populations an average of 380 cells were counted per population, a lower range of 100 cells and high range of 616 cells. Error bars represent the standard deviation.

The molecular influences and changes on the altered gene expression were then explored through the application of RICS, N&B and iMSD in order to study the variations in flDNA

mobility, aggregation and mechanisms of motion, respectively. A global analysis was performed in the first instance, providing an insight into changes in the cytoplasm as a whole (Figure 5.6).

The cells maintained in different conditions were transfected with a 1000bp DNA construct and immediately exhibited differences in cluster size and the extent of fluorescence (Figure 5.6A-D). The cells maintained in 20% serum, display large clusters within the cytoplasm, and after 24h these large clusters localised within the peri-nuclear region (Figure 5.6C).

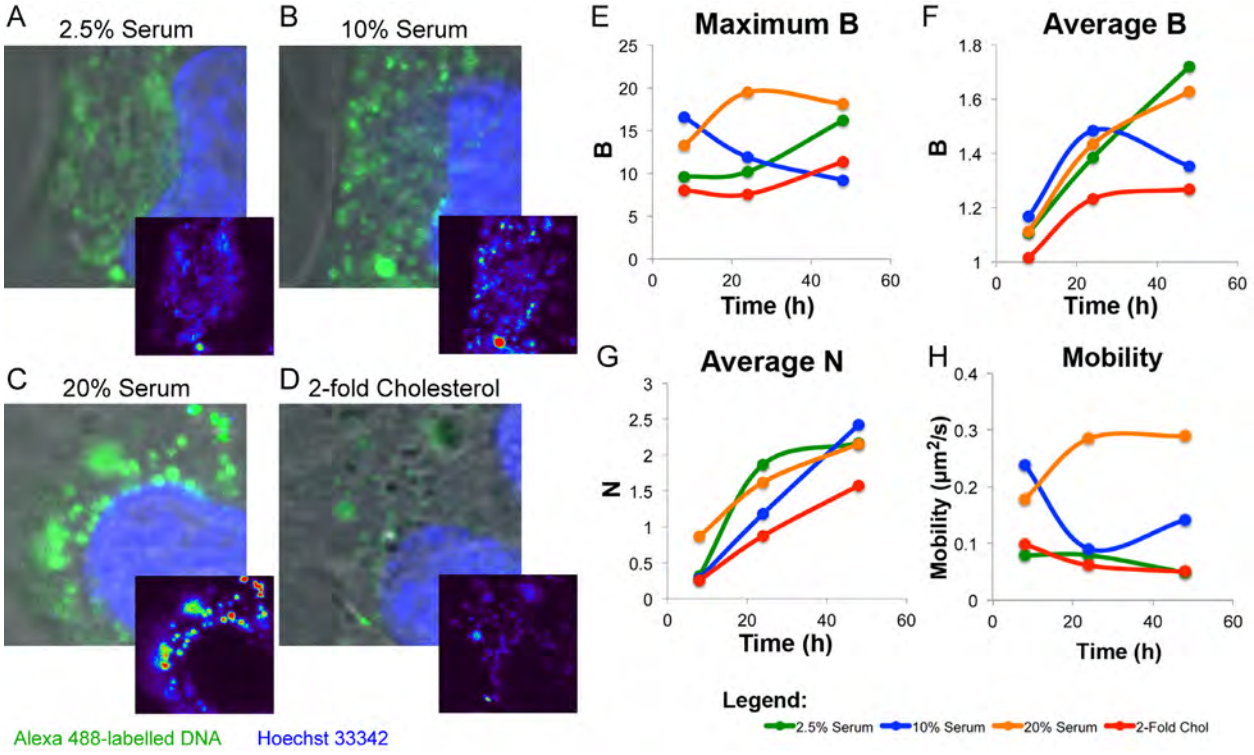

Figure 5.6 – Global Effects on DNA Behaviour

Cells were maintained in four conditions: 2.5% serum (starved), 10% serum (controls), 20% serum or 2-fold increase in cholesterol (A-D, respectively) and transfected with a fluorescently labelled 1000bp DNA. The cell populations were imaged at 8, 24 and 48h time point. A-D shown cells at the 24h time point showing the delivered DNA (green), and the nuclei counterstained by Hoechst 33342 (blue). The inserted images present the DNA channel coloured by a visible colour spectrum (blue--green-red) showing the fluorescence intensity and DNA distribution in the different conditions. A global cell analysis was then performed using N&B and RICS in order to study the variations in DNA aggregation and mobility, respectively. Graphs E and F shown the maximum aggregative states present, and average aggregation, respectively. The average particle number (N) is shown in G, and the mobility in H. (Cell images are 16.5x16.5 μm) (n = 8-10 cells per population)

The application of N&B analysis demonstrates that the control (10%) cell population displayed the largest extent and average of B values, representing aggregation. However, over time (24 and 48h) the aggregation within this population had decreased (maximum aggregative states, B = 16.6 at 8h, and 11.9 and 9.2 at 24 and 48h, respectively), whereas the other treatments had increased.

The 20% serum cells had displayed the highest extent of aggregation, whereas the cells treated with a 2-fold in cholesterol appear to have the lowest amount of aggregation, and generally less than the control group (Figure 5.6E, F).

In addition to aggregation, the N&B approach provides details on the particle number present within a sample. In the case of the cells transfected in different conditions, all populations demonstrated an increase in particle number within their cytoplasm, over the time course observed.

After 24h, the starved cells appeared to plateau by 48h. The controls, 20% serum and cholesterol-treated conditions demonstrated a constant increase in particle number. Additionally, the cells treated with a 2-fold increase in cholesterol demonstrated less flDNA particles (N = 0.25 at 8h) compared to other conditions (N = 0.3, 0.32 and 0.87 at 8h in 10%, 2.5% and 20% serum, respectively) throughout the time points observed (Figure 5.6G). Finally, by 48h the control cells appeared to contain the greatest flDNA particle number (N =2.4, compared to 2.1 in the 2.5% and 20% serum treated).

The RICS analysis demonstrated that the cells maintained in 20% serum appeared to have the most mobile flDNA. The overall mobility increased between the 8h and 24h observations, and then plateaued. The controls however, declined in mobility, which then increased between the 24 and 48h observations. Both the 2.5% serum and cholesterol-treated populations demonstrated slower mobility compared to the controls at all three time points (Figure 5.6H).

Following global analysis, the RICS, N&B and iMSD approaches were applied to study the molecular mechanisms and changes in three specific locations within the cell; the extremity of the cell along the plasma membrane (Figure 5.7), within the cytoplasm (Figure 5.8), and in the peri-nuclear region (Figure 5.9).

Cell Extremity

Along the cell extremity, the flDNA in control cells exhibited a low amount of aggregation at 8h, which then increased at 24h and then reduced by 20% at 48h (maximum aggregative state, B = 2.6, 7.6 and 6.1 at 8, 24 and 48h, respectively) (Figure 5.7A). Both the starved and cholesterol-treated

populations displayed a similar aggregative state at 8h (compared to the controls), however did not exhibit an increase in aggregation at 24h. In the starved populations, the aggregation was unchanged until 48h when it doubled (from B=3.6 at 8h, to B=7.6 at 48h). The cholesterol-treated cells exhibited a linear increase in aggregation along the cell edge over time, however the aggregation was lower than the control at 48h (B = 5.4). The 20% serum treated cells exhibited an aggregative state in the flDNA 4-fold greater than the controls at 8h. Over time, the 20% serum treated cells displayed a decrease in aggregation, and by 48h the aggregation was 20% less than the 8h time point.

The N&B approach also provided details on the particle number (Figure 5.7B), where the control group displayed an increase of 2-fold between the 8 and 24h points, and a further increase of almost 4-fold between the 24 to 48h points. Apart from cells maintained in 20% serum, the other populations had a similar particle number within the cell extremity at 8h. The 20% serum group was 2-fold greater then the rest, which may be related to the increase in observed aggregation. Over the time course, the cells maintained in 20% serum, and treated with cholesterol, exhibited the

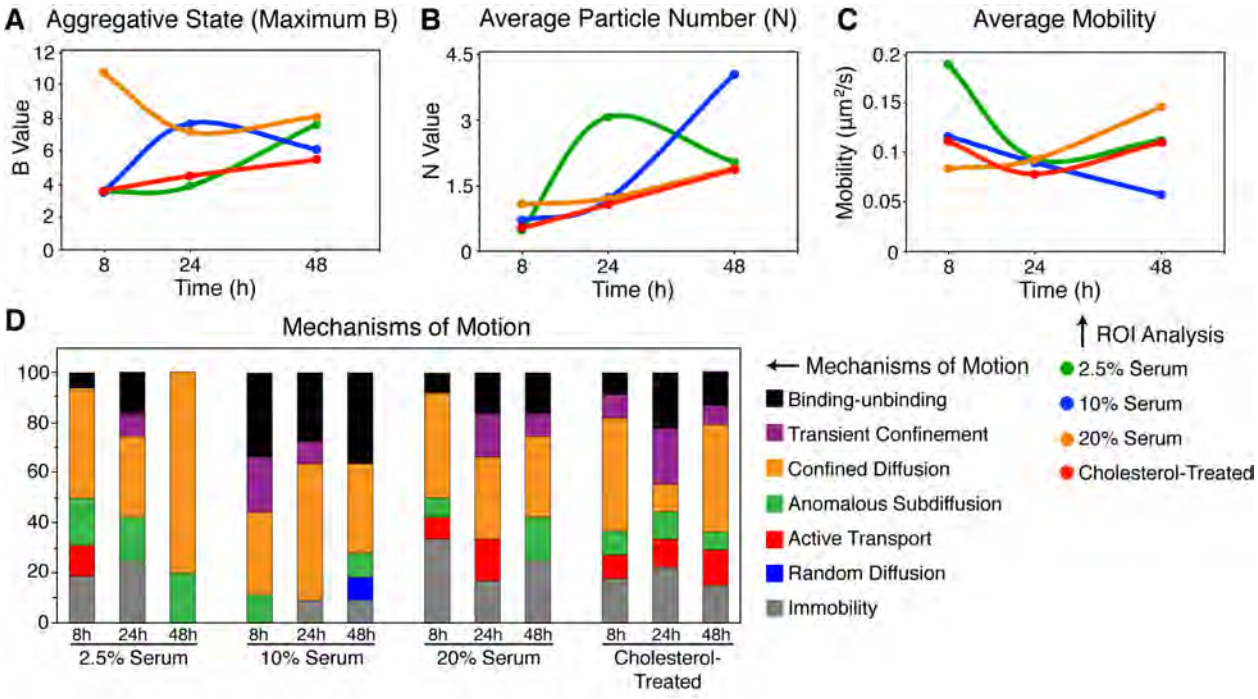

Figure 5.7 – DNA Behaviour Along the Extremities of the Cell
ROI analysis along the cell extremity was performed in cells transfected and exposed to different conditions. N&B analysis provided information on the aggregative state of the DNA (A) and particle number, N (B) over a 48h time course. The mobility of the delivered DNA was ascertained through the application of RICS (C), and the mechanisms behind the mobility was determined through iMSD analysis (D) (n = 8-10 cells per population, with each cell providing 2-5 values).

lowest particle number, only increasing by 4- and 2-fold over the 48h of the experiment. The starved cells on the other hand, demonstrated a dramatic increase in the particle number, which then declined from N=3 to 2 (between 24 and 48h). As previously observed (Chapter 2), the cells maintained in 10% serum (controls) demonstrated a decrease in mobility along the cell extremity (mobility was halved between 8 and 48h) (Figure 5.7C), and the majority of motion was identified as Confined Diffusion (CD) and Binding-unbinding (B-UB) events. All treated cell populations had exhibited changes in both the rates and mechanism of motion. Along the cell extremity, the starved cells shown a more rapid rate of motion compared to the control (0.18 $\mu m^2/s$ compared to 0.12 $\mu m^2/s$ at 8h), which had decreased but was still faster than the control. The iMSD analyses identified the presence of Active Transportation (AT), which was not typically observed in the control group. In addition, the starved population demonstrated less B-UB events to the control (none at the 48h observations).

The cells maintained in 20% serum, and treated with cholesterol, did not display a rate of motion that decreased over time (like the control group). In both the 20% serum-, and cholesterol-treated cells the rate of motion observed was slower at 8h compared to the control. By 24h, the rates of motion were similar to the control, however both groups exhibited more rapid mobility at 48h (20% serum: 3-fold and cholesterol-treated: 2-fold greater than the control) (Figure 5.7C). Both populations displayed at least double the amount of immobility compared to the control (9% in the controls at 24 and 48h, compared to 18% in the cholesterol treated to 48h and 33% in the 20% serum at 8h). A reduction in B-UB events was also demonstrated (Figure 5.7D).

Cytoplasm

Within the cytoplasm, the control group was consistent with previously shown studies (Chapters 2 and 3), where the aggregative state was relatively low but did increase by about 50% over the 48h experiment (Figure 5.8A). The particle number had increased by about 5-fold over the same time (Figure 5.8B). Across all populations, a reduced mobility at 24h appeared, however, in the control group the rate of motion remained unchanged between the 8 and 48h observations (Figure

5.8C). Finally, iMSD analysis demonstrated that the majority of motion was due to AT (42-60%) and B-UB (27-38%) (Figure 5.8D).

Cells that were starved exhibited similar properties as the control group. The aggregative states was in the order of 20% higher than the control group, across the time course of the experiment, have a significantly higher particle number, almost 2-fold greater at 24h (Figure 5.8A,B). The flDNA within this population of cells did have a mobility rate 20% slower than the controls (Figure 5.8C), as the iMSD analysis demonstrated the presence of immobility, and reduced rate of AT (42% of observations at 8 and 24h). Further, TC and CD was more apparent at the 48h time point compared to the control group (Figure 5.8D).

When cells are maintained in 20% serum, aggregation appeared to increase significantly compared to the controls (1.2-fold and 1.8-fold greater at 8 and 48, respectively) and other populations (Figure 59A). It should be noted that the particle number started higher than the controls (1.4-fold) at 8h, increased at 24h (2-fold greater than the control) but by 48h, had a lower particle number than the control cells (Figure 5.8B). At 8h, the mobility of the flDNA was 1.4-fold faster than the control, but was slower than the controls at 24h and then increased by 48h (Figure 5.8C). The occurrence of AT had increased (25%, 36% to 50% over the 8, 24 and 48h observations, respectively), and immobility which was present decreased (17%, 14% to 7% over the 8, 24 and 48h observations, respectively) (Figure 5.8C). By 48h, the transport mechanisms were almost the same as the control population at the same time point.

The cholesterol-treated cell population demonstrated almost the same aggregative states and particle number within the cytoplasm as the control group (Figure 5.8A, B). However, the mobility of the flDNA did differ, as the rate of motion was approximately 2-fold less than the control cell population (for example, cholesterol treated: 0.13 $\mu m^2/s$ compared to control: 0.25 $\mu m^2/s$ at 8h) (Figure 5.8C). The iMSD analysis provided an insight into the causation of the reduced mobility. Within the cytoplasm of cholesterol-treated cells, AT appeared to occur less compared to the

controls (20% of events compared to 42-60% events) with increase in CD (Figure 5.8D). It is worth noting in the cholesterol-treated cells, large cholesterol deposits appeared throughout the cytoplasm.

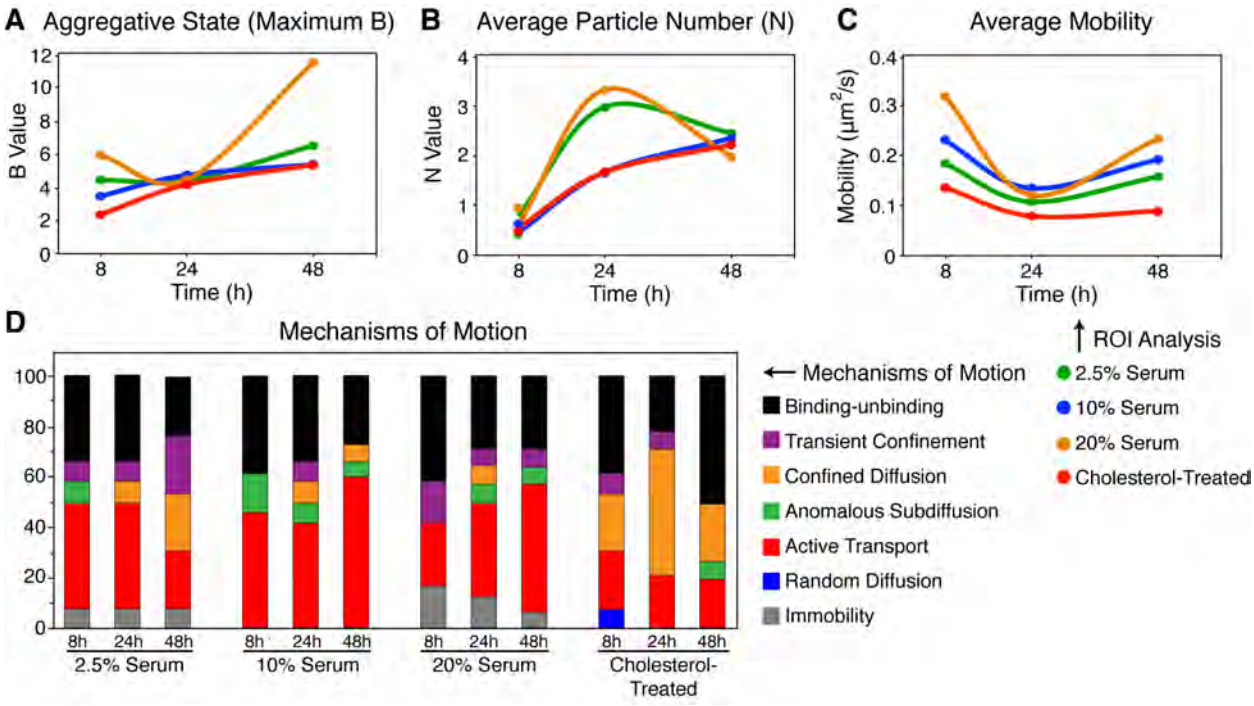

Figure 5.8 – DNA Behaviour within the Cytoplasm

ROI analysis within the cytoplasm along the cell extremity was performed in cells transfected and exposed to different conditions. N&B analysis provided information on the aggregative state of the DNA (A) and particle number, N (B) over a 48h time course. The mobility of the delivered DNA was ascertained through the application of RICS (C), and the mechanisms behind the mobility was determined through iMSD analysis (D) (n = 8-10 cells per population, with each cell providing 2-5 values).

Peri-nuclear Region

Within the peri-nuclear region, the flDNA delivered to the control population show a small amount of aggregation at 8h (B = 3.0), but had increased 4-fold by 24h (B = 13.8) and then decreased at 48h (B = 4.8) so that is was about 60% higher than the 8h time point (Figure 5.9A). This same pattern was observed along the cell extremity in the control population. Between the 8 and 24h time points, the particle number had increased 5-fold, and then plateaued (as did the 2.5% and 20% serum treated populations) (Figure 5.9B). The flDNA within this region had demonstrated a decrease in mobility over time resulting in a 40% decrease in mobility over the 48h experiment (Figure 5.9C). The iMSD analysis demonstrated a variety of transport mechanisms including immobility, AS, CD, TC and B-UB events, over the time course the number of B-UB events reduced and the AS events increased (Figure 5.9D).

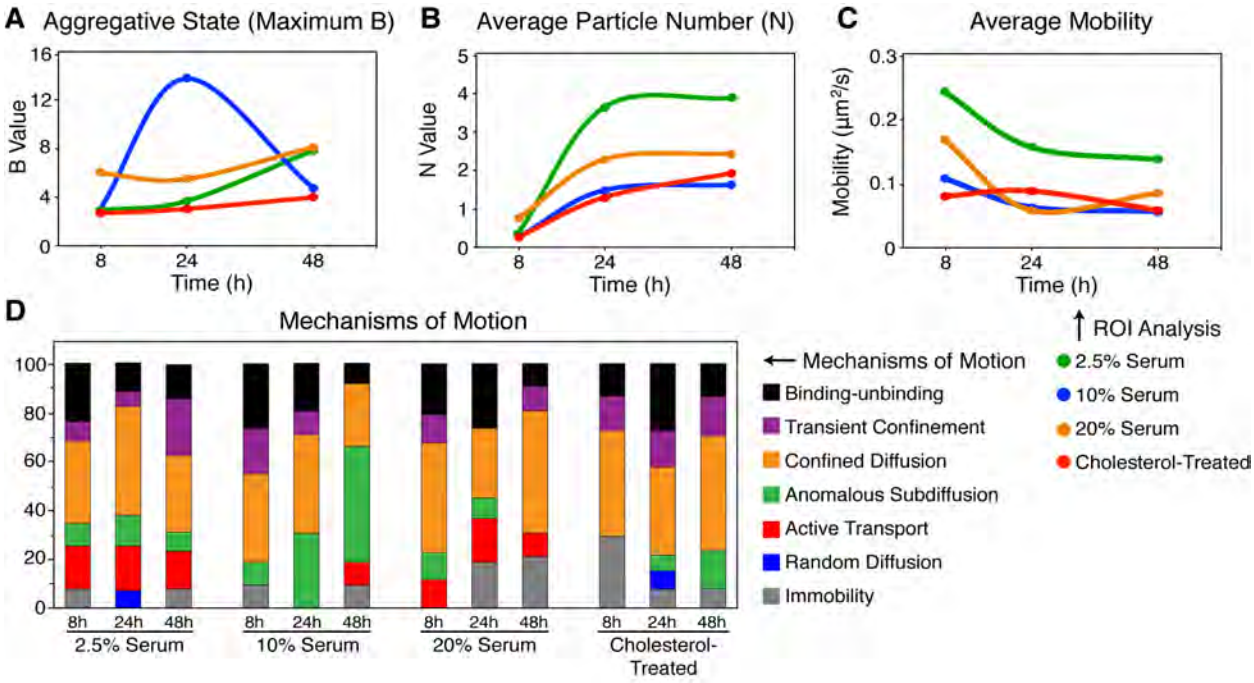

Figure 5.9 – DNA Behaviour within the Peri-nuclear Region
ROI analysis within the peri-nuclear region of the cell was performed in cells transfected and exposed to different conditions. N&B analysis provided information on the aggregative state of the DNA (A) and particle number, N (B) over a 48h time course. The mobility of the delivered DNA was ascertained through the application of RICS (C), and the mechanisms behind the mobility was determined through iMSD analysis (D) (n = 8-10 cells per population, with each cell providing 2-5 values).

In the stared cell population, over the 48h time course, the aggregation was initially the same as the control at 8h but gradually increased from B = 2.5 to B = 7.7 over the 48h of observation, where it was 2-fold greater than the control (Figure 5.9A). Along with the increase in aggregation, the particle number increased (2.4-fold greater than the control by 48h) (Figure 5.9B) and the mobility decreased albeit 2.4-fold greater than the control by 48h (Figure 5.9C). In the starved population AT was identified in the area, which was not observed in the control group. Additionally, the occurrence of AS remained the same over time, unlike the control group, which increased over time (Figure 5.9D).

Cells maintained in 20% serum had demonstrated a greater extent of aggregation within the peri-nuclear area, at both 8 and 48h being 2-fold greater than the control (Figure 5.9A). The particle number in these cells was higher than the controls at 48h (being 50% higher), and plateaued after the 24h observation (Figure 5.9B). The RICS analysis demonstrated that the flDNA was initially about 55% faster than the control, however at 24h was the same and just marginally faster by 48h

(Figure 5.9C). The drop in mobility appeared to be due to the occurrence of immobility at the 24 and 48h time points, but AT was also present in peri-nuclear region of this condition. Additionally unlike the control cells, the occurrence of AS remained the same over the analysed time points (Figure 5.9D).

Relative to the other treatments within the cholesterol-treated cells aggregation increased by about 2-fold, over the 48h (Figure 5.9A). Consistent with the other areas analysed within the cell, the cholesterol-treated cells had the least amount of flDNA within the peri-nuclear area up to the 48h point, when it was slightly (18%) greater that the control. Particle number did, however, increase by 6-fold over the course of the experiment (Figure 5.9B). The rate of mobility was similar to the control cells (at 8, 24 and 48h, 0.17 $\mu m^2/s$, 0.06 $\mu m^2/s$ and 0.08 $\mu m^2/s$, respectively) (Figure 5.9C). The cholesterol-treated cells had also shown the highest rate of immobility in the peri-nuclear area, with the other prominent mechanism being CD (Figure 5.9D).

Table 6 – Summary of flDNA Behaviour

Condition/Position		Aggregation	Particle Number	Mobility	Mechanism	Transgene Expression
Control	**Extremity**	Medium	High	Low	CD, B-UB	High
	Cytoplasm	Medium	Medium	High	AT	
	Peri-nuclear	Medium	Low	Low	CD, increasing AS	
Starved	**Extremity**	Low	Medium	High	CD	Medium
	Cytoplasm	Medium	High	Medium	AT	
	Peri-nuclear	High	High	High	CD, AT present	
20% Serum	**Extremity**	High	Low	High	CD, Immobile	Low
	Cytoplasm	High	High	High	AT (low then high)	
	Peri-nuclear	High	Medium	Medium	CD, AT present, immobility	
Cholesterol	**Extremity**	Low	Low	Medium	CD, Immobile	Low
	Cytoplasm	Medium	Medium	Low	CD	
	Peri-nuclear	Low	Low	Low	CD, immobility, late AS increase	

5.4 Discussions and Conclusion

This chapter explores the effects that serum and cholesterol concentrations have on cellular membranes that can then be translated to changes in the behaviour of DNA that is delivered through lipofection. The application of the spectral phasor approach enabled the changes in membrane fluidity and composition to be determined when cells were maintained in their optimal

condition (10% serum), starved or treated with an increase in serum (20%) or external cholesterol. Previously this technique has been applied to study changes in membrane fluidity in response to drugs that altered membrane physiology [274].

Previous studies that utilised the lipoplex reagent used in this project, have applied different serum concentrations (including 2.5% [276] 5% [277] 10% [276]), all resulting in transgene expression. However, no study found utilised it in higher amounts of serum (i.e. 20%). Based on the transfection efficiency at different concentrations, it was found here that the optional condition was with 10% serum. Therefore, this condition was considered the control for the most efficient gene delivery in the model here. This observation was found in other studies, including Marchini *et al.* (2009) demonstrating that transfections were more efficient in the presence of 10% serum, compared to no serum at all. In their study, four different lipoplex regents were used, however in the absence of serum, the amount of gene expression was within 10% of populations containing the serum [278]. It may be plausible that the presence of serum enhances gene delivery, as a study undertaken by Yoshikawa *et al.* (2011) identified that components of serum enhanced *in vivo* transfection of hepatocytes [279].

Previously published work focusing on the effects of serum on gene delivery mostly explored the effects on delivery outcomes and changes in the molecular structure of the lipoplex itself, not how the lipoplex behaviours within the cellular environment. Zuhorn *et al.* (2002) provided an interesting insight on how altering the lipoplex's exposure to serum can have an effect on gene delivery. In their study, lipoplexes were formed in the presence or absence of serum, then for those prepared in the absence of serum, were delivered to cells (COS-7) with or without serum [280]. It was found that lipoplexes were internalised 3-fold greater when prepared in the presence of serum, but transfection efficiency was 5-fold lower compared to those prepared in the absence of serum. The higher rate of internalisation could be due to the formation of smaller lipoplex structure in the presence of serum [281]. Zuhorn *et al.* (2002) had also found that lipoplexes prepared in the presence of serum resulted in the DNA changing from supercoiled to an open form, potentially exposing it to nucleases which may explain the low transfection efficiency [280].

Cholesterol appears to have an influential role in the gene delivery process, however the only studies to-date have addressed how the presence of cholesterol within the lipoplex structure affect gene delivery [282]. In addition, a study that applied CD (Circular Dichroism) spectroscopy to study the complexation of DNA to lipids in the formation of lipoplexes found that the DNA aggregates in the presence of high lipid and cholesterol content [259].

Little to no work to date has explored how changing conditions can affect the behaviour of the delivered DNA. Escriou *et al.* (1998) reported that delivered DNA in cells in the absence of serum formed large clusters that were few in number [260]. However, their study on aggregation was not quantitative, instead based on the intensity of fluorescence and physical size of clusters. In the work of this chapter, it was observed that aggregation in the absence of serum resulted in the least amount of aggregation. However, Escriou *et al.* (1998) had used a different cell line, DNA construct and lipid delivery approach.

The work undertaken by Escriou *et al.* (1998) also highlights an overarching trend in the study of gene delivery, which is that differences are observed due to a number of factors that can be changed, including the cell line, delivery approach and DNA sequences. This was further demonstrated by Mirsa *et al.* (2013), whose work demonstrated that the composition of the lipids in lipoplexes used are pivotal in the successful delivery, under different culture conditions. Mirsa *et al.* manufactured a range of lipoplexes composed of different lipids, with some achieving better transfection efficacy with or without serum, some lipoplexes even demonstrating transfection in serum concentrations as high as 50% [283].

In this chapter, the changes in flDNA dynamics and behaviour were explored by altering the membrane state and composition through different culture conditions. Through the application of the spectral phasor, RICS, N&B and iMSD approaches the work presented here demonstrates that changes in serum amounts (2.5%, 10% and 20%) or cholesterol (2-fold) altered the molecular behaviour reflecting changes in transfection efficiency. Prior to this study, the molecular dynamics

of delivered DNA have not been explored due to changes in culture conditions, and membrane physiology.

CHAPTER 6

Concluding Remarks

Throughout this thesis a number of FCS-based bioimaging approaches were applied in order to quantify and study the molecular behaviour of delivered flDNA in live cells. In this work two core hypotheses were addressed; firstly, that these bioimaging approaches can be applied to study the delivery process of exogenous compounds labelled with small molecular probes, and secondly, to gain a deeper understanding of DNA lipoplex dynamics as a model for the prior aim.

The application of the FCS based bioimaging approaches employed throughout this thesis, enabled the molecular mechanisms of individual particles to be investigated of fluorescently labelled particles. As the fluorescently labelled particle passes through the focus illumination volume, each will provide a signal enabling dynamic information to be exacted for each particle. The correlation of the fluctuations over time, gives information on mobility, mechanism of transport, aggregation and interactions. To date, these approaches, including RICS, iMSD, N&B and their cross-correlation extensions, have been applied to study endogenously encoded proteins, which have been tagged with a fluorescent protein, commonly GFP.

However, there is an interest in gaining an understanding of how exogenous compounds behave within cells. As such, the model presented in this thesis demonstrates the application of these bioimaging approaches to study live cell processes. In addition, this work utilised the small molecular probe, Alexa Fluor 488, which is a fraction of the size of GFP (with approximate

molecular weights to 570 and 26,900, respectively). The impact of the reduced flurophore size on the behaviour of labelled molecules is less likely to affect the behaviour of the particle of interest.

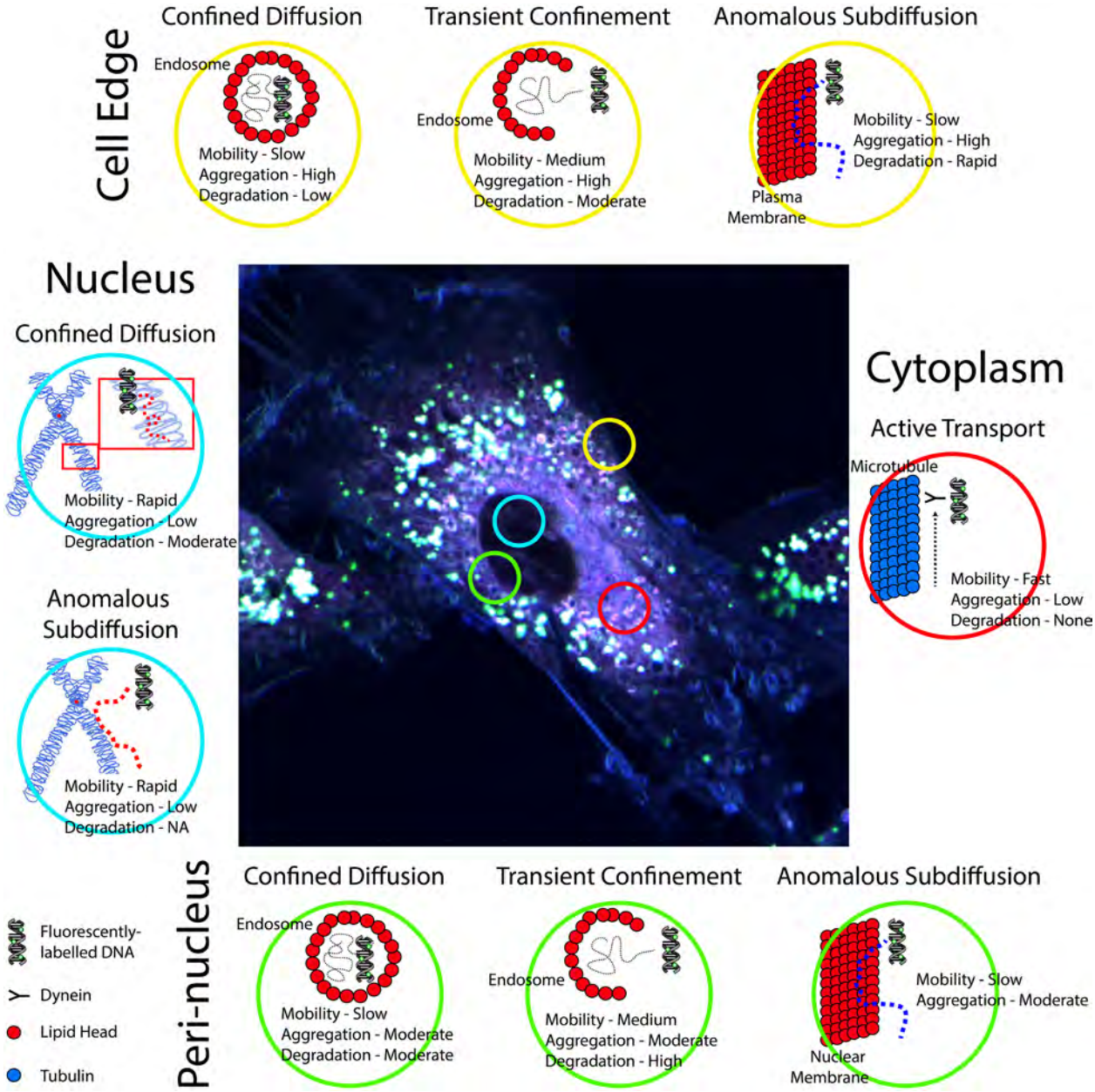

Figure 6.1 - Final Overview

Through the model devised in the thesis, it appeared that the delivered DNA followed a clear, redefined path through the cell, during normal physiology. The combination of RICS, N&B and iMSD demonstrated that that a slow mobility, and a high extent of aggregation would occur along the cell edge. Additionally, the main transport mechanisms included confined diffusion, transient confinement, and subdiffusion, exhibiting low, moderate and rapid degradative rates of the DNA, respectively. When within the cytoplasm, rapid, active transport was observed, resulting in little aggregation and degradation. Once localised within the peri-nuclear region, confined diffusion, transient confinement, and subdiffusion were again observed, however aggregation was lower, but degradation was higher. Finally, once within the nucleus only rapid mobility was observed, representing confined diffusion: likely due to the delivered DNA interacting within chromatin structures, or subdiffusion, possibly due to chromatin and nuclear structures acting as barriers. Within the nucleus, a low extent of aggregation was exhibited. The combination of these techniques provides an insight into the processing of delivered DNA throughout the entire cell simultaneously.

The dynamics of the delivered compounds are of great interest, previous studies utilising characterization techniques, including FRAP, often lack sensitivity and are potentially disruptive to the live cell milieu, or SPT, which is highly sensitive albeit lacking the capacity to investigate events of the entire cell. However, the bioimaging tools applied here have provided both spatial and temporal information in a non-disruptive approach. The combination of flDNA within lipoplexes has been utilised as a model for the delivery of macromolecules, which exhibited a pathway predefined by the cell, involving a 5-phase process of (i) slow directed into the cell, (ii) confined motion along the edge of the cell, followed by (iii) fast directed motion along microtubules, (iv) non-active motion within the peri-nuclear area, and then (v) confined- and sub-diffusion in the nucleus. This process through the cell appeared to go unchanged when the DNA size was altered between the 21bp to 5.5kbp range observed (approximately 12 to 3,300kDa).

Through this model, certain behaviours and phenomena of the delivered compound are expected to occur in specific areas of the cell. For example, along the cell extremity, the flDNA exhibited poor mobility contributed to non-active transport mechanisms (including confined- and sub-diffusion). In addition, the cell extremity exhibited the greatest extent of aggregation and particle number, and a moderate amount of degradation.

The flDNA within the core of the cytoplasm exhibited different behaviours compared to the cell extremity, and therefore, as a model within this area, a rapid mobility due to active transport would be expected. Additionally, this region lacked a great extent of aggregation, exhibited a low particle number and very little degradation.

The model presented also demonstrated the importance of the nature of the cell. By changing the cellular physiology, changes in the flDNA behaviour were observed throughout the cell. Other factors must also be taken into consideration, as outlined throughout this thesis and the literature including: the cell type, cell cycle and the nature of the delivered compound (in this case, the DNA size) can play a pivotal role in how a delivered macromolecule behaves at the molecular scale in a live cell.

A process that was not addressed in this study was the differentiation between the DNA being processed by gene delivery processes, and the DNA nucleotides that have been degraded and being recycled by the cell. In nucleotide metabolism, salvage pathways recover degraded base pairs and nucleosides from DNA and RNA, in order to produce nucleotides [286]. However, through the application of cross-correlation, it appears the DNA molecules labelled with two different probes cross correlate, thus enable intact and degraded DNA to be distinguished. Therefore, further work must be undertaken to gain a deeper understanding of these processes in live cells, although the work presented here sets the ground work to focus on nucleotide recycling.

In conclusion, the research presented in this thesis presents a model to characterise the delivery of macromolecules, which could include DNA lipoplexes, drugs, nanoparticles and other nucleic acids such as non-coding RNAs, and micro RNAs. The techniques utilised provided spatial and temporal information of the entire live cell, of single, dynamics particles.

REFERENCES

1 Brown, C. M. *et al.* Raster image correlation spectroscopy (RICS) for measuring fast protein dynamics and concentrations with a commercial laser scanning confocal microscope. *Journal of Microscopy* 229, 78-91 (2008).

2 Digman, M. A., Dalal, R., Horwitz, A. F. & Gratton, E. Mapping the number of molecules and brightness in the laser scanning microscope. *Biophysical Journal* 94, 2320-2332 (2008).

3 Digman, M. A., Wiseman, P. W., Horwitz, A. R. & Gratton, E. Detecting protein complexes in living cells from laser scanning confocal image sequences by the cross correlation raster image spectroscopy method. *Biophysical Journal* 96, 707-716 (2009).

4 Digman, M. A., Wiseman, P. W., Choi, C., Horwitz, A. R. & Gratton, E. Stoichiometry of molecular complexes at adhesions in living cells. *Proceedings of the National Academy of Sciences of the United States of America* 106, 2170-2175 (2009).

5 Antonie, J. W. G. V. & Hink, M. A. New perspectives of fluorescence correlation spectroscopy. *Journal of Fluorescence* 9, 81-87 (1999).

6 Digman, M. A. & Gratton, E. Lessons in fluctuation correlation spectroscopy. *Annual Review of Physical Chemistry* 62, 645-668 (2011).

7 Magde, D., Elson, E. & Webb, W. W. Thermodynamic fluctuations in a reacting system measurement by fluorescence correlation spectroscopy. *Physical Review Letters* 29, 705-708 (1972).

8 Rigler, R., Mets, U., Widengren, J. & Kask, P. Fluorescence correlation spectroscopy with high count rate and low background: Analysis of translational diffusion. *European Biophysics Journal* 22, 169-175 (1993).

9 Koppel, D. E. Study of Escherichia coli ribosomes by intensity fluctuation spectroscopy of scattered laser light. *Biochemistry* 13, 2712-2719 (1974).

10 Palmer 3rd, A. G. & Thompson, N. L. Theory of sample translation in fluorescence correlation spectroscopy. *Biophysical Journal* 51, 339-343 (1987).

11 Palmer 3rd, A. G. & Thompson, N. L. Molecular aggregation characterized by high order autocorrelation in fluorescence correlation spectroscopy. *Biophysical Journal* 52, 257-270 (1987).

12 Chen, Y., Müller, J. D., So, P. T. C. & Gratton, E. The photon counting histogram in fluorescence fluctuation spectroscopy. *Biophysical Journal* 77, 553-567 (1999).

13 Vaughan, E. E., DeGiulio, J. V. & Dean, D. A. Intracellular trafficking of plasmids for gene therapy: Mechanisms of cytoplasmic movement and nuclear import. *Current Gene Therapy* 6, 671-681 (2006).

14 Vaughan, E. E. & Dean, D. A. Intracellular trafficking of plasmids during transfection is mediated by microtubules. *Molecular Therapy* 13, 422-428 (2006).

15 Douglas, K. L. Toward development of artificial viruses for gene therapy: A comparative evaluation of viral and non-viral transfection. *Biotechnology Progress* 24, 871-883 (2008).

16 Kay, M. A. State-of-the-art gene-based therapies: The road ahead. *Nature Reviews Genetics* 12, 316-328 (2011).

17 Thomas, C. E., Ehrhardt, A. & Kay, M. A. Progress and problems with the use of viral vectors for gene therapy. *Nature Reviews Genetics* 4, 346-358 (2003).

18 Sheridan, C. Gene therapy finds its niche. *Nature Biotechnology* 29, 121-128 (2011).

19 Al-Dosari, M. S. & Gao, X. Nonviral gene delivery: Principle, limitations, and recent Progress. *AAPS Journal* 11, 671-681 (2009).

20 Wolff, J. A. *et al.* Direct gene transfer into mouse muscle in vivo. *Science* 247, 1465-1468 (1990).

21 Nishikawa, M. & Huang, L. Nonviral vectors in the new millennium: Delivery barriers in gene transfer. *Human Gene Therapy* 12, 861-870 (2001).

22 Felgner, P. L. *et al.* Lipofection: a highly efficient, lipid-mediated DNA-transfection procedure. *Proceedings of the National Academy of Sciences of the United States of America* 84, 7413-7417 (1987).

23 Wasungu, L. & Hoekstra, D. Cationic lipids, lipoplexes and intracellular delivery of genes. *Journal of Controlled Release* 116, 255-264 (2006).
24 Pedroso De Lima, M. C., Simões, S., Pires, P., Faneca, H. & Düzgüneş, N. Cationic lipid-DNA complexes in gene delivery: From biophysics to biological applications. *Advanced Drug Delivery Reviews* 47, 277-294 (2001).
25 Israelachvili, J. N., Marcelja, S. & Horn, R. G. Physical principles of membrane organization. *Quarterly Reviews of Biophysics* 13, 121-200 (1980).
26 Sternberg, B. New structures in complex formation between DNA and cationic liposomes visualized by freeze-fracture electron microscopy. *FEBS Letters* 356, 361-366 (1994).
27 Lin, A. J. *et al.* Three-dimensional imaging of lipid gene-carriers: Membrane charge density controls universal transfection behavior in lamellar cationic liposome-DNA complexes. *Biophysical Journal* 84, 3307-3316 (2003).
28 Tresset, G. The multiple faces of self-assembled lipidic systems. *PMC Biophysics* 2 (2009).
29 Wu, G. Y. & Wu, C. H. Receptor-mediated gene delivery and expression in vivo. *Journal of Biological Chemistry* 263, 14621-14624 (1988).
30 Boussif, O. *et al.* A versatile vector for gene and oligonucleotide transfer into cells in culture and in vivo: Polyethylenimine. *Proceedings of the National Academy of Sciences of the United States of America* 92, 7297-7301 (1995).
31 Goula, D. *et al.* Size, diffusibility and transfection performance of linear PEI/DNA complexes in the mouse central nervous system. *Gene Therapy* 5, 712-717 (1998).
32 Chemin, I. *et al.* Liver-directed gene transfer: A linear polyethylenimine derivative mediates highly efficient DNA delivery to primary hepatocytes in vitro and in vivo. *Journal of Viral Hepatitis* 5, 369-375 (1998).
33 Haensler, J. & Szoka Jr, F. C. Polyamidoamine cascade polymers mediate efficient transfection of cells in culture. *Bioconjugate Chemistry* 4, 372-379 (1993).
34 Hosseinkhani, H., Azzam, T., Tabata, Y. & Domb, A. J. Dextran-spermine polycation: An efficient nonviral vector for in vitro and in vivo gene transfection. *Gene Therapy* 11, 194-203 (2004).
35 Erbacher, P., Zou, S., Bettinger, T., Steffan, A. M. & Remy, J. S. Chitosan-based vector/DNA complexes for gene delivery: Biophysical characteristics and transfection ability. *Pharmaceutical Research* 15, 1332-1339 (1998).
36 Balicki, D. & Beutler, E. Histone H2A significantly enhances in vitro DNA transfection. *Molecular Medicine* 3, 782-787 (1997).
37 Park, Y. J., Liang, J. F., Ko, K. S., Kim, S. W. & Yang, V. C. Low molecular weight protamine as an efficient and nontoxic gene carrier: In vitro study. *Journal of Gene Medicine* 5, 700-711 (2003).
38 Balicki, D., Putnam, C. D., Scaria, P. V. & Beutler, E. Structure and function correlation in histone H2A peptide-mediated gene transfer. *Proceedings of the National Academy of Sciences of the United States of America* 99, 7467-7471 (2002).
39 Sokolova, V. & Epple, M. Inorganic nanoparticles as carriers of nucleic acids into cells. *Angewandte Chemie - International Edition* 47, 1382-1395 (2008).
40 Davis, P. B. & Cooper, M. J. Vectors for airway gene delivery. *AAPS Journal* 9 (2007).
41 Cai, X., Conley, S. & Naash, M. Nanoparticle applications in ocular gene therapy. *Vision Research* 48, 319-324 (2008).
42 Peng, X. H. *et al.* Targeted magnetic iron oxide nanoparticles for tumor imaging and therapy. *International Journal of Nanomedicine* 3, 311-321 (2008).
43 Marshall, E. Gene therapy death prompts review of adenovirus vector. *Science* 286, 2244-2245 (1999).
44 Bragonzi, A. *et al.* Biodistribution and transgene expression with nonviral cationic vector/DNA complexes in the lungs. *Gene Therapy* 7, 1753-1760 (2000).
45 Ishiwata, H., Suzuki, N., Ando, S., Kikuchi, H. & Kitagawa, T. Characteristics and biodistribution of cationic liposomes and their DNA complexes. *Journal of Controlled Release* 69, 139-148 (2000).
46 Wolff, J. A. & Rozema, D. B. Breaking the bonds: Non-viral vectors become chemically dynamic. *Molecular Therapy* 16, 8-15 (2008).

47 Wiethoff, C. M., Smith, J. G., Koe, G. S. & Middaugh, C. R. The potential role of proteoglycans in cationic lipid-mediated gene delivery: Studies of the interaction of cationic lipid-DNA complexes with model glycosaminoglycans. *Journal of Biological Chemistry* 276, 32806-32813 (2001).

48 Li, S. *et al.* Dynamic changes in the characteristics of cationic lipidic vectors after exposure to mouse serum: Implications for intravenous lipofection. *Gene Therapy* 6, 585-594 (1999).

49 Simões, S. *et al.* Human serum albumin enhances DNA transfection by lipoplexes and confers resistance to inhibition by serum. *Biochimica et Biophysica Acta - Biomembranes* 1463, 459-469 (2000).

50 Wiethoff, C. M. & Middaugh, C. R. Barriers to nonviral gene delivery. *Journal of Pharmaceutical Sciences* 92, 203-217 (2003).

51 Pozzi, D. *et al.* Surface adsorption of protein corona controls the cell uptake mechanism in efficient cationic liposome/DNA complexes in serum. *Journal of controlled release : official journal of the Controlled Release Society* 148, e94-95 (2010).

52 Kawabata, K., Takakura, Y. & Hashida, M. The fate of plasmid DNA after intravenous injection in mice: Involvement of scavenger receptors in its hepatic uptake. *Pharmaceutical Research* 12, 825-830 (1995).

53 Mumper, R. J. *et al.* Polyvinyl derivatives as novel interactive polymers for controlled gene delivery to muscle. *Pharmaceutical Research* 13, 701-709 (1996).

54 Ha, Y., Jin, Y. & Xia, Y. The Characterization of Cationic Fusogenic Liposomes Mediated Antisense Oligonucleotides into HeLa Cells. *Drug Development and Industrial Pharmacy* 30, 135-141 (2004).

55 Kunisawa, J. *et al.* Fusogenic liposome delivers encapsulated nanoparticles for cytosolic controlled gene release. *Journal of Controlled Release* 105, 344-353 (2005).

56 Medina-Kauwe, L. K., Xie, J. & Hamm-Alvarez, S. Intracellular trafficking of nonviral vectors. *Gene Therapy* 12, 1734-1751 (2005).

57 Zhou, X. & Huang, L. DNA transfection mediated by cationic liposomes containing lipopolylysine: Characterization and mechanism of action. *Biochimica et Biophysica Acta - Biomembranes* 1189, 195-203 (1994).

58 Zabner, J., Fasbender, A. J., Moninger, T., Poellinger, K. A. & Welsh, M. J. Cellular and molecular barriers to gene transfer by a cationic lipid. *Journal of Biological Chemistry* 270, 18997-19007 (1995).

59 Mukherjee, S., Ghosh, R. N. & Maxfield, F. R. Endocytosis. *Physiological Reviews* 77, 759-803 (1997).

60 Kessner, S., Krause, A., Rothe, U. & Bendas, G. Investigation of the cellular uptake of E-Selectin-targeted immunoliposomes by activated human endothelial cells. *Biochimica et Biophysica Acta - Biomembranes* 1514, 177-190 (2001).

61 Huang, M., Khor, E. & Lim, L. Y. Uptake and Cytotoxicity of Chitosan Molecules and Nanoparticles: Effects of Molecular Weight and Degree of Deacetylation. *Pharmaceutical Research* 21, 344-353, doi:Cited By (since 1996) 183

Export Date 21 March 2012 (2004).

62 Ma, Z. & Lim, L. Y. Uptake of Chitosan and Associated Insulin in Caco-2 Cell Monolayers: A Comparison between Chitosan Molecules and Chitosan Nanoparticles. *Pharmaceutical Research* 20, 1812-1819, doi:Cited By (since 1996) 83

Export Date 21 March 2012 (2003).

63 GonçalvesGon, C. *et al.* Macropinocytosis of polyplexes and recycling of plasmid via the clathrin-dependent pathway impair the transfection efficiency of human hepatocarcinoma cells. *Molecular Therapy* 10, 373-385, doi:Cited By (since 1996) 62

Export Date 21 March 2012 (2004).

64 Rejman, J., Oberle, V., Zuhorn, I. S. & Hoekstra, D. Size-dependent internalization of particles via the pathways of clathrin-and caveolae-mediated endocytosis. *Biochemical Journal* 377, 159-169, doi:Cited By (since 1996) 539

Export Date 21 March 2012 (2004).

65 Rejman, J., Bragonzi, A. & Conese, M. Role of clathrin- and caveolae-mediated endocytosis in gene transfer mediated by lipo- and polyplexes. *Molecular Therapy* 12, 468-474 (2005).

66 Colin, M. *et al.* Cell delivery, intracellular trafficking and expression of an integrin-mediated gene transfer vector in tracheal epithelial cells. *Gene Therapy* 7, 139-152 (2000).

67 Huth, U., Wieschollek, A., Garini, Y., Schubert, R. & Peschka-Süss, R. Fourier Transformed Spectral Bio-imaging for Studying the Intracellular Fate of Liposomes. *Cytometry Part A* 57, 10-21, doi:Cited By (since 1996) 19

68 Zuhorn, I. S., Kalicharan, R. & Hoekstra, D. Lipoplex-mediated transfection of mammalian cells occurs through the cholesterol-dependent clathrin-mediated pathway of endocytosis. *Journal of Biological Chemistry* 277, 18021-18028, doi:Cited By (since 1996) 136

69 Bartlett, J. S., Wilcher, R. & Samulski, R. J. Infectious entry pathway of adeno-associated virus and adeno-associated virus vectors. *Journal of Virology* 74, 2777-2785, doi:Cited By (since 1996) 224

70 Daecke, J., Fackler, O. T., Dittmar, M. T. & Kräusslich, H. G. Involvement of clathrin-mediated endocytosis in human immunodeficiency virus type 1 entry. *Journal of Virology* 79, 1581-1594, doi:Cited By (since 1996) 80

71 Vendeville, A. *et al.* HIV-1 Tat Enters T Cells Using Coated Pits before Translocating from Acidified Endosomes and Eliciting Biological Responses. *Molecular Biology of the Cell* 15, 2347-2360, doi:Cited By (since 1996) 94

72 Chung, S. K. *et al.* Internalization and trafficking mechanisms of coxsackievirus B3 in HeLa cells. *Virology* 333, 31-40, doi:Cited By (since 1996) 23

73 Meertens, L., Bertaux, C. & Dragic, T. Hepatitis C virus entry requires a critical postinternalization step and delivery to early endosomes via clathrin-coated vesicles. *Journal of Virology* 80, 11571-11578 (2006).

74 Cooper, A. & Shaul, Y. Clathrin-mediated endocytosis and lysosomal cleavage of hepatitis B virus capsid-like core particles. *Journal of Biological Chemistry* 281, 16563-16569, doi:Cited By (since 1996) 19

75 Mo, Y. & Lim, L. Y. Mechanistic Study of the Uptake of Wheat Germ Agglutinin-Conjugated PLGA Nanoparticles by A549 Cells. *Journal of Pharmaceutical Sciences* 93, 20-28, doi:Cited By (since 1996) 29

76 Fittipaldi, A. *et al.* Cell Membrane Lipid Rafts Mediate Caveolar Endocytosis of HIV-1 Tat Fusion Proteins. *Journal of Biological Chemistry* 278, 34141-34149, doi:Cited By (since 1996) 226

77 Basner-Tschakarjan, E., Mirmohammadsadegh, A., Baer, A. & Hengge, U. R. Uptake and trafficking of DNA in keratinocytes: Evidence for DNA-binding proteins. *Gene Therapy* 11, 765-774, doi:Cited By (since 1996) 35

78 Qaddoumi, M. G. *et al.* Clathrin and caveolin-1 expression in primary pigmented rabbit conjunctival epithelial cells: Role in PLGA nanoparticle endocytosis. *Molecular Vision* 9, 559-568, doi:Cited By (since 1996) 59

79 Brisson, M., Tseng, W. C., Almonte, C., Watkins, S. & Huang, L. Subcellular trafficking of the cytoplasmic expression system. *Human Gene Therapy* 10, 2601-2613, doi:Cited By (since 1996) 43

80 Nakase, I. *et al.* Cellular uptake of arginine-rich peptides: Roles for macropinocytosis and actin rearrangement. *Molecular Therapy* 10, 1011-1022, doi:Cited By (since 1996) 256

81 Hinshaw, J. E. & Schmid, S. L. Dynamin self-assembles into rings suggesting a mechanism for coated vesicle budding. *Nature* 374, 190-192 (1995).

82 Schmid, S. L., McNiven, M. A. & Camilli, P. D. Dynamin and its partners: A progress report. *Current Opinion in Cell Biology* 10, 504-512 (1998).

83 Mousavi, S. A., Malerød, L., Berg, T. & Kjeken, R. Clathrin-dependent endocytosis. *Biochemical Journal* 377, 1-16 (2004).
84 Rothman, J. E. & Schmid, S. L. Enzymatic recycling of clathrin from coated vesicles. *Cell* 46, 5-9 (1986).
85 Conner, S. D. & Schmid, S. L. Regulated portals of entry into the cell. *Nature* 422, 37-44 (2003).
86 Sargiacomo, M. *et al.* Oligomeric structure of caveolin: Implications for caveolae membrane organization. *Proceedings of the National Academy of Sciences of the United States of America* 92, 9407-9411 (1995).
87 Monier, S. *et al.* VIP21-caveolin, a membrane protein constituent of the caveolar coat, oligomerizes in vivo and in vitro. *Molecular Biology of the Cell* 6, 911-927 (1995).
88 Schnitzer, J. E. Caveolae: From basic trafficking mechanisms to targeting transcytosis for tissue-specific drug and gene delivery in vivo. *Advanced Drug Delivery Reviews* 49, 265-280 (2001).
89 Oh, P., McIntosh, D. P. & Schnitzer, J. E. Dynamin at the neck of caveolae mediates their budding to form transport vesicles by GTP-driven fission from the plasma membrane of endothelium. *Journal of Cell Biology* 141, 101-114 (1998).
90 Lewis, W. H. Pinocytosis. *Johns Hopkins Hosp. Bull.* 49, 17-27, doi:Cited By (since 1996) 29
91 Lim, J. P. & Gleeson, P. A. Macropinocytosis: An endocytic pathway for internalising large gulps. *Immunology and Cell Biology* 89, 836-843 (2011).
92 Hewlett, L. J., Prescott, A. R. & Watts, C. The coated pit and macropinocytic pathways serve distinct endosome populations. *Journal of Cell Biology* 124, 689-703 (1994).
93 Swanson, J. A. & Watts, C. Macropinocytosis. *Trends in Cell Biology* 5, 424-428 (1995).
94 Prabha, S., Zhou, W. Z., Panyam, J. & Labhasetwar, V. Size-dependency of nanoparticle-mediated gene transfection: Studies with fractionated nanoparticles. *International Journal of Pharmaceutics* 244, 105-115 (2002).
95 Davda, J. & Labhasetwar, V. Characterization of nanoparticle uptake by endothelial cells. *International Journal of Pharmaceutics* 233, 51-59 (2002).
96 Popielarski, S. R., Hu-Lieskovan, S., French, S. W., Triche, T. J. & Davis, M. E. A nanoparticle-based model delivery system to guide the rational design of gene delivery to the liver. 2. In vitro and in vivo uptake results. *Bioconjugate Chemistry* 16, 1071-1080 (2005).
97 Simões, S., Pires, P., Düzgünes, N. & Pedroso De Lima, M. C. Cationic liposomes as gene transfer vectors: Barriers to successful application in gene therapy. *Current Opinion in Molecular Therapeutics* 1, 147-157 (1999).
98 Harush-Frenkel, O., Debotton, N., Benita, S. & Altschuler, Y. Targeting of nanoparticles to the clathrin-mediated endocytic pathway. *Biochemical and Biophysical Research Communications* 353, 26-32 (2007).
99 Farrell, L. L. *et al.* A comparison of the effectiveness of cationic polymers poly-l-lysine (PLL) and polyethylenimine (PEI) for non-viral delivery of plasmid DNA to bone marrow stromal cells (BMSC). *European Journal of Pharmaceutics and Biopharmaceutics* 65, 388-397 (2007).
100 Mishra, S., Webster, P. & Davis, M. E. PEGylation significantly affects cellular uptake and intracellular trafficking of non-viral gene delivery particles. *European Journal of Cell Biology* 83, 97-111 (2004).
101 Douglas, K. L., Piccirillo, C. A. & Tabrizian, M. Effects of alginate inclusion on the vector properties of chitosan-based nanoparticles. *Journal of Controlled Release* 115, 354-361 (2006).
102 Shimizu, N., Kamezaki, F. & Shigematsu, S. Tracking of microinjected DNA in live cells reveals the intracellular behavior and elimination of extrachromosomal genetic material. *Nucleic Acids Research* 33, 6296-6307 (2005).
103 Liu, F. *et al.* Mechanism of in vivo DNA transport into cells by electroporation: Electrophoresis across the plasma membrane may not be involved. *Journal of Gene Medicine* 8, 353-361 (2006).
104 Pathak, A., Patnaik, S. & Gupta, K. C. Recent trends in non-viral vector-mediated gene delivery. *Biotechnology Journal* 4, 1559-1572 (2009).
105 Feng, M., Lee, D. & Li, P. Intracellular uptake and release of poly(ethyleneimine)-co-poly(methyl methacrylate) nanoparticle/pDNA complexes for gene delivery. *International Journal of Pharmaceutics* 311, 209-214 (2006).

106 Itaka, K. *et al.* In situ single cell observation by fluorescence resonance energy transfer reveals fast intra-cytoplasmic delivery and easy release of plasmid DNA complexed with linear polyethylenimine. *Journal of Gene Medicine* 6, 76-84 (2004).

107 Panyam, J., Zhou, W. Z., Prabha, S., Sahoo, S. K. & Labhasetwar, V. Rapid endo-lysosomal escape of poly(DL-lactide-co-glycolide) nanoparticles: Implications for drug and gene delivery. *FASEB Journal* 16, 1217-1226 (2002).

108 Lechardeur, D., Verkman, A. S. & Lukacs, G. L. Intracellular routing of plasmid DNA during non-viral gene transfer. *Advanced Drug Delivery Reviews* 57, 755-767 (2005).

109 Zelphati, O. & Szoka Jr, F. C. Mechanism of oligonucleotide release from cationic liposomes. *Proceedings of the National Academy of Sciences of the United States of America* 93, 11493-11498 (1996).

110 Rao, N. M. & Gopal, V. Cell biological and biophysical aspects of lipid-mediated gene delivery. *Bioscience Reports* 26, 301-324 (2006).

111 Hafez, I. M., Maurer, N. & Cullis, P. R. On the mechanism whereby cationic lipids promote intracellular delivery of polynucleic acids. *Gene Therapy* 8, 1188-1196 (2001).

112 Bhattacharya, S. & Mandal, S. S. Evidence of interlipidic ion-pairing in anion-induced DNA release from cationic amphiphile-DNA complexes. Mechanistic implications in transfection. *Biochemistry* 37, 7764-7777 (1998).

113 Lewis, R. N. A. H. & McElhaney, R. N. Surface charge markedly attenuates the nonlamellar phase-forming propensities of lipid bilayer membranes: Calorimetric and 31P-nuclear magnetic resonance studies of mixtures of cationic, anionic, and zwitterionic lipids. *Biophysical Journal* 79, 1455-1464 (2000).

114 Tarahovsky, Y. S., Koynova, R. & MacDonald, R. C. DNA release from lipoplexes by anionic lipids: Correlation with lipid mesomorphism, interfacial curvature, and membrane fusion. *Biophysical Journal* 87, 1054-1064 (2004).

115 Tarahovsky, Y. S., Arsenault, A. L., MacDonald, R. C., McIntosh, T. J. & Epand, R. M. Electrostatic control of phospholipid polymorphism. *Biophysical Journal* 79, 3193-3200 (2000).

116 De Kruijff, B. Lipid polymorphism and biomembrane function. *Current Opinion in Chemical Biology* 1, 564-569 (1997).

117 Zuhorn, I. S. *et al.* Nonbilayer phase of lipoplex-membrane mixture determines endosomal escape of genetic cargo and transfection efficiency. *Molecular Therapy* 11, 801-810 (2005).

118 Koynova, R., Wang, L., Tarahovsky, Y. & MacDonald, R. C. Lipid phase control of DNA delivery. *Bioconjugate Chemistry* 16, 1335-1339 (2005).

119 Ewert, K. K. *et al.* A columnar phase of dendritic lipid-based cationic liposome-DNA complexes for gene delivery: Hexagonally ordered cylindrical micelles embedded in a DNA honeycomb lattice. *Journal of the American Chemical Society* 128, 3998-4006 (2006).

120 Kichler, A., Leborgne, C., Coeytaux, E. & Danos, O. Polyethylenimine-mediated gene delivery: A mechanistic study. *Journal of Gene Medicine* 3, 135-144 (2001).

121 Urade, R., Hayashi, Y. & Kito, M. Endosomes differ from plasma membranes in the phospholipid molecular species composition. *Biochimica et Biophysica Acta - Biomembranes* 946, 151-163 (1988).

122 Bailey, A. L. & Cullis, P. R. Membrane fusion with cationic liposomes: Effects of target membrane lipid composition. *Biochemistry* 36, 1628-1634 (1997).

123 Pollard, H. *et al.* Polyethylenimine but not cationic lipids promotes transgene delivery to the nucleus in mammalian cells. *Journal of Biological Chemistry* 273, 7507-7511 (1998).

124 Tros de Ilarduya, C., Sun, Y. & Düzgüneş, N. Gene delivery by lipoplexes and polyplexes. *European Journal of Pharmaceutical Sciences* 40, 159-170 (2010).

125 Varkouhi, A. K., Scholte, M., Storm, G. & Haisma, H. J. Endosomal escape pathways for delivery of biologicals. *Journal of Controlled Release* 151, 220-228 (2011).

126 Sonawane, N. D., Szoka Jr, F. C. & Verkman, A. S. Chloride Accumulation and Swelling in Endosomes Enhances DNA Transfer by Polyamine-DNA Polyplexes. *Journal of Biological Chemistry* 278, 44826-44831 (2003).

127 Thomas, M. & Klibanov, A. M. Enhancing polyethylenimine's delivery of plasmid DNA into mammalian cells. *Proceedings of the National Academy of Sciences of the United States of America* 99, 14640-14645 (2002).
128 Cho, Y. W., Kim, J. D. & Park, K. Polycation gene delivery systems: Escape from endosomes to cytosol. *Journal of Pharmacy and Pharmacology* 55, 721-734 (2003).
129 Colin, M., Renaut, L., Mailly, L. & D'Halluin, J. C. Factors involved in the sensitivity of different hematopoietic cell lines to infection by subgroup C adenovirus: Implication for gene therapy of human lymphocytic malignancies. *Virology* 320, 23-39 (2004).
130 Pollard, H. *et al.* Ca2+-sensitive cytosolic nucleases prevent efficient delivery to the nucleus of injected plasmids. *Journal of Gene Medicine* 3, 153-164 (2001).
131 Lechardeur, D. *et al.* Metabolic instability of plasmid DNA in the cytosol: A potential barrier to gene transfer. *Gene Therapy* 6, 482-497 (1999).
132 Pampinella, F. *et al.* Analysis of differential lipofection efficiency in primary and established myoblasts. *Molecular Therapy* 5, 161-169 (2002).
133 Peitsch, M. C., Mannherz, H. G. & Tschopp, J. The apoptosis endonucleases: Cleaning up after cell death? *Trends in Cell Biology* 4, 37-41 (1994).
134 Torriglia, A. *et al.* L-DNase II, a molecule that links proteases and endonucleases in apoptosis, derives from the ubiquitous serpin leukocyte elastase inhibitor. *Molecular and Cellular Biology* 18, 3612-3619 (1998).
135 Vanderbilt, J. N., Bloom, K. S. & Anderson, J. N. Endogenous nuclease. Properties and effects on transcribed genes in chromatin. *Journal of Biological Chemistry* 257, 13009-13017 (1982).
136 Walker, P. R., Leblanc, J., Smith, B., Pandey, S. & Sikorska, M. Detection of DNA fragmentation and endonucleases in apoptosis. *Methods: A Companion to Methods in Enzymology* 17, 329-338 (1999).
137 Sasaki, A. & Kinjo, M. Monitoring intracellular degradation of exogenous DNA using diffusion properties. *Journal of Controlled Release* 143, 104-111 (2010).
138 Barry, M. A. & Eastman, A. Identification of deoxyribonuclease II as an endonuclease involved in apoptosis. *Archives of Biochemistry and Biophysics* 300, 440-450 (1993).
139 Polzar, B., Peitsch, M. C., Loos, R., Tschopp, J. & Mannherz, H. G. Overexpression of deoxyribonuclease I (DNase I) transfected into COS-cells: Its distribution during apoptotic cell death. *European Journal of Cell Biology* 62, 397-405 (1993).
140 Lukacs, G. L. *et al.* Size-dependent DNA mobility in cytoplasm and nucleus. *Journal of Biological Chemistry* 275, 1625-1629 (2000).
141 Drake, D. M. & Pack, D. W. Biochemical investigation of active intracellular transport of polymeric gene-delivery vectors. *Journal of Pharmaceutical Sciences* 97, 1399-1413 (2008).
142 de Bruin, K. *et al.* Cellular dynamics of EGF receptor-targeted synthetic viruses. *Molecular Therapy* 15, 1297-1305 (2007).
143 Coppola, S. *et al.* The role of cytoskeleton networks on lipid-mediated delivery of DNA. *Therapeutic Delivery* 4, 191-202 (2013).
144 Bukrinskaya, A., Brichacek, B., Mann, A. & Stevenson, M. Establishment of a functional human immunodeficiency virus type 1 (HIV- 1) reverse transcription complex involves the cytoskeleton. *Journal of Experimental Medicine* 188, 2113-2125 (1998).
145 Komano, J., Miyauchi, K., Matsuda, Z. & Yamamoto, N. Inhibiting the Arp2/3 complex limits infection of both intracellular mature vaccinia virus and primate lentiviruses. *Molecular Biology of the Cell* 15, 5197-5207 (2004).
146 Iyengar, S., Hildreth, J. E. K. & Schwartz, D. H. Actin-dependent receptor colocalization required for human immunodeficiency virus entry into host cells. *Journal of Virology* 72, 5251-5255 (1998).
147 McDonald, D. *et al.* Visualization of the intracellular behavior of HIV in living cells. *Journal of Cell Biology* 159, 441-452 (2002).
148 Sodeik, B., Ebersold, M. W. & Helenius, A. Microtubule-mediated transport of incoming herpes simplex virus 1 capsids to the nucleus. *Journal of Cell Biology* 136, 1007-1021 (1997).
149 Ogawa-Goto, K. *et al.* Microtubule network facilitates nuclear targeting of human cytomegalovirus capsid. *Journal of Virology* 77, 8541-8547 (2003).

150 Suomalainen, M. *et al.* Microtubule-dependent plus- and minus end-directed motilities are competing processes for nuclear targeting of adenovirus. *Journal of Cell Biology* 144, 657-672 (1999).
151 Suikkanen, S. *et al.* Exploitation of microtubule cytoskeleton and dynein during parvoviral traffic toward the nucleus. *Journal of Virology* 77, 10270-10279 (2003).
152 Pelkmans, L., Kartenbeck, J. & Helenius, A. Caveolar endocytosis of simian virus 40 reveals a new two-step vesicular-transport pathway to the ER. *Nature Cell Biology* 3, 473-483 (2001).
153 Döhner, K., Nagel, C. H. & Sodeik, B. Viral stop-and-go along microtubules: Taking a ride with dynein and kinesins. *Trends in Microbiology* 13, 320-327 (2005).
154 Capecchi, M. R. High efficiency transformation by direct microinjection of DNA into cultured mammalian cells. *Cell* 22, 479-488 (1980).
155 Bieber, T., Meissner, W., Kostin, S., Niemann, A. & Elsasser, H. P. Intracellular route and transcriptional competence of polyethylenimine-DNA complexes. *Journal of Controlled Release* 82, 441-454 (2002).
156 Holmes, A. R., Dohrman, A. F., Ellison, A. R., Goncz, K. K. & Gruenert, D. C. Intracellular compartmentalization of DNA fragments in cultured airway epithelial cells mediated by cationic lipids. *Pharmaceutical Research* 16, 1020-1025 (1999).
157 Ishii, T., Okahata, Y. & Sato, T. Mechanism of cell transfection with plasmid/chitosan complexes. *Biochimica et Biophysica Acta - Biomembranes* 1514, 51-64 (2001).
158 de Semir, D. *et al.* Non-viral vector-mediated uptake, distribution, and stability of chimeraplasts in human airway epithelial cells. *Journal of Gene Medicine* 4, 308-322 (2002).
159 Leonetti, J. P., Mechti, N., Degols, G., Gagnor, C. & Lebleu, B. Intracellular distribution of microinjected antisense oligonucleotides. *Proceedings of the National Academy of Sciences of the United States of America* 88, 2702-2706 (1991).
160 Brunner, S. *et al.* Cell cycle dependence of gene transfer by lipoplex polyplex and recombinant adenovirus. *Gene Therapy* 7, 401-407 (2000).
161 Mortimer, I. *et al.* Cationic lipid-mediated transfection of cells in culture requires mitotic activity. *Gene Therapy* 6, 403-411 (1999).
162 Elouahabi, A. & Ruysschaert, J. M. Formation and intracellular trafficking of lipoplexes and polyplexes. *Molecular Therapy* 11, 336-347 (2005).
163 Brunner, S., Fürtbauer, E., Sauer, T., Kursa, M. & Wagner, E. Overcoming the nuclear barrier: Cell cycle independent nonviral gene transfer with linear polyethylenimine or electroporation. *Molecular Therapy* 5, 80-86 (2002).
164 Grosse, S., Thévenot, G., Monsigny, M. & Fajac, I. Which mechanism for nuclear import of plasmid DNA complexed with polyethylenimine derivatives? *Journal of Gene Medicine* 8, 845-851 (2006).
165 Dabauvalle, M. C., Schulz, B., Scheer, U. & Peters, R. Inhibition of nuclear accumulation of karyophilic proteins in living cells by microinjection of the lectin wheat germ agglutinin. *Experimental Cell Research* 174, 291-296 (1988).
166 Dowty, M. E., Williams, P., Zhang, G., Hagstrom, J. E. & Wolff, J. A. Plasmid DNA entry into postmitotic nuclei of primary rat myotubes. *Proceedings of the National Academy of Sciences of the United States of America* 92, 4572-4576 (1995).
167 Brisson, M. & Huang, L. Liposomes: Conquering the nuclear barrier. *Current Opinion in Molecular Therapeutics* 1, 140-146 (1999).
168 Hinshaw, J. E., Carragher, B. O. & Milligan, R. A. Architecture and design of the nuclear pore complex. *Cell* 69, 1133-1141 (1992).
169 Akey, C. W. & Radermacher, M. Architecture of the Xenopus nuclear pore complex revealed by three-dimensional cryo-electron microscopy. *Journal of Cell Biology* 122, 1-19 (1993).
170 Goldberg, M. W. & Allen, T. D. The nuclear pore complex and lamina: Three-dimensional structures and interactions determined by field emission in-lens scanning electron microscopy. *Journal of Molecular Biology* 257, 848-865 (1996).

171 Cordes, V. C., Reidenbach, S., Rackwitz, H. R. & Franke, W. W. Identification of protein p270/Tpr as a constitutive component of the nuclear pore complex-attached intranuclear filaments. *Journal of Cell Biology* 136, 515-529 (1997).
172 Fahrenkrog, B. & Aebi, U. The nuclear pore complex: Nucleocytoplasmic transport and beyond. *Nature Reviews Molecular Cell Biology* 4, 757-766 (2003).
173 Talcott, B. & Moore, M. S. Getting across the nuclear pore complex. *Trends in Cell Biology* 9, 312-318 (1999).
174 Harel, A. & Forbes, D. J. Welcome to the nucleus: CAN I take your coat? *Nature Cell Biology* 3, E267-E269 (2001).
175 Kuersten, S., Ohno, M. & Mattaj, I. W. Nucleocytoplasmic transport: Ran, beta and beyond. *Trends in Cell Biology* 11, 497-503 (2001).
176 Imamoto, N. Diversity in nucleocytoplasmic transport pathways. *Cell Structure and Function* 25, 207-216 (2000).
177 Conti, E. & Izaurralde, E. Nucleocytoplasmic transport enters the atomic age. *Current Opinion in Cell Biology* 13, 310-319 (2001).
178 Greber, U. F. *et al.* The role of the nuclear pore complex in adenovirus DNA entry. *EMBO Journal* 16, 5998-6007 (1997).
179 Lechardeur, D. & Lukacs, G. L. Nucleocytoplasmic transport of plasmid DNA: A perilous journey from the cytoplasm to the nucleus. *Human Gene Therapy* 17, 882-889 (2006).
180 Ghosh, Y. K., Visweswariah, S. S. & Bhattacharya, S. Nature of linkage between the cationic headgroup and cholesteryl skeleton controls gene transfection efficiency. *FEBS Letters* 473, 341-344 (2000).
181 Wolff, J. A. & Budker, V. The mechanism of naked DNA uptake and expression. *Advances in genetics* 54, 3-20 (2005).
182 Ferrari, M. E., Nguyen, C. M., Zelphati, O., Tsai, Y. & Felgner, P. L. Analytical methods for the characterization of cationic lipid-nucleic acid complexes. *Human Gene Therapy* 9, 341-351 (1998).
183 Murray, K. D. *et al.* Enhanced cationic liposome-mediated transfection using the DNA-binding peptide μ (mu) from the adenovirus core. *Gene Therapy* 8, 453-460 (2001).
184 Dean, D. A., Strong, D. D. & Zimmer, W. E. Nuclear entry of nonviral vectors. *Gene Therapy* 12, 881-890 (2005).
185 Hama, S. *et al.* Quantitative comparison of intracellular trafficking and nuclear transcription between adenoviral and lipoplex systems. *Molecular Therapy* 13, 786-794 (2006).
186 Ding, W., Zhang, L., Yan, Z. & Engelhardt, J. F. Intracellular trafficking of adeno-associated viral vectors. *Gene Therapy* 12, 873-880 (2005).
187 Roe, T., Reynolds, T. C., Yu, G. & Brown, P. O. Integration of murine leukemia virus DNA depends on mitosis. *EMBO Journal* 12, 2099-2108 (1993).
188 Lewis, P. F. & Emerman, M. Passage through mitosis is required for oncoretroviruses but not for the human immunodeficiency virus. *Journal of Virology* 68, 510-516 (1994).
189 Anderson, J. L. & Hope, T. J. Intracellular trafficking of retroviral vectors: Obstacles and advances. *Gene Therapy* 12, 1667-1678 (2005).
190 Dvorin, J. D. & Malim, M. H. Vol. 281 179-208 (2003).
191 Zennou, V. *et al.* HIV-1 genome nuclear import is mediated by a central DNA flap. *Cell* 101, 173-185 (2000).
192 Yamashita, M. & Emerman, M. Capsid is a dominant determinant of retrovirus infectivity in nondividing cells. *Journal of Virology* 78, 5670-5678 (2004).
193 Fassati, A., Görlich, D., Harrison, I., Zaytseva, L. & Mingot, J. M. Nuclear import of HIV-1 intracellular reverse transcription complexes is mediated by importin 7. *EMBO Journal* 22, 3675-3685 (2003).
194 Ebina, H., Aoki, J., Hatta, S., Yoshida, T. & Koyanagi, Y. Role of Nup98 in nuclear entry of human immunodeficiency virus type 1 cDNA. *Microbes and Infection* 6, 715-724 (2004).
195 Dundr, M. & Misteli, T. Functional architecture in the cell nucleus. *Biochemical Journal* 356, 297-310 (2001).

196 Lanctôt, C., Cheutin, T., Cremer, M., Cavalli, G. & Cremer, T. Dynamic genome architecture in the nuclear space: Regulation of gene expression in three dimensions. *Nature Reviews Genetics* 8, 104-115 (2007).
197 Takizawa, T. & Meshorer, E. Chromatin and nuclear architecture in the nervous system. *Trends in Neurosciences* 31, 343-352 (2008).
198 Ching, R. W., Dellaire, G., Eskiw, C. H. & Bazett-Jones, D. P. PML bodies: A meeting place for genomic loci? *Journal of Cell Science* 118, 847-854 (2005).
199 Phair, R. D. & Misteli, T. High mobility of proteins in the mammalian cell nucleus. *Nature* 404, 604-609 (2000).
200 Cremer, T., Cremer, C. & Schneider, T. Analysis of chromosome positions in the interphase nucleus of Chinese hamster cells by laser-UV-microirradiation experiments. *Human Genetics* 62, 201-209 (1982).
201 Misteli, T. Concepts in nuclear architecture. *BioEssays* 27, 477-487 (2005).
202 Huang, M., Fong, C. W., Khor, E. & Lim, L. Y. Transfection efficiency of chitosan vectors: Effect of polymer molecular weight and degree of deacetylation. *Journal of Controlled Release* 106, 391-406 (2005).
203 Ahmad, A. *et al.* New multivalent cationic lipids reveal bell curve for transfection efficiency versus membrane charge density: Lipid - DNA complexes for gene delivery. *Journal of Gene Medicine* 7, 739-748 (2005).
204 Saito, Y., Kawakami, S., Yabe, Y., Yamashita, F. & Hashida, M. Intracellular trafficking is the important process that determines the optimal charge ratio on transfection by galactosylated lipoplex in HepG2 cells. *Biological and Pharmaceutical Bulletin* 29, 1986-1990 (2006).
205 Cornelis, S., Vandenbranden, M., Ruysschaert, J. M. & Elouahabi, A. Role of intracellular cationic liposome-DNA complex dissociation in transfection mediated by cationic lipids. *DNA and Cell Biology* 21, 91-97 (2002).
206 Bertschinger, M. *et al.* Disassembly of polyethylenimine-DNA particles in vitro: Implications for polyethylenimine-mediated DNA delivery. *Journal of Controlled Release* 116, 96-104 (2006).
207 Mearini, G., Nielsen, P. E. & Fackelmayer, F. O. Localization and dynamics of small circular DNA in live mammalian nuclei. *Nucleic acids research* 32, 2642-2651 (2004).
208 Clamme, J. P., Krishnamoorthy, G. & Mély, Y. Intracellular dynamics of the gene delivery vehicle polyethylenimine during transfection: Investigation by two-photon fluorescence correlation spectroscopy. *Biochimica et Biophysica Acta - Biomembranes* 1617, 52-61 (2003).
209 Dean, D. A. Import of plasmid DNA into the nucleus is sequence specific. *Experimental Cell Research* 230, 293-302 (1997).
210 Everett, R. D. The Spatial Organization of DNA Virus Genomes in the Nucleus. *PLoS Pathogens* 9 (2013).
211 Silva, L., Cliffe, A., Chang, L. & Knipe, D. M. Role for A-type lamins in herpesviral DNA targeting and heterochromatin modulation. *PLoS Pathogens* 4 (2008).
212 Everett, R. D. & Murray, J. ND10 components relocate to sites associated with herpes simplex virus type 1 nucleoprotein complexes during virus infection. *Journal of Virology* 79, 5078-5089 (2005).
213 Gasiorowski, J. Z. & Dean, D. A. Postmitotic nuclear retention of episomal plasmids Is altered by DNA labeling and detection methods. *Molecular Therapy* 12, 460-467 (2005).
214 Plautz, S. A., Boanca, G., Riethoven, J. J. M. & Pannier, A. K. Microarray analysis of gene expression profiles in cells transfected with nonviral vectors. *Molecular Therapy* 19, 2144-2151 (2011).
215 Bos, J. L., De Rooij, J. & Reedquist, K. A. Rap1 signalling: Adhering to new models. *Nature Reviews Molecular Cell Biology* 2, 369-377 (2001).
216 Bengali, Z. *et al.* Gene delivery through cell culture substrate adsorbed DNA complexes. *Biotechnology and Bioengineering* 90, 290-302 (2005).
217 Bengali, Z., Rea, J. C., Gibly, R. F. & Shea, L. D. Efficacy of immobilized polyplexes and lipoplexes for substrate-mediated gene delivery. *Biotechnology and Bioengineering* 102, 1679-1691 (2009).
218 Pannier, A. K. & Shea, L. D. Controlled release systems for DNA delivery. *Molecular Therapy* 10, 19-26 (2004).

219 Noonan, E. J., Place, R. F., Giardina, C. & Hightower, L. E. Hsp70B′ regulation and function. *Cell Stress and Chaperones* 12, 219-229 (2007).
220 Leung, T. K. C., Rajendran, M. Y., Monfries, C., Hall, C. & Lim, L. The human heat-shock protein family: expression of a novel heat-inducible HSP70 (HSP70B') and isolation of its cDNA and genomic DNA. *Biochemical Journal* 267, 125-132 (1990).
221 Noonan, E., Giardina, C. & Hightower, L. Hsp70B′ and Hsp72 form a complex in stressed human colon cells and each contributes to cytoprotection. *Experimental Cell Research* 314, 2468-2476 (2008).
222 Cheng, X., Belshan, M. & Ratner, L. Hsp40 facilitates nuclear import of the human immunodeficiency virus type 2 Vpx-mediated preintegration complex. *Journal of Virology* 82, 1229-1237 (2008).
223 Lu, D., Chen, J. & Hai, T. The regulation of ATF3 gene expression by mitogen-activated protein kinases. *Biochemical Journal* 401, 559-567 (2007).
224 Reits, E. A. J. & Neefjes, J. J. From fixed to FRAP: Measuring protein mobility and activity in living cells. *Nature Cell Biology* 3, E145-E147 (2001).
225 Digman, M. A. *et al.* Measuring fast dynamics in solutions and cells with a laser scanning microscope. *Biophysical Journal* 89, 1317-1327 (2005).
226 Di Rienzo, C., Gratton, E., Beltram, F. & Cardarelli, F. Fast spatiotemporal correlation spectroscopy to determine protein lateral diffusion laws in live cell membranes. *Proceedings of the National Academy of Sciences of the United States of America* 110, 12307-12312 (2013).
227 Rossow, M. J., Sasaki, J. M., Digman, M. A. & Gratton, E. Raster image correlation spectroscopy in live cells. *Nature Protocols* 5, 1761-1774 (2010).
228 Digman, M. A. & Gratton, E. Analysis of diffusion and binding in cells using the RICS approach. *Microscopy Research and Technique* 72, 323-332 (2009).
229 Digman, M. A. in *5th LFD Workshop in Advanced Fluorescence Imaging and Dynamics.*
230 Levi, V. & Gratton, E. Exploring dynamics in living cells by tracking single particles. *Cell Biochemistry and Biophysics* 48, 1-15 (2007).
231 Godinez, W. J. *et al.* Deterministic and probabilistic approaches for tracking virus particles in time-lapse fluorescence microscopy image sequences. *Medical Image Analysis* 13, 325-342 (2009).
232 Sbalzarini, I. F. & Koumoutsakos, P. Feature point tracking and trajectory analysis for video imaging in cell biology. *Journal of Structural Biology* 151, 182-195 (2005).
233 Levi, V. & Gratton, E. Chromatin dynamics during interphase explored by single-particle tracking. *Chromosome Research* 16, 439-449 (2008).
234 Lam, A. P. & Dean, D. A. Progress and prospects: Nuclear import of nonviral vectors. *Gene Therapy* 17, 439-447 (2010).
235 Neves, C., Escriou, V., Byk, G., Scherman, D. & Wils, P. Intracellular fate and nuclear targeting of plasmid DNA. *Cell Biology and Toxicology* 15, 193-202 (1999).
236 Munkonge, F. M. *et al.* Identification and functional characterization of cytoplasmic determinants of plasmid DNA nuclear import. *Journal of Biological Chemistry* 284, 26978-26987 (2009).
237 Ruthardt, N. & Bräuchle, C. Vol. 296 283-304 (2010).
238 Robertson, R. M., Laib, S. & Smith, D. E. Diffusion of isolated DNA molecules: Dependence on length and topology. *Proceedings of the National Academy of Sciences of the United States of America* 103, 7310-7314 (2006).
239 Suh, J., Wirtz, D. & Hanes, J. Efficient active transport of gene nanocarriers to the cell nucleus. *Proceedings of the National Academy of Sciences of the United States of America* 100, 3878-3882 (2003).
240 Suh, J., Wirtz, D. & Hanes, J. Real-time intracellular transport of gene nanocarriers studied by multiple particle tracking. *Biotechnology Progress* 20, 598-602 (2004).
241 Balint, S., Vilanova, I. V., Ålvarez, Å. S. & Lakadamyali, M. Correlative live-cell and superresolution microscopy reveals cargo transport dynamics at microtubule intersections. *Proceedings of the National Academy of Sciences of the United States of America* 110, 3375-3380 (2013).
242 King, S. J. & Schroer, T. A. Dynactin increases the processivity of the cytoplasmic dynein motor. *Nature Cell Biology* 2, 20-24 (2000).

243 Lakadamyali, M., Rust, M. J., Babcock, H. P. & Zhuang, X. Visualizing infection of individual influenza viruses. *Proceedings of the National Academy of Sciences of the United States of America* 100, 9280-9285 (2003).
244 Clarke, M., Köhler, J., Heuser, J. & Gerisch, G. Endosome fusion and microtubule-based dynamics in the early endocytic pathway of dictyostelium. *Traffic* 3, 791-800 (2002).
245 King, S. J., Brown, C. L., Maier, K. C., Quintyne, N. J. & Schroer, T. A. Analysis of the Dynein-Dynactin Interaction in Vitro and in Vivo. *Molecular Biology of the Cell* 14, 5089-5097 (2003).
246 Politz, J. C., Browne, E. S., Wolf, D. E. & Pederson, T. Intranuclear diffusion and hybridization state of oligonucleotides measured by fluorescence correlation spectroscopy in living cells. *Proceedings of the National Academy of Sciences of the United States of America* 95, 6043-6048 (1998).
247 Politz, J. C., Tuft, R. A., Pederson, T. & Singer, R. H. Movement of nuclear poly(A) RNA throughout the interchromatin space in living cells. *Current Biology* 9, 285-291 (1999).
248 Kaur, G. *et al.* Probing transcription factor diffusion dynamics in the living mammalian embryo with photoactivatable fluorescence correlation spectroscopy. *Nature Communications* 4 (2013).
249 Hinde, E. *et al.* The impact of mitotic versus interphase chromatin architecture on the molecular flow of EGFP by pair correlation analysis. *Biophysical Journal* 100, 1829-1836 (2011).
250 Ossato, G., Digman, M. A., Lukacsovich, T., Marsh, J. L. & Gratton, E. N&B and cross-N&B analysis detect oligomerization of Huntingtin in live cells. *Biophysical Journal* 98, 3387-Pos (2010).
251 Chiti, F. & Dobson, C. M. Vol. 75 333-366 (2006).
252 Mao, H. Q. *et al.* Chitosan-DNA nanoparticles as gene carriers: Synthesis, characterization and transfection efficiency. *Journal of Controlled Release* 70, 399-421 (2001).
253 Dalal, R. B., Digman, M. A., Horwitz, A. F., Vetri, V. & Gratton, E. Determination of particle number and brightness using a laser scanning confocal microscope operating in the analog mode. *Microscopy Research and Technique* 71, 69-81 (2008).
254 Qian, H. & Elson, E. L. Distribution of molecular aggregation by analysis of fluctuation moments. *Proceedings of the National Academy of Sciences of the United States of America* 87, 5479-5483 (1990).
255 James, Nicholas G. *et al.* Number and Brightness Analysis of LRRK2 Oligomerization in Live Cells. *Biophysical Journal* 102, L41-L43, doi:10.1016/j.bpj.2012.04.046 (2012).
256 Adu-Gyamfi, E., Digman, Michelle A., Gratton, E. & Stahelin, Robert V. Investigation of Ebola VP40 Assembly and Oligomerization in Live Cells Using Number and Brightness Analysis. *Biophysical Journal* 102, 2517-2525, doi:10.1016/j.bpj.2012.04.022 (2012).
257 Sharma, V. K., Thomas, M. & Klibanov, A. M. Mechanistic studies on aggregation of polyethylenimine-DNA complexes and its prevention. *Biotechnology and Bioengineering* 90, 614-620 (2005).
258 Sun, C., Tang, T. & Uluda«ß, H. Molecular dynamics simulations of PEI mediated DNA aggregation. *Biomacromolecules* 12, 3698-3707 (2011).
259 Marty, R. *et al.* Structural analysis of DNA complexation with cationic lipids. *Nucleic acids research* 37, 849-857 (2009).
260 Escriou, V., Ciolina, C., Helbling-Leclerc, A., Wils, P. & Scherman, D. Cationic lipid-mediated gene transfer: Analysis of cellular uptake and nuclear import of plasmid DNA. *Cell Biology and Toxicology* 14, 95-104 (1998).
261 Friend, D. S., Papahadjopoulos, D. & Debs, R. J. Endocytosis and intracellular processing accompanying transfection mediated by cationic liposomes. *Biochimica et Biophysica Acta - Biomembranes* 1278, 41-50 (1996).
262 Patil, S. D., Rhodes, D. G. & Burgess, D. J. DNA-based therapeutics and DNA delivery systems: A comprehensive review. *AAPS Journal* 7, E61-E77 (2005).
263 Hui, S. W. *et al.* The role of helper lipids in cationic liposome-mediated gene transfer. *Biophysical Journal* 71, 590-599 (1996).
264 Fumoto, S. *et al.* Enhanced hepatocyte-selective in vivo gene expression by stabilized galactosylated liposome/plasmid DNA complex using sodium chloride for complex formation. *Molecular Therapy* 10, 719-729 (2004).
265 Ross, P. C. & Hui, S. W. Lipoplex size is a major determinant of in vitro lipofection efficiency. *Gene Therapy* 6, 651-659 (1999).

266 Srinivasan, C., Siddiqui, S., Silbart, L. K., Papadimitrakopoulos, F. & Burgess, D. J. Dual fluorescent labeling method to visualize plasmid DNA degradation. *Bioconjugate Chemistry* 20, 163-169 (2009).

267 Choi, C. K., Zareno, J., Digman, M. A., Gratton, E. & Horwitz, A. R. Cross-correlated fluctuation analysis reveals phosphorylation-regulated paxillin-fak complexes in nascent adhesions. *Biophysical Journal* 100, 583-592 (2011).

268 Sixou, S. *et al.* Intracellular oligonucleotide hybridization detected by fluorescence resonance energy transfer (FRET). *Nucleic Acids Research* 22, 662-668 (1994).

269 De Smedt, S. C. *et al.* Studying biophysical barriers to DNA delivery by advanced light microscopy. *Advanced Drug Delivery Reviews* 57, 191-210 (2005).

270 Rattan, R., Bielinska, A. U. & Banaszak Holl, M. M. Quantification of cytosolic plasmid DNA degradation using high-throughput sequencing: Implications for gene delivery. *Journal of Gene Medicine* 16, 75-83 (2014).

271 Omata, D. *et al.* Involvement of Ca 2+ and ATP in enhanced gene delivery by bubble liposomes and ultrasound exposure. *Molecular Pharmaceutics* 9, 1017-1023 (2012).

272 Digman, M. A., Caiolfa, V. R., Zamai, M. & Gratton, E. The phasor approach to fluorescence lifetime imaging analysis. *Biophysical Journal* 94, L14-L16 (2008).

273 Golfetto, O., Hinde, E. & Gratton, E. Laurdan fluorescence lifetime discriminates cholesterol content from changes in fluidity in living cell membranes. *Biophysical Journal* 104, 1238-1247 (2013).

274 Golfetto, O., Hinde, E. & Gratton, E. in *Methods in Membrane Lipids* Vol. 1232 (ed Dylan M. Owen) 273-290 (Springer New York, 2014).

275 Greenspan, P. & Fowler, S. D. Spectrofluorometric studies of the lipid probe, nile red. *Journal of Lipid Research* 26, 781-789 (1985).

276 Liu, X. J. *et al.* Lumican Accelerates Wound Healing by Enhancing α2β1 Integrin-Mediated Fibroblast Contractility. *PLoS ONE* 8 (2013).

277 Sakurai, T. *et al.* Live cell imaging of primary rat neonatal cardiomyocytes following adenoviral and lentiviral transduction using confocal spinning disk microscopy. *Journal of Visualized Experiments* (2014).

278 Marchini, C. *et al.* Structural stability and increase in size rationalize the efficiency of lipoplexes in serum. *Langmuir* 25, 3013-3021 (2009).

279 Yoshikawa, N. *et al.* Multiple components in serum contribute to hepatic transgene expression by lipoplex in mice. *Journal of Gene Medicine* 13, 632-643 (2011).

280 Zuhorn, I. S., Visser, W. H., Bakowsky, U., Engberts, J. B. F. N. & Hoekstra, D. Interference of serum with lipoplex-cell interaction: Modulation of intracellular processing. *Biochimica et Biophysica Acta - Biomembranes* 1560, 25-36 (2002).

281 Esposito, C., Generosi, J., Mossa, G., Masotti, A. & Castellano, A. C. The analysis of serum effects on structure, size and toxicity of DDAB-DOPE and DC-Chol-DOPE lipoplexes contributes to explain their different transfection efficiency. *Colloids and Surfaces B: Biointerfaces* 53, 187-192 (2006).

282 Betker, J. L., Kullberg, M., Gomez, J. & Anchordoquy, T. J. Cholesterol domains enhance transfection. *Therapeutic Delivery* 4, 453-462 (2013).

283 Misra, S. K., Biswas, J., Kondaiah, P. & Bhattacharya, S. Gene Transfection in High Serum Levels: Case Studies with New Cholesterol Based Cationic Gemini Lipids. *PLoS ONE* 8 (2013).

SUPPLEMENTARY INFORMATION

Table of Contents

Supplementary Information 1 (SI 1) – DNA Labelling Approaches

Three DNA labelling approaches were explored: the use of an ULYSIS Nucleic Acid Labelling Kit (Alexa Fluor488) – this approach was used to label DNA plasmids, and the generation of DNA using fluorescently labelled primers, both homemade by labelling primers with an ULYSIS Nucleic Acid Labelling Kit, or purchased from Integrated DNA Technologies (IDT). SI-1 presents cells that were transfected with a 1000bp fragment. In SI-1A the DNA was generated through PCR and then labelled with the ULYSIS Nucleic Acid Labelling Kit, whereas in SI-1B the fragments were amplified with the IDT purchased Alexa Fluor488 labelled primer.

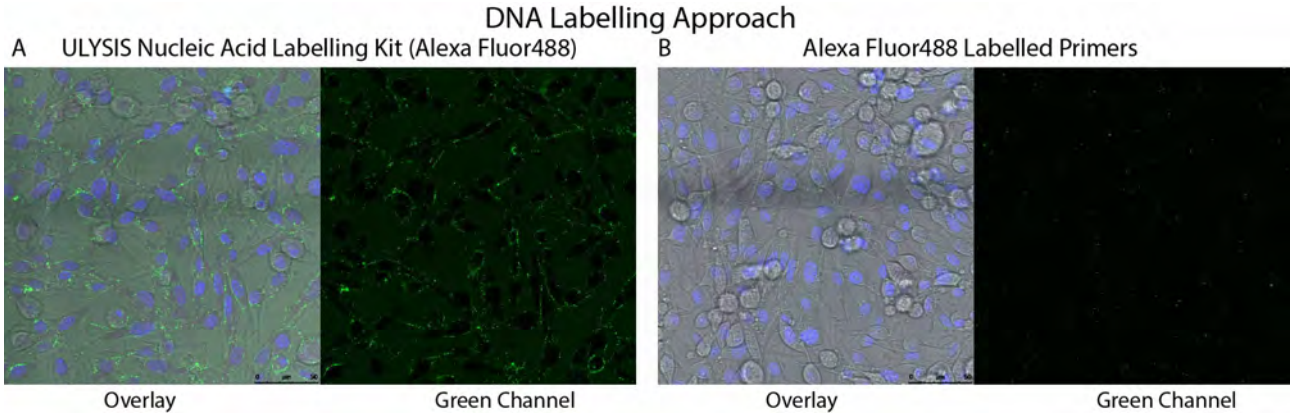

Supplementary Figure 1 - DNA Labelling Approach

As seen in the DNA labelled with the ULYSIS Nucleic Acid Labelling Kit the fluorescence signal was very high and while attempting to acquire data for FCS, RICS or N&B it would saturate the APDs. Therefore, this approach was not employed for the project. When labelling plasmids more DNA was labelled, and less labelling reagent was utilised than the manufacturer's guidelines had stated.

Supplementary Information 2 (SI 2) – Transfection Approaches

Three different transfection reagents were screened: Lipofectamine 2000 (Invitrogen), X-treme Gene 9 (Roche) and X-treme Gene HP (Roche). Of these three X-treme Gene 9 had demonstrated the most rapid uptake of the fluorescently labelled plasmid. Additionally, the X-treme Gene 9 had shown the least amount of cell death and toxicity.

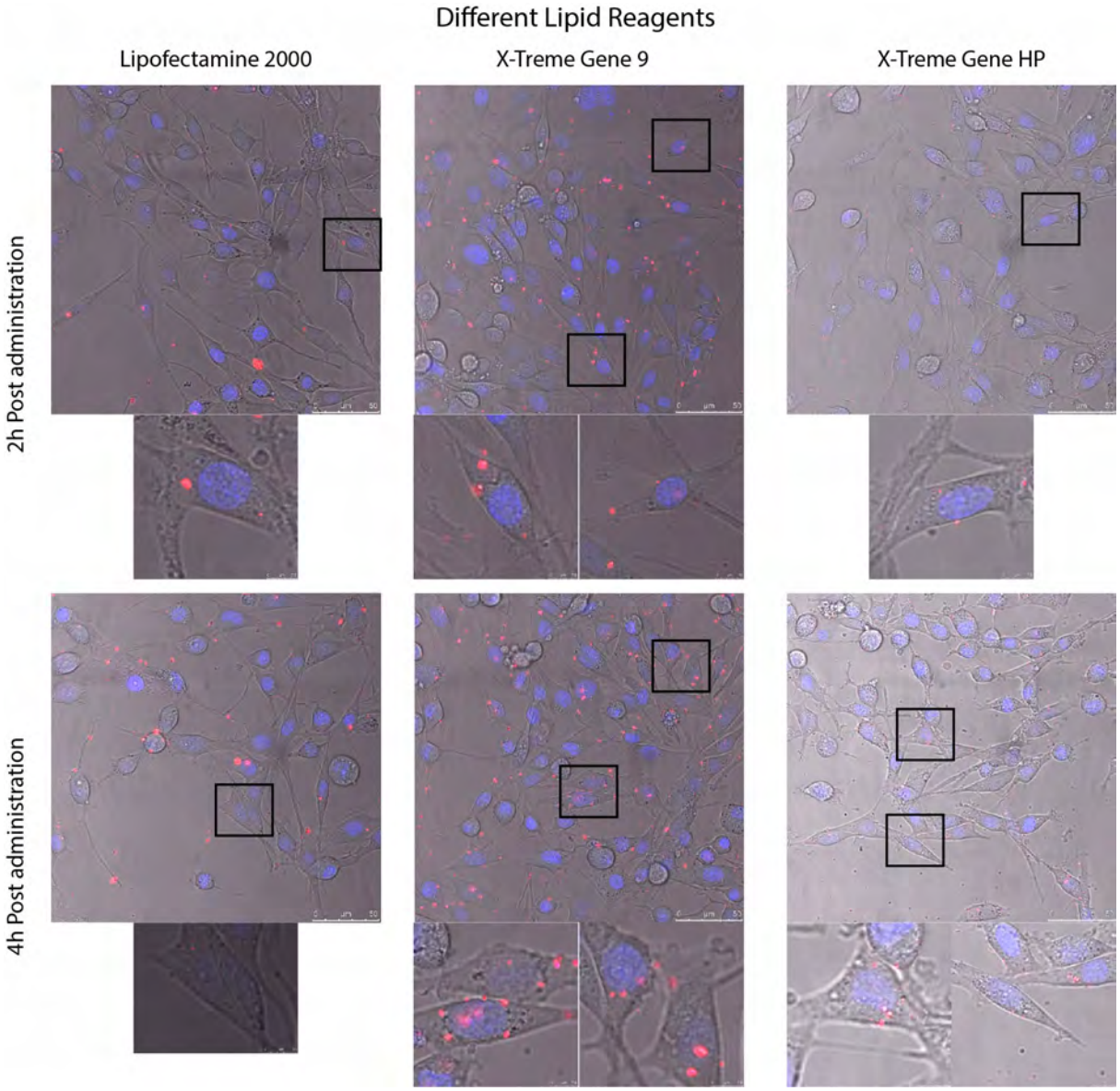

Supplementary Figure 2 - Lipofection Approaches

Supplementary Information 3 (SI 3) – DNA Sequences

PCI-Neo Vector Map

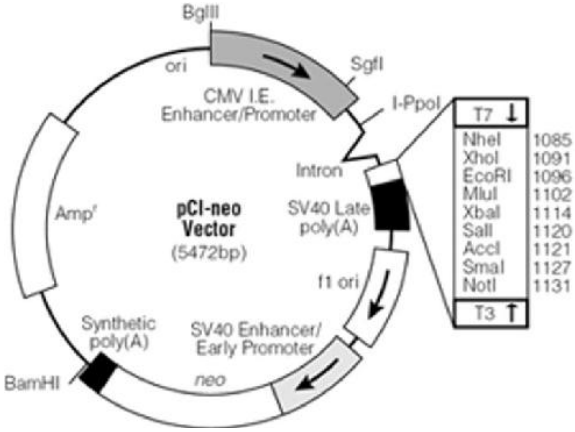

Supplementary Figure 3 - PCI-Neo Vector Map

PCI-Neo Sequence and Primer Hybridisation Sites

TCAATATTGGCCATTAGCCATATTATTCATTGGTTATATAGCATAAATCAATATTGGCTATTGGCCATTGCA
TACGTTGTATCTATATCATAATATGTACATTTATATTGGCTCATGTCCAATATGACCGCCATGTTGGCATTG
ATTATTGACTAGTTATTAATAGTAATCAATTACGGGGTCATTAGTTCATAGCCCATATATGGAGTTCCGCGT
TACATAACTTACGGTAAATGGCCCGCCTGGCTGACCGCCCAACGACCCCCGCCCATTGACGTCAATAATGAC
GTATGTTCCCATAGTAACGCCAATAGGGACTTTCCATTGACGTCAATGGGTGGAGTATTTACGGTAAACTG
CCCACTTGGCAGTACATCAAGTGTATCATATGCCAAGTCCGCCCCCTATTGACGTCAATGACGGTAAATGG
CCCGCCTGGCATTATGCCCAGTACATGACCTTACGGGACTTTCCTACTTGGCAGTACATCTACGTATTAGTC
ATCGCTATTACCATGGTGATGCGGTTTTGGCAGTACACCAATGGGCGTGGATAGCGGTTTGACTCACGGG
GATTTCCAAGTCTCCACCCCATTGACGTCAATGGGAGTTTGTTTTGGCACCAAAATCAACGGGACTTTCCAA
AATGTCGTAACAACTGCGATCGCCCGCCCCGTTGACGCAAATGGGCGGTAGGCGTGTACGGTGGGAGGTC
TATATAAGCAGAGCTCGTTTAGTGAACCGTCAGATCACTAGAAGCTTTATTGCGGTAGTTTATCACAGTTA
AATTGCTAACGCAGTCAGTGCTTCTGACACAACAGTCTCGAACTTAAGCTGCAGTGACTCTCTTAAGGTAG
CCTTGCAGAAGTTGGTCGTGAGGCACTGGGCAGGTAAGTATCAAGGTTACAAGACAGGTTTAAGGAGACC
AATAGAAACTGGGCTTGTCGAGACAGAGAAGACTCTTGCGTTTCTGATAGGCACCTATTGGTCTTACTGAC
ATCCACTTTGCCTTTCTCTCCACAGGTGTCCACTCCCAGTTCAATTACAGCTCTTAAGGCTAGAGTACTTAAT
ACGACTCACTATAGGCTAGCCTCGAGAATTCACGCGTGGTACCTCTAGAGTCGACCCGGGCGGCCGCTTCC
CTTTAGTGAGGGTTAATGCTTCGAGCAGACATGATAAGATACATTGATGAGTTTGGACAAACCACAACTAG
AATGCAGTGAAAAAAATGCTTTATTTGTGAAATTTGTGATGCTATTGCTTTATTTGTAACCATTATAAGCTG
CAATAAACAAGTTAACAACAACAATTGCATTCATTTTATGTTTCAGGTTCAGGGGGAGATGTGGGAGGTTT
TTTAAAGCAAGTAAAACCTCTACAAATGTGGTAAAATCCGATAAGGATCGATCCGGGCTGGCGTAATAGCG
AAGAGGCCCGCACCGATCGCCCTTCCCAACAGTTGCGCAGCCTGAATGGCGAATGGACGCGCCCTGTAGC
GGCGCATTAAGCGCGGCGGGTGTGGTGGTTACGCGCAGCGTGACCGCTACACTTGCCAGCGCCCTAGCGC
CCGCTCCTTTCGCTTTCTTCCCTTCCTTTCTCGCCACGTTCGCCGGCTTTCCCCGTCAAGCTCTAAATCGGGG
GCTCCCTTTAGGGTTCCGATTTAGTGCTTTACGGCACCTCGACCCCAAAAAACTTGATTAGGGTGATGGTT
CACGTAGTGGGCCATCGCCCTGATAGACGGTTTTTCGCCCTTTGACGTTGGAGTCCACGTTCTTTAATAGT
GGACTCTTGTTCCAAACTGGAACAACACTCAACCCTATCTCGGTCTATTCTTTTGATTTATAAGGGATTTTG
CCGATTTCGGCCTATTGGTTAAAAAATGAGCTGATTTAACAAAAATTTAACGCGAATTTTAACAAAATATTA
ACGCTTACAATTTCCTGATGCGGTATTTTCTCCTTACGCATCTGTGCGGTATTTCACACCGCATACGCGGAT
CTGCGCAGCACCATGGCCTGAAATAACCTCTGAAAGAGGAACTTGGTTAGGTACCTTCTGAGGCGGAAAG
AACCAGCTGTGGAATGTGTGTCAGTTAGGGTGTGGAAAGTCCCCAGGCTCCCCAGCAGGCAGAAGTATGC
AAAGCATGCATCTCAATTAGTCAGCAACCAGGTGTGGAAAGTCCCCAGGCTCCCCAGCAGGCAGAAGTAT
GCAAAGCATGCATCTCAATTAGTCAGCAACCATAGTCCCGCCCCTAACTCCGCCCATCCCGCCCCTAACTCC
GCCCAGTTCCGCCCATTCTCCGCCCCATGGCTGACTAATTTTTTTTATTTATGCAGAGGCCGAGGCCGCCTC
GGCCTCTGAGCTATTCCAGAAGTAGTGAGGAGGCTTTTTTGGAGGCCTAGGCTTTTGCAAAAAGCTTGATT
CTTCTGACACAACAGTCTCGAACTTAAGGCTAGAGCCACCATGATTGAACAAGATGGATTGCACGCAGGTT
CTCCGGCCGCTTGGGTGGAGAGGCTATTCGGCTATGACTGGGCACAACAGACAATCGGCTGCTCTGATGC
CGCCGTGTTCCGGCTGTCAGCGCAGGGGCGCCCGGTTCTTTTTGTCAAGACCGACCTGTCCGGTGCCCTGA
ATGAACTGCAGGACGAGGCAGCGCGGCTATCGTGGCTGGCCACGACGGGCGTTCCTTGCGCAGCTGTGCT
CGACGTTGTCACTGAAGCGGGAAGGGACTGGCTGCTATTGGGCGAAGTGCCGGGGCAGGATCTCCTGTC
ATCTCACCTTGCTCCTGCCGAGAAAGTATCCATCATGGCTGATGCAATGCGGCGGCTGCATACGCTTGATC
CGGCTACCTGCCCATTCGACCACCAAGCGAAACATCGCATCGAGCGAGCACGTACTCGGATGGAAGCCGG
TCTTGTCGATCAGGATGATCTGGACGAAGAGCATCAGGGGCTCGCGCCAGCCGAACTGTTCGCCAGGCTC
AAGGCGCGCATGCCCGACGGCGAGGATCTCGTCGTGACCCATGGCGATGCCTGCTTGCCGAATATCATGG
TGGAAAATGGCCGCTTTTCTGGATTCATCGACTGTGGCCGGCTGGGTGTGGCGGACCGCTATCAGGACAT
AGCGTTGGCTACCCGTGATATTGCTGAAGAGCTTGGCGGCGAATGGGCTGACCGCTTCCTCGTGCTTTAC
GGTATCGCCGCTCCCGATTCGCAGCGCATCGCCTTCTATCGCCTTCTTGACGAGTTCTTCTGAGCGGGACTC
TGGGGTTCGAAATGACCGACCAAGCGACGCCCAACCTGCCATCACGATGGCCGCAATAAAATATCTTTATT
TTCATTACATCTGTGTGTTGGTTTTTTGTGTGAATCGATAGCGATAAGGATCCGCGTATGGTGCACTCTCA
GTACAATCTGCTCTGATGCCGCATAGTTAAGCCAGCCCCGACACCCGCCAACACCCGCTGACGCGCCCTGA
CGGGCTTGTCTGCTCCCGGCATCCGCTTACAGACAAGCTGTGACCGTCTCCGGGAGCTGCATGTGTCAGA
GGTTTTCACCGTCATCACCGAAACGCGCGAGACGAAAGGGCCTCGTGATACGCCTATTTTTATAGGTTAAT
GTCATGATAATAATGGTTTCTTAGACGTCAGGTGGCACTTTTCGGGGAAATGTGCGCGGAACCCCTATTTG
TTTATTTTTCTAAATACATTCAAATATGTATCCGCTCATGAGACAATAACCCTGATAAATGCTTCAATAATAT
TGAAAAAGGAAGAGTATGAGTATTCAACATTTCCGTGTCGCCCTTATTCCCTTTTTTGCGGCATTTTGCCTT
CCTGTTTTTGCTCACCCAGAAACGCTGGTGAAAGTAAAAGATGCTGAAGATCAGTTGGGTGCACGAGTGG
GTTACATCGAACTGGATCTCAACAGCGGTAAGATCCTTGAGAGTTTTCGCCCCGAAGAACGTTTTCCAATG
ATGAGCACTTTTAAAGTTCTGCTATGTGGCGCGGTATTATCCCGTATTGACGCCGGGCAAGAGCAACTCGG
TCGCCGCATACACTATTCTCAGAATGACTTGGTTGAGTACTCACCAGTCACAGAAAAGCATCTTACGGATG
GCATGACAGTAAGAGAATTATGCAGTGCTGCCATAACCATGAGTGATAACACTGCGGCCAACTTACTTCTG
ACAACGATCGGAGGACCGAAGGAGCTAACCGCTTTTTTGCACAACATGGGGGATCATGTAACTCGCCTTG
ATCGTTGGGAACCGGAGCTGAATGAAGCCATACCAAACGACGAGCGTGACACCACGATGCCTGTAGCAAT
GGCAACAACGTTGCGCAAACTATTAACTGGCGAACTACTTACTCTAGCTTCCCGGCAACAATTAATAGACTG

GATGGAGGCGGATAAAGTTGCAGGACCACTTCTGCGCTCGGCCCTTCCGGCTGGCTGGTTTATTGCTGAT
AAATCTGGAGCCGGTGAGCGTGGGTCTCGCGGTATCATTGCAGCACTGGGGCCAGATGGTAAGCCCTCCC
GTATCGTAGTTATCTACACGACGGGGAGTCAGGCAACTATGGATGAACGAAATAGACAGATCGCTGAGAT
AGGTGCCTCACTGATTAAGCATTGGTAACTGTCAGACCAAGTTTACTCATATATACTTTAGATTGATTTAAA
ACTTCATTTTTAATTTAAAAGGATCTAGGTGAAGATCCTTTTTGATAATCTCATGACCAAAATCCCTTAACGT
GAGTTTTCGTTCCACTGAGCGTCAGACCCCGTAGAAAAGATCAAAGGATCTTCTTGAGATCCTTTTTTTCTG
CGCGTAATCTGCTGCTTGCAAACAAAAAAACCACCGCTACCAGCGGTGGTTTGTTTGCCGGATCAAGAGCT
ACCAACTCTTTTTCCGAAGGTAACTGGCTTCAGCAGAGCGCAGATACCAAATACTGTTCTTCTAGTGTAGCC
GTAGTTAGGCCACCACTTCAAGAACTCTGTAGCACCGCCTACATACCTCGCTCTGCTAATCCTGTTACCAGT
GGCTGCTGCCAGTGGCGATAAGTCGTGTCTTACCGGGTTGGACTCAAGACGATAGTTACCGGATAAGGCG
CAGCGGTCGGGCTGAACGGGGGGTTCGTGCACACAGCCCAGCTTGGAGCGAACGACCTACACCGAACTG
AGATACCTACAGCGTGAGCTATGAGAAAGCGCCACGCTTCCCGAAGGGAGAAAGGCGGACAGGTATCCG
GTAAGCGGCAGGGTCGGAACAGGAGAGCGCACGAGGGAGCTTCCAGGGGGAAACGCCTGGTATCTTTAT
AGTCCTGTCGGGTTTCGCCACCTCTGACTTGAGCGTCGATTTTTGTGATGCTCGTCAGGGGGGCGGAGCC
TATGGAAAAACGCCAGCAACGCGGCCTTTTTACGGTTCCTGGCCTTTTGCTGGCCTTTTGCTCACATGGCTC
GACAGATCT

Primer Binding Sites:

Yellow: FWD Primer

Green: 120bp REV

Cyan: 240bp REV

Red: 492bp REV

Purple: 1,000bp REV

Blue: 1,985bp REV

AseI restriction site highlighted in grey

Supplementary Information 4 (SI 4) – RICS Analysis of DNA in solution

A

	DNA Size (bp)	Mean (μm²/s)	Standard Deviation	Range (μm²/s) Minimum	Maximum
DNA Fragment	21	55.11	4.79	45.77	64.89
	120	20.86	2.45	16.65	26.90
	240	13.16	0.81	11.46	13.92
	495	6.01	1.15	3.59	7.88
	1000	3.43	0.51	2.34	4.86
	1985	2.80	0.50	1.92	3.99
	5472 (Linear)	1.23	0.10	0.94	1.44
	5472 (Circular)	1.83	0.17	1.51	2.36
Lipoplex	21	18.65	5.58	12.95	29.76
	120	4.37	2.38	1.45	15.59
	240	2.94	0.43	2.05	3.61
	495	1.96	0.79	0.77	4.15
	1000	1.26	0.24	0.56	1.78
	1985	1.10	0.51	0.51	4.15
	5472 (Linear)	0.89	0.23	0.31	2.13
	5472 (Circular)	3.71	0.50	1.87	5.18

*All samples were separately repeated 10 times, and sampled 10 times (n = 100)

B

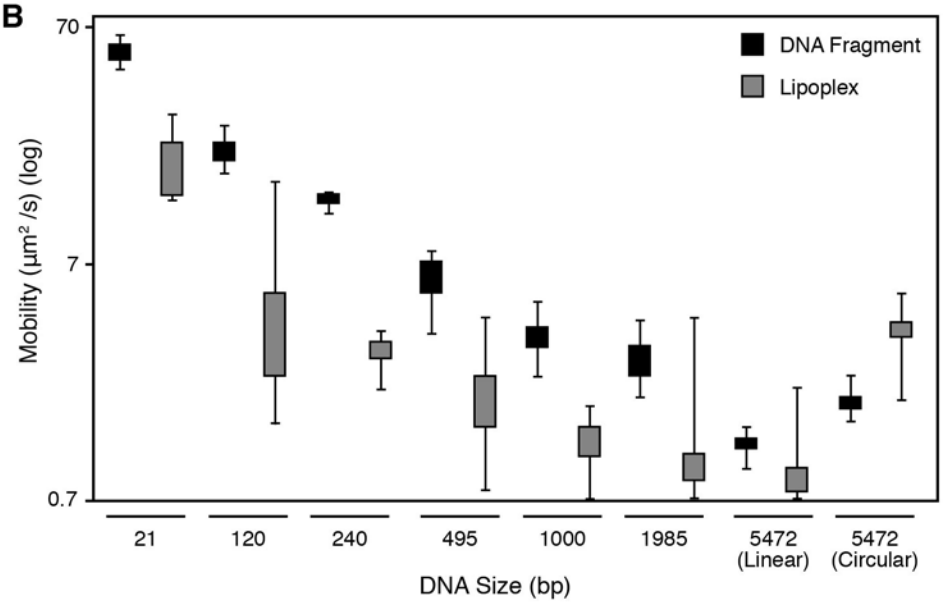

Supplementary Figure 4 - RICS Analysis of DNA and Lipoplexes in Solution

SI 4A presents the values of the DNA and DNA lipoplex diffusion on solution analysed through RICS. The values include the mean, standard deviation and range observed. SI 4B shows a box and whisker plot of these values, showing the first and third quartile and the range observed for each fragment as naked DNA and lipoplexes.

Supplementary Information 5 (SI 5) – Cytoplasmic Values of DNA Mobility

A

DNA Size (bp)	Slow Species from Global Analysis					ROI Analysis				
	Mean (μm²/s)	Standard Deviation	Variance	Range (μm²/s) Minimum	Range (μm²/s) Maximum	Mean (μm²/s)	Standard Deviation	Variance	Range (μm²/s) Minimum	Range (μm²/s) Maximum
21	0.97	0.65	0.42	0.20	3.05	0.66	0.61	0.37	0.02	3.92
120	1.06	1.03	1.07	0	3.80	0.48	0.34	0.12	0	1.67
240	0.83	1.17	1.38	0	4.78	0.43	0.33	0.11	0	1.79
495	0.93	1.02	1.04	0	3.64	0.44	0.25	0.06	0	1.12
1000	0.73	0.64	0.42	0	3.12	0.40	0.28	0.08	0	1.30
1985	0.65	0.65	0.43	0	2.03	0.33	0.31	0.09	0	1.94
5472 (Linear)	0.71	0.83	0.68	0	2.72	0.31	0.29	0.08	0	1.89
5472 (Circular)	0.55	0.71	0.51	0	3.42	0.44	0.45	0.20	0	3.39

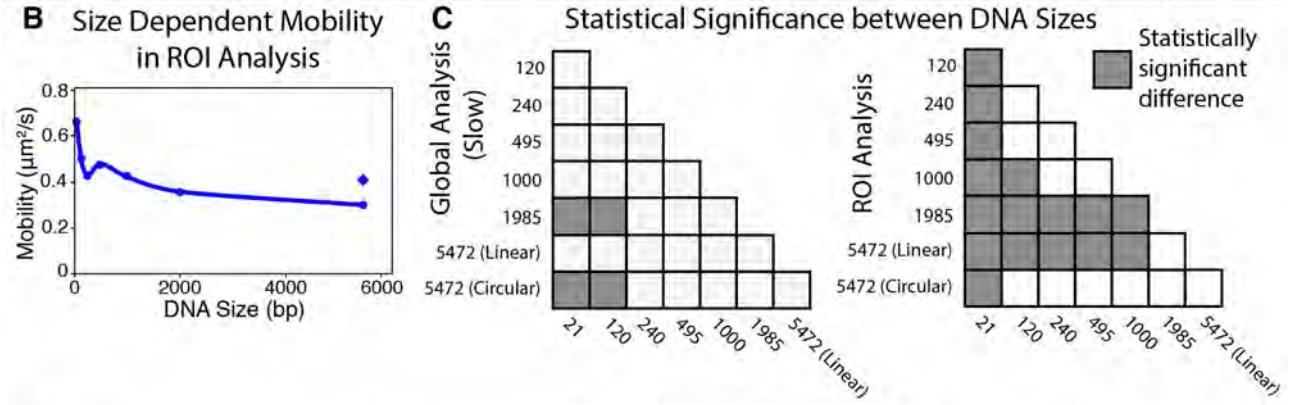

D

DNA Size (bp)	Cell Position			Cluster Size		
	Cell Extremity	Cytoplasm	Peri-nuclear	Diffuse	Small Cluster	Large Cluster
21	NA	NA	NA	0.57	0.82	0.55
120	0.44	0.51	0.47	0.78	0.56	0.27
240	0.34	0.46	0.38	0.49	0.46	0.35
495	0.39	0.46	0.42	0.60	0.47	0.37
1000	0.34	0.48	0.34	0.48	0.40	0.39
1985	0.17	0.39	0.32	0.51	0.36	0.22
5472 (Linear)	0.20	0.36	0.29	0.32	0.38	0.24
5472 (Circular)	0.21	0.48	0.38	0.66	0.48	0.34

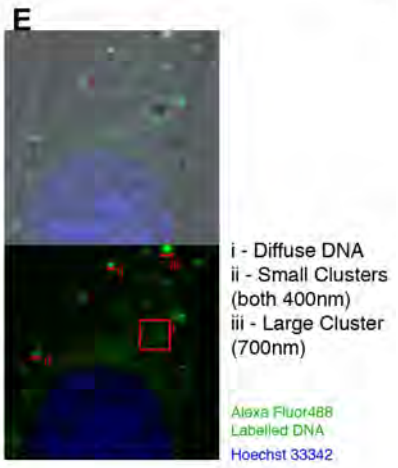

Supplementary Figure 5 - Cytoplasmic Mobility of Transfected DNA Lipoplexes

(A) The mean, standard deviation, variance and upper and lower ranges of the cytoplasmic localised DNA has been presented for the global and ROI analysis. (B) The mean mobility obtained in the ROI analysis has been plotted in a scatter plot demonstrating the size dependent mobility of the DNA. (C) Statistical analysis was performed using a T Test assuming unequal variances showing that the global analysis resulted in mobility rates that were statistically insignificant from each other. However, in the ROI analysis, the mobility of most fragments was statistically significant. (D) The values obtained in the ROI analyses representing the cell position and cluster size have been presented, in addition an example of different cluster sizes in a cell (E).

A Random Diffusion

DNA Size (bp)	Mean (μm²/s)	Standard Deviation	Variance	Range (μm²/s) Minimum	Range (μm²/s) Maximum
21*	NA				
120	0.40	0.39	0.16	0.09	1.02
240	0.45	0.002	3.3^{-6}	0.44	0.46
495	0.34	0.12	0.04	0.09	0.44
1000	0.22	0.18	0.03	0.03	0.46
1985	0.12	0.004	1.5^{-5}	0.11	0.13
5472 (Linear)	0.13	0.06	0.01	0.08	0.15
5472 (Circular)	0.13	0.03	0.001	0.10	0.15

*No events isolated

B Active Transport

DNA Size (bp)	Mean (μm²/s)	Standard Deviation	Variance	Range (μm²/s) Minimum	Range (μm²/s) Maximum
21	0.71	0.44	0.14	0.16	1.89
120	0.64	0.35	0.12	0.12	1.67
240	0.54	0.39	0.16	0.03	1.78
495	0.50	0.21	0.04	0.15	1.05
1000	0.59	0.27	0.08	0.13	1.29
1985	0.53	0.31	0.09	0.10	1.66
5472 (Linear)	0.53	0.23	0.05	0.12	0.88
5472 (Circular)	0.67	0.33	0.11	0.21	1.49

C Anomalous Subdiffusion

DNA Size (bp)	Mean (μm²/s)	Standard Deviation	Variance	Range (μm²/s) Minimum	Range (μm²/s) Maximum
21	0.51	0.14	0.02	0.31	0.68
120	0.21	0.14	0.02	0.05	0.52
240	0.34	0.18	0.03	0.12	0.52
495	0.32	0.19	0.04	0.09	0.75
1000	0.28	0.13	0.02	0.06	0.54
1985	0.38	0.25	0.06	0.10	0.96
5472 (Linear)	0.26	0.21	0.04	0.01	0.89
5472 (Circular)	0.42	0.18	0.03	0.16	0.77

D Confined Diffusion

DNA Size (bp)	Mean (μm²/s)	Standard Deviation	Variance	Range (μm²/s) Minimum	Range (μm²/s) Maximum
21	0.38	0.29	0.089	0.02	1.39
120	0.43	0.34	0.11	0.12	1.14
240	0.40	0.26	0.07	0.03	1.09
495	0.45	0.20	0.04	0.10	0.90
1000	0.37	0.25	0.07	0.06	0.81
1985	0.24	0.18	0.03	0.04	0.65
5472 (Linear)	0.26	0.19	0.04	0.04	0.74
5472 (Circular)	0.26	0.22	0.05	0.09	0.67

E Transient Confinement

DNA Size (bp)	Mean (μm²/s)	Standard Deviation	Variance	Range (μm²/s) Minimum	Range (μm²/s) Maximum
21	0.73	0.21	0.15	0.09	1.65
120	0.63	0.23	0.05	0.08	0.88
240	0.52	0.29	0.09	0.09	1.24
495	0.49	0.35	0.16	0.11	1.12
1000	0.39	0.37	0.13	0.02	1.39
1985	0.24	0.15	0.02	0.01	0.48
5472 (Linear)	0.35	0.17	0.03	0.14	0.55
5472 (Circular)	0.33	0.22	0.05	0.10	0.67

F Binding-unbinding

DNA Size (bp)	Mean (μm²/s)	Standard Deviation	Variance	Range (μm²/s) Minimum	Range (μm²/s) Maximum
21	0.74	0.37	0.14	0.13	1.28
120	0.46	0.33	0.11	0.03	1.39
240	0.49	0.36	0.12	0.05	1.78
495	0.46	0.24	0.06	0.05	1.06
1000	0.32	0.29	0.08	0.05	0.97
1985	0.37	0.34	0.12	0.03	1.94
5472 (Linear)	0.36	0.34	0.11	0.03	1.88
5472 (Circular)	0.49	0.39	0.15	0.01	2.05

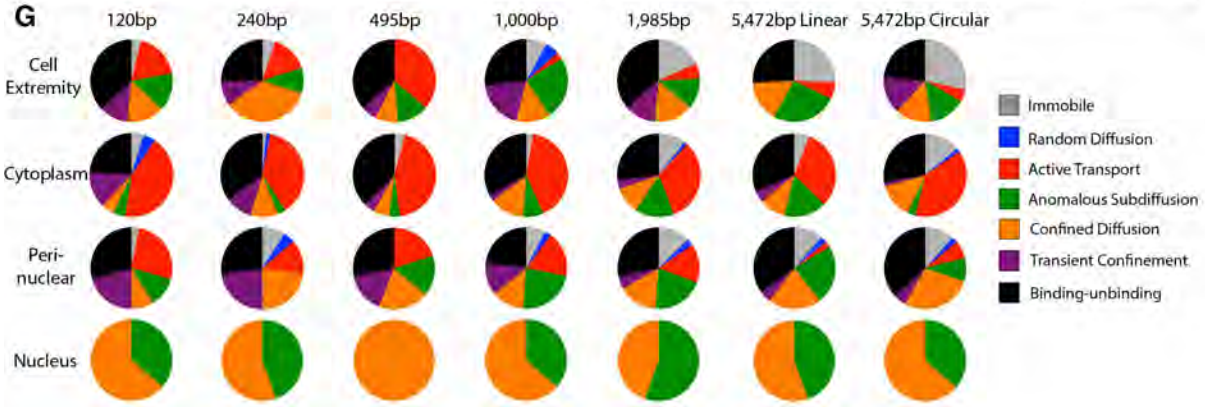

Supplementary Figure 6 - Values for the Mechanisms of Motion

The mean, standard deviation, variance and upper and lower range values for the different mechanisms of motion including random diffusion (A), active transport (B), anomalous subdiffusion (C), confined diffusion (D), transient confinement (E) and binding-unbinding (F). (G) The spatial distribution of the mechanisms of motion has been presented for all of the DNA fragment sizes.

Supplementary Information 7 (SI 7) – Examples of Cells

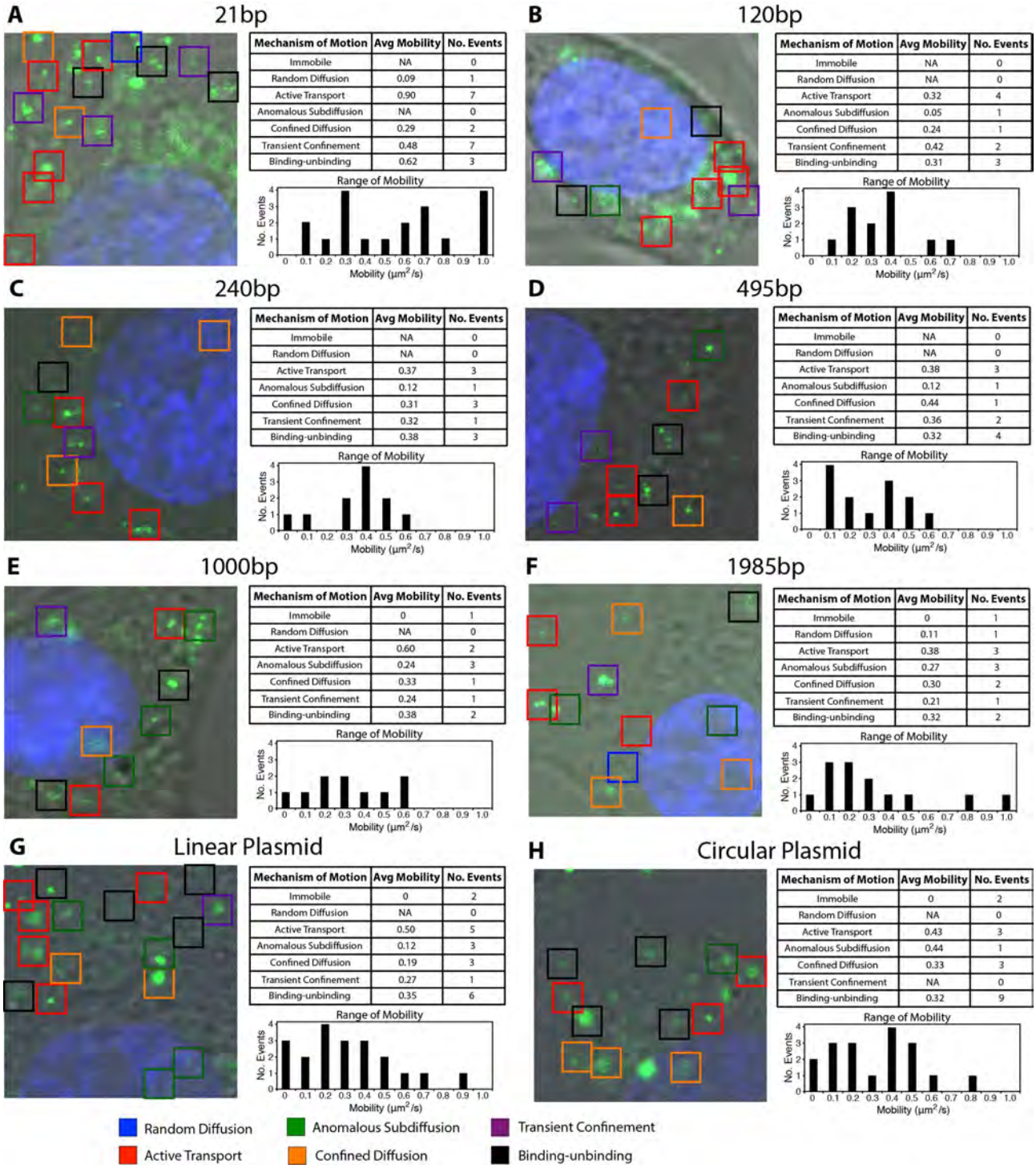

Supplementary Figure 7 - Examples of Cells

A cell example for each DNA fragment including 21bp (A), 120bp (B), 240bp (C), 495bp (D), 1000bp (E), 1985bp (F) and, linear (G) and circular (H) plasmid has been presented. Each example has ROIs selected representative of the different mechanisms of motion identified in each cell. In addition summaries of the types of mechanisms found and range of motion observed have been presented.

Supplementary Information 8 (SI 8) – Summary of Nuclear Dynamics

		Mobility				N
		Mean Mobility (um2/s)	Standard Deviation	Range		
				Min	Max	
DNA Base Pairs	21	3.67	3.07	0.28	14.09	1.27
	120	1.63	1.40	0.19	6.01	2.17
	240	2.31	1.81	0.03	7.72	3.17
	495	2.12	1.34	0.18	5.07	1.84
	1000	2.65	2.46	0.08	11.90	1.63
	1985	1.79	2.13	0.11	10.50	1.36
	5485 (Linear)	1.31	1.31	0.07	3.73	0.44
	5485 (Circular)	2.30	3.79	0.01	14.40	0.18

Supplementary Information 9 (SI 9) – Examples of Internalisation Event

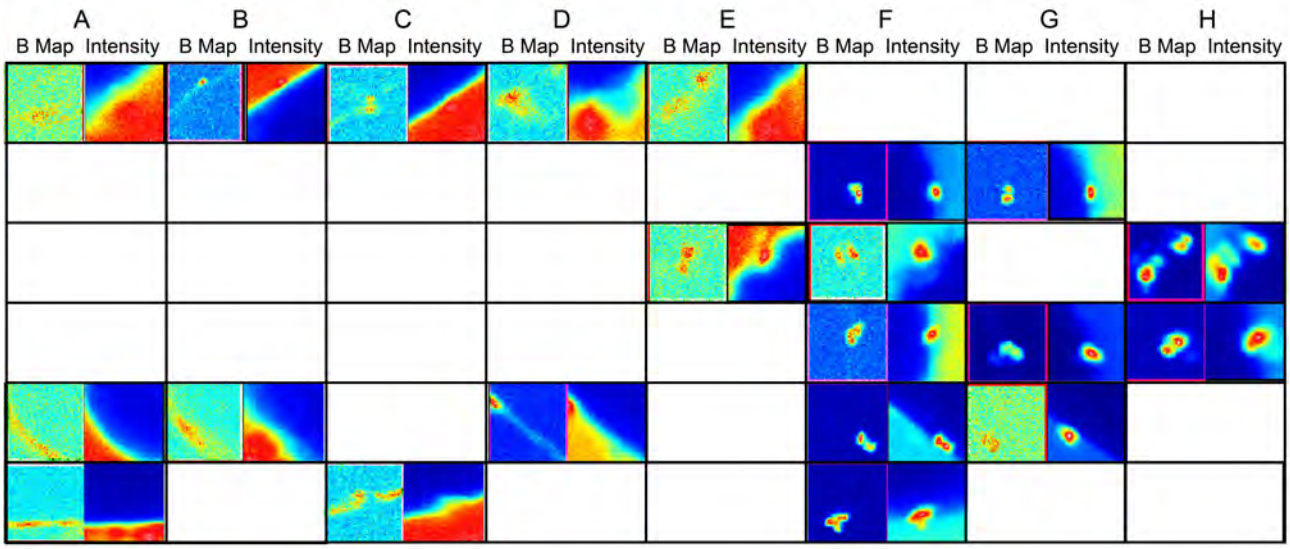

Six different internalisation (in each row) events have been presented at different stages of internalisation. Over the event an accumulation of the DNA lipoplex was observed (A), then the DNA slowly accumulates into a single cluster (B-E), until a clearly defined cluster/aggregation was seen (F). The cluster then further accumulates DNA (G), before being internalised (H). All stages have two images, the B map (left) and intensity map (right).

Supplementary Information 10 (SI 10) – Spatial Aggregation and Diffusion

	Cell Extremity				Cytoplasm				Peri-nuclear			
	Max B	Avg B	Avg N	D	Max B	Avg B	Avg N	D	Max B	Avg B	Avg N	D
Average	6.491	2.224	2.468	0.077	4.792	1.892	1.795	0.181	5.123	1.774	1.266	0.079
Std. Dev.	3.301	0.947	2.116	0.067	2.501	0.800	1.315	0.136	2.352	0.553	0.747	0.062
Min	2.435	1.224	0.347	0.000	2.272	1.208	0.345	0.024	2.074	1.116	0.197	0.000
Max	15.302	5.513	6.948	0.228	10.063	4.717	7.134	0.795	9.849	2.965	2.746	0.254
Data Values	2.435	1.224	0.585	0.020	2.485	1.381	0.889	0.281	2.272	1.219	0.409	0.069
	2.747	1.265	0.797	0.228	2.272	1.301	0.590	0.399	2.074	1.161	0.496	0.149
	11.582	5.513	1.412	0.200	3.012	1.564	0.779	0.191	2.239	1.134	0.261	0.188
	7.547	2.327	0.772	0.096	6.410	2.150	0.637	0.153	6.218	1.277	0.227	0.254
	4.626	2.344	1.668	0.099	3.297	1.526	0.689	0.298	3.023	1.116	0.197	0.149
	4.571	1.989	1.196	0.157	3.962	1.318	0.345	0.159	2.680	1.212	0.296	0.016
	13.060	3.740	1.436	0.000	2.549	1.350	1.443	0.135	6.444	1.692	1.563	0.091
	4.835	1.735	0.453	0.072	2.858	1.408	1.572	0.187	4.341	1.628	2.134	0.034
	5.322	1.970	1.489	0.109	8.540	2.581	1.767	0.237	9.727	2.338	0.736	0.092
	5.408	1.980	1.542	0.035	2.599	1.252	0.983	0.164	7.146	2.403	0.762	0.004
	4.535	1.940	1.116	0.062	9.654	3.084	3.012	0.024	4.507	1.562	1.530	0.126
	15.302	2.177	0.347	0.068	3.172	1.505	2.204	0.092	6.169	2.744	2.142	0.061
	5.924	2.163	4.862	0.121	4.507	1.652	1.804	0.138	9.849	2.965	1.354	0.101
	5.055	1.979	6.114	0.067	2.975	1.617	1.519	0.147	5.693	1.925	1.258	0.112
	4.789	2.097	4.588	0.186	3.526	1.596	1.819	0.115	4.066	1.704	1.513	0.005
	7.158	2.305	3.571	0.019	3.851	1.522	2.101	0.107	8.159	2.256	2.029	0.009
	6.861	1.885	6.948	0.047	3.277	1.401	1.102	0.169	3.232	1.323	0.966	0.013
	4.822	1.476	1.916	0.015	8.798	3.134	0.617	0.105	6.412	1.930	1.067	0.049
	10.249	2.183	5.045	0.010	6.400	1.597	2.822	0.179	3.492	1.501	1.891	0.085
	2.760	1.234	6.369	0.015	4.587	1.851	2.017	0.100	7.667	2.866	1.762	0.057
	4.208	1.351	2.876	0.021	4.587	1.830	2.007	0.105	3.671	1.579	0.978	0.070
	7.747	3.157	0.561	0.125	10.063	4.717	0.777	0.250	3.949	1.674	1.327	0.111
	7.761	3.108	1.092	0.000	8.413	3.817	2.270	0.235	2.571	1.381	2.669	0.049
					8.797	2.479	2.301	0.073	4.446	1.635	1.325	0.077
					6.085	1.811	2.131	0.133	8.039	2.118	2.746	0.000
					2.942	1.386	1.631	0.119				
					9.279	2.640	2.355	0.122				
					2.655	1.441	1.241	0.089				
					3.422	1.633	0.867	0.119				
					3.246	1.352	1.651	0.338				
					2.499	1.208	1.249	0.121				
					4.178	1.759	7.134	0.109				
					3.248	1.579	4.920	0.795				

Supplementary Information 11 (SI 11) – Changes in Aggregation due to Serum Concentration

	Starved									10% Serum									20% Serum								
	Extremity			Cytoplasm			Perinuclear			Extremity			Cytoplasm			Perinuclear			Extremity			Cytoplasm			Perinuclear		
	Avg B	Max B	Avg N	Avg B	Max B	Avg N	Avg B	Max B	Avg N	Avg B	Max B	Avg N	Avg B	Max B	Avg N	Avg B	Max B	Avg N	Avg B	Max B	Avg N	Avg B	Max B	Avg N	Avg B	Max B	Avg N
Mean	4.291	1.632	1.666	5.154	1.705	2.086	4.703	1.635	2.775	6.491	2.224	2.468	4.792	1.892	1.795	5.123	1.774	1.266	9.132	2.701	1.324	7.357	2.464	2.084	6.483	2.187	1.884
Std. Dev.	1.844	0.492	1.646	2.329	0.570	1.771	2.995	0.468	2.237	3.301	0.947	2.116	2.501	0.800	1.315	2.352	0.553	0.747	7.273	1.911	0.851	5.354	1.789	2.869	5.336	1.337	1.717
Min	2.252	1.155	0.148	2.124	1.109	0.107	0.496	1.061	0.094	2.435	1.224	0.347	2.272	1.208	0.345	2.074	1.116	0.197	2.328	1.215	0.296	2.003	1.047	0.190	2.195	1.104	0.419
Max	9.743	3.201	5.366	10.25	3.753	6.065	14.31	2.964	9.926	15.30	5.513	6.948	10.06	4.717	7.134	9.849	2.965	2.746	27.26	9.013	3.851	22.03	8.096	13.44	25.13	5.845	6.724
Data Values	3.310	1.386	0.387	9.765	1.919	0.919	3.981	1.304	0.824	2.435	1.224	0.585	2.485	1.381	0.889	2.272	1.219	0.409	21.22	5.969	0.521	3.260	1.179	0.190	2.401	1.104	0.709
	3.618	1.321	0.446	7.282	1.386	1.050	2.023	1.112	0.626	2.747	1.265	0.797	2.272	1.301	0.590	2.074	1.161	0.496	15.51	5.196	0.916	11.23	5.262	0.459	2.722	1.104	0.460
	4.801	1.510	0.148	10.25	3.753	2.756	2.151	1.066	0.405	11.58	5.513	1.412	3.012	1.564	0.779	2.239	1.134	0.261	6.864	2.308	2.918	7.753	1.297	0.260	2.624	1.220	0.575
	4.871	1.770	0.509	2.255	1.160	0.776	2.389	1.147	0.498	7.547	2.327	0.772	6.410	2.150	0.637	6.218	1.277	0.227	21.12	4.423	1.157	2.660	1.075	0.729	2.244	1.179	0.640
	5.028	2.053	0.983	5.799	1.725	1.186	3.012	1.348	0.497	4.626	2.344	1.668	3.297	1.526	0.689	3.023	1.116	0.197	5.583	1.929	1.425	2.921	1.159	0.566	25.13	5.845	1.516
	2.749	1.233	0.407	3.405	1.139	0.458	3.031	1.234	0.506	4.571	1.989	1.196	3.962	1.318	0.345	2.680	1.212	0.296	5.480	1.911	0.296	3.382	1.047	0.243	5.926	1.447	1.562
	5.103	1.498	0.312	2.517	1.287	0.641	3.930	1.428	0.568	13.06	3.740	1.436	2.549	1.350	1.443	6.444	1.692	1.563	8.731	2.011	1.176	3.828	1.559	0.662	3.185	1.245	0.419
	3.508	1.400	0.548	2.124	1.183	1.090	2.611	1.270	0.282	4.835	1.735	0.453	2.858	1.408	1.572	4.341	1.628	2.134	3.277	1.510	0.666	6.322	1.781	1.578	2.532	1.177	0.466
	2.901	1.258	0.712	2.146	1.110	0.225	2.721	1.068	0.130	5.322	1.970	1.489	8.540	2.581	1.767	9.727	2.338	0.736	4.846	1.840	0.761	3.828	1.350	0.533	6.269	1.461	0.911
	2.412	1.224	0.940	2.663	1.109	0.192	3.662	1.300	0.560	5.408	1.980	1.542	2.599	1.252	0.983	7.146	2.403	0.762	4.111	1.757	0.645	2.354	1.180	0.809	3.944	1.597	1.104
	2.451	1.155	0.307	2.457	1.118	0.124	2.023	1.061	0.197	4.535	1.940	1.116	9.654	3.084	3.012	4.507	1.562	1.530	21.62	4.283	1.589	16.90	2.773	0.951	2.662	1.286	0.531
	3.276	1.214	0.455	2.387	1.158	0.261	3.119	1.185	0.094	15.30	2.177	0.347	3.172	1.505	2.204	6.169	2.744	2.142	2.328	1.260	0.644	8.668	2.492	2.106	16.20	4.954	0.706
	2.917	1.169	0.346	6.607	2.297	0.750	3.906	1.557	1.546	5.924	2.163	4.862	4.507	1.652	1.804	9.849	2.965	1.354	3.064	1.278	0.745	3.350	1.350	0.512	2.195	1.258	1.244
	3.284	1.176	0.196	5.886	2.391	1.518	0.496	1.733	1.845	5.055	1.979	6.114	2.975	1.617	1.519	5.693	1.925	1.258	2.766	1.215	1.152	2.662	1.329	0.548	2.411	1.295	0.933
	2.634	1.244	0.231	2.883	1.448	3.469	4.488	1.785	1.756	4.789	2.097	4.588	3.526	1.596	1.819	4.066	1.704	1.513	3.383	1.231	0.787	2.622	1.245	0.838	3.181	1.530	3.925
	4.265	1.389	2.501	3.135	1.425	2.144	4.070	1.606	4.478	7.158	2.305	3.571	3.851	1.522	2.101	8.159	2.256	2.029	27.26	9.013	1.605	2.113	1.152	0.706	4.138	1.453	5.550
	2.252	1.521	1.660	4.527	1.407	1.860	3.293	1.650	5.888	6.861	1.885	6.948	3.277	1.401	1.102	3.232	1.323	0.966	4.286	1.601	2.199	5.647	1.632	2.650	7.633	3.248	3.748
	6.607	1.871	0.401	3.237	1.297	2.133	3.419	1.730	4.849	4.822	1.476	1.916	8.798	3.134	0.617	6.412	1.930	1.067	11.24	2.954	0.744	2.850	1.172	0.584	5.776	1.955	2.647
	3.325	1.539	1.106	4.000	1.328	2.019	2.784	1.119	2.432	10.24	2.183	5.045	6.400	1.597	2.822	3.492	1.501	1.891	5.424	1.807	1.721	2.850	1.220	0.476	6.220	2.125	2.566
	3.532	1.617	3.403	5.180	1.764	3.223	2.073	1.143	2.220	2.760	1.234	6.369	4.587	1.851	2.017	7.667	2.866	1.762	10.83	3.098	1.172	2.264	1.217	0.837	12.43	3.467	1.006
	4.837	2.041	2.551	3.029	1.625	5.639	2.526	1.184	2.113	4.208	1.351	2.876	4.587	1.830	2.007	3.671	1.579	0.978	10.66	2.297	1.281	6.112	1.928	6.695	12.34	2.760	6.724
	4.981	2.595	2.284	4.487	1.637	3.310	3.930	1.571	4.196	7.747	3.157	0.561	10.06	4.717	0.777	3.949	1.674	1.327	3.711	1.717	2.479	13.06	4.069	4.598	6.431	2.968	1.622
	2.414	1.161	5.324	4.333	1.882	4.373	4.648	1.612	5.505	7.761	3.108	1.092	8.413	3.817	2.270	2.571	1.381	2.669	6.678	1.525	3.851	2.003	1.153	10.27	3.706	1.446	0.946
	2.901	1.365	4.478	5.111	2.240	5.246	3.019	1.466	5.368				8.797	2.479	2.301	4.446	1.635	1.325				3.110	1.176	13.44	2.710	1.274	0.776
	3.421	1.592	5.366	6.526	1.576	0.750	6.778	2.722	2.201				6.085	1.811	2.131	8.039	2.118	2.746				4.448	1.560	2.166	3.848	1.505	2.646
	4.412	1.683	2.261	6.249	1.145	0.107	3.094	1.506	5.543				2.942	1.386	1.631							8.265	2.596	0.512	8.812	2.431	1.280
	3.374	1.467	4.965	9.144	2.281	3.107	4.173	1.546	5.119				9.279	2.640	2.355							17.99	7.812	1.996	5.866	1.892	1.617
	8.675	2.727	0.947	6.882	2.196	3.774	4.601	1.635	3.181				2.655	1.441	1.241							19.03	6.060	1.270	15.37	5.124	1.940
	9.743	3.201	1.717	7.635	2.738	0.735	5.773	2.086	5.562				3.422	1.633	0.867							5.197	2.590	1.101	9.074	4.069	5.864
	6.189	1.837	0.909	8.814	1.743	0.823	13.30	2.268	5.109				3.246	1.352	1.651							9.722	2.713	7.320			
	6.599	2.222	2.195	3.521	1.163	0.273	4.709	1.914	9.926				2.499	1.208	1.249							11.98	3.065	1.759			
	6.914	1.784	4.302	4.463	1.276	0.271	4.665	1.515	1.316				4.178	1.759	7.134							6.585	2.182	0.705			
				8.968	2.299	2.942	10.26	2.058	1.289				3.248	1.579	4.920							7.437	2.039	3.260			
				4.776	1.981	6.065	8.762	1.941	2.119													10.23	3.244	1.359			
				6.178	1.888	3.593	4.295	1.293	1.987													10.23	3.812	1.009			
				6.465	2.265	5.325	6.595	2.324	4.820													22.03	8.096	0.237			
				5.593	1.736	4.062	14.31	2.964	2.046													9.414	2.918	2.053			
							11.16	2.070	4.091													15.19	4.135	3.187			
							5.996	2.290	4.723																		
							6.523	2.210	4.425																		
							4.497	2.024	2.942																		

Supplementary Information 12 (SI 12) – Solution Size Dependent Aggregation

Base Pair	Avg B	Max B
120	1.32	56.17
240	1.57	72.95
495	1.69	72.58
1000	1.21	75.95
1985	1.06	88.22
Linear - 5485	1.34	79.44
Circular - 5485	1.17	86.51

Supplementary Information 13 (SI 13) – Cytoplasmic Size Dependent Aggregation

	DNA Size	Avg B	Max B	Avg N
8 Hr	120	1.17	13.41	0.44
	240	1.18	17.71	0.52
	495	1.05	11.59	0.40
	1000	1.08	11.79	0.38
	1985	1.11	7.09	0.57
	5485	1.05	7.74	0.68
	5485	1.29	27.78	0.29
	DNA Size	**Avg B**	**Max B**	**Avg N**
24Hr	120	1.19	7.31	0.71
	240	1.21	11.59	0.71
	495	1.08	7.36	0.36
	1000	1.06	6.77	0.38
	1985	1.19	5.59	1.59
	5485	1.02	5.55	0.81
	5485	1.03	6.68	0.73

Supplementary Information 14 (SI 14) – ccRICS Controls: Bleed through check

Description	Green Channel		Red Channel		Cross		Ratio Cross/ch1,ch2
	G0	D1	G0	D1	G0	D1	
Green primer alone	0.003196	40.48	0.000158	35.43			
	0.00344	35.18	0.000232	5.35	0.0002115	12.77	
	0.003803	59.68			0.0002944	81.42	
	0.003468	43.06					
	0.003704	57.37					
Red primer alone			0.024488	58.80			
			0.026006	59.24			
			0.025128	52.27			
			0.025285	69.00			
			0.024517	59.35			
Both primers together	0.006421	57.61	0.032504	67.92			
	0.006659	81.64	0.034084	57.40			
	0.006693	58.94	0.030869	59.54			
	0.006688	59.98	0.033285	61.88			
Dual labelled DNA	0.00601	36.07	0.031028	71.94			
	0.153118	13.06	0.237726	12.89	0.145792	10.05	0.75
	0.168629	18.29	0.254659	11.59	0.160024	9.94	0.76
	0.168202	16.76	0.25507	12.48	0.1752375	9.39	0.83
	0.161089	16.62	0.240512	11.46	0.17793	9.70	0.89
	0.161865	15.68	0.246243	11.92	0.1615108	8.04	0.79
Digested DNA	0.004898	30.54	0.008227	13.66			0.00
	0.004972	30.77	0.018781	10.87			0.00
	0.004669	28.21	0.007516	13.69	0.000491	22.11	0.08
	0.004394	19.92	0.007134	11.63	0.000538	8.66	0.09
	0.003997	29.93	0.006393	15.07	0.000423	9.32	0.08
	0.003869	22.27	0.006044	12.06			0.00
	0.003537	20.19	0.005749	14.19	0.00011	10.39	0.02

* Absence of a value represents zero

When primers were imaged alone, or together no or very little cross-correlation was observed. Only significant cross-correlation was determined when the primers were used to produce the dual labelled DNA, as all cross-G0 values were >75% of the green and red channel G0 averages. When degraded this ratio was <9%, or no cross-correlation was observed at all.

Supplementary Information 15 (SI 15) – PCR of Cell Fractions

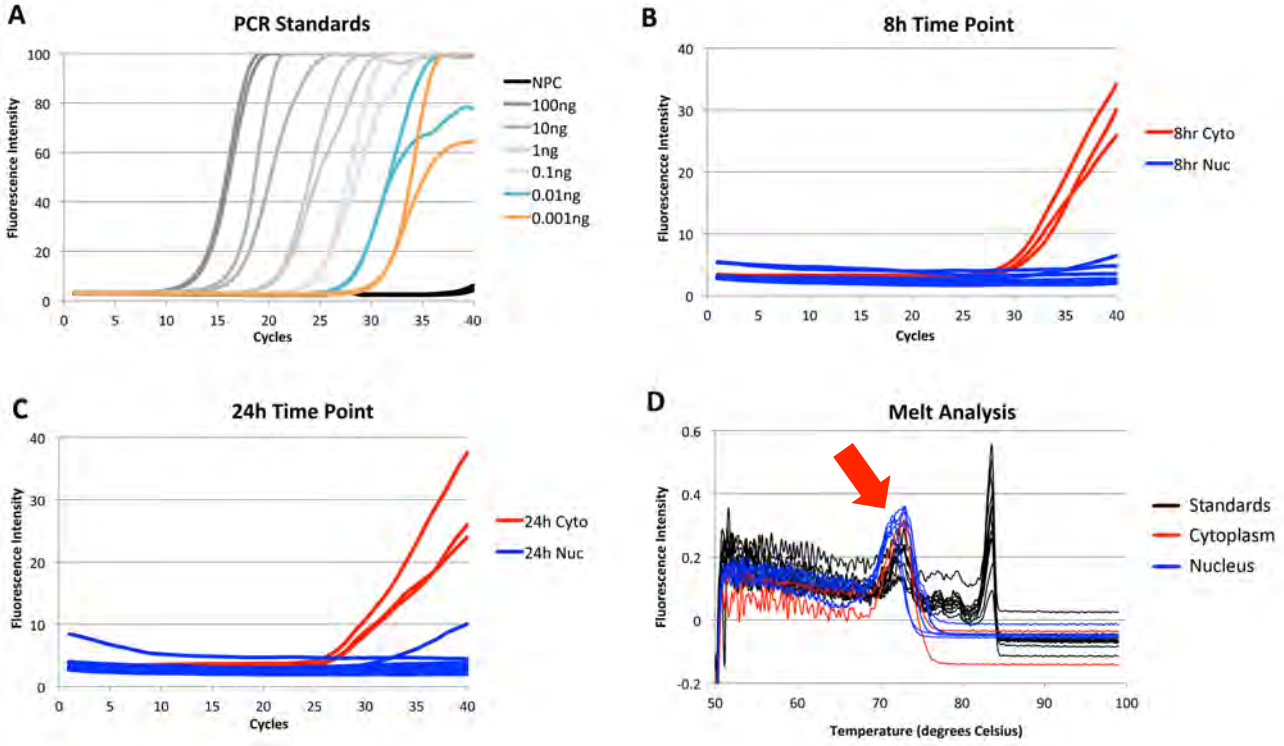

(A) Standards were run of various amount of DNA using the PCI-Neo plasmid as a template. Following delivery of the 495bp fragment cytoplasmic and nuclear extracts were obtained after 8h (B) and 24h (C). DNA was always present in the cytoplasm and at a greater amount compared to the nucleus, indicated by the earlier increase in fluorescence. (D) A high-resolution melt analysis was run in order to check for amplification specificity. All of the standards exhibited two peaks, at around 72 and 85°C. The first peak was representative of the 495bp fragment amplified, whereas the later peak was due to the plasmid backbone present in the reaction. All positive samples demonstrated the first peak highlighted by a red allow, showing specific amplification.

Supplementary Information 16 (SI 16) – Spectral Phasor 20% Serum

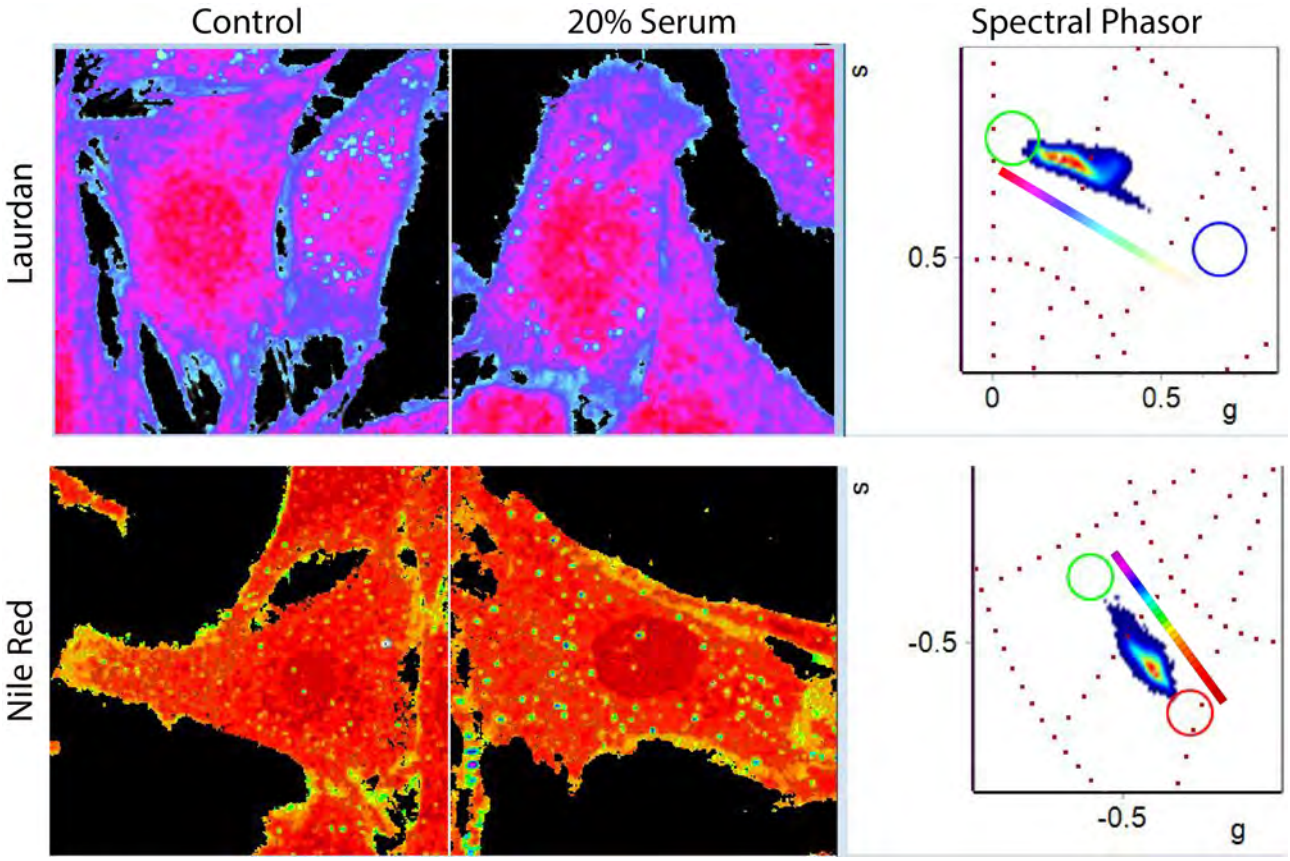

No significant differences were observed between the control cells (maintained in 10% serum), and those maintained in 20% serum. Through the use of the spectral phasor approach, the spectrum of laurdan and nile red appear very similar between the two conditions throughout the cell. The images of the cells are coloured based on the linked cursors selected in the spectral phasor plots.